IMAGING T_1, T_2 AND MYELIN WATER FRACTION IN THE POST-MORTEM MULTIPLE-SCLEROSIS CENTRAL NERVOUS SYSTEM

Amy Rebecca McDowell

Thesis submitted to Queen Mary University of London for the Degree of Doctor of Philosophy

September 2016

STATEMENT OF ORIGINALITY

I, Amy Rebecca McDowell, confirm that the research included within this thesis is my own work or that where it has been carried out in collaboration with, or supported by others, that this is duly acknowledged below and my contribution indicated. Previously published material is also acknowledged below.

I attest that I have exercised reasonable care to ensure that the work is original, and does not to the best of my knowledge break any UK law, infringe any third party's copyright or other Intellectual Property Right, or contain any confidential material.

I accept that the College has the right to use plagiarism detection software to check the electronic version of the thesis.

I confirm that this thesis has not been previously submitted for the award of a degree by this or any other university.

The copyright of this thesis rests with the author and no quotation from it or information derived from it may be published without the prior written consent of the author.

Signature:

Date:

Details of publications:

Optimising Phase Sensitive Inversion Recovery at 3T for cortical lesion detection in post-mortem Multiple Sclerosis brain; McDowell AR, Carassiti D, Papchatzaki MM, Miquel ME, Schmierer K. Accepted for poster presentation at the International Society for Resonance in Medicine meeting in May 2013 in London

Phase Sensitive Inversion Recovery in Post Mortem Multiple Sclerosis Spinal Cord: Shades of Grey and White; McDowell AR, Miquel ME, Thomas D, Papachatzaki MM, Carassiti D, Schmierer K. Accepted for poster presentation at the International Society for Resonance in Medicine meeting in May 2014 in Milan, Italy

Myelin and More: mcDESPOT applied to Post Mortem Multiple Sclerosis Spinal Cord; McDowell AR, Wood TC, Petrova N, Carassiti D, Miquel M, Thomas D, Barker GJ and Schmierer K. Accepted for poster presentation at the International Society for Resonance in Medicine meeting in June 2015 in Toronto, Canada

Myelin Water Imaging in Multiple Sclerosis Post Mortem Spinal Cord; McDowell AR, Petrova N, Vavasour I, Thomas D, Carassiti D, Miquel M, Kolind S and Schmierer K Accepted for poster presentation at the International Society for Resonance in Medicine meeting in May 2016 in Singapore

Details of collaborations:

The mcDESPOT work on the preclinical Aglient scanner detailed in sections 6.10, 7.4.2 and 9.7 was performed in collaboration with Dr Tobias Wood at the Preclinical Unit at King's College London

ABSTRACT

The subject of this thesis is the use of Magnetic Resonance (MR) Imaging to quantify biometric MR indices in the Multiple Sclerosis (MS) fixed post-mortem central nervous system (CNS) tissue. Evaluating these indices in fixed tissue allows for the use of histology to verify the findings of MRI. However, it must first be discovered if the indices can be evaluated in fixed post-mortem spinal cord tissue. There is very little literature in this specific area, though some in the fixed brain, the results of which have been assumed to be equivalent in the spinal cord without proof. Therefore, the methodology must first be verified before the consideration of any index as useful and translatable to in-vivo spinal cord.

This thesis concentrates on the evaluation of MR relaxometry methods using the indices T_1 and T_2 by themselves and to evaluate the myelin content of fixed post-mortem CNS tissue. The Carr-Purcell-Meiboom-Gill (CPMG) and Multi-component Driven Equilibrium Single Pulse Observation of T_1 & T_2 (mcDESPOT) sequences are used to calculate T_1, T_2 and the Myelin Water Fraction (MWF) which is believed to be proportional to myelin content in the CNS. This is performed at 3T in a clinical scanner and at 7T in a small animal and whole-body scanner. The methods are first evaluated for use in fixed post-mortem CNS tissue. The two myelin measurement methods are then compared to histological staining if appropriate and where available to verify that the results obtained are proportional to myelin content.

The T_1 and T_2 values in fixed tissue were found to be shortened in fixed tissue, T_2 values were so short as to be at the limits of measurement by a clinical scanner, and values converged in white and grey matter, and therefore contrast was found to be limited between these tissues. Proton density images provided the most contrast between tissues. However, even with shortened T_2 values, the CPMG sequence was able to identify the myelin water component in fixed tissue. The mcDESPOT algorithm struggled to separate the myelin water component due to clinical scanner limitations and the shortened, converging T_1 and T_2 values. However, the mcDESPOT algorithm was successful in discerning

the myelin water component in the high signal situation of a small bore 7T pe-clinical scanner.

An evaluation was then made of the usefulness of these indices for translation into clinical imaging. The CPMG sequence was found to be proportional to myelin content under all conditions, and therefore useful for disease monitoring in demyelinating diseases. The mcDESPOT sequence, was found to be proportional to myelin in some conditions, and is likely to be useful for monitoring myelination, though the sequence could not be fully validated in this thesis.

ACKNOWLEDGEMENTS

This work was funded by Barts and the London Charity and was undertaken at Barts and the London NHS Trust which is comprised of St Bartholomew's Hospital and the Royal London Hospital. Imaging was carried out at the MRI departments of both hospitals in Barts and the London NHS Trust, the Sir Peter Mansfield Magnetic Resonance Centre in Nottingham University and the Preclinical Imaging Unit in King's College London. The software used in this thesis for the calculation of DESPOT1, DESPOT2 and mcDESPOT was developed by Dr. Tobias Wood at the Preclinical Imaging Unit in King's College London, T_1 curve fitting software was developed by Joelle Barral at Stanford University, USA and CPMG T_2 curve fitting software by Dr. Irene Vavasour and Dr Thomas Prasloski at University of British Columbia, Canada.

In the generation of this work I owe sincere gratitude to many people along the way. A very special debt of gratitude is owed to the people with Multiple Sclerosis and those without who were generous enough to donate themselves to the MS Tissue Bank at Imperial College. Without these selfless acts of giving this project would not have been possible. I would also like to thank my supervisors, Dr Klaus Schmierer and Dr Marc Miquel who gave me the opportunity to undertake this project, with special thanks to Dr Schmierer for the education in Neurology which was definitely necessary and very interesting. I am especially grateful to Dr David Thomas who was utterly patient with my endless questions, always gently guided me in the right direction when I didn't know how to proceed and always managed to renew and inspire my positivity. I am incredibly grateful for your time.

And to all those who helped me and cheered me on, Sam, Shannon, Sean, Laura, Allison, Matt, Natalia to name but a few. Your help was invaluable; I couldn't have done it without you.

Last but in no way least my husband David, who always listened, was always on my side and was always ready with cups of tea. Quite frankly, there are no words for how much I appreciate your support in my thesis and everything else.

CONTENTS

List of Abbreviations

BFGS	Broyden–Fletcher–Goldfarb–Shanno
bSSFP	balanced Steady-State Free Precession
CPMG	Carr-Purcell-Meiboom-Gill
CNS	Central Nervous System
DDWM	Diffusely Damaged White Matter
DESPOT1	Driven Equilibrium Single Pulse Observation of T1
DESPOT2	Driven Equilibrium Single Pulse Observation of T2
DIR	Double Inversion Recovery
ETL	Echo Train Length
FWF	Free Water Fraction
GM	Grey Matter
IEWF	Intra/extra-cellular water fraction
LFB	Luxol Fast Blue
LGM	Lesional Grey Matter
LLS	Linear Least Squares
LM	Levenberg–Marquardt
LWM	Lesional White Matter
MBP	Myelin Basic Protein

mcDESPOT	multi-component Driven Equilibrium Single Pulse Observation of T1 and T2
MRI	Magnetic Resonance Imaging
MS	Multiple Sclerosis
MWF	Myelin Water Fraction
NAGM	Normal Appearing Grey Matter
NAWM	Normal Appearing White Matter
NLGM	Non-lesional Grey Matter
NLLS	Non-Linear Least Squares
NLWM	Non-lesional White Matter
NNLS	Non-negative Least Squares
NSA	Number of Signal Averages
OD	Optical Density
PD	Proton Density
PSIR	Phase Sensitive Inversion Recovery
pwMS	people with Multiple Sclerosis
RF	Radiofrequency
ROI	Region of Interest
SAR	Specific Absorption Rate
SE-IR	Spin Echo Inversion Recovery
SENSE	Sensitivity Encoding
SPGR	Spoiled Gradient Echo
SNR	Signal to Noise Ratio
TE	Echo Time
TI	Time of Inversion
TR	Time of Repetition
TSE-IR	Turbo Spin Echo Inversion Recovery
VISTA	Visualisation of Short Transverse relaxation time
WLLS	Weighted Linear Least Squares
WM	White Matter

Table of Figures

Table of Tables

1 AIMS, OBJECTIVES AND HYPOTHESIS

The aim of this work is the use of MR relaxometry to quantify T_1, T_2 and the calculation of myelin water fraction using the CPMG, DESPOT1, DESPOT2 and mcDESPOT sequences in the Multiple Sclerosis (MS) fixed *post-mortem* central nervous system (CNS). We hypothesise that once optimised, application of these techniques will enable their correlation with histological indices. This will allow the implementation of the first, key translational step between the 'ground truth' of histology with quantitative MR in people with MS (pwMS) *in-vivo*. This work mainly concentrates on the MS spinal cord given (i) the clinical importance of this part of the CNS for chronic disability in pwMS (see chapter 3) and (ii) previous studies have mainly investigated these MR indices in the brain, with the untested assumption that values acquired in the brain can simply be applied to the spinal cord.

First, however it must first be established if the chosen techniques can be successful in fixed *post-mortem* tissue. There is a larger body of work in the fixed brain than the spinal cord in MS. Therefore, sequence optimisation is first performed in fixed brain and then in the fixed spinal cord.

The CPMG sequence is used as a gold standard in myelin measurement as it has been histologically validated as corresponding to myelin content in the brain. This sequence is, however, time consuming, and the fast steady-state method of mcDESPOT to evaluate myelin content is clinically more practical. The mcDESPOT technique has not been histologically validated in either the brain or spinal cord in the literature. It is a combination of the fast steady-state methods of DESPOT1 to evaluate T_1 values and DESPOT2 to evaluate T_2 values. T_1 and T_2 values are then assigned to myelin component to create a quantitative map.

It is not known whether DESPOT1 is capable of determining the T_1 values of fixed post-mortem tissue and the T_1 values of fixed spinal cord at 3T is not known. Therefore, first the gold standard method of inversion recovery is applied to determine the T_1 values and then these are compared to the values from DESPOT1.

The same applies to the DESPOT2 sequence and therefore the T_2 values produced by this sequence are compared to single exponential CPMG evaluation.

The CPMG sequence is used to evaluate myelin content using a multi-exponent approach. However, it has not been verified in fixed spinal cord at 3T. The values obtained will be compared to the mcDESPOT algorithm myelin fraction values in fixed tissue at 3T.

The DESPOT1, DESPOT2 and mcDESPOT algorithms have not been applied at 7T, preliminary work at this field strength is presented here.

The double inversion recovery (DIR) Visualisation of Short Transverse relaxation time component (VISTA) sequence suppresses signal from all except myelin to give a myelin water image. The sequence is applied in post-mortem tissue, alongside the phase-sensitive inversion recovery sequence.

Chapter 1 is an explanation of the aims of this thesis

Chapter 2 consists of MR theory pertinent to the content of the thesis.

Chapter 3 consists of the clinical basis of MS

Chapter 4 is an evaluation of MRI in post-mortem tissue, MR in the spinal cord and finally a summary of the papers that have imaged fixed tissue with MR and compared to histology.

Chapter 5 is an explanation of the materials and methods developed to image *post-mortem* tissue successfully in a clinical scanner. As a number of scanners were used for imaging, they are detailed here.

Chapter 6 details T_1 map acquisition. As there is absence of published T_1 values at 3T in the *post-mortem* spinal cord, the methodology for producing T_1 maps using inversion-recovery spin echo and DESPOT1 is first evaluated in the post-mortem brain and compared to published literature *in-vivo*. The DESPOT1 algorithm has not been validated against standard measurement of T_1, therefore a choice of iterations and curve fitting methods is first verified, then T_1 maps of the *post-mortem* spinal cord are then created. Acquisitions in brain

and spinal cord at 3T and 7T on wholebody scanners are detailed. Section 6.13 contains separate work with the VISTA sequence for myelin imaging in a fixed *post-mortem* brain hemisphere.

Chapter 7 looks at T_2 in *post-mortem* brain and spinal cord. T_2 mapping methodology using a single-component T_2 method and DESPOT2 is first evaluated in the brain and then the spinal cord. The DESPOT2 algorithm has not been validated against standard measurement of T_2, therefore a choice of iterations, curve fitting methods in combination with the T_1 curve fitting method previously chosen in chapter 5 is verified. Acquisitions in brain and spinal cord at 3T and 7T on wholebody scanners are detailed.

The CPMG sequence examining the use of the multicomponent nature of T_2 to map the myelin water fraction is detailed in Chapter 8. Acquisitions at 3T of a brain hemisphere and then spinal cords with histological verification are shown. A preliminary acquisition of non-fixed tissue has also been described.

Chapter 9 contains work on the mcDESPOT sequence. The number of iterations and bounds for the search algorithm at 3T and in fixed *post-mortem* tissue had not been evaluated and were first determined in a brain hemisphere. This was then applied in the fixed *post-mortem* spinal cord. Joint preliminary work with King's College in the fixed *post-mortem* spinal cord imaged on a 7T pre-clinical scanner is also described.

Chapter 10 is a discussion of the work contained in this thesis with the conclusion in Chapter 11.

2 MAGNETIC RESONANCE IMAGING

Theory detailed in this section has been researched from Berstein, The Handbook of MRI Pulse Sequences[1]; Tofts, Quantitative MRI of the Brain[2]; Brown, Magnetic Resonance Imaging: Physical Principles and Sequence Design, Second Edition[3]; Elster, Questions and answers in Magnetic Resonance Imaging[4] and published research papers (referenced separately in the text).

2.1 NUCLEAR MAGNETIC RESONANCE (NMR)

In the quantum model, a nucleus has a nuclear spin number, I. This number is directly proportional to the particle's angular momentum and therefore its ability to undergo NMR. Nuclei with even numbers of both neutrons and protons have I = 0 possessing no angular momentum and are unable to undergo NMR under any conditions. All other nuclei have I > 0. The value for I for a particular nucleus determines the number of measureable discrete (Zeeman) energy levels when placed in an external magnetic field B_0. These energy levels E_m are equal to:

$$E_m = -m\gamma\hbar B \qquad \text{EQUATION 1}$$

Where γ is called the gyromagnetic ratio, ħ is Planck's constant divided by 2π, and m is a number that may assume the values –I, -I +1, …. , I – 1, +I.

There are (2I + 1) energy levels, each separated by

$$\Delta E = \gamma\hbar B \qquad \text{EQUATION 2}$$

According to Planck's law, the frequency (ω) of a photon corresponding to a quantized energy transition of size ΔE can be written:

$$\Delta E = \hbar\omega \qquad \text{EQUATION 3}$$

Combining the last two equations we obtain

$$\omega = \gamma B \qquad \text{EQUATION 4}$$

known as the Larmor relationship. Nuclei that possess I = ½ in biological tissue are ^{1}H, ^{13}C, ^{19}F, ^{23}Na, ^{31}P and ^{39}K. The most numerous nuclei in the clinical setting that exhibit the NMR phenomena is ^{1}H. ^{1}H has I = ½, and therefore two Zeeman energy levels, separated by a transition frequency $\omega = \gamma B_0$. These energy levels correspond to the two principal quantized states of a proton, denoted $|½\rangle$ and $|-½\rangle$, also known as the 'spin-up' and 'spin-down' states. The separation of Zeeman states is linearly dependent on the strength of the external field B_0, and hence the higher the field, the larger the separation and the larger the transition frequency between them (Fig. 1).

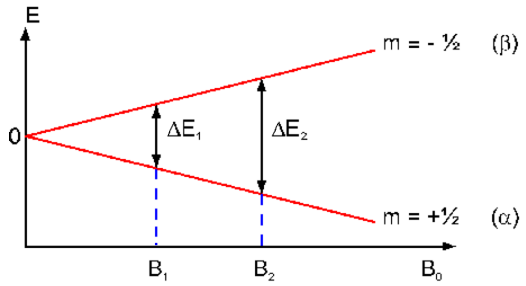

FIGURE 1: THE SEPARATION OF THE DISCRETE ZEEMAN STATES WITH VARYING B_0

2.2 APPLICATION OF A B_1 FIELD

The time dependent solution to the Schrödinger wave equation for a hydrogen nucleus is:

$$\Psi(t) = a\left|\frac{1}{2}\right\rangle + b\left|-\frac{1}{2}\right\rangle \qquad \text{EQUATION 5}$$

For a single proton placed in an external magnetic field, the terms a and b contain a single harmonic frequency ($\omega_0/2$ and $-\omega_0/2$, respectively), whose difference $[\omega_0/2-(-\omega_0/2)]$ is the Larmor frequency, $\omega_0 = \gamma B_0$. The probability of observing the two states $|½\rangle$ and $|-½\rangle$ can be shown to be $|a|^2$ and $|b|^2$ respectively. When a rotating radiofrequency (RF) field, B_1, is applied at the Larmor frequency perpendicular to B_0, its action on the wave function is to change the values of the a and b components while preserving their total amplitudes ($|a|^2+|b|^2$). Therefore, the amount of transverse magnetisation after a 90° 'rotation' is the same as the amount of longitudinal magnetisation

before the pulse. An B_1 pulse may be used to 'rotate' these components to any value of θ and ϕ where $0 \leq \theta \leq \pi$ and $0 \leq \phi \leq 2\pi$ as shown by the Bloch sphere (Fig. 2).

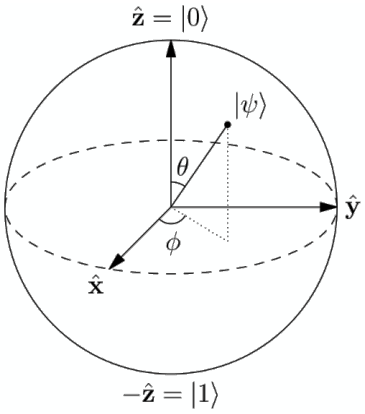

FIGURE 2: THE BLOCH SPHERE

The B_1 field must be applied at precisely the Larmor frequency in order to induce a precession in the B_1 plane. The angle of rotation or flip angle is given by:

$$\alpha = \gamma B_1 t_p \qquad \text{EQUATION 6}$$

where t_p represents the length of time the B_1 field is applied. Theoretically therefore, the flip angle can be controlled by varying magnitude or duration of the B_1 field. In practice however, B_1 is never a perfect pulse and the nuclei may be in or out of phase with it, meaning a different flip angle is applied than expected. After the B_1 pulse the nuclei return to the equilibrium state by interacting and releasing energy to the environment, called 'spin-lattice' relaxation, and other nuclei, called 'spin-spin' relaxation. The two relaxation methods are known as, spin-lattice relaxation or longitudinal relaxation T_1 and spin-spin relaxation or transverse relaxation T_2.

2.2.1 THE BLOCH EQUATIONS

The Bloch equations describe the phenomenon of NMR. $\mathbf{M} \times \mathbf{B}$ is the torque experienced by the nuclei when exposed to an external field B_0 where **M** is the induced magnetisation vector per unit volume of a substance and **B** is the static magnetic induction field vector measured in Tesla. The torque is equal to

the time rate of change of its angular momentum and the magnetic moment is proportional to the angular momentum through the gyromagnetic ratio γ which gives:

$$\frac{d\underline{M}}{dt} = \gamma\left[\mathbf{M}\times\mathbf{B}\right] \qquad \text{EQUATION 7}$$

This equation predicts simple precessional motion of **M** around **B** if the system is constant. However, the nuclei release energy to their environment and do not infinitely precess around B_0. To account for this, Bloch modified his original equation to account for this to:

$$\frac{\mathbf{d}\underline{\mathbf{M}}}{\mathbf{dt}} = \gamma\left[\mathbf{M}\times\mathbf{B}\right] - \mathbf{R}\left(\mathbf{M_t} - \mathbf{M_0}\right) \qquad \text{EQUATION 8}$$

where **R** is the relaxation matrix. Examining its individual components:

$$\frac{dM_x(t)}{dt} = \gamma M_y B_0 - \frac{M_x(t)}{T_2} \qquad \text{EQUATION 9}$$

$$\frac{dM_y(t)}{dt} = -\gamma M_x B_0 - \frac{M_y(t)}{T_2} \qquad \text{EQUATION 10}$$

$$\frac{dM_z(t)}{dt} = \frac{M_0 - M_z(t)}{T_1} \qquad \text{EQUATION 11}$$

The transverse magnetisation terms are governed by the T_2 relaxation constant. This is the transverse or spin-spin relaxation time, where the energy applied to the spins by a B_1 pulse is transferred to other spins. T_1 is the longitudinal or spin-lattice relaxation time and governs the evolution of M_z toward its equilibrium value M_0, where the energy is given to the 'lattice' or electrons surrounding the spins.

2.3 T_1 AND T_2 RELAXATION

2.3.1 LONGITUDINAL RELAXATION – T_1

The emission of energy from the spin system once the B_1 pulse has been applied can either be spontaneous or induced. The emission of energy is related to the frequency by $\Delta E = \hbar\omega$ (Eqn. 3). If the number of atoms in two states given by n_j and n_k, transition rates per atom are given by:

Absorption	j -> k	$B_{j->k}\upsilon(\omega)$
Stimulated emission	k -> j	$B_{k->j}\upsilon(\omega)$
Spontaneous emission	k -> j	$A_{k->j}\upsilon(\omega)$

Where $\upsilon(\omega)$ denotes energy density of radiation.

A and B are known as Einstein's A and B coefficients and are properties of atomic states. A and B can be shown to be related by:

$$B_{j\to k} = B_{k\to j} \quad and \quad A_{k\to j}\left(\omega\right) = B_{k\to j}\frac{\hbar\omega}{\pi c} \qquad \text{EQUATION 12}$$

The above equations show that emission is strongly frequency dependent. In the radiofrequency range used in NMR, spontaneous emission is very improbable therefore all energy emission in NMR must be stimulated. The reestablishment of thermal equilibrium of the nuclear magnetisation longitudinally following a B_1 pulse requires exchange of energy to the environment. The stimulated emission of energy occurs only when a proton encounters another magnetic field fluctuating near the Larmor frequency. This field is usually another proton or electron and this is known as a dipole-dipole interaction, either intramolecular dipole-dipole interaction or intermolecular dipole-dipole interaction. In order to produce a fluctuating magnetic field, the molecule must be moving. For rapid relaxation, the molecule must be rotating at the Larmor frequency. Water has a small molecular size and is moving too rapidly to be efficient at energy transfer. T_1 values for water are the longest of

the substances in the human body. When water is bound in proteins and macromolecules, its movement is slowed and the T_1 values are longer.

2.3.2 TRANSVERSE RELAXATION – T_2

T_2 relaxation results from any process that causes the spins to lose their phase coherence. Most frequently, it results from static or slowly fluctuating magnetic fields local to the spin. If a spin experiences a change in its local field, it will temporarily resonate at a different frequency and therefore gain or lose phase in comparison with other spins. T_2 relaxation occurs with or without energy exchange, therefore a process which causes T_1 relaxation will also cause T_2 relaxation but T_2 relaxation may occur without T_1 relaxation. It follows that T_2 values will always be shorter than T_1 values.

The T_2^* relaxation constant is equal to T_2 plus the dephasing effect from field inhomogeneity. T_2* can be considered the observed or effective T_2 produced by either intrinsic inhomogeneities in the magnet itself or susceptibility induced field distortions from tissue.

2.3.3 PROTON DENSITY

Proton density refers to the concentration of protons in the imaged tissue. Most protons in tissue are in water, and PD can be related to water content of the tissue. However, proton density in lipid is also high. All images have an intensity proportional to PD, in addition to other parameters such as T_1 or T_2-weighting. Therefore, any changes in PD, such as the removal of water by fixation of the tissue, will always affect the image obtained. Tissues with a low proton density such as white brain matter appear dark on the image, whereas a high proton density such CSF appear bright. Fluids have highest proton density (>95%) and water- and fat-based tissues have very similar proton densities (60% to 85%) because both water and lipids contain abundant hydrogen atoms.

The purpose of B_1 pulse sequences is to create a difference between the signal-generating transverse magnetisation components (spins), which optimally reflects the difference in T_1, T_2 or PD.

2.3.4 IMAGE FORMATION

An oscillating wave has three fundamental properties: amplitude, frequency, and phase.

$$S(t) = Asin(\omega_0 t + \phi) \qquad \text{EQUATION 13}$$

Where S(t) is the signal as a function of time, A is the amplitude, ω_0 is the angular frequency, and ϕ is the instantaneous phase. Varying these three parameters changes the appearance of the, in this case, sine wave. The NMR signal is a superposition of many waves, one from each spin. This signal is digitised by samples being taken of its amplitude and phase at certain time intervals. The sampling rate should be high to be sure that the waveform has been fully mapped.

2.3.5 THE GRADIENT FIELDS

When the NMR signal is sampled, it gives the waveform that is a sum of the whole signal given by every spin. It would be impossible to find which part of this accumulated signal came from which part of the object. To do this, each spin must be distinguished from its neighbour by some method. This is accomplished by manipulating the magnetic field to give a magnetic gradient across the sample or gradient field. Gradient fields establish a linear relation between the resonance frequency of the magnetic moment and its location (x, y, z) in the imaging volume. The frequency [Hz] and angular velocity [rad/s] will be directly proportional to the location. There are two spatially locating gradient fields G_x and G_y in two-dimensional imaging. An additional slice selective gradient is used in two-dimensional imaging, which in three-dimensional volume imaging is a spatially locating gradient in the z-direction, G_z. The 'read' gradient G_x changes the resonant Larmor frequency of the spins by a different amount at each point of the gradient. This therefore does not change the amplitude that gives the image but changes the frequency so each row in the sample differs from the next row. The gradient pulse G_y distinguishes each column from one another. It advances the nuclei by a certain amount that depends on G_y's duration and amplitude. It does not

change the amplitude, only changing the position of the nuclei in its precession, the phase.

2.3.6 SEQUENCE DESCRIPTION

Whenever a RF pulse is applied at the Larmor frequency to a sample, some component of the net magnetisation is tipped into the transverse plane. This generates a free induction decay (FID) signal which persists until the phase coherence is completely destroyed by T_2* decay. It therefore has the form of a rapidly decaying sine wave. The flip angle (FA) is the degree of tipping of the magnetisation from the z-axis by the RF pulse.

The repetition time (TR) is the time between the excitation of an imaging plane and the re-excitation of this same plane in an imaging sequence. The echo time (TE) is the time to a refocusing of magnetisation during the sequence.

2.3.7 K-SPACE

K-space is a plane that is used to store the information that composes an image. The sample emits a signal only while the spins precess around the z-axis until recovery after a B_1 pulse. The precession of the spins induces a fluctuating current in the receive part of the B_1 coil. This analogue waveform is sampled at a certain frequency and digitally stored in k-space. It is composed of many different sinusoidal waves which are decomposed by the use of the Fourier transform into the MR image. The signal is digitised and plotted in k-space, with its frequency and amplitude determining its position. The low frequency signals at the centre of k-space contribute to the main features of the image and if just those were converted into image space, only the main features and main contrast would be shown. The higher frequency signals at the edges of k-space form the fine features and contrast of the image. Noise related frequencies are spread across k-space, but the higher frequencies are more affected by these, causing degradation in fine feature resolution.

2.3.8 SIGNAL AVERAGING

Due to the low sensitivity of NMR, the signal-to-noise ratio may be improved by the addition of N successive experiments. With successive addition, the signals add coherently while the random phase of the noise causes it to add incoherently. As the noise power is additive, the root-mean-square noise amplitude is proportional to $N^{1/2}$, because of this the signal-to-noise ratio improves as $N/N^{1/2}$ or $N^{1/2}$. However, there is a limitation to the rate at which successive additions can be performed. The nuclear spin system must be allowed to recover its z-axis magnetisation to maintain full signal strength. For full recovery, there must be a delay of several T_1 relaxation times. Therefore, a limit is set on the number of co-additions that are possible in a given time.

2.3.9 SUSCEPTIBILITY ARTEFACTS

Magnetic field distortions are created by diamagnetic (calcium) and paramagnetic (ferritin) substances in the body. However, the difference in susceptibility between biological tissues and air also creates these distortions. These result in variations in precessional frequency across the object and even within individual voxels. This causes geometric distortion with signal loss from dephasing and incorrect spatial mapping, resulting in a signal void and bright areas of signal accumulation. Susceptibility artefacts are worse at high fields[5]. This can be seen in the equation Ludeke et al.[6] used to define the parameter γ_c to define the magnitude of susceptibility artefacts for a cylindrical compartment:

$$\gamma_c = \left(\frac{\Delta\chi}{2}\right)\left(\frac{B_0}{RG_z}\right) \qquad \text{EQUATION 14}$$

Where $\Delta\chi$ is the difference in magnetic susceptibility of adjoining substances, B_0 is the magnetic field strength, R is the cross-section radius, and G_z is the read gradient. The magnitude of the susceptibility artefact will increase with larger field strength.

2.3.10 STEADY-STATE IMAGING

Steady-state imaging occurs when the excitation pulses are applied at intervals less than the time taken for full recovery. The spins establish an equilibrium longitudinal magnetisation before each excitation pulse, which is less than the thermal equilibrium value. Given a repetition time TR and longitudinal relaxation time T_1 the equilibrium magnetisation immediately before the B_1 pulse for a repetitive single θ pulse experiment is:

$$M_z = M_0 \frac{1 - e^{-TR/T_1}}{1 - \cos\theta\, e^{-TR/T_1}} \qquad \text{EQUATION 15}$$

This equilibrium is established by equating the z-magnetisation just before the B_1 pulse, M_z at T = 0 to the z-magnetisation at T = T_R that remains from the preceding sequence, following relaxation.

The initial amplitude of the transverse magnetisation just after the θ pulse is:

$$M_y = M_0 \frac{1 - e^{-TR/T_1}}{1 - \cos\theta e^{-TR/T_1}} \sin\theta \qquad \text{EQUATION 16}$$

The maximum partial saturation signal amplitude is therefore not obtained for θ = 90° except where TR/T_1 is large. An optimum condition can be found by adjusting the flip (turn) angle θ to a value known as the Ernst angle, θ_E, for which:

$$\cos\theta_E = e^{-TR/T_1} \qquad \text{EQUATION 17}$$

For a ratio of T_R/T_1 of around 3 the relaxation between pulses is fairly complete and the optimum flip angle is close to 90°. Use of the Ernst angle requires care as incomplete transverse relaxation between successive experiments can lead to unexpected signals appearing in multiple pulses sequences. However, using correct spoiling gradient pulses during acquisition of the signal, these unwanted coherence signals can be eliminated.

2.3.11 OFF RESONANCE EFFECTS

In section 2.1.1.1, it was said that the B_1 field must be applied at precisely the Larmor frequency in order to induce a precession in the B_1 plane. As no RF or B_1 pulse is perfect, it is unlikely that the B_1 field is applied across the whole field of view at precisely the Larmor frequency. This leads to off-resonance effects; a state occurring when the Larmor frequency of a spin isochromat is different from that of the exciting RF field. It leads to a precession of the magnetisation in the transverse plane away from the on-resonance frequency. With an on-resonance RF pulse, the magnetisation will be rotated into the transverse plane and returned to the longitudinal axis at the same frequency. When the RF pulse is off-resonance, the magnetisation is rotated into the transverse plane and precesses in the transverse plane leading to a decrease in signal magnitude.

If an angular frequency offset is defined as $\Delta\omega = \gamma B_0 - \omega_{rf}$ and inserted into the Bloch equations shown in section 2.1.12, we have:

$$\frac{dM_x(t)}{dt} = \Delta\omega M_y - \frac{M_x(t)}{T_2} \qquad \text{EQUATION 18}$$

$$\frac{dM_y(t)}{dt} = \omega_1 M_z - \Delta\omega M_x - \frac{M_y(t)}{T_2} \qquad \text{EQUATION 19}$$

$$\frac{dM_z(t)}{dt} = -\omega_1 M_y + \frac{M_0 - M_z(t)}{T_1} \qquad \text{EQUATION 20}$$

where $\omega_1 = \gamma B_1$, the angular frequency of the B_1 field applied[1]. If ω_1 does not equal ω_0 then the B_0 field does not completely disappear in the rotating frame, and there is some residual magnetisation along the z-axis $B_{z'}$. The two fields B_1 and $B_{z'}$ vectorially add together to produce an effective field (B_{eff}) in the rotating frame. In this case, the trajectory of M becomes more complex. Instead of precessing around B_1, M now precesses in a cone around B_{eff} at frequency $\omega_{eff} = \gamma B_{eff}$.

There are also other causes of off-resonance effects that are inherent to the imperfect conditions of clinical imaging. The differing magnetic susceptibilities

of human tissues causes magnetic field gradients at the interfaces between tissues, and between tissue and air, causing signal loss, and signals not at the resonant frequency or off-resonance. These static susceptibility effects are the most common source of off-resonance effects. Eddy currents are another source of off-resonance effects which arise in conducting structures in the MR scanner when changes in the amplitude of the applied magnetic field gradients occur, such as during a sequence. Eddy currents decay away, and so produce time-varying off-resonance effects.

2.4 T_1 MAPPING

The T_1 values of a tissue (or a combination of the tissues in a voxel) can be displayed as a T_1 map, in which the pixel value shows the T_1 value, usually in milliseconds. The T_1 recovery rate can tell us about the mobility of the molecules (particularly water molecules) and hence the binding of water molecules, for instance, to macromolecules.

2.4.1 BIOLOGY

In normal tissues, T_1 values are related to macro-molecular concentration, water-binding and water content. In the brain for example, there is T_1 contrast between white and grey matter in the brain as the myelin in white matter has a shorter T_1 value. An increased water content in an area with abnormal pathology, such as inflammation, will show an increased T_1 value in line with increased water content. Molecules containing paramagnetic materials (such as deoxyhaemoglobin or contrast agents such as Gd-DTPA) give rise to much larger local magnetic fields, which gives rapid longitudinal relaxation.

2.4.2 SPIN-ECHO INVERSION RECOVERY SEQUENCE

The conventional method for quantitative T_1 map creation is the Inversion Recovery (IR) sequence. In its simplest form, the longitudinal magnetisation is inverted from equilibrium with a 180° pulse. The rate that the magnetisation recovers along the z-axis is given by T_1. After an Inversion Time (TI), a 90° pulse is applied which tips the current magnetisation into the transverse plane. It is then refocused with a 180° pulse (in a Spin Echo (SE) sequence), giving rise to an echo proportional to the magnetisation at TI on the z-axis.

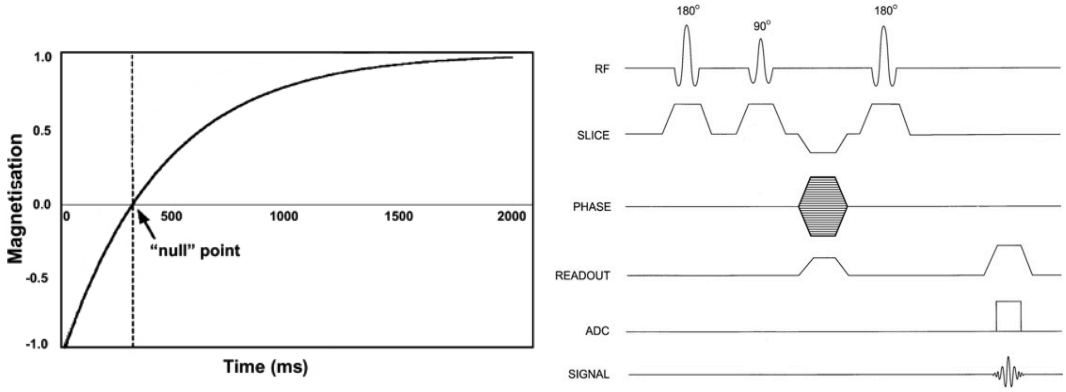

FIGURE 3: THE INVERSION RECOVERY CURVE (LEFT) AND SEQUENCE DIAGRAM (RIGHT)

The ideal theoretical equation of this process of recovery is:

$$S(TI) = S_0\left(1 - 2e^{-TI/T_1}\right) \qquad \text{EQUATION 21}$$

2.4.3 THE TURBO SPIN ECHO SEQUENCE

The turbo spin echo (TSE) sequence has, rather than one 180° refocusing pulse as a standard spin echo, a train of refocusing pulses. As the signal fades away the amount of information gained from each 180° decreases but much more information is gained. The sequence uses the information from the first Echo Time (TE) to fill the middle of k-space and the subsequent echoes (at multiples of the nominal TE) to fill in the rest of k-space. This means that the dominant contribution to the image is formed by the chosen TE time but the other echoes are used to speed up the sequence.

2.4.4 CONSIDERATIONS

2.4.4.1 When Repetition Time (TR) is not >>T_1

If the TR of the sequence is not larger than 5*T_1, the magnetisation will not fully recover about the longitudinal axis before the next inversion pulse is applied. After about five applications of a sequence with fixed TI and TR, the longitudinal magnetisation will reach a steady-state condition.

In a steady-state condition, the signal is proportional to

$$S \propto S_0\left(1-2e^{-TI/T_1}+e^{-TR/T_1}\right) \qquad \text{EQUATION 22}$$

T_1 quantification will be incorrect if a steady-state signal is fitted to equation 21. It is worth noting that both these methods rely on the assumption of a mono-exponential, one-pool-of-protons model. The multi-exponential nature of T_1 signal decay has been examined by Deoni et al.[7] and is accounted for in the mcDESPOT sequence.

2.4.4.2 Crushing the transverse magnetisation

All the signal models used in these sequences assume that the transverse magnetisation is crushed after acquisition of the FID. If this is not the case, there will be formation of spin and stimulated echoes. One method of doing this is the application of equal and opposite crusher gradients, but application of many B_1 pulses and crusher gradients may lead to transverse coherences occurring. This may be avoided by applying a phase shift of 117° which is incremented each TR as the method by Zur et al.[8].

2.4.4.3 Timing

The model above assumes a perfect knowledge of TI. TI is usually defined as the time between the middle of the inversion pulse θ_1 and the middle of the imaging pulse θ_2. However, inversion is not complete until the end of the inversion pulse. The program by Barral et al.[9] (see section 2.4.4.5) absorbs the timing error into their fit equation.

2.4.4.4 Imperfect B_1 Pulses

Amplitude errors in the B_1 pulse are the single most common cause of errors in T_1 measurements. For instance, in the case of an inversion recovery sequence, with an imperfect inversion pulse of flip angle θ, rather than 180°, the signal recovery curve will be modified from -1 at full inversion to -(1-cosθ)

So the theoretical equation is modified to:

$$S(TI) = S_0\left[-\left(-\cos\theta\right)e^{-TI/T_1}\right] \qquad \text{EQUATION 23}$$

The signal can then be fitted to find S_0, T_1 and the true θ_1.

There is also the error in the 90° pulse. This can be corrected by mapping the B_1 field across the slice, to provide the correct value of θ_2. There is also θ_3, the second 180° refocusing pulse, to be considered in the SE-IR sequence. According to Barral et al.[9] if TR >> T_1 and θ_1 is 180° then everything reduces back to Equation 20.

2.4.4.5 Processing

The processing of SE-IR data involves fitting the acquired TI points with an algorithm to the inversion recovery equation. However, deciding which equation and fitting model to use and which assumptions can be made to get an accurate value of T_1 with a reasonable processing time is key. The method given by Barral et al.[9] was used, which uses a non-linear least squares algorithm to fit to a five-parameter model. This is given by:

$$S(TI_n) = a + be^{-\frac{TI_n}{T_1}} \qquad \text{EQUATION 24}$$

where a and b are complex-valued parameters. This model has five unknown real-valued parameters: Re{a}, Im{a}, Re{b}, Im{b}, and T_1. This method has the advantages of resolving the B_1 errors and timing considerations described above. The Matlab program is provided on the internet at http://www-mrsrl.stanford.edu/~jbarral/t1map.html.

2.4.4.6 Processing considerations - Polarity Restoration

The Siemens scanner saves the data as magnitude images or polarity-restored with the 'real' reconstruction option. The use of the real reconstruction option on the scanner means that the relaxation curve is already polarity-restored for noise and accuracy considerations. This is covered more fully in section 2.5.

2.4.4.7 Processing considerations – Noise

In a real or imaginary image, the random noise distribution is Gaussian. In the case of modulus images, the effect of taking the modulus is to make this distribution Rician (always greater than zero and skewed). If the signal is measured close to zero where there is low signal to noise (SNR) ratio, the signal is over-estimated. The problem can also be reduced by using polarity-restored data from IR sequences. The noise contribution in polarity-restored data is neither Gaussian nor Rician but is at least symmetric about zero.

2.4.5 SPOILED GRADIENT ECHO SEQUENCES

In a gradient echo sequence, a B_1 pulse along with a constant gradient is applied along one axis of the scanner, and frequency and phase encoding applied along the other two axes. The frequency-encoding gradient is reversed to refocus the magnetisation vectors and generate a gradient-recalled echo.

If a train of B_1 pulses in a sequence has a TR significantly greater than T_2, the transverse magnetisation will have decayed before the next B_1 pulse. Therefore, the B_1 pulse will only act on the longitudinal magnetisation and the signal will depend on T_1. If TR is less than T_2 however, a remnant of the transverse magnetisation will remain as the next B_1 pulse is applied. This will result in 'Hahn' or partial echoes which add to the FID in a regularly spaced train of B_1 pulses. 'Spoiling' removes these transverse coherences. The SPoiled GRadient echo (SPGR) has T_1-weighting, with the degree of weighting depending on FA and TR. This sequence is known under several names dependent on manufacturer Siemens – FLASH (Fast Low Angle SHot), GE - SPGR and Philips - T1-FFE. This sequence uses low FA pulses with frequency and phase encoding blocks after,

then another low FA pulse with encoding blocks. Low flip angles create an appreciable amount of transverse magnetisation while the longitudinal magnetisation is left mostly undisturbed, i.e. the transverse magnetisation gained is greater than the longitudinal magnetisation spent. This property means that TR values can be very short (~2ms) giving a fast acquisition time.

2.4.5.1 Magnetisation transfer effects in SPGR

Magnetisation transfer (MT) is the exchange of spin magnetisation between the free water protons and macromolecular protons in biological systems after an off-resonance RF pulse. MT occurs when applying the RF pulse to tissue with two proton pools (e.g. a free water pool and a restricted pool coresponding the macromoecular protons). The thermal equilibrium between the pools is broken, resulting in spin exchange between these two pools. However, this also occurs when applying an on-resonance RF pulse or any RF pulse that effects the two pools differently. Also, as it is very unlikely that a RF pulse is perfectly on-resonance (or at the Larmor frequency) across the whole volume, parts will experience a off-resonance RF pulse and MT effects.

2.4.6 VARIABLE FA METHOD

Wang first developed the variable flip angle method in 1987[10]. In this method, data is acquired from different flip angles and used to calculate T_1 relaxation times. In a normal SE-IR sequence (described above in section 2.4.2) used for calculating T_1, a 90° pulse is applied (after a 180° inversion pulse), then a 180° refocusing pulse, generating a signal dependent on the amount of signal left in the exponential decay from the original 90° pulse. A modification of this method uses a gradient echo sequence, which does not use refocusing 180° B_1 pulses. A set of images can be acquired at various flip angles and used to generate a T_1 map, with less scanning time than a conventional saturation recovery or inversion recovery method.

The variable FA method linearises the Spoiled Gradient Echo (SPGR) equation

$$S_{SPGR} = \frac{M_0\left(1-E_1\right)\sin\left(\alpha\right)}{1-E_1\cos\left(\alpha\right)} \text{ where } E_1 = \exp^{\left(-TR/T_1\right)} \text{ and } \alpha \text{ is the flip angle} \quad \text{EQUATION 25}$$

TR is kept constant and a range of flip angles acquired. T_1 can then be found from fitting these values[11]. An extension of this method includes using only two values to fit the equation, and much work has been performed on optimising these two values to give the correct value of T_1 [10].

2.4.6.1 DESPOT1

Driven-Equilibrium Single-Pulse Observation of T_1 (DESPOT1) Relaxation was first proposed by Homer and Beevers in 1985[12] as a re-examination of the variable nutation method, and then modified for *in-vivo* by Deoni et al. in 2003[13]. The sequence used is a Spoiled Gradient Echo (SPGR) sequence. Unlike the inversion recovery techniques, the longitudinal magnetisation is driven into a steady state by the repeated application of the sequence and this is referred to by the Driven-Equilibrium part of the title.

Homer and Beevers proposed the variation of FA in this sequence in order to eliminate the need to measure M_0 in T_1 measurement as can be seen from the equation below

$$M_z = M_z \cos\theta \exp^{-t_i/T_1} + M_0\left(1-\exp^{-t_i/T_1}\right) \qquad \text{EQUATION 26}$$

the regression of M_z on $M_z\cos\theta$ for a fixed time t_i (TR) will yield a linear plot of slope $\exp(-t_i/T_1)$ from which to obtain T_1 as demonstrated below.

An *in-vivo* application of this technique was proposed by Deoni et al. in 2003[13]. The measured SPGR signal intensity (S_{SPGR}) is a function of the longitudinal relaxation time, T_1, repetition time, TR, flip angle a and a factor which is proportional to the equilibrium longitudinal magnetisation, M_0:

$$S_{SPGR} = \frac{M_0\left(1-E_1\right)\sin\left(\alpha\right)}{1-E_1\cos\left(\alpha\right)} \qquad where\ E_1 = \exp^{-TR/T_1} \qquad \text{EQUATION 27}$$

By holding TR constant and incrementally increasing α, a curve characterized by T_1 is generated. As demonstrated in Homer and Beevers[12], this equation can be rearranged to the linear form, y = mx + b as:

$$\frac{S_{SPGR}}{\sin(\alpha)} = E_1 \frac{S_{SPGR}}{\tan(\alpha)} + M_0(1 - E_1)$$ EQUATION 28

from which the slope, m, and the Y-intercept, b, can be estimated by linear regression, allowing T_1 and M_0 to be extracted:

$$T_1 = -\frac{TR}{\ln(m)}, \quad M_0 = \frac{b}{1-m}$$ EQUATION 29

In order to correct the off-resonance effects mentioned above a B_1 map must also be acquired.

2.5 PHASE SENSITIVE INVERSION RECOVERY

The Phase Sensitive Inversion Recovery (PSIR) imaging pulse sequence is a T_1-weighted sequence with an IR pre-pulse. There are two methods of 2DFT image reconstruction of IR sequence. The first is a modulus-image reconstruction algorithm which is common clinically. The second has a phase-correction for reconstructing "phase-sensitive" real IR-images. The second option generates "in-phase" images with an extended scale of contrast compared to the first option. The inversion pulse flips the longitudinal magnetisation from the +z to the -z direction. The magnetisation at the time of readout can therefore be positive or negative depending on the TI and tissue T_1 values. By preserving the sign of the MR signal intensity in the reconstruction, the scale of contrast is extended. The selection of TI should be made for optimum contrast of the tissue of interest.

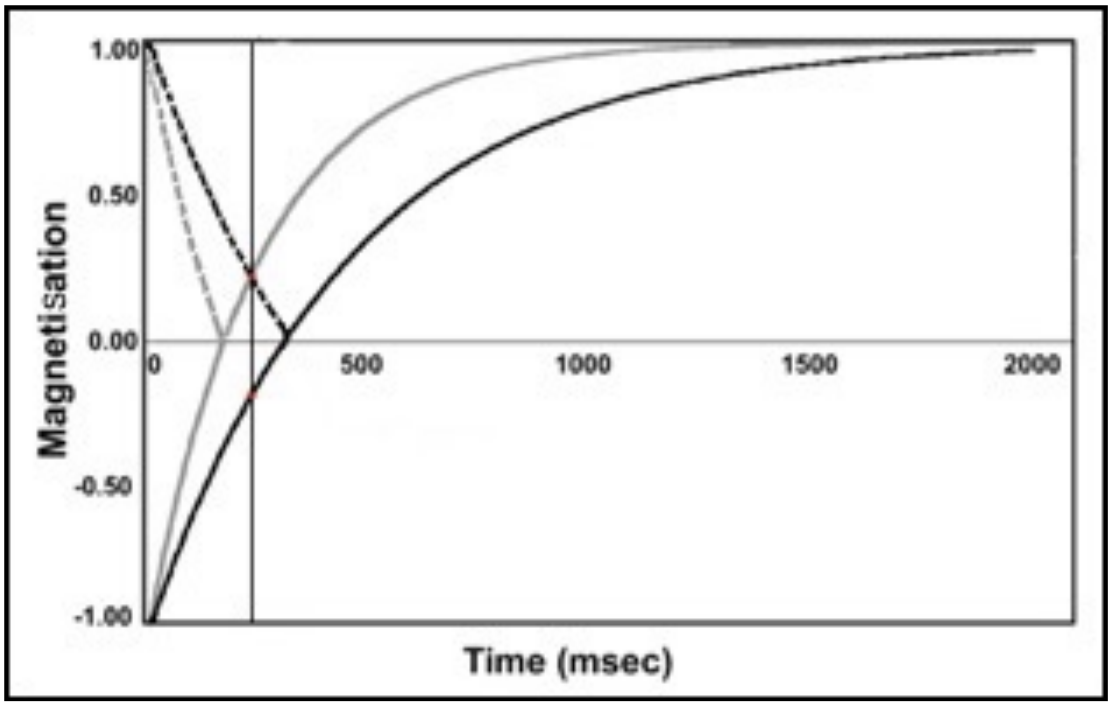

FIGURE 4: GRAPH SHOWING T_1 RECOVERY SHOWING THE EXTENDED RANGE OF CONTRAST GAINED OVER MAGNITUDE IMAGES

As soon as the longitudinal magnetisation is tipped into the transverse plane by an excitation pulse, phase errors begin to accumulate, obscuring the phase that would be used to determine the polarity of the longitudinal magnetisation immediately before excitation. Many factors contribute to the phase error. Examples include magnetic susceptibility variations, receiver resonance offset, phase associated with the B_1 field, eddy currents, gradient group delays, mismatches of frequency-encoding gradient and data acquisition window timing motion and flow. With the inclusion of the phase error, the 2D complex IR image intensity I(x,y) can be expressed as:

$$I(x,y) = I_{mag}(x,y)P(x,y)e^{-i\theta(x,y)} \qquad \text{EQUATION 30}$$

Where $I_{mag}(x,y)$ is the magnitude image intensity, P(x,y) is a binary function (i.e. P(x,y) = 1 or -1) describing the polarity of the longitudinal magnetisation immediately prior to the RF excitation pulse, and $\theta(x,y)$ is the phase error, which in general is spatially dependent. Thus the goal of phase-sensitive reconstruction is to recover $I_{mag}(x,y)P(x,y)$ from I(x,y). In the above equation, the polarity function and the phase error are coupled. If the phase error $\theta(x,y)$ is

known, then it can be removed from the equation and a real image $R(x,y) = I_{mag}(x,y)P(x,y)$ is easily obtained[1].

The method of phase correction proposed by Kellman et al.[14] using gradient echo imaging usually applied in fast cardiac imaging. This acquires two images at two different flip angles, 5° and 20°. The first 5° image is a reference image acquired without the IR pulse, and interleaved during the acquisition with the actual IR 20° image. This minimizes the spatial misregistration. The spatial phase map obtained from the reference images, is subtracted from the phase of the actual IR images on a pixel-by-pixel basis without assuming a specific spatial dependence. This method of phase correction improves image quality due to the correction of all the contributions to phase error but the acquisition time is greatly increased in comparison to a simple sign correction (e.g. 3h42m in contrast to 31m for a comparable standard TSE-IR sequence).

2.6 T_2 MAPPING

2.6.1 CARR-PURCELL-MEIBOOM-GILL (CPMG) SEQUENCE

The CPMG sequence was proposed in 1958 by Meiboom and Gill[15] as a modification of the sequence proposed by Carr and Purcell in 1954[16]. It is a 90° excitation with an echo train of 180° RF pulses as shown in figure 5 below. The magnetisation is repeatedly refocused and a number of echoes formed by each 180° pulse. Therefore, the T_2 decay curve can be plotted by the magnetisation remaining after each refocusing pulse, and the T_2 value calculated.

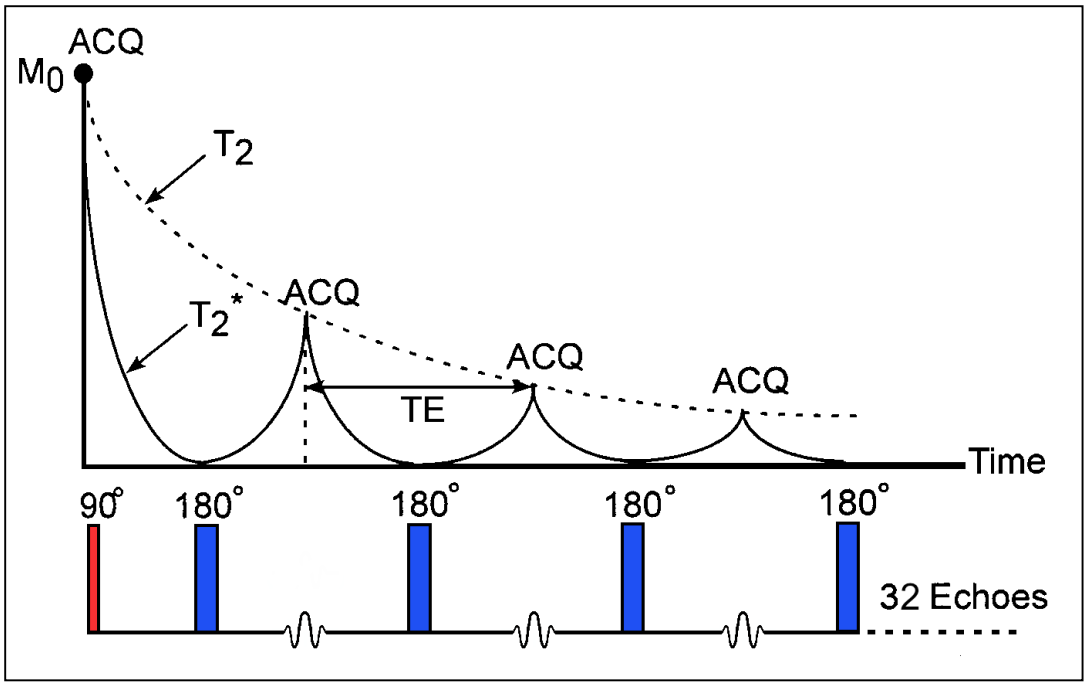

FIGURE 5: T_2 SIGNAL ACQUISITION USING THE CPMG SEQUENCE

The transverse magnetisation that forms the spin-echo can be repeatedly refocused by the addition of RF pulses into an echo-train. This series of echoes will reform additional echoes as the original signal decays exponentially at TE_1, TE_2, TE_3 … TE_n. Each echo fills its own independent k-space for an independent image at each echo time. The number of useful echoes will be limited by the T_2 decay in the material.

In this sequence, imperfections in the refocusing pulse flip angles due to B_1 inhomogeneity can cause image artefacts. If the magnetisation is flipped into the transverse plane with a 90°, then refocussed with an imperfect 180-ε° RF pulse, the magnetisation will not lie on the transverse axis again, but at ε° away from the axis. The application of a second, imperfect refocusing180-ε° RF pulse will then bring the magnetisation back into the transverse plane correctly. Therefore, only the even echoes will measure the true T_2 decay.

Careful sequence design can insure that echoes only occur at the desired temporal locations and that the echoes at each position are in phase with each other by applying certain conditions for the CPMG. If system experiences an imperfect refocusing RF pulse, then subsequent phase reversals, it will produce secondary spin echoes, in which case stimulated echoes will occur.

The more echoes there are in the train, the more unwanted echoes will be produced. They are unlikely to be in phase or coincide temporally with each other. The first condition uses phase cycling, where the phase of the RF pulses is changed between successive excitations in the echo train. In the CPMG sequence the phase and refocusing pulses are offset by 90° to each other:

($\alpha_{excitation,x}$) -> ($\alpha_{refocus,y}$) -> ($\alpha_{refocus,y}$) -> ($\alpha_{refocus,y}$)

This is the modification of the Carr-Purcell sequence by Meiboom and Gill to form the CPMG sequence. There should also be equal spacing between the consecutive refocusing pulses and the spacing must be twice the time interval between the first excitation RF pulse and the first refocusing RF pulse. The second condition stipulates that the phase accumulated by a spin isochromat between any two consecutive refocusing RF pulses must be equal:

$$\int_{t_1}^{t_2} G(t)dt = \int_{t_2}^{t_3} G(t)dt = \ldots = \int_{t_{N-1}}^{t_N} G(t)dt \qquad \text{EQUATION 31}$$

Where G(t) is a linear gradient along any axis. When these two conditions are both satisfied, the primary and the stimulated echoes occur only at the mid-point between two consecutive refocusing RF pulses and have the same phase.

Key issues for accurate *in-vivo* T_2 decay measurement are maintaining perfect 180° pulses in the presence of inhomogeneous B_1 and B_0 fields, and elimination of all contributions from stimulated echoes accruing from signal excited outside the selected slice[17]. In reality, inhomogeneities caused by the presence of the patient in the scanner and imperfections in the transmit of the B_1 pulse means the situation can never be perfect. A significant cause of B_1 field inhomogeneities is interference of the RF waves due to standing wave effects within the subject. This effect was found to be pronounced in the head in a paper by Yang et al.[18].

3D imaging techniques must be used with this technique, as the RF pulse train delivered during 2D multi-slice imaging to a given slice can serve as an off-resonance magnetisation transfer pulse for the other slices, leading to MT-related signal loss and incorrect T_2 calculation. In a very long echo train the MT

effect progressively increases. This does lead to time considerations, as 3D imaging results in a long acquisition time for a comparable resolution 2D scan.

2.6.2 BALANCED STEADY-STATE FREE PRECESSION (BSSFP)

The bSSFP sequence is a steady-state sequence as the SPGR sequence in section 2.4.5, however the transverse magnetisation is not spoiled leading to a coherent build-up of signal to steady-state value that is a mixture of the initial longitudinal and transverse components. The SSFP steady state is established during the sequence if the RF excitation pulses in the a-TR- a-TR- a-TR… sequence are phase coherent and TR is less than or of the order of T_2. Phase coherent here means that RF pulses all have the same phase or only a simple sign alteration phase cycle (a_x-TR- a_{-x}-TR- a_x-TR) is applied. A further condition for steady state is that the phase accumulated by the transverse magnetisation should be equal in each TR interval, therefore the gradient area in each TR interval must be equal to achieve this. If another additional consideration is added that the total gradient area on any axis is zero during each TR interval, a balanced steady state results. The bSSFP sequence provides larger signal than the SPGR sequences, but with various considerations that reduce image quality, such as signal banding.

If all these conditions are met, steady states for both the longitudinal and transverse magnetisation will be established, resulting in a signal that is dependent on both T_1 and T_2. The transverse magnetisation comprises two parts, a FID signal (S^+) that forms just after each RF pulse and a time-reversed FID-like signal (S^-) that forms just before (see below in Figure 6).

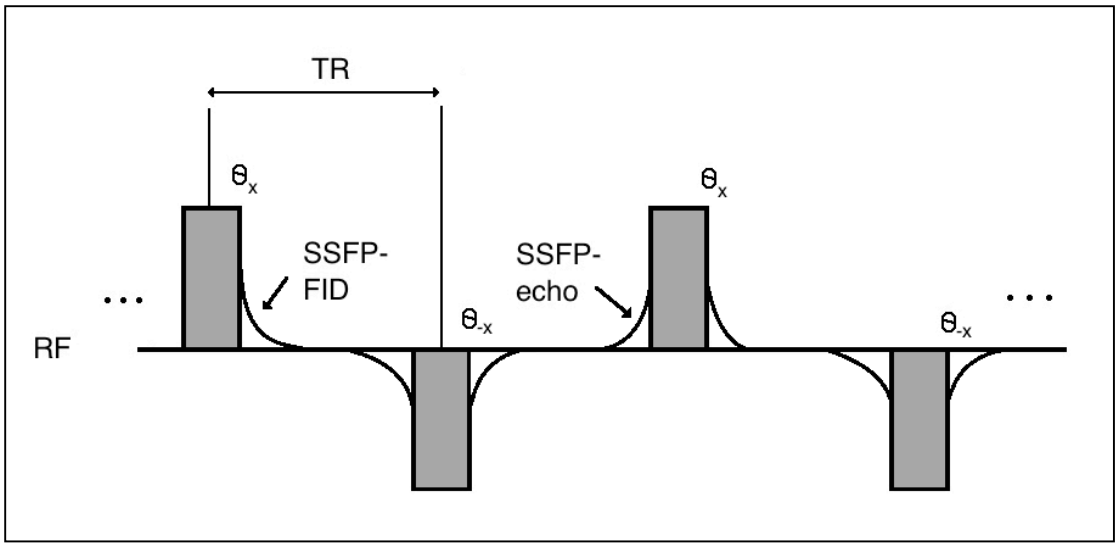

FIGURE 6: SCHEMATIC REPRESENTATION OF THE TRANSVERSE STEADY STATE FOR A SIGN-ALTERNATED PULSE TRAIN WHERE θ_X AND θ_{-X} ARE ALTERNATING POSITIVE AND NEGATIVE RF PULSES RESPECTIVELY

In a balanced steady state these two signals rephase at the same TE, and the bSSFP signal is the coherent sum of the two signals. The use of the sign alternated RF pulses increases signal as the RF pulses with a negative flip angle help drive the longitudinal magnetisation back to the equilibrium position. This increases signal when TR is much smaller than T_1.

It was stated earlier that the bSSFP is dependent on T_2, rather than T_2*. This is correct only if the bSSFP signal is rephased in the centre of the TR interval (TE=TR/2)[19]. As the peak of the signal is moved away from the centre T_2* weighting is introduced. This can be kept negligible by using a very short TR, but should be a consideration.

2.6.2.1 Banding Artefact

From Brown et al.[3], the steady-state magnetisation is determined by the total precession angle of the transverse magnetisation components during each TR given by

$$\beta_{total}(TR) = \gamma \Delta B TR + \gamma \vec{r} \cdot \int_0^{TR} \vec{G}(t) dt \qquad \text{EQUATION 32}$$

Where β_{total} is the resonance offset angle and ΔB are the background field inhomogeneities. The first term is the static field inhomogeneity-induced resonance offset angle and the second the gradient field. The condition that

the total gradient area during a TR must be zero means in a balanced SSFP sequence, the gradient term is zero. Therefore, the resonance offset angle depends only on the static field inhomogeneities.

As the static field varies as a function of position, β varies as a function of position within the image, leading to signal variation. Therefore, a varying static field will lead to a changing $\beta(\vec{r})$ and the dependence of the magnetisation components on the resonance offset angle.

Deoni et al. implemented a RF phase cycling scheme in DESPOT2 in 2004[20] in order to remove banding artefacts (RF phase is the term used to refer to the angle of the axis about which the RF pulse is applied). This phase cycling scheme can be used to remove the banding artefacts from the image if correctly applied, with no difference between acquisition of the same flip angle other than the increment of phase. Each flip angle is acquired with different phase values such as 0 and 180°. Incrementing the phase of the RF pulse from the standard 0° moves the banding artefact across the image, then with the application of a simple averaging calculation between the RF images at each flip angle, the banding artefact can be removed.

2.6.3 DESPOT2

Deoni et al.[13] first proposed the combination T_1 and T_2 mapping technique that combined the use of the SPGR sequence to calculate T_1 which is then used to inform the calculation for T_2 from the bSSFP sequence. The paper uses the SSFP signal equation first proposed in Perkins et al.[21]

$$S_{SSFP} = \frac{M_0\left(1-E_1\right)\sin\left(\alpha\right)}{1-E_1E_2-\left(E_1-E_2\right)\cos\left(\alpha\right)} \qquad \text{EQUATION 33}$$

Where $E_1 = \exp(-TR/T_1)$ and $E_2 = \exp(-TR/T_2)$. If TR is held constant and α is incrementally increased the signal curve depends on both T_1 and T_2. This equation can be converted into a linear form (y = mx + b) for straightforward fitting as below:

$$\frac{S_{SSFP}}{\sin(\alpha)} = \frac{E_1 - E_2}{1 - E_1 E_2} \times \frac{S_{SSFP}}{\tan(\alpha)} + \frac{M_0(1 - E_1)}{1 - E_1 E_2}$$ EQUATION 34

If T_1 and therefore E_1 is known then T_2 and M_o can be found from the slope (m) and intercept (b) of Eqn. 34:

$$T_2 = \frac{-TR}{\ln\left(\frac{m - E_1}{mE_1 - 1}\right)}$$ EQUATION 35

$$M_0 = \frac{b(E_1 E_2 - 1)}{1 - E_1}$$ EQUATION 36

2.6.3.1 Off-Resonance Effects in DESPOT2

The balanced steady-state sequence is sensitive to off-resonance effects. The DESPOT2 fitting algorithm maps the phase procession (frequency multiplied by the repetition time) in each voxel caused by off-resonance effects and combines this with RF phase-cycled bSSFP acquisition data to calculated phase corrected T_2 values. This was termed in Deoni et al.[22] as DESPOT2 with full modelling (DESPOT2-FM), which performs simultaneous voxel-wise off-resonance ($\Delta\omega$TR or f0) and voxel-wise T_2 calculation.

The RF phase cycling scheme moves the signal dropout caused by the procession of the phase in the transverse plane by an off-resonance RF pulse across the image. Figure 7 demonstrates a 0/180° phase cycling scheme. The solid line is the signal magnitude found in a voxel with phase precession according to a 0° RF pulse. The dotted line is the signal magnitude found in a voxel with a 180° RF pulse. As can be seen in this Figure 73 in this thesis where there is signal drop-off in the 0° acquisition, there is maximal signal in the 180° acquisition and vice-versa. Combining the images by taking the maximal signal in each voxel in each acquisition should remove the signal drop-out or banding artefact.

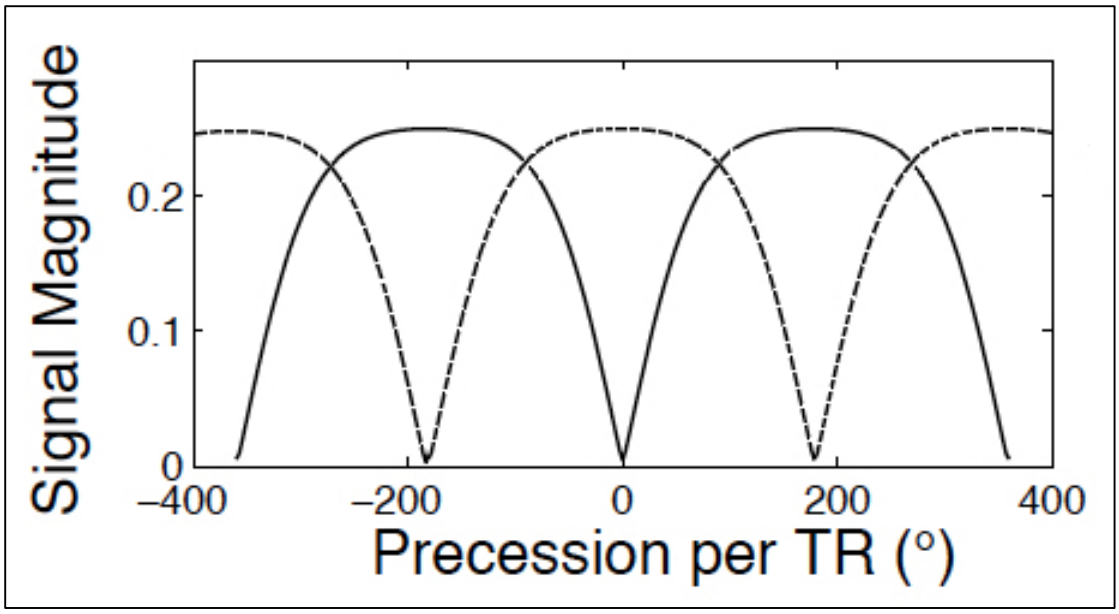

FIGURE 7: AN EXAMPLE PLOT OF THE SIGNAL (M_{XY}-MAGNETISATION) MAGNITUDE AS A FUNCTION OF RESONANCE FREQUENCY ADAPTED FROM HARGREAVES ET AL.[23]

The effect of off-resonance on the bSSFP signal can be examined in the general expressions for the equilibrium transverse magnetisation immediately preceding each RF pulse

$$M_x^- = \rho(1 - E_1)E_2 \, sin\alpha \, sin\beta / d \qquad \text{EQUATION 37}$$

and

$$M_y^- = \rho(1 - E_1)E_2 \, sin\alpha \, (cos\beta - E_2)/d \qquad \text{EQUATION 38}$$

where $E_1 = \exp(-TR/T_1)$, $E_2 = \exp(-TR/T_2)$, ρ is proportional to the equilibrium longitudinal magnetization, d is given by:

$$d = (1 - E_1 cos\alpha)(1 - E_2 cos\beta) - E_2(E_1 - cos\alpha)(E_2 - cos\beta) \qquad \text{EQUATION 39}$$

and β is the precession angle of the transverse magnetisation over the TR interval, expressed as:

$$\beta = \theta_{RF} + \Delta\omega TR \qquad \text{EQUATION 40}$$

In Eq. 40, θ_{RF} is the phase increment of the RF pulse and ω is the off-resonance frequency with respect to the central water peak.

The DESPOT2-fm algorithm performs a three-parameter nonlinear fit for ρ, $\Delta\omega$TR and T_2 using bSSFP data, to calculate T_2 even when $\Delta\omega$ is not equal to 0. The bSSFP data should be sampled over a range of RF phase increments and flip angles to give a robust fit in the presence of the banding artefact. All bSSFP data is normalised with respect to the mean value in order to eliminate the need to explicitly fit for ρ. The stochastic region contraction technique is used to fit for $\Delta\omega$TR and T_2.

2.7 MCDESPOT

DESPOT1 and DESPOT2 are based on the hypothesis that the relaxation in each voxel is characterized by a combination of a single T_1 and a single T_2. This assumes a single water environment within the voxel, ignoring the cellular structure (see section 4.4 for a clinical analysis of the water environments).

As given in Spencer et al.[24] and Deoni et al.[7], the steady-state SPGR magnetisation (M^{SS}_{bSSFP}) arising from two physically separated but exchanging species, F (fast relaxing) and S (slow relaxing), is given by:

$$M^{SS}_{SPGR} = M_{SPGR}(I - e^{A_{SPGR}TR})\sin\alpha \times \left(I - e^{A_{SPGR}TR}\cos\alpha\right)^{-1} \qquad \text{EQUATION 41}$$

Where

$$M_{SPGR} = \rho\left[f_F \; f_S\right]^T \qquad \text{EQUATION 42}$$

T denotes the transpose of the matrix; a is the flip angle; A_{SPGR} is given by:

$$A_{SPGR} = \begin{bmatrix} -\frac{1}{T_{1,F}} - k_{F\to S} & k_{S\to F} \\ k_{F\to S} & -\frac{1}{T_{1,S}} - k_{S\to F} \end{bmatrix} \qquad \text{EQUATION 43}$$

The column vector for the SPGR magnetisation can be written as:

$$M^{SS}_{SPGR} = \left[M^{SPGR,SS}_{z,F}, M^{SPGR,SS}_{z,S}\right]^T \qquad \text{EQUATION 44}$$

ρ is a factor proportional to the equilibrium longitudinal magnetisation; f_F and f_S are the volume fractions of the fast and slow species, respectively; T denotes the transpose of the matrix; and I represents the 2 × 2 identity matrix. k_{FS} and k_{SF} represent the exchange rates between the two species and are the reciprocals of the mean residence times τ_F and τ_S (the average time a proton is expected to remain in each compartment before exchanging to the to the other). In chemical equilibrium, these terms may be related as $f_F k_{FS} = f_S k_{SF}$.

The extension of this analysis to include both the longitudinal and transverse steady-state bSSFP magnetisation components (as both are driven to dynamic equilibrium) is given in Deoni et al.[25].

$$M_{bSSFP}^{SS} = \left(e^{A_{bSSFP}TR} - I\right) A_{bSSFP}^{-1} C \times \left[I - e^{A_{bSSFP}TR} R(\alpha)\right]^{-1} \qquad \text{EQUATION 45}$$

where I is the 6 × 6 identity matrix; R(α) is the rotation matrix (or the RF pulse); A_{bSSFP} is the expanded form of A_{SPGR} containing T_1, T_2 and off-resonance effects (with respect to the central water peak, Δω):

$$A_{bSSFP} = \begin{bmatrix} -\frac{1}{T_{2,F}} & k_{SF} & \Delta\omega_F & 0 & 0 & 0 \\ k_{FS} & -\frac{1}{T_{2,S}} - k_{SF} & 0 & \Delta\omega_s & 0 & 0 \\ -\Delta\omega_F & 0 & -\frac{1}{T_{2,F}} - k_{FS} & k_{SF} & 0 & 0 \\ 0 & -\Delta\omega_s & k_{FS} & -\frac{1}{T_{2,S}} - k_{SF} & 0 & 0 \\ 0 & 0 & 0 & 0 & -\frac{1}{T_{1,F}} - k_{FS} & k_{SF} \\ 0 & 0 & 0 & 0 & k_{FS} & -\frac{1}{T_{1,S}} - k_{SF} \end{bmatrix}$$

EQUATION 46

M_{bSSFP}^{SS} is now a vector containing the x, y, and z magnetisation of each species given by:

$$M_{bSSFP}^{SS} = \begin{bmatrix} M_{x,F}^{SS} & M_{x,S}^{SS} & M_{y,F}^{SS} & M_{y,S}^{SS} & M_{z,F}^{SS} & M_{z,S}^{SS} \end{bmatrix}^T \quad \text{EQUATION 47}$$

and C is related to the equilibrium longitudinal magnetisation

$$C = \rho \begin{bmatrix} 0 & 0 & 0 & 0 & \frac{f_F}{T_{1,F}} & \frac{f_S}{T_{1,S}} \end{bmatrix} \quad \text{EQUATION 48}$$

The measured two-component SPGR and bSSFP signals are

$$S_{SPGR}^{2-component} = M_{z,F}^{SPGR,SS} + M_{z,S}^{SPGR,SS} \quad \text{EQUATION 49}$$

and

$$S_{bSSFP}^{2-component} = M_{x,F}^{bSSFP,SS} + M_{x,IE}^{bSSFP,SS} + i\left(M_{y,M}^{bSSFP,SS} + M_{y,IE}^{bSSFP,SS}\right) \quad \text{EQUATION 50}$$

As the two pool model may not describe the situation fully, in 2013 Deoni et al.[26] expanded the model to three pools denoted by M, IE and F (Myelin water, Intra/extracellular water and Free water, please see section 4.4 for a clinical explanation of these water compartments). The M and IE pools are considered exchanging but the F pool is assumed to have no exchange with either M or IE.

The term M_{SPGR} from Eqn 41. is now rewritten from Eqn. 42 to:

$$M_{SPGR} = \rho \begin{bmatrix} M_F & IE_F & 1-\left(M_F + IE_F\right) \end{bmatrix}^T \quad \text{EQUATION 51}$$

and A_{SPGR} (Eqn. 43) is now written as:

$$A_{SPGR} = \begin{bmatrix} -\frac{1}{T_{1,M}} - k_{M\to IE} & k_{IE\to M} & 0 \\ k_{M\to IE} & -\frac{1}{T_{1,IE}} - k_{IE\to M} & 0 \\ 0 & 0 & -\frac{1}{T_{1,F}} \end{bmatrix} \quad \text{EQUATION 52}$$

Now A_{bSSFP} (Eqn. 46) is expanded to:

$$A_{bSSFP} = \begin{bmatrix} -\frac{1}{T_{2,M}} - k_{M\to IE} & k_{IE\to M} & 0 & \Delta\omega & 0 & 0 & 0 & 0 & 0 \\ k_{M\to IE} & -\frac{1}{T_{2,IE}} - k_{IE\to M} & 0 & 0 & \Delta\omega & 0 & 0 & 0 & 0 \\ 0 & 0 & -\frac{1}{T_{2,F}} & 0 & 0 & \Delta\omega & 0 & 0 & 0 \\ -\Delta\omega & 0 & 0 & -\frac{1}{T_{2,M}} - k_{M\to IE} & k_{IE\to M} & 0 & 0 & 0 & 0 \\ 0 & -\Delta\omega & 0 & k_{M\to IE} & -\frac{1}{T_{2,IE}} - k_{IE\to M} & 0 & 0 & 0 & 0 \\ 0 & 0 & -\Delta\omega & 0 & 0 & -\frac{1}{T_{2,F}} & 0 & 0 & 0 \\ 0 & 0 & 0 & 0 & 0 & 0 & -\frac{1}{T_{1,M}} - k_{M\to IE} & k_{IE\to M} & 0 \\ 0 & 0 & 0 & 0 & 0 & 0 & k_{M\to IE} & -\frac{1}{T_{1,IE}} - k_{IE\to M} & 0 \\ 0 & 0 & 0 & 0 & 0 & 0 & 0 & 0 & -\frac{1}{T_{1,F}} \end{bmatrix}$$

EQUATION 53

And C is now:

$$C = \rho \begin{bmatrix} 0 & 0 & 0 & 0 & 0 & 0 & \frac{M_F}{T_{1,M}} & \frac{IE_F}{T_{1,IE}} & \frac{F_F}{T_{1,F}} \end{bmatrix}^T$$

EQUATION 54

M_{SPGR}^{SS} and M_{bSSFP}^{SS} are now redefined as

$$M_{SPGR}^{SS} = \left[M_{z,M}^{SPGR,SS}, M_{z,IE}^{SPGR,SS}, M_{z,F}^{SPGR,SS} \right]^T$$

EQUATION 55

and

$$M_{bSSFP}^{SS} = \left[M_{x,M}^{bSSFP,SS}, M_{x,IE}^{bSSFP,SS}, M_{x,F}^{bSSFP,SS}, M_{y,M}^{bSSFP,SS}, M_{y,IE}^{bSSFP,SS}, M_{y,F}^{bSSFP,SS}, M_{z,M}^{bSSFP,SS}, M_{z,IE}^{bSSFP,SS}, M_{z,F}^{bSSFP,SS} \right]^T$$

EQUATION 56

The three-component SPGR and bSSFP signal is then given by

$$S_{SPGR}^{3\text{–}Component} = M_{z,M}^{SPGR,SS} + M_{z,IE}^{SPGR,SS} + M_{z,F}^{SPGR,SS}$$

EQUATION 57

and

$$S_{bSSFP}^{3\text{–}Component} = M_{x,M}^{bSSFP,SS} + M_{x,IE}^{bSSFP,SS} + M_{x,F}^{bSSFP,SS} + i\left(M_{y,M}^{bSSFP,SS} + M_{y,IE}^{bSSFP,SS} + M_{y,F}^{bSSFP,SS}\right)$$

EQUATION 58

This gives nine free parameters $T_{1,M}$, $T_{1,IE}$, $T_{1,F}$, $T_{2,M}$, $T_{2,IE}$, $T_{2,F}$, M_F, F_F and τ_M to be estimated. This cannot be done with a technique such as least squares, as these techniques rely on tight parameter estimates and converge to local minima and there is a large range of values that the residence time term τ may take. So a global technique, stochastic region contraction[27] (see section 2.6) is used to fit the data.

2.7.1 ACTUAL FLIP-ANGLE IMAGING: A METHOD FOR RAPID MAPPING OF THE B_1 FIELD

The mcDESPOT method is highly sensitive to variation in the B_1 excitation across the imaging volume. In order to correct for this, a map of the spatial distribution of B_1 must be acquired along with the mcDESPOT acquisition. This maps individual variations in the B_1 field which depend on the RF coil position relative to the sample, dielectric properties of the tissues, and the sample's size. The method available on the Philips scanner is an actual flip imaging (AFI) sequence proposed by Yarnykh[28]. This technique is a single-scan 3D acquisition of the actual flip-angle distribution in an entire object. The method employs a pulse sequence that consists of two identical RF pulses followed by two delays of different duration, where the first TR value (TR_1) is smaller than the second (TR_2). The ratio between TR_1 and TR_2 should be large enough in order to create sufficient signal difference between images. After each pulse, a gradient echo is acquired. It has been shown theoretically and experimentally that if delays TR_1 and TR_2 are sufficiently short so a the first-order approximation can be applied to exponential terms and the transverse magnetisation is completely spoiled, the ratio $r = S_2/S_1$ of signal intensities S_1 and S_2, acquired at the beginning of the time intervals TR_1 and TR_2, depends on the flip angle of applied pulses as

$$r \approx \frac{\left(1 + n\cos\alpha\right)}{n + \cos\alpha}$$

EQUATION 59

where n = TR_2/TR_1. This can be rearranged to

$$\alpha \approx \arccos\frac{rn-1}{n-r} \qquad \text{EQUATION 60}$$

This can then be used to calculate α for each voxel in the 3D volume. It is assumed that longitudinal relaxation is negligible during TR_1 ($TR_1 << T_1$) otherwise the signal will also depend on T_1, and that spoiling is ideal i.e. all transverse magnetisation is completely destroyed at the end of the delays TR_1 and TR_2.

The method allows fast 3D implementation and provides accurate B_1 measurements that are insensitive to T_1. It is a pulsed steady-state signal acquisition, which avoids long relaxation delays between sequence repetitions. The method has been shown to be useful for time-efficient whole-body B_1 mapping and correction of T_1 maps obtained using a variable flip-angle technique when non-uniform RF excitation exists.

2.8 FITTING ALGORITHMS

All of the techniques described in this thesis required curve fitting techniques used in the processing algorithms to calculate the desired parameter. Maps are calculated on a voxel-by-voxel basis.

i. DESPOT1 is available with the Linear Least Squares (LLS), Weighted Linear Least Squares (WLLS), and Non-linear Least Squares (NLLS) algorithm
ii. CPMG uses the Non-Negative Least Squares (NNLS) algorithm for fitting
iii. DESPOT2 has the options of the Broyden, Fletcher, Goldfarb and Shanno (BFGS) algorithm and a 2 step Levenberg–Marquardt (LM) algorithm
iv. mcDESPOT is implemented with stochastic region contraction (RC)

2.8.1 THE LINEAR LEAST SQUARES ALGORITHM

The LLS algorithm calculates T_1 by fitting to a linear transformation of a function relating signal intensity, flip angle, TR, T_1, and equilibrium longitudinal magnetisation M_0 (see section 2.4.6.1 for a mathematical explanation). TR is assumed constant and the SPGR equation arranged into linear form. This LLS

fitting method was first described by Gupta et al.[29] in 1977. The model is considered linear when it comprises a linear combination of the parameters i.e. a linear equation. Therefore, the slope, b, and the y-intercept, a, can be estimated by linear regression, i.e., by minimising the χ^2 objective function through an iterative fitting process:

$$\chi^2_{LLS}(a,b) = \sum_{i=1}^{n} \frac{1}{\sigma_i^2}(y_i - bx_i - a)^2 \qquad \text{EQUATION 61}$$

$$\chi^2_{LLS}(a,b) = \sum_{i=1}^{n} \frac{1}{\sigma_i^2}\left(\frac{s_i}{sin(\alpha_i)} - E_1\frac{s_i}{tan(\alpha_i)} - M_0(1-E_1)\right)^2$$

Where E_1 is exp(-(TR/T_1)), σ is the expected signal standard deviation due to noise.

2.8.2 NON-LINEAR LEAST SQUARES ALGORITHM

The NNLS algorithm is used when there is no closed-form solution to a least squares problem i.e. it cannot be arranged in a linear form. Instead the algorithm minimises the residuals for a best fit line to a non-linear equation as given below.

$$\chi^2_{NLLS}\left(M_0, T_1\right) = \sum_{i=1}^{n} \frac{1}{\sigma_i^2}\left(s_i - M_0 \sin\left(\alpha_i\right)\frac{1-\exp\left(-\frac{TR}{T_1}\right)}{1-\exp\left(-\frac{TR}{T_1}\right)\cos\left(\alpha_i\right)}\right)^2 \qquad \text{EQUATION 62}$$

Where σ is the expected signal standard deviation due to noise.

2.8.3 WEIGHTED LINEAR LEAST SQUARES ALGORITHM

The WLLS algorithm is similar to the LLS algorithm, but differs in that instead of treating all data points equally during the fitting, they are weighted according to noise, so the high SNR data influences the fit to a greater extent. Each image is weighted with the uncertainty that takes into account the adjustment of noise contribution due to the rearrangement of a nonlinear model into a linear one

$$\chi^2_{WLLS} = \sum_{i=1}^{n} \frac{1}{\sigma_i^2}\left(s_i - M_0 sin(\alpha_i)\frac{1-E_1}{1-E_1 cos(\alpha_i)}\right)^2$$ EQUATION 63

$$\chi^2_{WLLS} = \sum_{i=1}^{n} \frac{1}{\sigma_i^2}\left(\frac{sin(\alpha_i)}{1-E_1 cos(\alpha_i)}\right)^2\left(\frac{S_i}{sin(\alpha_i)} - E_1\frac{S_i}{tan(\alpha_i)} - M_0(1-E_1)\right)^2$$

Where E1 is exp(-(TR/T_1)), σ is the expected signal standard deviation due to noise. It can be seen when comparing Eqn. 63 with Eqn. 61, that the weighting term can be defined as

$$w_{WLLS}(i) = \frac{1}{\sigma_i^2}\left(\frac{\sin(\alpha_i)}{1-E_1\cos(\alpha_i)}\right)^2$$ EQUATION 64

2.8.4 NON-NEGATIVE LEAST SQUARES

The NNLS algorithm is used with T_2 mapping method described in Chapter 8, reconstructing maps from the CPMG sequence described in section 2.6.1. In this technique the NNLS algorithm is used in conjunction with the extended phase graph algorithm, described below in section 2.8.5.

The NNLS algorithm is a version of the least squares algorithm where the coefficients are constrained to be non-negative. This algorithm is a function that is available with the Matlab program (www.mathworks.co.uk), and is used to solve non-negative least-squares curve fitting problems of the form

$$\min_x \|C \cdot x - d\|_2^2, where\ x \geq 0$$ EQUATION 65

2.8.5 THE EXTENDED PHASE GRAPH ALGORITHM

Generally, the Extended Phase Graph (EPG) algorithm[30] is a iterative method which calculates the echo amplitudes (M_1, . . ., M_{ETL}) as a fraction of initial longitudinal magnetisation after the application of each 180° pulse in a long echo train. Here the EPG method is applied in conjunction with the NNLS algorithm to the 32-echo train of the CPMG sequence. It allows calculation of all echoes given flip angles, T_1, T_2, and interecho time (TE) as inputs.

$$\begin{bmatrix} M_1 \\ M_2 \\ \vdots \\ M_{ETL} \end{bmatrix} = M_0 \cdot \sin\alpha_{ex} \cdot PD \cdot EPG\left(ETL, TE, T1, T2, \alpha_{1,2,\ldots,ETL}\right) \qquad \text{EQUATION 66}$$

$$\alpha_i = A\left(x, y, z\right) \cdot \alpha_{prescribed,i} \quad \left(i = ex, 1, \ldots, ETL\right) \qquad \text{EQUATION 67}$$

The equation above describes the calculation of an echo decay vector, where M_0 is the longitudinal magnetisation preceding the excitation pulse, is the excitation pulse a_{ex} flip angle, PD is the proton density, ETL represents the echo train length, and TE is the interecho spacing. In Eqn. 67, A is a unitless, spatially varying constant unique to each voxel, which describes the effects of field inhomogeneities on the refocusing angle, with the assumption that B_1 is a linear system. It can be assumed that factors affecting the B_1 value at each voxel are unchanged during the application of the echo train and that the actual value of each angle is scaled by the same factor in each voxel. It is assumed that neither the angle of the pulse applied changes or is there movement of the sample.

It tracks the populations of phase states after dividing the spins into three different states representing spins in the transverse plane, both dephasing and rephasing, and spins along the longitudinal axis. A constant echo spacing is assumed.

$$MPSV = \begin{bmatrix} F_1 \\ F_1^* \\ Z_1 \\ F_2 \\ \vdots \\ F_{ETL} \\ F_{ETL}^* \\ Z_{ETL} \end{bmatrix} \quad where \quad \sum_{n=1}^{n=ETL} F_n + F_n^* + Z_n = 1 \qquad \text{EQUATION 68}$$

A Magnetisation Phase State Vector (MPSV) is first initialised with a normalization condition stipulating the total number of spins in each state is

equal to 1 before relaxation. F states refer to spins in the transverse plane that are dephasing, F* states refer to spins in the transverse plane that are rephasing, and Z states refer to spins along the longitudinal axis that maintain their phase

The number of sub-states which must be accounted for is equal to the length of the echo train (ETL), as this is the maximum number of phase increments a spin may dephase. Therefore, the MPSV has a length equal to 3 × ETL.

Before excitation, all spins are along the longitudinal axis and do not have any phase. After excitation, all spins are in the transverse plane and dephasing so the population of F_1 is 1. We now use a series of matrices to apply the effects of RF refocusing, phase transitions, and relaxation.

Each refocusing pulse is applied to each set of F, F*, and Z where the superscript ''+'' indicates new values reflecting the application of the RF pulse.

$$\begin{bmatrix} F_n \\ F_n^* \\ Z_n \end{bmatrix}^+ = \begin{bmatrix} \cos^2(\alpha/2) & \sin^2(\alpha/2) & -i\sin\alpha \\ \sin^2(\alpha/2) & \cos^2(\alpha/2) & i\sin\alpha \\ -\frac{1}{2}i\sin\alpha & \frac{1}{2}i\sin\alpha & \cos\alpha \end{bmatrix} \begin{bmatrix} F_n \\ F_n^* \\ Z_n \end{bmatrix} \qquad \text{EQUATION 69}$$

To simultaneously apply the RF pulse to all states, we construct square block matrix R(a) of size 3 x ETL with the above 3 x 3 matrix located along its diagonal.

Between refocusing pulses, spins are allowed to transition between phase states such that the spins in F_n transition to F_{n+1}, F_n^* transition to F_{n-1}^*, Z_n states are

unchanged but most importantly F_1^* transitions to F_1 as given by the matrix below.

$$\begin{bmatrix} F_1 \\ F_1^* \\ Z_1 \\ F_2 \\ F_2^* \\ Z_2 \\ F_3 \\ F_3^* \\ Z_3 \end{bmatrix}^+ = \begin{bmatrix} 0 & 1 & 0 & 0 & 0 & 0 & 0 & 0 & 0 \\ 0 & 0 & 0 & 0 & 1 & 0 & 0 & 0 & 0 \\ 0 & 0 & 1 & 0 & 0 & 0 & 0 & 0 & 0 \\ 1 & 0 & 0 & 0 & 0 & 0 & 0 & 0 & 0 \\ 0 & 0 & 0 & 0 & 0 & 0 & 0 & 1 & 0 \\ 0 & 0 & 0 & 0 & 0 & 1 & 0 & 0 & 0 \\ 0 & 0 & 0 & 1 & 0 & 0 & 0 & 0 & 0 \\ 0 & 0 & 0 & 0 & 0 & 0 & 0 & 0 & 0 \\ 0 & 0 & 0 & 0 & 0 & 0 & 0 & 0 & 1 \end{bmatrix} \begin{bmatrix} F_1 \\ F_1^* \\ Z_1 \\ F_2 \\ F_2^* \\ Z_2 \\ F_3 \\ F_3^* \\ Z_3 \end{bmatrix}$$

EQUATION 70

An echo is formed when F_1^* transitions to F_1 because the change from rephasing to dephasing necessitates a period of coherence when spins are in phase and are measurable.

Relaxation is described using a complex version of the Bloch rotation matrix derived by Hennig in 1998. It is described by a diagonal matrix that simply multiplies each component of the MPSV by a relaxation factor quantifying the exponential relaxation for a period of TE/2.

$$\begin{bmatrix} F_1 \\ F_1^* \\ Z_1 \\ F_2 \\ F_2^* \\ Z_2 \\ F_3 \\ F_3^* \\ Z_3 \end{bmatrix}^+ = \begin{bmatrix} E2 & 0 & 0 & 0 & 0 & 0 & 0 & 0 & 0 \\ 0 & E2 & 0 & 0 & 0 & 0 & 0 & 0 & 0 \\ 0 & 0 & E1 & 0 & 0 & 0 & 0 & 0 & 0 \\ 0 & 0 & 0 & E2 & 0 & 0 & 0 & 0 & 0 \\ 0 & 0 & 0 & 0 & E2 & 0 & 0 & 0 & 0 \\ 0 & 0 & 0 & 0 & 0 & E1 & 0 & 0 & 0 \\ 0 & 0 & 0 & 0 & 0 & 0 & E2 & 0 & 0 \\ 0 & 0 & 0 & 0 & 0 & 0 & 0 & E2 & 0 \\ 0 & 0 & 0 & 0 & 0 & 0 & 0 & 0 & E1 \end{bmatrix} \begin{bmatrix} F_1 \\ F_1^* \\ Z_1 \\ F_2 \\ F_2^* \\ Z_2 \\ F_3 \\ F_3^* \\ Z_3 \end{bmatrix}$$

EQUATION 71

Where

$$E1 = \exp\left(-\frac{TE}{2T_1}\right) \quad and \quad E2 = \exp\left(-\frac{TE}{2T_2}\right)$$ EQUATION 72

As a result, the echo decay curve is a function of not only T_2 but also T_1 and refocusing pulse flip angle.

Many of these decay curves are calculated over a range of 40 logarithmically spaced T_2 values ranging from 0.015 to 2s[31] yields an objective function for a Non-Negative Least Squares fit. However, this assumes that the sequence of refocusing pulse angles is known and that A itself is known. As A cannot be known without acquiring a B_1 map (adding time to the acquisition), multiple values of A (eight points linearly spaced between 0.28 and 1) are calculated, each via a single NNLS fit without smoothing. This calculated decay curve is then back projected from the NNLS solution and evaluated against the experimental decay curve[32].

2.8.6 2 STEP LEVENBERG–MARQUARDT ALGORITHM

The Levenberg-Marquardt algorithm[33,34] is a combination of gradient descent and Gauss-Newton methods. The gradient descent method starts with an initial guess then will descent towards a solution, minimising the cost function most quickly for a given change in parameter values after every iteration. However, the algorithm tends to zigzag along the bottom of long shallow canyons of solution space (where the solution space is the feasible region defining the set of all possible solutions) approaching the best fit solution very slowly. The Gauss-Newton algorithm converges quickly but the parameters returned by the algorithm can be far from reasonable values, and also algorithm will converge slowly or not at all if initial guess is far from minimum. The combination of these two algorithms means that the benefits of each algorithm of quick convergence from the initial guess and quick convergence when the minimum is difficult to find.

2.8.7 THE BROYDEN, FLETCHER, GOLDFARB AND SHANNO (BFGS) ALGORITHM

The BFGS algorithm is based on Newton's method for unconstrained minimisation which minimises the function f(x) where f(x) is twice continuously differentiable. The algorithm computes the gradient of solution space, until $\nabla f(x) = 0$ is found. This method results in a fast convergence but is computationally expensive as the second derivatives must be calculated at each point. It should also be noted that the iterates of Newton's method are equally attracted to local minima and local maxima.

2.8.8 STOCHASTIC REGION CONTRACTION

A full description of stochastic region contraction is included in Deoni et al.[7]. The initial set of boundary conditions (maximum and minimum) of all parameters to be determined by the algorithm is chosen by the user. After this, the 100 combinations of pairs within these boundaries with the lowest sum-of-squares residuals are chosen to seed the simplex optimisation. Then pairs of these "parent" combinations are chosen using roulette-wheel selection and combined to create new "child" combinations. To create each child, the parameters are individually selected from either parent with a 50/50 random chance. The residuals for all parent and child combinations are then calculated, and the 100 combinations with the lowest residuals are again chosen and used to seed the next cycle of the optimisation. This process repeats until the five combinations with the lowest residuals are unchanged over three successive iterations. The solution with the lowest residuals when the algorithm terminates is taken as the global optimum.

3 MULTIPLE SCLEROSIS

This section is based on Compston et al., McAlpine's Multiple Sclerosis[35] and published research papers (referenced separately in the text).

Multiple sclerosis (MS) is an inflammatory and degenerative disease of the CNS white & grey matter that currently has no cure. Disease onset is usually between the ages of 20 and 40 and it is the commonest disabling neurological disease in young adults, though it is unusual for it to occur before adolescence. MS is two to three times more common in females than in males and affects about 120,000 people in the UK[36]. A person has an increased risk of developing the disease from the teenage years to age 50 with the risk gradually declining thereafter[37].

3.1 THE CLINICAL PHENOTYPES OF MS

MS has been divided into several clinical phenotypes; primary progressive, secondary progressive, relapsing-remitting and progressive-relapsing MS[35].

Relapsing remitting MS (RRMS): A type of MS characterised by clearly defined episodes (periods when patients experience new symptoms or when their old symptoms reoccur) followed by partial (residual deficit) or complete remission periods free of disability progression.

Primary progressive MS (PPMS): The symptoms of MS gradually become worse over time rather than occurring episodically. There is disease progression from onset with occasional plateaus and temporary minor improvements possible.

Secondary progressive MS (SPMS): This begins as RRMS and proceeds to a secondary stage with progression of disability without discrete relapses. In some instances however, some people with secondary progressive MS may experience relapses, but these are characterised by incomplete recovery.

Progressive relapsing MS (PR-MS): Progressive disease from onset but differs from primary progressive with clear acute relapses, with or without recovery but the periods between relapses are characterised by continuing progression.

Symptoms vary from person to person and can change over time in the same person. The most common early symptoms include:

- Limb weakness
- Numbness, tingling and other sensory symptoms
- Decreased co-ordination
- Double vision
- Optic neuritis – Inflammatory demyelination of the optic nerve leading to blurred, vision, scotoma and (colour) blindness.

As the disease progresses, symptoms may include:

- Muscle stiffness (spasticity)
- Pain
- Lack of sphincter control
- Cognitive decline, sometimes dementia

During the relapsing-remitting stage of the disease, symptoms occur during attacks, and are followed by a period without or improved symptoms known as remission. A relapse is defined by the appearance of new symptoms, or the return of old symptoms, for a period of 24 hours or more – in the absence of a change in core body temperature or infection. For example, inflammation in the optic nerve may result in visual problems. Relapses usually take a few days to develop and can last for days, weeks (most commonly) or months, varying from mild to severe.

3.2 THE NERVE CELLS IN THE CENTRAL NERVOUS SYSTEM

There are two major types of cells in the nervous system: neurons and glia. Neurons consist of a cell body with protrusions; short dendrites and longer axons. It is the axon of the nerve which is surrounded by the myelin sheath. Myelin is a dielectric (electrically insulating) material that forms a layer, the myelin sheath, around the axon of a neuron. It is a complex assembly of proteins and lipids produced by cells lying in close contact with the axon membrane called oligodendrocytes and is composed of about 80% lipid and about 20% protein. Myelin insulates segments of long axons bioelectrically and accelerates action-potential conduction velocity. Myelin basic protein (MBP), myelin oligodendrocyte glycoprotein (MOG), and proteolipid protein (PLP), and others, make up the protein component of myelin.

In embryonic development, the growth cone of the axon in the central nervous system (CNS) encounters an oligodendrocyte. The oligodendrocyte pairs with one or more axons that requires myelination. Through cell signalling, the oligodendrocyte is 'told' by the axon to stretch out alongside the axon and produce myelin. At the same time, the contact with the axon stimulates the oligodendrocyte to divide and interact with new regions of the growing axon. While producing myelin, the oligodendrocyte winds a sheath-like protrusion around the axon yielding multiple layers. Finally, these layers are compacted resulting in a tightly packed insulating coat around the axon. Bigger axons have thicker myelin sheaths. The axon regulates the thickness of the sheath but the process is still poorly understood. The myelin sheath is discontinuous; along the length of the axon there are gaps up to a millimetre apart where the axon is not covered by myelin. The gaps are called 'Nodes of Ranvier'. This is where electrical signals originate in the healthy brain. The signal jumps from one node to the next allowing it to move 100 times faster than in non-myelinated axons[38].

In the peripheral nervous system Schwann cells myelinate the axons, but only one Schwann cell per axon. The reason for this difference between CNS and PNS is not yet clear. The peripheral nervous system also differs from the CNS in that there are efficient repair mechanisms by the glial cells. So understanding

how this process works in the PNS might suggest ways of improving repair in the CNS.

The glia are the supporting cells of the nervous system. Macroglia are the most abundant supportive cell type in the CNS. There are two types, astrocytes and the myelin-producing cells, the oligodendroglia. Astrocytes play a variety of metabolic support roles, including furnishing energy intermediates and providing for the supplementary removal of excessive extracellular neurotransmitter secretions. Microglia are relatively uncharacterised supportive cells believed to be of mesodermal origin and related to the macrophage/monocyte lineage. Some microglia reside quiescently within the brain[39].

Macrophages are immune system cells that phagocytose myelin debris in normal function, removing it from the area so remyelination can occur from the oligodendrocytes[38].

3.3 THE AETIO-PATHOGENESIS OF MS

The cause of MS is unknown. Evidence suggests MS is a complex disease with both environmental exposure and genetic susceptibility implicated. Environmental factors include global location (with incidence higher with distance away from the equator) and the hygiene hypothesis (low incidence of infection in early childhood), in particular, on the basis of a population of 3 million, infection with Epstein-Barr virus as a young adult increases the risk of subsequently developing multiple sclerosis. Studies investigating pathological changes suggest that a high proportion of B cells, accumulating in lesions of chronic multiple sclerosis, are infected by Epstein-Barr virus. Genetic susceptibility is shown with a familial recurrence rate of about 20%. The reduction in risk changes from 3% in first-degree relatives (siblings, 5%; parents, 2%; and children, 2%), to 1% in second-degree and third-degree relatives[40].

The process starts with increased migration of autoreactive lymphocytes across the blood–brain barrier. A pathological cascade arises from regulatory defects that allow these cells to set up an immune response within the brain.

Regulatory lymphocytes from people with MS fail to suppress the effector cells. These autoreactive lymphocytes do not effectively apoptose on stimulation, because of overexpression of β-arrestin, a protein that promotes T-cell survival. Presumably, failure of local regulatory mechanisms within the brain accounts for the particular sites of inflammation. As a result, activated T-cells migrate through the Blood Brain Barrier (BBB) where they accumulate, multiply following antigen restimulation and release a multitude of proinflammatory molecules. This further activates microglia or infiltrated macrophages and B cells. Activated microglia and astroglia can express a number of neurotoxic molecules, including TNFa, nitric oxide (NO), and various interleukins. They can also kill the oligodendroglia. This chain of events produces a marked inflammatory response, which causes axonal injury and demyelination through various antigen-specific and bystander mechanisms[41]. It is not understood why Schwann cells in the peripheral nervous system are not affected. Without the myelin surrounding the axon, electrical signals transmitted throughout the brain and spinal cord are disrupted or delayed causing symptoms. The failure to repair the lost myelin or the process of remyelination, (as well as progressive axonal loss), is the cause of increasing levels of disability during the course of the disease. The demyelinated areas of the brain and spinal cord form scar tissue or lesions which can be identified on MR images.

3.4 HISTOLOGICAL FEATURES

Chronic or inflammatory, active lesions display a sharp edge. Along this edge an inflammatory infiltrate can be detected alongside lipid-laden and myelin-laden macrophages, hypertrophic astrocytes, some degenerating axons and demyelination in progress. An increase in the number of oligodendrocytes and some remyelination is not unusual in chronic lesions. The centres of such lesions are hypo-cellular and contain denuded axons embedded in a matrix of scarring (fibrous) astrocytes, lipid-laden macrophages, a few infiltrating leukocytes, and virtually no oligodendrocytes.

The histological features of acute or inactive lesions include an indistinct margin, hyper-cellularity, intense perivascular infiltration by small lymphocytes,

parenchymal edema, loss of myelin and oligodendrocytes, acute axonal damage, plasma cells, myelin-laden macrophages, hypertrophic astrocytes, and little or no astroglial scarring.

Lesions of chronic silent disease display sharp edges, astroglial scar tissue, a reduced number of demyelinated axons, macrophages, and vessels with thickened (hyalinized) walls around which occasional leukocytes are seen. These lesions contain few or no oligodendrocytes[42]. Occasionally, some remyelination is seen in these older lesions.

3.5 WALLERIAN DEGENERATION

Wallerian degeneration is the process of progressive demyelination and disintegration of the distal axonal segment following the damage to the neuron. Wallerian degeneration may result from cerebral infarction, haemorrhage, trauma, necrosis, and focal demyelination.

Wallerian degeneration develops through various stages.

- **First stage** is characterized by the physical disintegration of the axons and myelin sheaths with little chemical changes.
- **Second stage** is characterized by rapid destruction of the myelin fragments observed in first stage. In humans, within three months most of myelin breaks down into simple lipids and neutral fats.
- In the **Third stage**, the myelin sheath has almost disappeared, and gliosis occupies the area of the degenerated axons and myelin sheaths.
- The **Fourth stage** is characterized by volume loss following atrophy of the white matter tracts.

In the first stage is not visible by conventional MR imaging, though Wallerian degeneration in the case of stroke has been detected by Diffusion Tensor Imaging. Thomalla et al.[43] detected changes of water diffusion related to beginning pyramidal tract degeneration within the first 2 weeks after stroke. In the second stage, the tissue becomes more hydrophobic and results in

hypointense signal intensity in T_2-weighted and Proton density images. The third stage results from subsequent myelin lipid breakdown, gliosis, and tissue becomes hydrophilic that gives hyperintense signal on T_2-weighted and FLAIR images[44]. After several years, in the end stage, we see volume loss from atrophy that in brain is seen as unilateral shrinkage following Wallerian degeneration[45].

3.6 DIAGNOSIS AND TREATMENT

The diagnosis of MS is made by demonstrating of dissemination in space and time of demyelinating lesions based on clinical and/or MRI. Any differential diagnosis better explaining the symptoms, signs and findings on investigation must be ruled out. In 2010, the so-called McDonald criteria for the diagnosis of MS were revised[46]. Using MRI dissemination in space (DIS) can be demonstrated by at least one lesion on T_2 weighted MRI in at least 2/4 locations considered characteristic for MS, i.e. the juxtacortical, periventricular, infratentorial regions of the brain and the spinal cord.

Dissemination in Time (DIT) can be demonstrated either clinically, or demonstrating (i) a new T_2 and/or gadolinium-enhancing lesion(s) on follow-up MRI or (ii) simultaneous presence of asymptomatic gadolinium-enhancing and non-enhancing lesions at a given time point.

Additional diagnostic information can be obtained by examining the Cerebrospinal Fluid (CSF) for the presence of oligoclonal bands. Oligoclonal bands are a group of proteins called immunoglobulins, which suggest inflammation of the CNS. A positive CSF finding reduces the MRI requirements for reaching DIS criteria (requiring only 2 or more MRI-detected lesions consistent with MS if the CSF was positive) [46].

The level of disability at each stage of the disease course is measured using the Expanded Disability Status Score (EDSS). A better understanding of the role of the spinal cord in MS may achieve a better understanding of the mechanisms underlying the development of irreversible disability in MS.

3.7 MS AND THE SPINAL CORD

The spinal cord is an approximately cylindrical bundle of nerve axons surrounded by the vertebral column, cerebrospinal fluid and dura mater, arachnoid and pia mater meninges which are continuous with the corresponding membranes of the brain. There are 31 pairs of spinal nerves in the cord which extends to L1 in the vertebra. Each region has different functions, with pathways located in specific regions of the white matter. The large majority of grey matter neurons in the spinal cord are interneurons, relaying impulses between afferent and efferent neurons, connecting sensory and motor pathways for reflex actions. The spinal cord is topographically organised with respect to motor, co-ordination and sensory modalities and peripheral nerve input and damage results in specific functional deficits. Knowledge of this topographic and functional anatomy enables deduction of the likely location of spinal cord lesions, including MS lesions.

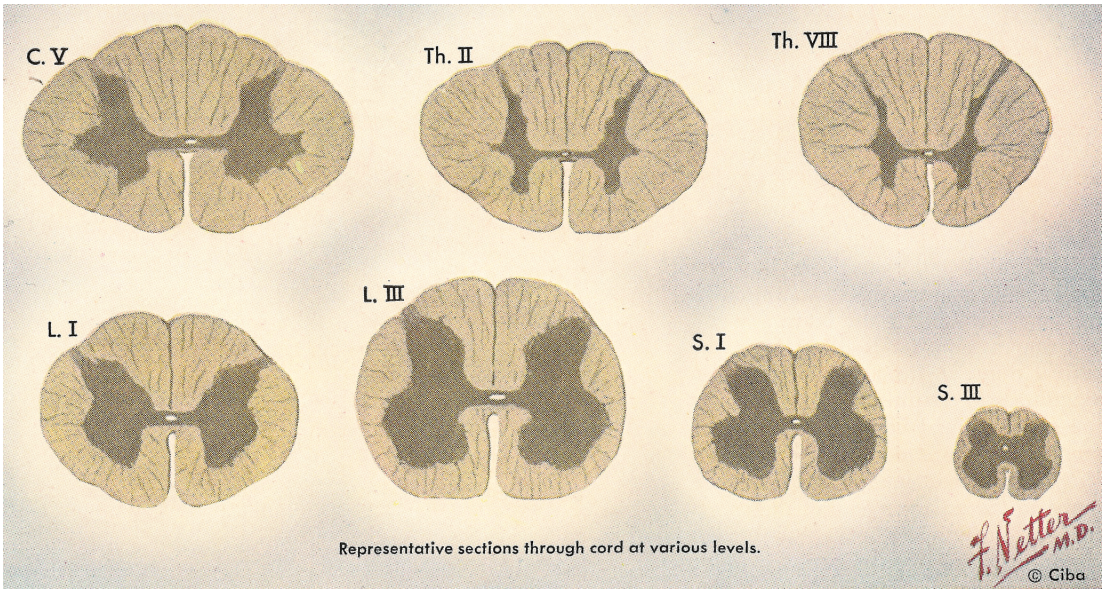

FIGURE 8: SECTIONS THROUGH THE SPINAL CORD BY FRANK NETTER, MD
HTTP://WWW.NETTERIMAGES.COM/IMAGE/14944.HTM

MS pathology in the spinal cord, which comprises both white and grey matter, can contain white matter, grey matter and mixed (both white and grey matter) lesions, display axonal loss and cord atrophy and microscopic changes such as inflammation. The visualisation and measurement of this pathology and such questions as 'to what degree axonal loss in the CortioSpinal Tract (CST) of MS

spinal cord correlates with the extent of inflammation and demyelination in the grey and white matter of the brain?' are key to understanding this disease.

Predicting disease course in MS is problematic. MS is an inflammatory and a degenerative disease. The association between inflammation, demyelination and axonal degeneration is not linear, and varies between patients and with age. Changes over time are still largely assessed in the clinic using the non-linear ranking scale EDSS. It is difficult to find a correlation between structural changes and the patient's symptoms such as disability. For instance, while there is size-dependent axonal loss in the CNS in MS, there is no correlation between disease duration and axonal loss[47-51]. MS spinal cord pathology also seems to be, at least in part, independent of brain changes and to develop at different rates according to disease phenotype[52]. It is also postulated that there is more damage in the cervical area than elsewhere in the spinal cord[53]. However, these findings are often based on MRI studies which in themselves are biased towards the cervical proportion of the cord given good image quality can be more easily achieved; and pathology studies often suffer from selection bias too, given they are based on very limited sampling.

3.7.1 MR IMAGING OF THE SPINAL CORD IN MS

The imaging of the spinal cord in MS did not begin until the 1990s when multi-array coils and fast spin-echo (FSE) sequences made it possible to image the spinal cord in a clinically acceptable time. One of the first papers, Kidd et al.[53], examined 80 patients and found that spinal cord lesions were equally prevalent in disabled and non-disabled patients, and benign and progressive subgroups alike. They also showed that spinal cord atrophy was common and that there was an association between cord atrophy and disability. They continued this work with a paper in 1996[54] which carried out serial monitoring of the spinal cord in the progressive MS patient group. They found there was no relation between either brain or cord MRI lesion activity and change in disability over the study period but they felt that serial measurement of cord cross sectional area may be important. Losseff et al.[55] investigated this more thoroughly and used a semi-automated approach to measure cord area in

sixty patients and thirty controls, finding a significant correlation (P<0.001) between cord area and EDSS score.

Thorpe et al.[56] studied the same parameters in the relapsing-remitting patient group, performing serial MRI over a year in 10 patients. They found no cord atrophy over time, which they believed fitted in with the good recovery found after an attack during the relapsing-remitting phase of the disease. In the same year Thorpe et al.[57] found that 20 of the patients at their centre with suspected MS from a group of 180 had a normal brain MRI scan. By imaging the spinal cord, they found that all 20 of these patients had spinal cord lesions and were able to confirm the diagnosis of MS.

There is a poor correlation between conventional MRI measures and disability[58]. Therefore, quantitative measures are being developed to predict more accurately the clinical course of the disease. These measures include volumetric measures of cord atrophy, Magnetisation Transfer Ratio (MTR) and Diffusion MRI. The exact relationship between the pathology of MS and quantitative MRI indices can only be established in *post-mortem* tissue.

There is a very small body of work on MR sequences measuring myelin quantitatively in the spinal cord, with one pilot study in fixed *post-mortem* tissue.

Myelin water fraction imaging in the cervical spinal cord has been performed by Kolind et al.[59] as a pilot study in seven healthy controls. The mcDESPOT sequence was acquired over the cervical spinal cord and the MWF calculated. They found that MWF values were constant across subjects and time, and that MWF values did not differ significantly between any of the white matter columns (Lateral vs. ventral P = 1.0, dorsal vs. ventral P = 0.7, lateral vs. dorsal P = 0.7). They varied considerably (as expected) along the length of the cervical spinal cord, finding that the average MWF values were significantly lower at the C6 and C7 levels than for C2 through C5 with a value of $P < 0.00001$. They believed that the study showed that mcDESPOT can reliably acquire high quality, high spatial resolution multicomponent relaxation data in the spinal cord, with greater volumetric coverage per unit scan time. Macmillan et al. also acquired myelin water fraction images in the cervical cord but using the 32-echo short T_2 method. They acquired 3D CPMG scans of

the whole cervical cord of twelve healthy controls. MWF was defined as the area under the T2 distribution between 15 ms and 35 ms relative to the area under the entire distribution. They found myelin fractions of 0.296 (SD 0.039) in the white matter and 0.049 (SD 0.032) in the grey matter.

White et al.[60] acquired two-dimensional multi-echo recombined gradient echo (MERGE) images, a technique which automatically sums multiple gradient echoes at different echo times to increase contrast in the grey matter. They tested this technique against T2-weighted fast spin echo (T2WFSE). Nineteen people with Multiple Sclerosis (pwMS) were imaged with both techniques and they found that T2WFSE imaging showed 46 lesions and missed 34 that were depicted on MERGE imaging. Quantitative analysis showed the lesion-to-background CNR in MERGE imaging was significantly higher than that upon T2WFSE imaging ($P < 0.001$). They concluded that MERGE imaging in the cervical spinal cord increased detection and conspicuity of MS lesions.

Laule et al. conducted the first study in fixed *post-mortem* tissue in 2016 using the CPMG 32-echo short T2 sequence. The whole fixed spinal cord was imaged at 7T. Samples were placed in six separate containers that were each imaged in two segments using a 7T small bore system. They found that grey matter MWF varied along the length of the cord, with the thoracic region having less grey matter myelin than the cervical and lumbar areas, which was confirmed by histology. They did not observe any obvious grey matter lesions, they believed that variation in grey matter MWF and myelin staining along the length of the cord may have been due to grey matter demyelination, which is well recognised in MS spinal cord. However, another cause may have been diffuse damage in the spinal cord[61] though it is not known how this affects the grey matter.

3.7.2 AXONAL DEGENERATION AND LOSS, AND SPINAL CORD ATROPHY

Studies have shown that axonal loss can reach up to 80 to 85% in MS plaques in the spinal cord[62,63] though the mechanisms underlying this loss are still unclear. Evidence suggests inflammatory mechanisms alone cannot explain the magnitude of this loss[64,65]. Nijeholt et al. [66] have shown that abnormal signal

on T_2-weighted MR closely reflects the extent of demyelination. However, Bergers et al. found that axonal pathology seems to occur relatively independently of demyelination[47]. This group performed a combined MR/pathology study focusing on the relationship between axonal damage and signal abnormalities on T_2 weighted high-resolution MRI in MSSC. SC specimens of nine pwMS and four controls were imaged at 4.7 T in an axial plane and semi-quantitatively scored for lesions with increased signal intensity (SI) (normal (compared to normal appearing cord tissue (NACT)), mildly increased (grey matter ≥ SI > NACT), or high (> grey matter)). Histopathologic sections were cut and immunostained using the neurofilament marker NE14, and Luxol fast blue for myelin. For each area, axonal density and diameter were quantified; axonal irregularity, NE14 axonal staining intensity, and myelin content were semi-quantitatively scored. Included were 209 areas from MS cases and 109 from control cases distributed over the lateral, posterior, and anterior columns. No SI changes were found in the control cases. The mean density of axons was 26,989/mm^2, and the mean diameter 1.1 µm. All scores for axonal irregularity, NE14 staining intensity, and myelin were normal. In MS cases, in areas with increased SI, mean axonal density was 11,807/mm^2 ($p < 0.0001$), and mean axonal diameter 2.0 µm. Areas with high SI on MRI had the lowest axonal density (average count: 10,504/mm2; range: 3,433 to 26,325/mm2), largest diameter (average: 2.3 µm; range: 1.0 to 4.0 µm), and highest axonal irregularity and NE14 staining intensity compared to NACT. However, NACT of MS cases also had lower axonal density (14,158/mm^2) and higher mean axonal diameter (1.6 µm) than controls. The authors concluded that axonal loss occurs in MS spinal cords largely independent of the degree of signal abnormality on T_2-weighted MRI. This study is limited by the number of spinal cords studied, as in the in-vivo work below, the axonal degeneration patterns varied according to disease type. Bergers' results are in line with histopathologic studies from other groups suggesting axonal loss in the chronic MS spinal cord occurs largely independent of the degree of signal abnormality on T_2-weighted MRI[50,67,68]. Of note, results based on an animal model of inflammatory demyelination (experimental autoimmune encephalitis in mice) suggested that permanent disability is determined by axonal loss in the spinal cord rather than by inflammation[69]. It may be proposed therefore, if the degree of disability

correlates with cord atrophy (as a marker for axonal loss) as suggested by Losseff et al.[55] and others[70,71] then this explains the poor correlation between Expanded Disability Status Scale (EDSS) score and the number of spinal cord focal lesions [72]. However, the relationship between axonal loss and cord atrophy as measured by cross-sectional area is not clear and the two may not correlate.

A straightforward relationship between SC atrophy and axonal pathology may be confounded by variations in axon diameter depending on their metabolic state; an increase of axonal diameter in both active, chronically demyelinated areas as well as inactive demyelinated areas and even in the NACT of pwMS has been reported. Shintaku et al.[73] suggested that there is an increased axonal diameter in lesions and Klein et al.[74] showed that MS caused both expansion and contraction of the cord dependent on disease course. They found that patients with primary progressive MS demonstrated a trend toward upper cervical cord atrophy, as confirmed by Bjartmar et al[63], who found cervical cord atrophy in the PM SC of five severely disabled MS patients. But patients with relapsing-remitting MS showed a trend toward increased volume at the cervical and thoracic levels, which most likely reflects inflammation or edema-related cord expansion. The axon diameter itself is dependent on the phosphorylation status of axonal neurofilaments[75,76]. Neurofilament hyperphosphorylation, as has been shown in acute lesions, may lead to an increase of axonal diameter whilst the eventual loss of axons would lead to constriction of the cord. Thus, while spinal cord atrophy may be pronounced in progressive forms of MS, it may not be a reliable measure in earlier disease stages where even cord expansion may occur[70].

3.7.3 GREY MATTER OR CORTICAL LESIONS

Grey matter or Cortical lesions (when the grey matter lesions in the brain) have been known to be a part of MS since the early histological studies of Dawson in 1916. A paper by Kidd et al.[77] examined the visualisation of cortical lesion by MRI. While white matter lesions are visualised well in T_2-weighted images due to the increase in relaxation times by the accumulation of free water in the lesion, this cannot be said of cortical lesions. They proposed that this was due to high

cellular density in the grey matter not permitting a sufficient expansion of the extracellular space to allow an increase in relaxation time. They identified six types of cortical lesions as shown in Table 1 below.

Lesion Type	Description	Schematic	Image
1	located in the deeper cortical laminae and subcortical white matter	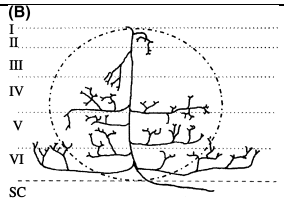	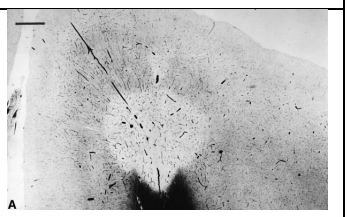
2	affects all cortical layers, but without involving the underlying subcortical white matter	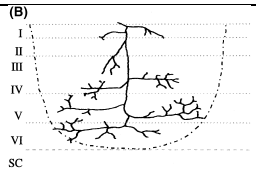	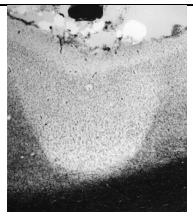
3	usually extensive and located only in the superficial cortical layers	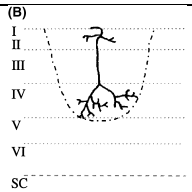	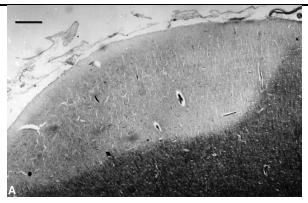
4	affect only the subcortical U-fibres	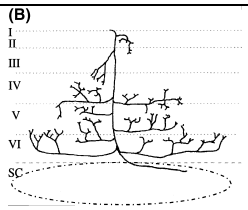	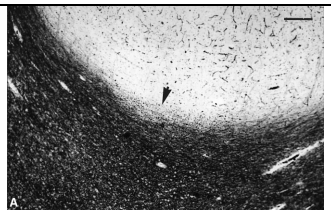
5	a large cortical lesion affecting all cortical laminae and subcortical white matter	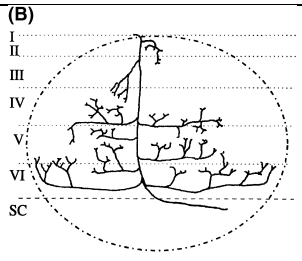	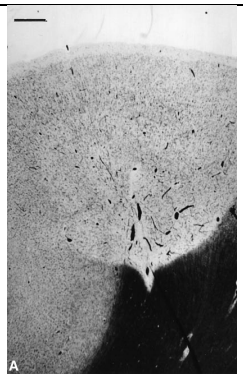

6	small and occur in any part of the cortical ribbon	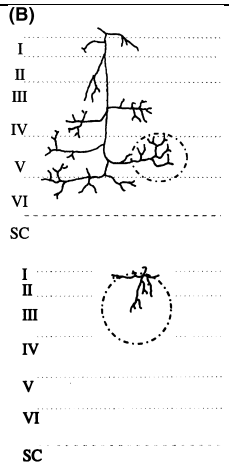	

TABLE 1: CORTICAL LESION TYPES REPRODUCED FROM KIDD ET AL. [77]

An early *post-mortem* study by Geurts et al.[78] examined the ability of MRI to distinguish cortical lesions in standard clinical sequences at 1.5T by comparing *post-mortem* MRI scans with histological findings. They studied 49 brain samples from 9 patients, scanning the samples after sectioning using a dual-echo T_2-weighted SE and a 3D FLAIR sequence. Histologically, equal numbers of WM and GM lesions were found but of these in GM, only 3% were detected by T_2-weighted imaging and 5% by 3D FLAIR. In contrast, in WM T_2-weighted imaging detected 63%, and 3D FLAIR imaging 71% of the total. Even when the histological images were read next to the MRI images, 44% and 29% of intracortical lesions remained invisible on T_2-weighted and 3D FLAIR, respectively.

The invisibility of intra-cortical lesions is the likely reason for poor correlation of MRI with disability. Kangarlu et al.[79] found that the images of a *post-mortem* brain at 8T distinguished all of the intra-cortical lesions and the images could actually be a guide to the histologist to find lesions not easily distinguishable after staining. The work by Schmierer et al. [80] agreed with this conclusion. Geurts et al[81] imaged at a higher field strength of 4.7T but did not find an increase in intra-cortical lesion detection on *post-mortem* MR imaging. However, they compared T_2-weighted and FLAIR imaging at 1.5T to PD imaging at 4.7T unlike Kangarlu et al. who used T_2-weighted imaging at 8T. This raises the idea that very high field strengths may give better delineation of cortical lesions, but

other quantitative sequences should be developed for the detection of cortical lesions at more easily tolerated field strengths.

3.7.4 PSIR IMAGING IN MS

The main application of PSIR imaging at this time is in cardiac work, but there have been papers that propose PSIR as advantageous in cortical or grey matter lesion detection in the brain. The first of these was by Nelson et al.[82] who compared PSIR and Double Inversion Recovery (DIR) and conventional Fluid Attenuated Inversion Recovery (FLAIR) Imaging *in-vivo* (FLAIR is an inversion recovery sequence that uses a TI which attenuates the signal from fluid). They recommended the combine use of PSIR and DIR finding a 337% improvement in the total number of lesions and 417% improvement in intra-cortical lesion detection in comparison to FLAIR alone. A second paper published the year after by the same author[83] did suggest that a high resolution three-dimensional (3D) magnetisation-prepared rapid acquisition with gradient echo (MPRAGE) improves the classification of cortical lesions over PSIR and DIR (MPRAGE is a steady-state spoiled gradient echo sequence with an inversion pulse). However, in the most recent paper by the author[84], a PSIR/DIR combination was most favoured, with the author saying '[MPRAGE] does not seem to be the most sensitive for cortical lesion detection. The high spatial resolution of this sequence is helpful to evaluate details (i.e. lesion borders) but when used for detection purposes only, lesion presence is less obvious than on DIR/PSIR'. This gives a somewhat confusing picture where validation of this sequence with histology would be most valuable. Recently Sethi et al. published two papers[85,86], the second dividing the patients into disease type, both compared DIR with PSIR imaging *in-vivo* at 3T. PSIR imaging identified more cortical lesions than DIR as shown in the table below, though it is not clear exactly which of the methods of phase correction was used.

Table 4 Lesion counts in MS subtypes

MS sub-type	DIR		PSIR				PD/T2
	IC	LC	IC	LC	JC	WM	WM
PP (n=15)	3.7±4.6	6.1±4.8	12.3±8.8	11.6±12.7	6.1±5.5	50.4±31.7	48.3±27.6
SP (n=15)	6.5±5.3	12.2±9.6	21.3±10.0	20.8±13.6	11.1±11.2	80.5±40.7	72.9±33
RR (n=30)	6.6±3.9	5.5±7.6	19.5±9.2	10.5±11.4	5.8±6.8	63.4±57.2	61.2±51.2
All (n=60)	5.9±4.5	7.3±8.0	18.1±9.8	13.4±12.9	7.1±8.1	64.5±48.5	60.9±42.5

p values comparing PSIR versus DIR (all patients): IC <0.001 and LC <0.001.
IC, intracortical grey lesion; LC, leucocortical; JC, juxtacortical white matter lesions; WM, other white matter lesions (other than JC lesions); PP, primary progressive; SP, secondary progressive; RR, relapsing remitting MS.

TABLE 2: CORTICAL LESIONS IDENTIFIED BY DIR AND PSIR IMAGING. REPRODUCED FROM SETHI ET AL.[85]

They found that the intrinsically low signal-to-noise ratio in DIR imaging limited the improvement of this sequence while maintaining clinically acceptable scan times but the PSIR sequence could be acquired at much higher resolution in an acceptable time. The authors acquired 2D sequences but the optimisation of a 3D sequence may reveal more information, possibly in the long ribbon-like cortical lesions.

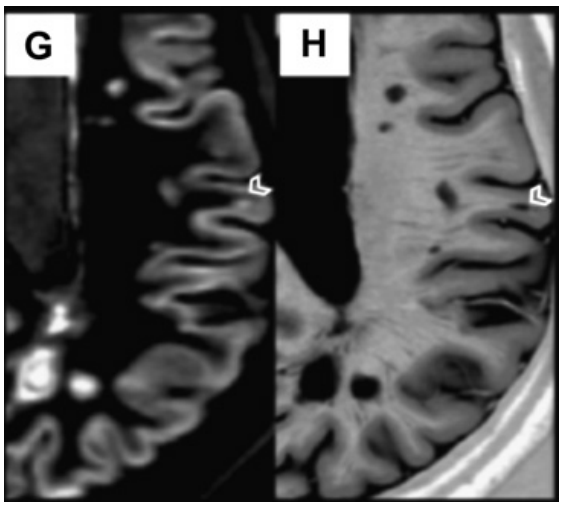

FIGURE 9: FIGURE SHOWING DIR (G) AND PSIR (H) *IN-VIVO* IMAGES FROM SETHI ET AL.[85]. THE PSIR SEQUENCE SHOWS SHARP DELINEATION OF THE JUXTACORTICAL LESION (ARROW)

It can be clearly seen that in the case of in-vivo studies the PSIR sequence shows improved imaging for lesions in the brain and the difficult areas of visualisation in the juxtacortical and cortical lesions.

The only study to examine PSIR imaging in the spinal cord *in-vivo* was Kearney et al.[87] who used the images for cord cross-sectional area calculations at 3T. They believed it is axonal loss rather than lesions that represent the main pathological substrate of irreversible physical disability in MS. In the discussion

in section 3.7.2 on axonal loss of this work, it was shown that the relationship between cord cross-sectional area (CSA) and axonal pathology is not clear and the use of this as a marker is questionable until a definitive study with histopathological verification is performed. No clinical trial has been performed with sufficient power to prove an association either due to the challenging nature of in-vivo measurement of the CSA. Kearney et al. tested two algorithms for measuring CSA, Semi-automated Edge-Detection and Active Surface Model on two types of images T_1-weighted 3D-TFE and PSIR. The 3D-TFE images had $1\times1\times1mm^3$ voxel size taking 6 minutes for acquisition and the PSIR images were $0.5\times0.5\times3mm^3$ taking 15 minutes for acquisition. The image resolution was noticeably improved in the PSIR but this is most likely due to the difference in scan time and voxel size, and the authors note this as a limitation. The author's preferred combination of Active Surface Model segmentation and PSIR imaging may show some advantage on equal comparison and should be investigated.

4 IMAGING FIXED POST-MORTEM TISSUE

In the 1980s it was proposed that *post-mortem* MRI may provide complementary information to the routine neuropathological examination of *post-mortem* fixed brains[88]. In the 1990s, Tovi et al. and Blamire et al.[89,90] recognised that the standard sequences used *in-vivo* would not be suitable for *post-mortem* tissue due to the change in relaxation parameters with fixation. They measured these changes in order to allow optimisation of the sequence parameters for *post-mortem* work. Tovi et al[89] measured the change in T_1 and T_2 in five formalin-fixed human whole-brain specimens as a function of time and found that GM/WM contrast reversal was observed around the fourth day. They considered that the most rapid changes occurred during the first one to two weeks followed by a slower decline over the following weeks. Furthermore, the values of T_1 for GM/WM appeared to converge, leading to a reduction in the contrast available from a T_1-weighted imaging sequence. It has later been proven that the contrast in GM/WM, although decreased, remains proportional[91]. T_2 fell particularly over the first 2 weeks of fixation after which changes were only small. They observed T_2 values in the prolonged (>1yr) fixed brain of 50ms in WM and 75ms in frontal GM. Blamire et al.[90] measured T_2 and the contrast between GM/WM in spin/proton density (PD) images at 2.0T. Three *post-mortem* brains were examined weekly during formalin fixation from the unfixed state to 35 days post-fixation. They found that the T_2 relaxation times fell rapidly with the largest change occurring during the first week, reaching a plateau by the fifth week of fixation. Interestingly, the grey to white matter PD contrast ratio increased from 1.19±0.01 to 1.54±0.06 over the five weeks of fixation. This work was confirmed in the findings of Schumann et al.[92] who obtained a 3D image of a *post-mortem* brain from an autistic patient at 1.5T. They first acquired an in-plane resolution of 0.6 x 0.3mm, and with post-processing interpolation between slices of 1.6mm created a 3D volume. They also concluded that standard *in-vivo* sequences gave poor T_1/T_2 contrast, preferring the use of the proton-density image, and emphasised the difficulty in obtaining high-resolution 3D images with the available sequences and computing power of the time, and suggested future work would benefit from a higher field strength such as 3T. Pfefferbaum et al.[93] carried on this work,

recommending increasing the number of signal averages to offset the decrease in resolution with a smaller voxel size, as the time of acquisition can be easily increased when imaging *post-mortem* tissue for improved images. They showed that diffusion weighted imaging was much more challenging in the *post-mortem* brain compared to in vivo; they attributed this to poor water molecular motility in fixed brain specimens. They suggested that there may be some degradation in the fibre tracts and postulated that for diffusion imaging to be feasible, it would require very short gradient duration, separation, and echo times to observe anisotropy in long-fixed brain specimens.

4.1.1 UNFIXED TISSUE COMPARED WITH FIXED

The use of post-mortem tissue in MS gives insight into the composition of lesions with histopathological comparison. There has been mixture of both unfixed and fixed *post-mortem* tissue used in the literature. It is important to study whether the properties of fixed and unfixed tissue are comparable. The composition of the fixed tissue differs significantly from the unfixed tissue. The fixation process causing cross-linking of functional groups of macromolecules, notably primary amines (e.g., lysine) and thiols (e.g., cystein) to form crosslinks[91], and removal of water from the tissues causing changes in relaxation parameters and diffusion. As long as the sample is properly handled and refrigerated, there is very little difference between the unfixed *post-mortem* brain and *in-vivo* brain. This finding was confirmed by Schmierer et al. [94] in the normal appearing white matter (NAWM) and in later work in the GM[91]. They found T_1, T_2, MTR, and f_B obtained in unfixed MS brain was similar to published values obtained in patients with MS *in-vivo*. Following fixation T_1, T_2 and MTR dropped, whereas f_B (bound proton fraction) increased. Compared to published *in-vivo* data, all diffusivity measures were lower in unfixed MS brain and dropped further following fixation (except for FA). MTR was the best predictor of myelin in unfixed MS brain whereas post-fixation T_2, T_1 and f_B were superior. It should be considered therefore that the unfixed post mortem brain should be used as a tool to match the *in-vivo* results with histological confirmation of the findings. However, the window of opportunity is short with unfixed tissue and the benefit of fixed tissue is the opportunities for repeat scanning with many different

methods and larger sample sizes with higher SNR due to longer scanning times as once completely fixed there is little change in the tissue. The fixed tissue can be compared to the *in-vivo* brain when looking at relaxation parameters such as T_1, T_2 and MTR. The effects of fixation on diffusion are more complex. The findings of Schmierer et al. were confirmed by Kim et al.[95], who imaged four human cervical cords and three segments of pig cervical spinal cord specimens both before and after tissue fixation using 3D multi-shot diffusion weighted imaging (ms-DWEPI). They found that fixation caused a significant decrease in the longitudinal diffusivity, but the relative anisotropy (RA) and radial diffusivity remained unaffected, though they did not speculate on why just the longitudinal diffusivity was affected. Additionally, they confirmed that once adequately preserved, the diffusivity parameters of fixed tissue remain constant over time.

4.1.2 REGISTRATION BETWEEN MRI AND HISTOLOGY

When performing combined studies using MRI and histology, a fundamental issue is the registration of MRI with the histological sections. Correctly matching the location of MS lesions is challenging given the thickness of an MR slice is usually between 1-3mm whilst the thickness of a histological section is often less than 10μm. A variety of methods have been used to achieve accurate registration. De Groot et al.[96] and Barkhof et al.[58] reported this issue in *post-mortem* brains, and Schmierer et al. [97] suggested a solution using a stereotactic method of localization. Qualitative methods have often been reported [61,66,98,99] where histopathological sections were matched with MRI scans according to the shape and size of the spinal cord, the configuration of grey matter, and the presence and configuration of lesions. In high field MRI scans, the improved resolution of lesions and spinal cord anatomy allows for corresponding areas to be readily identified on both the histological slides and the MRI scans using anatomical landmarks such as the morphology of the GM[100,101]. Kim et al.[95] used a stereotactic method where all the samples were placed in a rectangle-shaped acryl box to help localize the cords within the coil during the MRI experiment. Klawiter et al.[102] was the only study to use computer post-processing to register the images. Inter-modality registration of the spinal cord

MR images was performed using a manual, 2D registration. Corresponding landmarks were manually placed on the diffusion tensor imaging (DTI) parameter maps and each of the digital histological images. Landmarks included vessels, prominent white and grey matter boundaries, and points along the perimeter of the cord. The co-registration of histological images to MR images was performed using a modification of a method by Budde et al. [103]. Histologic images were warped to the pixelated MR image using a thin-plate spline warp deformation grid. Regions of interest identified on histologic sections were mapped on co-registered DTI slices. Similarly, ROIs identified by DTI parameters were mapped on co-registered histologic sections. Values for each DTI parameter were determined for each ROI. It is likely that the anatomy of the spinal cord, with different patterns of grey and white matter at the different levels, will not be such a challenge as the brain but as losing the location of a lesion means it cannot be included in the analysis, it is of importance. The method that should be used will depend on field strength and image type. The images obtained at higher field strengths, as discussed in the papers above, will often be comparable to the histological images, and registration will be simple. At clinical field strengths and with poorer quality images such as diffusion, a more robust, reproducible, computer aided registration approach would be preferable.

4.2 POST-MORTEM ANALYSIS OF THE SPINAL CORD IN MS

In the first study of the MS post-mortem spinal cord in 1999, Ganter et al[51], looked at the occurrence of MS plaques in the spinal cord in a solely histopathological study. However, it was not until 2001 when Nijeholt et al. [66] combined the two methods of MRI and histopathological verification in the MS spinal cord. They performed PD-weighted SE images at 1.0T and 4.7T on 3cm fixed sections from the cervical, thoracic and lumbar areas, finding that higher field strengths improved resolution of white and grey matter structure in the spinal cord. After MRI, the samples were cut into 5mm sections and stained for myelin (Luxol fast blue/cresyl violet) and axons (Bodian method). All histopathologically abnormal areas were shown on their MRI images. Bergers et al. [61] compared direct *post-mortem* in-situ (whole-corpse) sagittal spinal

cord MRI at 1.5T of seven MS cases with *in-vitro* axial 4.7T MRI and histopathology. In-situ PD/T2-weighted conventional SE images were acquired, and then 5cm cord specimens (6 cervical, 1 thoracic) were removed and fixed, then imaged axially at 4.7T. These specimens were cut and stained with hematoxylin-eosin and Luxol fast blue. All spinal cords showed abnormalities on high resolution MRI and histopathology, but not all were shown in-situ (one presented a normal scan). Mottershead et al.[100] took 2cm fresh *post-mortem* sections from the cervical, thoracic and lumbar areas in a reference patient and one 2cm piece from an area which on visual inspection contained MS lesions from three pwMS spinal cords. A variety of quantitative MRI indices were obtained including T_1, T_2, MTR and diffusion maps on a 7T scanner. At over 10 years old, published in 2001, this still remains the most comprehensive study of MRI indices and histological correlation. In 2004, Bot et al.[48] examined the changes in T_1, T_2, MTR and cord area between controls and MS patients in the cervical spinal cord. Fixed 6 cm long cervical spinal cord specimens from 11 patients with MS and 2 controls were examined at 4.7T. After MR imaging, specimens were cut into six equal pieces of approximately 1 cm each. Thereafter, 5 µm thick slices were cut at 1 cm intervals (six per subject) and stained with Kluver for myelin and NE-14 (phosphorylated neurofilaments) for axons. MR quantitative measures were taken as an average across the specimen and showed a 30% increase of T_1 in MS specimens in comparison to controls ($P<0.001$), a mean 13% increase of T_2 ($P<0.001$) and MS specimens showed, on average, lower MTR with a reduction of 10.5% compared with the MTR in control specimens ($P < 0.001$). With increasing demyelination in the MS cases, T_1 and T_2 relaxation times increased and MTR values decreased ($P < 0.001$ for all); with decreasing cord area, a steady decrease in MTR values was measured. With decreasing number of axons, there was an increase in T_1 and T_2 relaxation and a decrease in MTR ($P < 0.01$). Using a multi-level analysis to provide a model, T_2 was found to be the strongest independent predictor for myelin density. However, no single quantitative index was predictive of axonal loss.

In 2009, Gilmore et al.[101] performed a basic study imaging fixed cervical and upper thoracic *post-mortem* spinal cord at 4.7T. There were eleven MS cases and two controls. After imaging the tissue was sectioned at 1cm intervals and stained for Myelin Basic Protein. They compared the PD-weighted images and histopathology marker and found that *post-mortem* imaging detected 87% of white matter lesions and 73% of grey matter lesions.

4.3 CPMG IN THE CNS

Quantitative MRI has potential to improve contrast, inter- and intra-site repeatability and easier interpretation compared to qualitative MRI. Multi component relaxometry (MCR) offers quantitative assessment of myelin in the CNS in people with MS. Structurally, myelin is composed of a lipid bilayer membrane wrapped many times around the neuronal axon, with thin layers of water molecules between layers of membrane. MCR exploits the difference in environment and thus relaxation values between free water, intra-cellular water and water trapped between these myelin bilayers to measure the ratio of myelin water signal to total water signal, termed the myelin water fraction (MWF)[104].

4.3.1 INITIAL IN-VIVO WORK

The idea of dividing the T_2 signal obtained from the voxels in a brain scan and associating them with myelination and physiological processes was first proposed by Gersonde et al.[105] in 1985. They performed this in a healthy adult volunteer and a 6-year old child with Bertrand disease. They commented on the movement of a peak around T_2 = 0.1 s in the T_2 histogram of the paediatric scan is reduced or shifted to smaller T_2 values because of the demyelination process (as they considered this peak to correspond to myelin content), whereas the amount of voxels for the tail area is increased indicating a higher water content of the brain. However, the first implementation to fully separate the myelin component was MacKay et al. in 1994[104] following on from their work in quantitative separation of NMR images of water in wood on the basis of T_2[106], an animal EAE model and an analysis of appropriate fitting algorithms[31,107]. They

scanned five controls and four pwMS at 1.5T using the CPMG sequence (section 2.6.1) and fitting using the NNLS algorithm (section 2.8.4), obtaining reasonable images of the short T_2 component considered to be myelin.

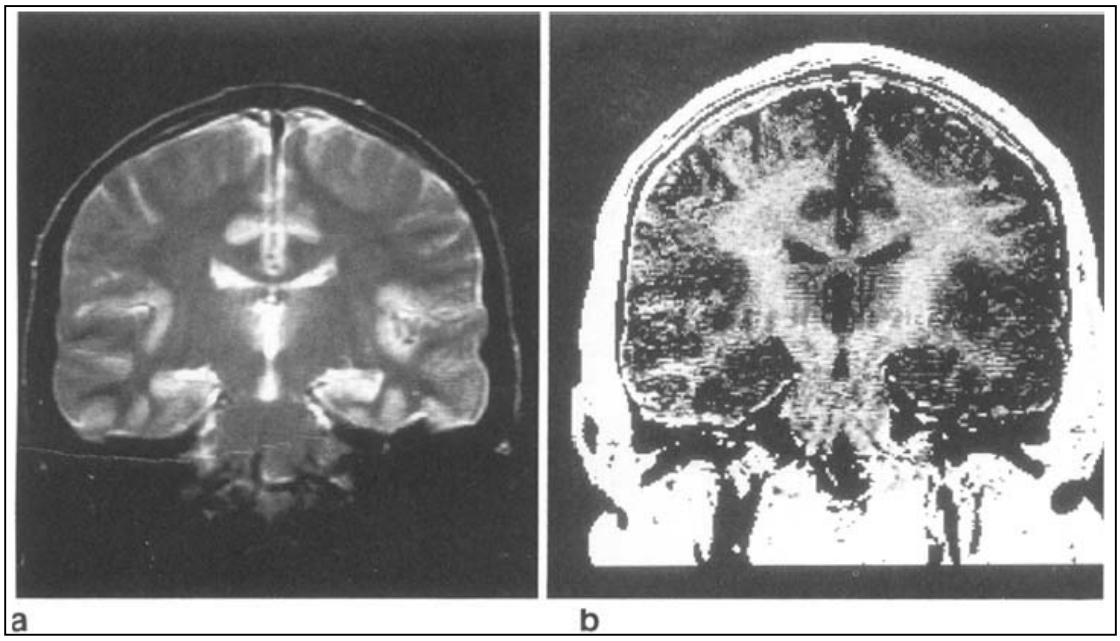

FIGURE 10: (A) A CORONAL IMAGE (TE 6.0MS) FROM THE BRAIN OF A NORMAL VOLUNTEER USING THE 32 ECHO IMAGING PULSE SEQUENCE, (B) THE CORRESPONDING IMAGE OF THE SHORT T2 FRACTION INDICATIVE OF MYELIN FROM MACKAY ET AL[104]

They concluded that this was possible due to water diffusion within the myelin sheath being sufficiently slow that there is no appreciable exchange with cytoplasmic and extracellular water on the short T_2 time scale of 10 to 55ms. This work was expanded to include an examination of myelin content in grey and white matter structures in the brain in 12 normal volunteers[108]. Eight male and four females, mean age 31 years, range 24-46 years, the five white-matter structures outlined were the genu and splenium of the corpus callosum, posterior internal capsules, arid major and minor forceps. The six grey-matter structures were the putamen, head of the caudate nucleus, thalamus, insular cortex, cingulate gyrus, and cortical regions.

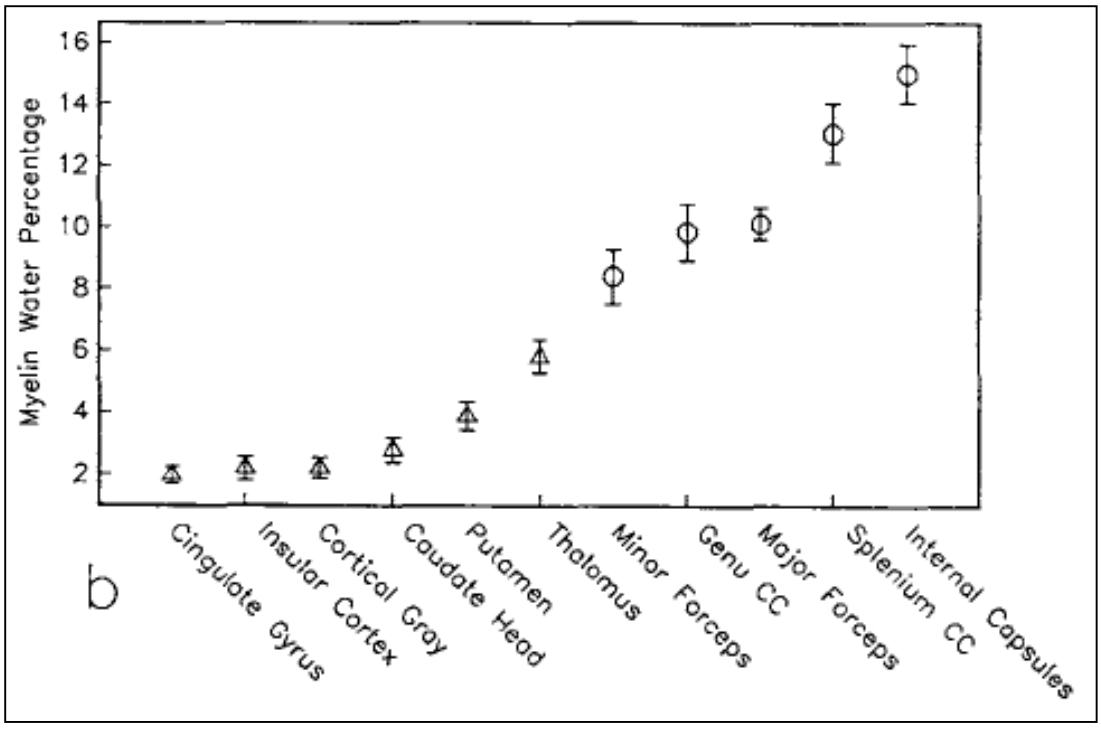

FIGURE 11: MYELIN WATER PERCENTAGES IN MAJOR STRUCTURES OF THE BRAIN FROM WHITTALL ET AL.[108]

They divided the tissue water region of the T_2 distributions into two parts; one between 50 and 150ms and the other between 150 and 600ms. They found for a few structures an extra T_2 peak, which was observed in the longer T_2 region.

4.3.2 CPMG IN POST-MORTEM TISSUE

The CPMG sequence was then histologically validated in the brain by Moore et al.[109]. Two fixed *post-mortem* brains from pwMS were imaged using a 32-echo CPMG sequence, then cut along the centre of the 5-mm slices scanned, embedded in paraffin and stained with LFB and by the Bielschowsky technique for axons. They found that the anatomical distribution of the short-T_2 component signal corresponded to the myelin distribution. Chronic, silent MS plaques with myelin loss correlated with areas of absence of short-T_2 signal. The numbers of axons within lesions were reduced, but many surviving axons were also seen in these areas of complete loss of myelin. This work was then expanded in Laule et al.[110] where the multi-component T_2 distribution of water was determined from 25 fixed *post-mortem* MS brain samples using the multi-echo T_2 CPMG sequence. As well as an examination of the qualitative

correspondence of the short T_2 image with LFB, the authors also conducted a comparison of the quantitative measurement of percentage myelination in both histology and MR.

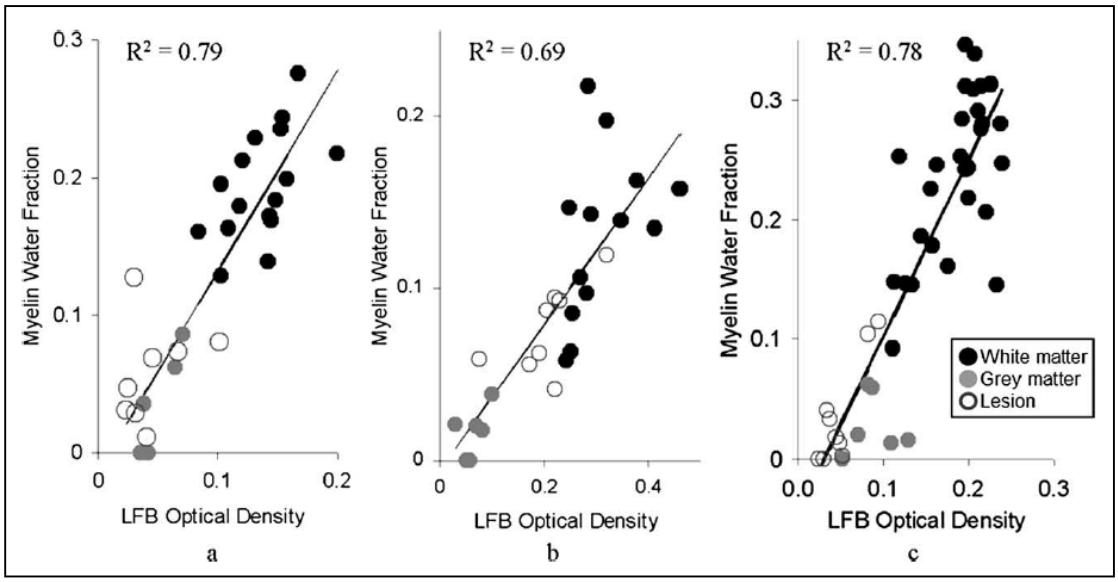

FIGURE 12: QUANTITATIVE CORRELATION BETWEEN MWF AND LFB OPTICAL DENSITY (OD). THREE SAMPLES WHICH HAD STRONG CORRELATIONS BETWEEN MWF AND OD OF LFB (A) $R^2 = 0.79$, (B) $R^2 = 0.69$, (C) $R^2 = 0.78$, FOR VARIOUS REGIONS OF INTEREST MADE UP OF WHITE MATTER (BLACK CIRCLES), GREY MATTER (GREY CIRCLES) AND LESION (OPEN CIRCLES). REPRODUCED FROM LAULE ET AL.

They found that a comparison of myelin water fraction and optical density of LFB staining of myelin for individual samples demonstrated a very strong average correlation, concluding that myelin water imaging was a valid MRI measure of myelin content in CNS tissue. The correlation remained when they examined white matter ROIs only, suggesting the observed relationship is not a bimodal effect due to the separation of white and grey matter values. However, they determined that while the technique is sensitive to myelin loss, it is not able to distinguish between myelin decreases accompanying axonal loss versus primary demyelination or remyelination. The sensitivity of the technique may be improved at higher field strengths, and so Laule et al.[111] compared small bore 7T short T_2 myelin water imaging with histopathology. Ten brain samples (1cm thick) were examined from 3 pwMS (2 females, 1 male; mean age = 36 years (range 24–49 years)). Samples were imaged, then stained for LFB.

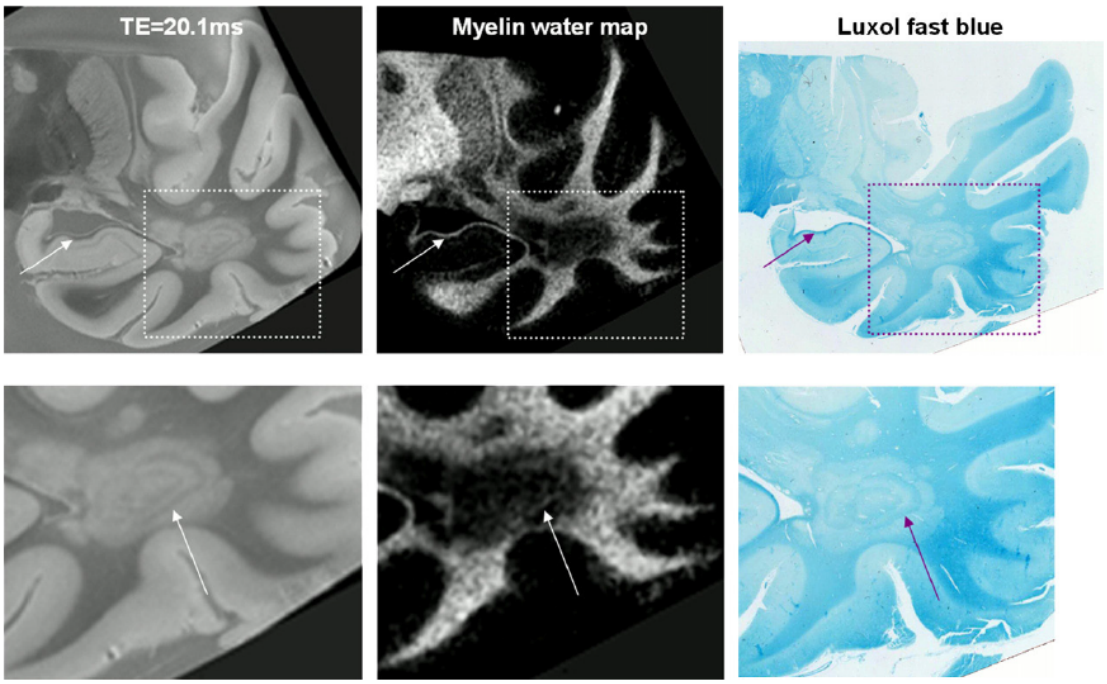

FIGURE 13: EXAMPLE OF A 7 T TE=20.1MS IMAGE AND MYELIN WATER MAP, AND CORRESPONDING LFB HISTOLOGY IMAGE OF THE TEMPORAL-LOBE REGION OF AN MS PATIENT. THE ALVEUS OF THE HIPPOCAMPUS (UPPER PANEL) AND FAINT RINGS OF PRESERVED MYELIN IN THE CONCENTRIC BALO'S LESION (LOWER PANEL, ENLARGEMENT OF THE DASHED BOX IN THE UPPER PANEL) ARE VISIBLE AND INDICATED BY ARROWS. REPRODUCED FROM LAULE ET AL.[111]

There was a correlation of $R^2 = 0.78$ (across the range of all the ROIs), this was a higher correlation coefficient found at 7T than at 3T, very likely because of the increase in SNR due to the higher field strength and smaller bore/coil size.

The authors examined the potential confounding factor with the 7T data that a relatively short TR combined with the known effect of increases in T_1 at higher field strength, which could potentially lead to substantial T_1-weighting of the T_2 relaxation data. However, in this case the reduction of the T_1 values with fixation (see section 4.1.1) meant that the TR used (1500ms) was approximately five times that of the T_1 in the fixed hemispheres. They concluded that that normal appearing white matter, dirty appearing white matter, lesions and grey matter all exhibit the same relationship between MWF and LFB staining.

The short T_2 myelin water imaging has been evaluated *in-vivo* at 3T by Kolind et al.[112] They refined scan parameters including gradient crusher height and slew rate, bandwidth, echo spacing, matrix size, repetition time, and phase

rewinding in water-based phantoms, and in fixed and *in-vivo* brain. The results were classified by the standard deviation of the residuals of the multi-exponential fit, MWF, T_2, and peak width of the intra/extracellular water. Subsequently, the multicomponent T_2 measurements at 1.5T and 3.0T for 10 healthy volunteers were compared, and the differences in SNR, fit residuals, MWF, and T_2 and peak width of the intra/extracellular water at higher magnetic field examined. They found that MWF maps were qualitatively similar between field strengths but MWFs were found to be significantly higher at 3.0T than at 1.5T, but there was a strongly significant correlation between measurements ($R^2 > 0.92$, $P < 0.0005$). The SNR was nearly double at 3.0T, but the standard deviation of residuals was increased in most cases.

In the spinal cord there have been the two previously mentioned studies (see section 3.7.1) by Laule[113] and White[60], as well as Minty et al.[114] who applied the 32-echo short T_2 relaxation sequence for measuring the MWF in healthy control SC *in-vivo* at 1.5T. Their findings were supplemented with studies in bovine SC samples *in-vitro*. For human *in-vivo* experiments, 22 32-echo relaxation studies were performed on 17 normal controls (mean age = 29 years, range: 20–52 years, nine males, eight females). The *in-vivo* human measurements took one sagittal slice through the whole spinal cord at the midline, resulting in a MWF that was averaged if there was grey matter present. Mean human MWF varied according the level of the SC examined: cervical, thoracic, and lumbar MWF was found to be 21.8 (SD = 2.1)%, 24.3 (3.6)%, and 11.4 (6.4)%, respectively. Noteworthy reductions were observed in areas consistent with the expected locations of the cervical and lumbar enlargements. Average bovine MWF was 30.0 (2.7)% in white matter and 8.2 (0.4)% in grey matter. The authors note that an increased SC MWF was found in comparison to the brain, which was confirmed by the bovine work and also previously in bovine optical nerve[115] in another study.

The authors made an interesting examination of the influence water molecule exchange rate has in nerve fibres in the spinal cord. It is expected that the smaller fibres would undergo increased myelin water exchange relative to the larger, and as a result would have artefactually lower short T_2 measurements. Animal models have shown a link between a large fibre size and a thicker

myelin sheath[116]. They considered the influence of short T_2 component measurement to total fibre size (axon + myelin), positing a greater expected residency time of myelin water molecules in fibres with more myelin bilayers. They referred to a simple calculation of compartment mixing times, carried out by Koenig[117] to examine this theory. Given an estimated lower bound membrane permeability of 10^{-4} cm/s (from sphingomyelin:cholesterol bilayers at 14.5°C) and considering a fibre consisting of 10 lamellae, Koenig estimated a mixing time of 64ms for the axonal and myelin components, a value that scales linearly with the number of myelin lamellae.

However, the authors found that experimental measurements of myelin water exchange do not support the above conclusion. Using a four-pool model to explain magnetisation exchange in WM, two studies estimated much longer myelin mixing times of roughly 560ms in bovine optic nerve in vitro at room temperature[115] and 1,024ms in bovine WM in-vitro at 37°C[118]. Although these modelling studies pointed out that as inter-reservoir exchange increases, the short T_2 component reduces in size, and its relative magnitude underestimates the true myelin water content[118], the estimated reductions in measured MWF were around 10% to 20%. They concluded, on the basis of a fibre size argument alone, it might be expected that MWFs measured in structures containing smaller fibres to be somewhat lower; but this cannot explain an observed threefold difference between SC and corpus callosum MWF. They believed their conclusion was supported by the observations that the bovine SC *in-vitro* MWF measurements in the study acquired at 24°C were slightly larger than human SC MWF values acquired *in-vivo*, because the exchange rate would be slower at the lower temperature. It will be important to keep these points in mind while examining the MWF in fixed tissue imaged at room temperature and also to consider any effect fixation may have on exchange between the compartments in the rest of this thesis.

4.4 MCDESPOT IN THE CNS

Rapid gradient acquisition steady-state methods allow clinically practical time-efficient quantification of the fundamental relaxation time constants, T_1 and T_2,

via the Variable Flip Angle or the driven-equilibrium single-pulse observation of T_1 (DESPOT1) and T_2 (DESPOT2) methods. DESPOT1 and DESPOT2 derive T_1 and T_2 information from sets of spoiled gradient recalled echo (SPGR) and fully-balanced steady-state free precession (bSSFP) data acquired over a range of flip angles, α, with constant interpulse spacing, TR, instead of a spin–echo approach. The combination of the DESPOT1/2 methods into the multicomponent driven equilibrium single pulse observation of T_1 and T_2 (mcDESPOT) was first proposed by Deoni et al.[7]. By combining T_1 and T_2 information, separate water pools can be detected with short, medium and long T_2 values, which are thought to correspond to myelin water fraction (MWF), intra/extra-cellular water fraction (IEWF), and free water fraction (FWF) or cerebral spinal fluid (CSF). The MWF is thought to correspond to the water trapped between the myelin bilayers surrounding the axons, the IEWF is contained inside the axonal cells themselves and other cell types such as astrocytes and glial cells, and the free water component containing all other water.

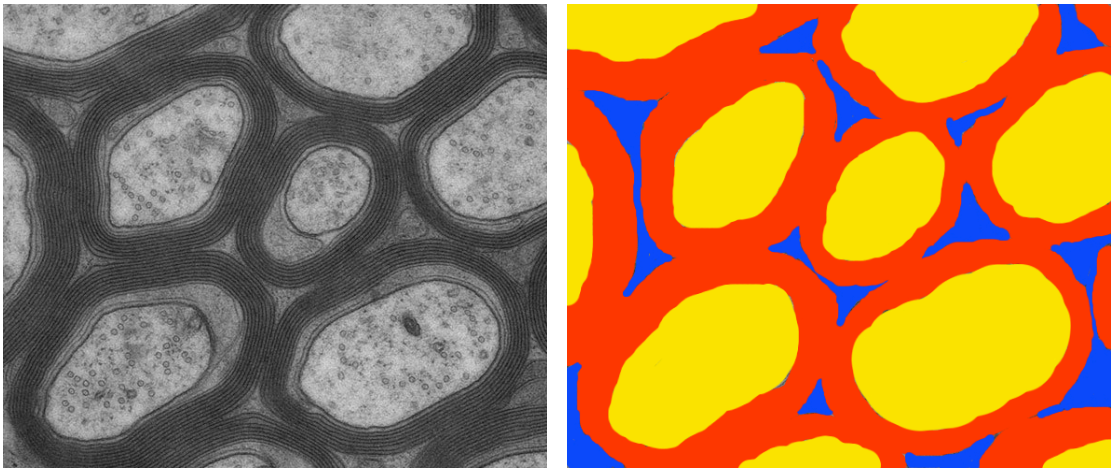

FIGURE 14: ON THE LEFT AN ELECTRON MICROSCOPE CROSS-SECTION IMAGE OF THE NERVE FIBRES (AXONS) OF THE OPTIC NERVE. AXONS ARE SURROUNDED BY SPECIAL GLIAL CELLS, THE OLIGODENDROCYTES, WRAPPING THEMSELVES AROUND THE AXONS IN SEVERAL LAYERS. BETWEEN THE AXONS, THERE ARE EXTENSIONS OF ASTROCYTES, ANOTHER TYPE OF GLIAL CELLS. REPRODUCED FROM K.-A.Nave/MPI f. Experimental Medicine[119] (LEFT), HOW THE ENVIRONMENT IS POSSIBLY DIVIDED INTO THREE POOLS, RED FOR MYELIN, YELLOW FOR INTRA-CELLULAR, BLUE FOR FREE WATER (RIGHT).

Demyelination and axonal loss of the spinal cord are fundamental causes of disability affecting pwMS, with spinal cord pathology remaining difficult to

assess in-vivo. Kolind et al.[59] used the mcDESPOT sequence to image the *in-vivo* spinal cord. Sagittally oriented mcDESPOT data were acquired of seven healthy volunteers, the imaging protocol consisted of SPGR, bSSFP, and inversion-recovery prepared SPGR scans for B_1 correction. Data for each volunteer were linearly co-registered to account for intrascan motion, and non-spinal cord voxels were masked using a semi-automated fuzzy connection approach. The B_0 and B_1 maps combined with the SPGR and bSSFP and used to calculate the MWF, myelin water residence time, and the intra/extra-cellular water and myelin water T_1 and T_2 at each voxel in the spinal cord. The MWF values in the white matter were, on average, 25.1% ± 1.3% and in grey matter, 10.9% ± 1.1%. They also found that MWF values varied between upper and lower cervical spinal cord, this follows from the varying global T_1 values that were also found (3.5%). They stated that this change was not caused by increases in the IE water or myelin water T_1 values as neither rose significantly for the lower cervical cord, but could reflect the lower myelin proportion in the cervical enlargement as myelin water has a shorter T_1 value. This results ties in with Harkins et al.[120] work in rat brain who concluded that while myelination is likely the dominant determinant of T_1 in white matter, variations in white matter microstructure, independent of myelin volume fraction, may also be reflected in T_1 differences between regions or subjects. Kolind et al. concluded with suggesting that further work would be needed to fully appreciate the microstructural underpinnings of these measurements and how they may be altered in different pathology. This introduces the idea that histological validation of the mcDESPOT sequence in spinal cord may be able to answer some of these questions of microstructural correlation with the information provided by mcDESPOT.

The mcDESPOT technique was then applied to investigate white matter development in infancy and early childhood by Deoni et al.[121-124], whether breast feeding altered development[125] and examining loss of myelin in other pathological conditions e.g primary lateral sclerosis[126]. It was utilised to develop a clinical measure of deficient MWF volume (DVF) in the brain of MS patients by Kitzler et al.[127], calculated by dividing the MWF in each volume (WM, WM lesion etc.) by the corresponding spatial region volume. Their measurements of

DVF in normally appearing white matter correlated significantly with the EDSS score (R^2=0.37; $p < 0.001$). The same quantity discriminated clinically isolated syndrome patients from a normal control population ($p < 0.001$) and discriminated relapsing–remitting from secondary-progressive patients ($p < 0.05$). They proposed that this technique may sense early disease-related myelin loss and transitions to progressive disease. The multivariate analysis indicated that global atrophy, mean whole-brain myelin water fraction and white matter atrophy were the three most important image-derived parameters for predicting clinical disability. From these papers, it can be seen that mcDESPOT has been used successfully *in-vivo*, correlating with a score of disability. This establishes that mcDESPOT provided myelin maps have a correlation with the symptomatic state *in-vivo*.

In 2013, Deoni et al. introduced a third component into the mcDESPOT model as the two water-pool model (myelin-associated water, and intra/extra cellular water), was inadequate within partial-volume voxels, i.e. containing brain tissue and ventricle or meninges, resulting in MWF under-estimation. To address this, a third, non-exchanging 'free-water' component was introduced to the mcDESPOT model. However this complicates the model, increasing the number of free parameters to be determined from stochastic region fitting from seven to nine, $T_{1,M}$, $T_{1,IE}$, $T_{1,F}$, $T_{2,M}$, $T_{2,IE}$, $T_{2,F}$, M_F, F_F , and τ_M. They performed a study of fitting algorithm stability, as the stochastic nature of the fitting method is a potential source of error in mcDESPOT. The fitting was repeated on the same data 500 times and the CoV of the estimates calculated. The CoV, averaged over the whole slice was 0.0094, indicating the algorithm converges similarly despite its random nature. A potential issue encountered in fitting complex models is the occurrence of local minima: multiple parameter sets providing similar curves and model residuals. Deoni stated that the high reproducibility noted suggests the fitting algorithm consistently converges to the same unique solution showing its stability.

The accuracy of the two pool mcDESPOT fitting algorithm was questioned in a publication by Lankford et al.[128] who, through theoretical calculations of the Cramer-Rao lower bounds (CRLB) of the variance of fitted model parameters, stated that mcDESPOT acquired at feasibly attainable signal-to-noise ratios

cannot provide parameter estimates of a two-pool system with usable precision. They validated this with Monte Carlo simulations. However, this paper calculated the CRLB when the fitting parameters were unconstrained i.e. all possible T_1, T_2 and water exchange rate values available for fitting, and when only constraining T_2 and water exchange rate values. In the unconstrained case, they found that using RF phase cycling schemes improved estimate precision by up to an order of magnitude. The scenario in which the exchange and transverse relaxation rates were constrained gave superior precision; an improvement of up to three orders of magnitude, regardless of bSSFP acquisition scheme. The calculated CRLB bounds can be seen in the figure below.

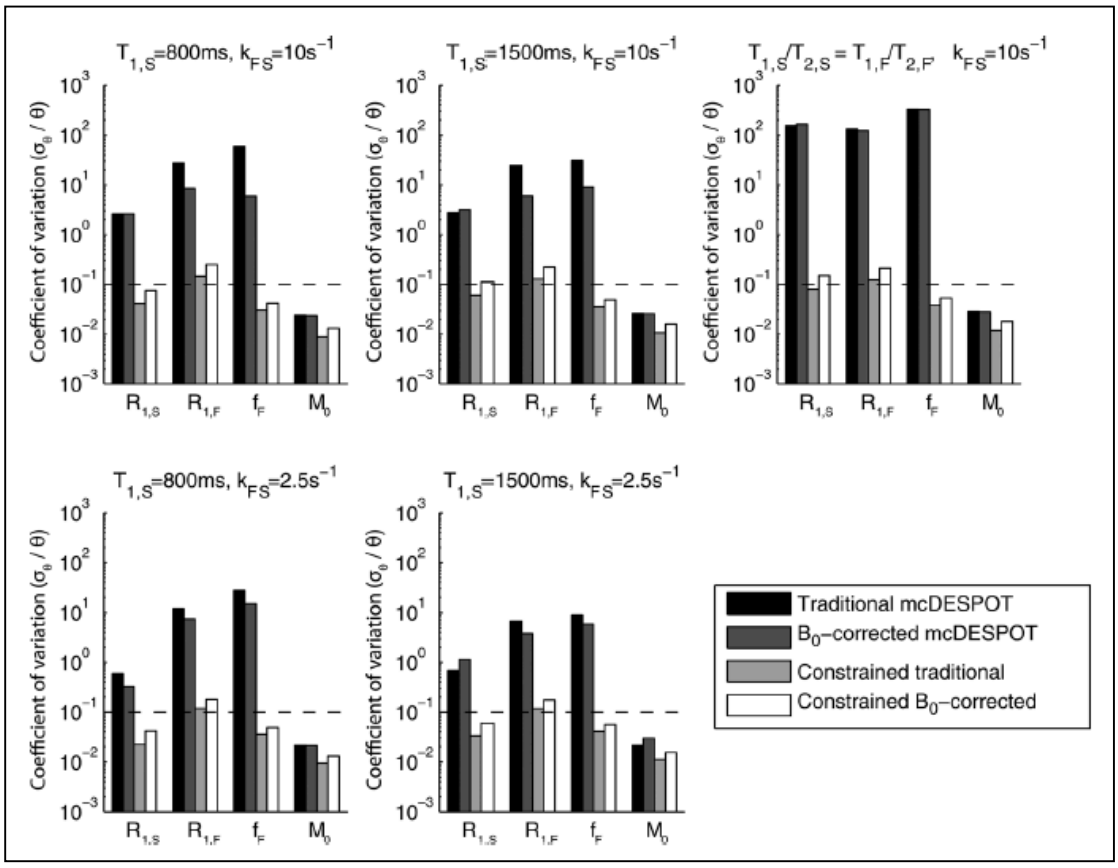

FIGURE 15: FIGURE REPRODUCED FROM LANKFORD ET AL.[128] SHOWING PARAMETER DETERMINATION ACCURACY WITH DIFFERENT T_1 AND T_2 VALUES AND EXCHANGE RATES

The constrained parameter calculations were found to be within quantitative precision (dotted line). Therefore, while the ideal situation would be to have an estimator that converges correctly without constraint, it can be seen the

addition of constraints on the T_2 values and the added modification of constraints on T_1 values may increase precision to an acceptable level.

Deoni et al.[129] answered these criticisms with a paper that, while acknowledging the criticisms laid out in Lankford's paper, stated that with reasonable bounds the stochastic region contraction algorithm could obtain robust parameter values. Several assumptions are made which are acknowledged as limitations. The first, that the three-pool tissue model used in mcDESPOT assumes similar T_1 and T_2 values for both the intra- and extra-axonal water pools, which may not be correct and modelling these pools separately is not straight-forward because mcDESPOT includes water exchange. Modelling these pools separately would also introduce an additional four parameters (T_1, T_2, relative volume fraction, and relative exchange rate), likely necessitating the acquisition of more data to reliably fit. The second, that their analysis does not preclude the possibility of non-unique mcDESPOT solutions as not all parameter combinations could be systematically examined. For example, there may be 2 or more myelin water fraction values (VF_M) values with other differing parameters that provide the same least-squares residual value. In these cases, the algorithm could jump between possible solutions, or be preferentially biased toward one. If the former, this would be visualised with neighbouring voxels in the VF_M map taking on a noise-like appearance without anatomical structure. This was not visualised with *in-vivo* data tested in the paper however. The paper acknowledged that more work needs to done to characterise the effect of MT and diffusion in the mcDESPOT model and also calls for histological verification of mcDESPOT.

It was noted in Deoni's paper that f_Ms estimated by mcDESPOT were significantly higher than myelin water fraction derived from multi-echo spin echo T2-decay curve approaches, this was explored in Zhang et al.[130]. It was supposed that this was due to MT effects, as it has been recently discovered that they can have a considerable impact on the estimate precision and accuracy of T_1 and T_2 times extracted from fast steady-state sequences[131,132]. They predicted that mcDESPOT measurements with longer RF pulses would give rise to smaller f_M values due to the reduction in MT from the non-aqueous tissue. The mcDESPOT method was performed with both short and long RF pulses in

order to investigate effect of MT on the f_M maps. While longer RF pulses increased the bSSFP signal, influencing T_2 calculation, lowering the MT saturation had little effect on estimates of f_M. The authors postulated this may be due to the complexity of the 6D searching space of the mcDESPOT analysis.

Bouhrara et al.[133] examined both the mcDESPOT and CPMG residuals over a range of parameters using energy surface analysis. They modelled finite relaxation time effects, which are omitted from the conventional signal models of both mcDESPOT and CPMG. These were the effect of finite T_2* on mcDESPOT and the effect of finite TR on CPMG. A limitation of their study was that they restricted their comparison to a two-component system without chemical exchange. The effects of finite TR on CPMG was considered negligible when TR was 3000ms.

Liu et al.[134] examined the effect that MT has on the mcDESPOT sequence as there is a limitation with relaxometry using steady-state imaging as the exchange of magnetisation between the water and macromolecular protons is not considered. For instance, Ou et al.[131] showed that this error can be up to 10% in determination of T_1 by the use of the SPGR sequence. Liu et al. introduced an additional macromolecular proton pool in exchange with the two original mcDESPOT water proton pools and expanded the set of mcDESPOT measurements by magnetisation transfer sensitive bSSFP acquisitions. They called this technique multicomponent relaxation imaging using steady-state signal evolution or mcRISE. They tested this sequence in an *in-vivo* study of the articular cartilage in the human knee joint and by numerical simulations. From their simulations they found that In these simulations, f_F and $T_{1,F}$ were increased by 41.2% and 1.5%, respectively, and $T_{2,F}$, $T_{2,S}$, and $T_{1,S}$ were decreased by 14.5%, 11%, and 3.4%, respectively, at the maximum bias. These overestimations increased rapidly with increased macromolecular fraction f. They believe that the estimated f_F will likely reflect macromolecular content in addition to the fast-relaxing water fraction. However, these simulations were performed in cartilage, and should be verified in other situations.

4.5 OTHER MYELIN MEASUREMENT TECHNIQUES

MTR histogram analysis reveals significant differences in MS patients when compared to healthy controls that worsen over the course of disease. MTR is heterogeneously reduced in both MS lesions and NAWM. Focally demyelinated MS plaques have severely reduced MTR (20–80% of NAWM MTR). Agosta et al.[135] found that a multivariable model included baseline GM MTR histogram peak height [P = 0.029, odds ratio (OR) = 0.97], and average MS lesion MTR percentage change after 12 months (P = 0.016, OR = 0.88) as independent predictors of disability worsening at 8 years (r2 = 0.28). Early animal studies and MRI–pathology correlation studies of MS lesions revealed strong correlations between MTR and myelin content[136,137]. For reasons that remain uncertain, some MTR reductions precede lesion formation[138]. However MTR, while being probably the most available MRI technique to approach the assessment of myelin content, shows suboptimal specificity for myelin, as water content, inflammation and axonal damage still represent relevant contributors to the signal modifications[139,140]. Moll et al.[139] found that when lesions were excluded, there was no correlation between MTR and myelin in diffusely damaged white matter as seen in pwMS, concluding that other factors influence MTR changes in lesions. It is desirable to have a measure that is not influenced by these other factors, unrelated to physically present myelin structure, such as inflammation or oedema. The method of the short T2 CPMG sequence and mcDESPOT algorithm is to decompose the signal in each voxel into myelin, intra/extra-cellular fluid and free water pools. Inflammatory changes causing collection of water around the cells should be included in the intra/extra cellular water pool, with the water signal from the restricted laminar structure of myelin being unaffected and remaining proportional to the myelin present. Confirmation of this proportionality of the MR signal to myelin can only be examined with reference to histological staining.

Diffusion methods have also been used to make a measure of myelin. The hypothesis being that reduced myelin would lead to an increase in radial diffusivity, i.e., the diffusion perpendicular to the axonal tracts, as measured by diffusion tensor imaging. The water molecules in the restricted tubular

environment of the axon should have free diffusion along the axon, but be restricted in their movement by the walls of the axon surrounded by myelin in the perpendicular direction. If the myelin were destroyed this restriction would be removed, leading to an increase in radial diffusivity. Naismith et al.[141] found Increased diffusivity in acute multiple sclerosis lesions predicted risk of severe demyelination and axonal injury, and in a second paper in 2013[142] found that spinal cord diffusion tensor imaging reveals that EDSS scores were correlated with radial diffusivity and fractional anisotropy in demyelinating disease. This was also found by Oh et al in 2012[143], though these are just a few papers in the body of work that shows that diffusion imaging is sensitive to the pathology of MS.

The limitation of diffusion imaging is partial volume averaging between tissue components with large voxel sizes in clinical sequences, resulting artificially reduced FA values. If there is a mix of tissues within the voxel, the diffusion tensor model of tightly packed tubes is not appropriate and results can be inaccurate. Also, disease processes like oedema, can make it difficult to accurately describe the underlying WM fibre properties. In the brain, diverging fibres and crossing fibres require a highly complex model, though these are currently being developed. Even if the diffusion model is correct in the tissue being imaged, the radial diffusivity, considered the diffusion measure most associated with myelin reduction, is unfortunately also influenced by changes in the axonal diameter or density of axons[144].

The myelin g-ratio is a technique developed by Stikov et al.[145] The g-ratio can be expressed as a function of the myelin volume fraction, and the axon or fibre volume fraction. The myelin volume fraction can be calculated by MT methods, for instance, in the paper by Schmierer et al in 2008, the macromolecular proton fraction (f_B) in unfixed brain was calculated using a research MT sequence with a Gaussian MT pulse of 14.6 ms duration was applied at 10 different combinations of MT pulse offsets and three pulse powers, or by using short T2 methods or any other method that calculates myelin volume fraction such as mcDESPOT. The combination of myelin volume measurement and axon volume measurement with diffusion gives more information about the microstructure imaged as computation of the g-ratio

captures exactly how the myelin volume fraction changes with axon volume fraction. Developing the most accurate myelin measure to add into this technique will be useful in characterising the changes in myelination and axonal loss associated with MS.

5 MATERIALS AND METHODS

5.1 SCANNERS

Two scanners were used at Barts Health Trust. The first was a Siemens Verio 3T system. The Siemens Verio system has a 70cm bore, is 173cm in length and has a gradient strength of 45 mT/m and a slew-rate of 200 mT/m/s. The Philips Achieva 3T system has a 50cm field of view (FoV), and a gradient strength of 80 mT/m and a slew-rate of 200 mT/m/s.

Before running any sequence, there are automatic preparation steps performed by clinical scanner. These include central frequency determination, active shimming of the field of view, power optimisation, receiver gain and echo phase determination. The echo phase determination is needed to ensure that the channel phases are correct. If disabled, then an incorrect phase correction is used at later echo times. Although the main sequence parameters are entered by the operator, these options are limited by clinical scanners and unknown subroutines adjust parameters such as RF pulse length, gradient rise time and other 'behind the scenes' parameters that would not need to be accessed by a clinical operator. These limitations mean that the settings actually used by the scanner are not known without running a directly programmed sequence. This did lead to some difficulties in acquiring the DESPOT1, DESPOT2 and mcDESPOT sequences, detailed in the respective chapters.

As difficulties were encountered in acquiring the mcDESPOT sequences on the clinical scanners without pulse programming available, an opportunity became available for preliminary work using the Agilent 7T preclinical scanner at King's Hospital. It is used for small animal imaging studies. The maximum gradient strength is 400 mT/m. The useful field of view is approximately 5cm in length. The diameter of the bore is dependent on the RF and gradient coils used; the maximum diameter is 15cm. It is considered best to use the smallest diameter coils possible, in order to have the most homogeneous B_0 field over the sample.

As the Agilent scanner is a preclinical research scanner, all preparation phases are performed and evaluated by the operator. The sequence parameters are set by the operator and are not adjusted by any automatic routine. This gives complete control over all aspects of the sequence. This ensures the sequence set is the sequence run, but an untrained operator can cause significant damage to the scanner if unsuitable values are set.

After the success of the mcDESPOT sequence in the small field-of-view pre-clinical scanner, an opportunity arose to acquire a larger brain hemisphere in the Philips Achieva 7T wholebody scanner at the Sir Peter Mansfield Centre at Nottingham University. The 7T scanner offers a higher signal to noise ratios giving high resolution scans, but B_0 inhomogeneities are higher due to the interaction of high frequency (298 MHz) electromagnetic energy with the body, and higher energy deposition, as measured by the specific absorption ratio (SAR). There is a research setting that does allow higher SAR constraints, but is still limited to within clinical limits.

The current gradient configuration has a maximum strength of 33 mT/m with a slew-rate of 166 mT/m/s. The receive head coil has 32 channels. Again, before running any sequence, there are automatic preparation steps performed by the 7T wholebody scanner.

5.2 BRAIN HEMISPHERES AND SPINAL CORD SAMPLES

The samples used in this study were provided by the MS Tissue Bank. Samples were extracted from the cadaver within the first 48 hours. The post mortem delay (PMD) from time of death to extraction is given, where known, in the table below. Once extracted, the whole brain and whole spinal cord for each patient was placed into formalin. All the samples had been fixed in formalin for over a year before this project was started. This meant that all samples were fully fixed and stable before scanning.

The samples used in this project are given in the tables below

Hemipheres	Sex	Age at Death	Date of Death	PMD (hours)	Disease Duration (years)
C56	Male	82	unknown	50	N/A
MS436R	Female	61	unknown	unknown	unknown
MS442L	Female	57	03/2010	29	18

Spinal Cords	Sex	Age at Death	Date of Death	PMD (hours)	Disease Duration (years)
C58	Male	89	06/2011	15	N/A
C60	Male	78	09/2011	10	N/A
MS232	Male	92	11/2004	23	60
MS345	Female	96	09/2007	39	unknown
MS436	Female	61	unknown	8	unknown
MS454	Male	67	11/2010	33	44
MS455	Female	69	11/2010	32	19
MS464	Female	61	04/2011	41	4
MS471	Female	87	03/2011	47	8
MS475	Male	72	unknown	12	unknown
MS484	Female	81	10/2011	24	35
MS493	Male	65	01/2012	45	17
MS561	Female	56	11/2013	unknown	27

TABLE 3: HEMISPHERES AND SPINAL CORDS USED FOR SCANNING

5.3 EXPERIMENTAL SET-UP FOR SCANNING BRAIN HEMISPHERES

All experimental methods were first tested on a fixed post-mortem brain hemisphere. The brain hemisphere has larger, recognisable structural elements, and with more comparable published research in the post-mortem brain, methods could be confirmed before use in the smaller, more challenging spinal cord.

Before scanning the hemisphere is first inserted into the holder, surrounded by Perfluorpolyether (an oil containing no hydrogen, therefore has no signal using the standard H^1 coils). Care must be taken as the hemisphere, although fixed, is still delicate and may be damaged. The meninges were not removed before scanning as these were to be used for further histological work (not part of this project) and needed to be kept in-situ. This did mean that formalin could be

trapped underneath even when the hemisphere had been dried with paper towels before set-up in Perfluorpolyether.

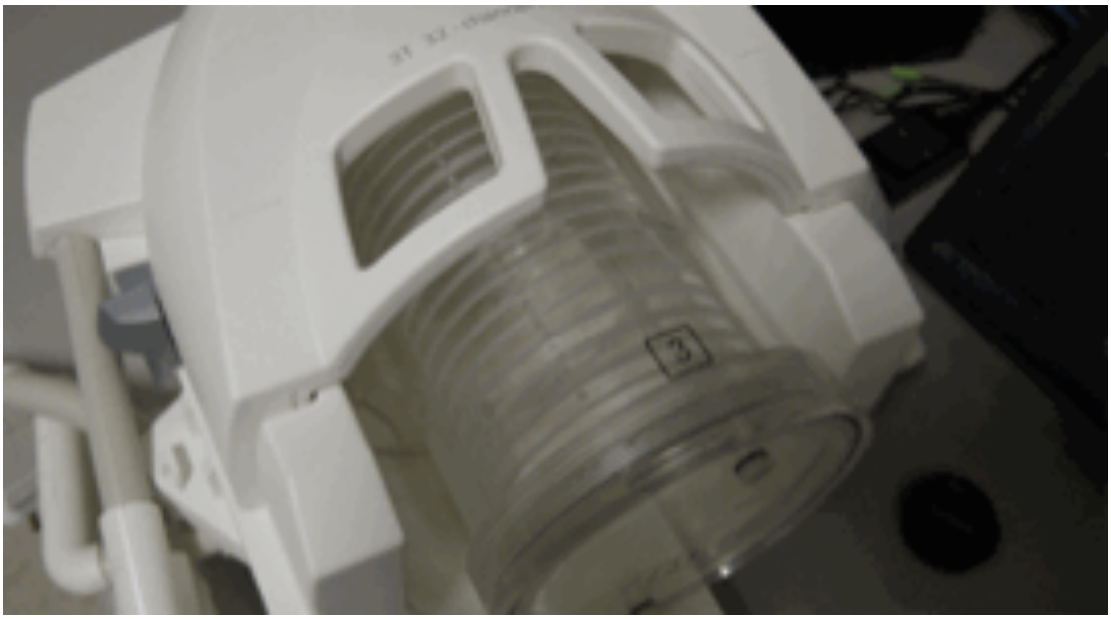

FIGURE 16: THE HOLDER INSERTED IN THE HEAD COIL

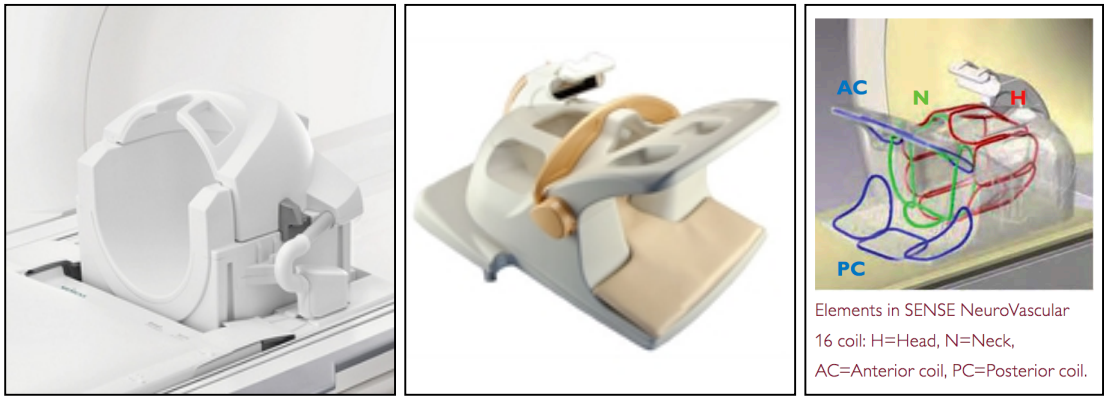

FIGURE 17: THE 32-CHANNEL HEAD COIL (LEFT) REPRODUCED FROM THE SIEMENS WEBSITE HTTP://WWW.HEALTHCARE.SIEMENS.CO.UK/, THE 16-CHANNEL COIL (CENTRE AND RIGHT) REPRODUCED FROM HTTP://WWW.PHILIPS.CO.UK

The Siemens Verio 3T system which is equipped with the 32-channel head coil, each coil contains an integrated preamplifier. The upper part of the coil is removable, containing 12 elements, the lower part contains 20 elements. The dimensions of the coil are 300 mm × 390 mm × 315 mm (L × W × H).

The Philips Achieva 3T system has a SENSE head and neck coil with 16 elements. The dimensions of the coil are 690 mm x 390 mm x 390 mm (L × W × H).

5.4 WHOLE SPINAL CORDS

The Philips Achieva 3T system is based at St Bartholomew's hospital. It is equipped with a spinal coil used *in-vivo* for imaging the whole spine. Imaging the complete spine, keeps the experimental set-up as close as possible to the clinical situation. The SENSE spinal coil is multi-transmit enabled and has 15 elements. The coil has a 125cm FoV. The patient is positioned on top of the element array which is contained in a hard plastic flat bed, which makes it simple to position the spinal cords on top of the coil. The field of view extends approximately 20cm above the coil so it is important to position the spinal cords as close as possible to the face of the coil. The container used to hold the spinal cords was chosen to have a flat bottom, and thin plastic in order to ensure this. The container is necessary to hold water to increase the loading on the coil, otherwise the pre-scan fails as the f0 determination in the preparation does not have enough signal.

The dura is removed from the spinal cords as this would cause formalin to be trapped next to the spinal cords under the dura.

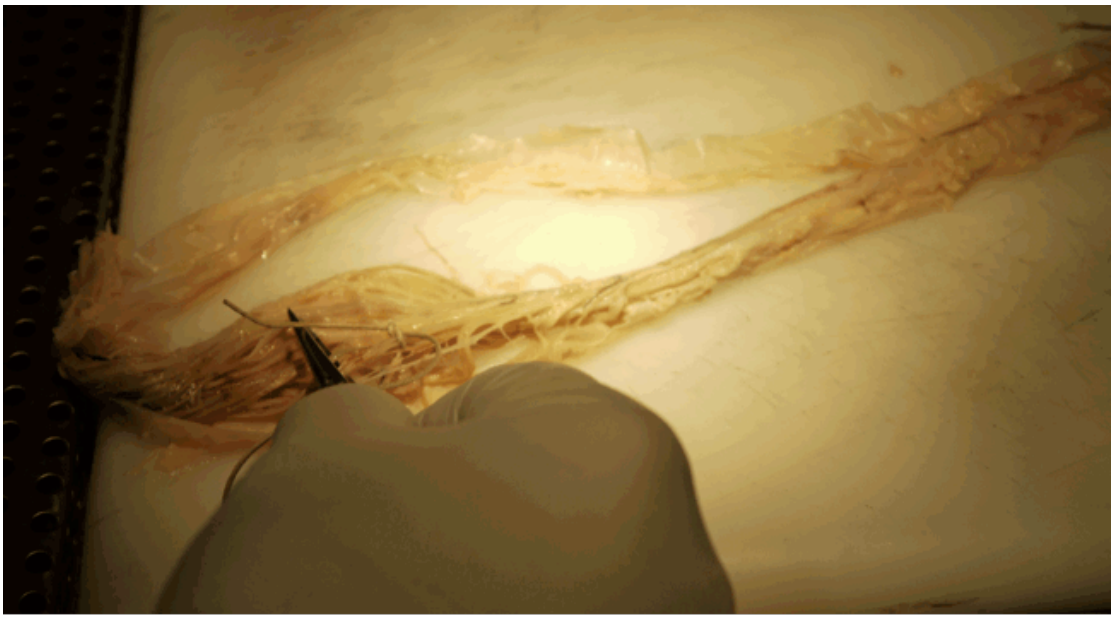

FIGURE 18: DURA BEING REMOVED FROM THE SPINAL CORDS, AND A KNOT MARKING THE L5 NERVE ROOT

Several iterations were imaged at the start of the project in order to find a suitable imaging set-up for the whole spinal cords.

FIGURE 19: ABOVE, 1ST ITERATION; THE SPINAL CORD WRAPPED IN CLOTH, 2ND THE SPINAL CORD SUSPENDED BETWEEN TWO CARBON FIBRE RODS INSERTED INTO DRILLED HOLES IN A PERSPEX DISC, 3RD THE FINAL DESIGN THE SPINAL CORD SUSPENDED BETWEEN PERSPEX RODS WITH FISHING WIRE

Wrapping the spinal cord in material was unsuitable due to bubbles trapped between the layers causing susceptibility artefacts. At that point, two rods inserted in plastic discs with the spinal cord tied between the two were tried to keep the spinal cord in the centre of the tube. 4mm carbon fibre rods were the first iteration of this setup but they gave an unusual artefact, seen in the figure 20.

FIGURE 20: SHOWN AT THE TOP IS AN IMAGE OF THE CARBON FIBRE ROD SET UP WITH AN UNUSUAL ARTEFACT, ON THE BOTTOM THE SAME SET UP WITH PERSPEX RODS (RED ARROW)

There is what looks like a Gibbs ringing artefact on the top image of the figure, which completely obscures the spinal cord. This is possibly due to an unexpected signal in the carbon fibre rod as ringing artefacts occur at sharp changes in image intensity or vibration of the rod during imaging. The bottom of the figure shows the same set up with 4mm Perspex rods, (the black line at the bottom of the image with a red arrow) which have no signal and do not affect the image quality.

The spinal cords are placed in glass tubes, kept in place by nylon fishing line (0.4mm thick) on Perspex holders. The glass tubes were 45 or 55cm long with a 3cm diameter. The nylon fishing line is wrapped very carefully in order to ensure the tension holds the delicate fixed spinal cord in place but without damaging it. The glass tube is made waterproof with a glass stopper. The spinal cords are surrounded by Perfluorpolyether.

FIGURE 21: A SPINAL CORD INSIDE A GLASS TUBE

At first a larger container was used to hold the spinal cords and water surrounding them on the scanner, taking 9 spinal cords at a time. The

dimensions of the plastic box were L:100 x W:60 x D:30 cm, but this gave an uneven signal across the coil (which is optimised for a narrow field) so this was replaced with a narrower plastic box (L:80 x W:20 x D:18 cm), which held 3 spinal cords at a time.

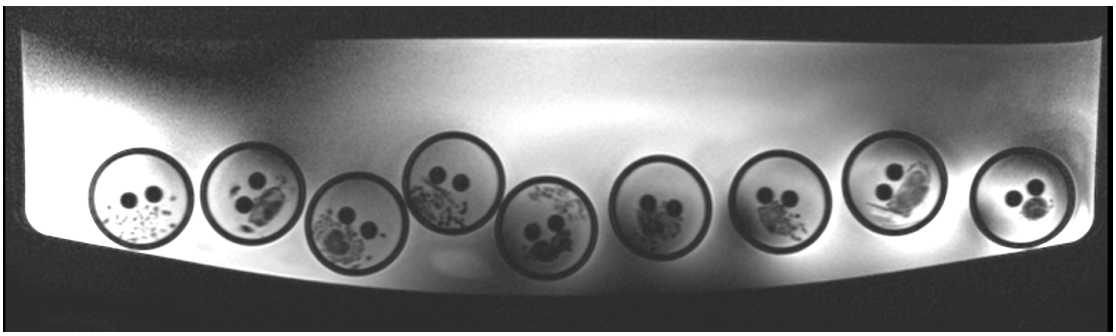

FIGURE 22: MR IMAGE OF THE LARGER CONTAINER, SHOWING UNEVEN SIGNAL ACROSS THE COIL WITH DIFFERENT SIGNAL INTENSITIES IN DIFFERENT AREAS IN THE IMAGE

FIGURE 23: SPINAL CORDS IN THEIR HOLDERS. IN THE SCANNER, THEY ARE COVERED IN WATER TO ENSURE ENOUGH SIGNAL TO SCAN

5.4.1 WHOLE SPINAL CORDS IN THE 7T PRECLINICAL SCANNER

Four spinal cords were taken to King's College in their glass tubes for scanning. This is a small animal or preclinical scanner with insertable B_1 coils and gradient coils. The 100G gradient coil and a standard quadrature RF coil (Rapid GmbH), diameter 3.3cm coils were used in this case, as this was the smallest coil that the glass tube fitted into, this optimised the shim within the FoV. The FoV is 5cm long in this scanner so I designed a method for the lesions to be located. The spinal cords were scanned with MR visible markers attached at a point on their length. The position of this marker could then be noted on the images and the position of the lesion from this point calculated in cm. This can then be measured on the outside of the tube and the tube positioned accordingly in the preclinical scanner so the lesion is within the FoV.

5.5 DISSECTED SPINAL CORDS

After the cords had been scanned using the SENSE spinal coil, in order to examine them in detail and provide a better shim, they were cut into approximately 10cm sections to fit into 1.5cm diameter falcon tubes. The sections were cut at nerve root levels, so the size of the sections slightly differed. The spinal cord sections were dried with paper towels before insertion into the tubes. In order to keep the spinal cords at a distance from the sides of the tubes to prevent susceptibility artefacts, small sections of Perspex rod were inserted between the cord and the sides of the tubes. This also kept the cord straight within the tubes.

The spinal cords in their tubes are positioned inside a larger box full of water. The water is necessary to have enough hydrogen in the field of view for coil tuning purposes. The tubes are positioned using a plastic waffle material with a honeycomb structure. The plastic waffle had to be arranged with its tubular structure in the vertical direction so air bubbles could rise to the surface with gentle agitation. Otherwise susceptibility effects occurred, spoiling the images where the bubbles were trapped in the walls if the tubes were horizontal.

FIGURE 24: SET-UP USED TO POSITION SPINAL CORDS FOR IMAGING. LEFT HAND IMAGE OF EMPTY PLASTIC WAFFLE CONSTRUCTION AND WATERTIGHT BOX, RIGHT HAND IMAGE SHOWING TUBES INSIDE BOX

6 T_1 MAP ACQUISITION

6.1 ACQUISITION OF T_1 MAPS IN THE BRAIN

At the start of the project, it was necessary to validate the methods used to determine T_1 values in fixed post-mortem tissue. There has been a reasonable amount of data acquired for the values of T_1 in the *post-mortem* brain, at that time there were no values published for the spinal cord at 3T. Therefore, sequence testing was performed on a control brain. Single-slice Spin Echo-Inversion Recovery (SE-IR) sequences were acquired on the Siemens Verio 3T scanner and 32-channel head coil. The T_1 map of the single slice, processed with the MATLAB program discussed in section 2.4.4.5, is shown on the left in the figure 25. The Siemens scanner has an option for 'real' or phase-correct values in the images. This means the signal values will have the correct sign when plotted for T_2 determination. The scanning parameters are a 2mm slice, TE 15ms, 1 NSA, FoV 199×199mm, matrix 384×384, acquired using both 3000ms and 5000ms as a TR, TIs of 50, 400, 1100 and 2000ms. The centre slice was then kept in the same place by using the 'copy parameter' option from the single slice acquisition, and the slices changed to 33 (whole brain coverage). Multi-slice SE-IR images of the control brain C56 with TIs of 50, 400, 1100 and 2000ms were then acquired. This was to test the theory above, that the T_1 values are unchanged if multi-slice images with interleaved slice acquisition are acquired. Slice 17 is the centre slice and its T_1 map is shown on the right in Figure 25.

6.1.1 RESULTS IN A CONTROL BRAIN

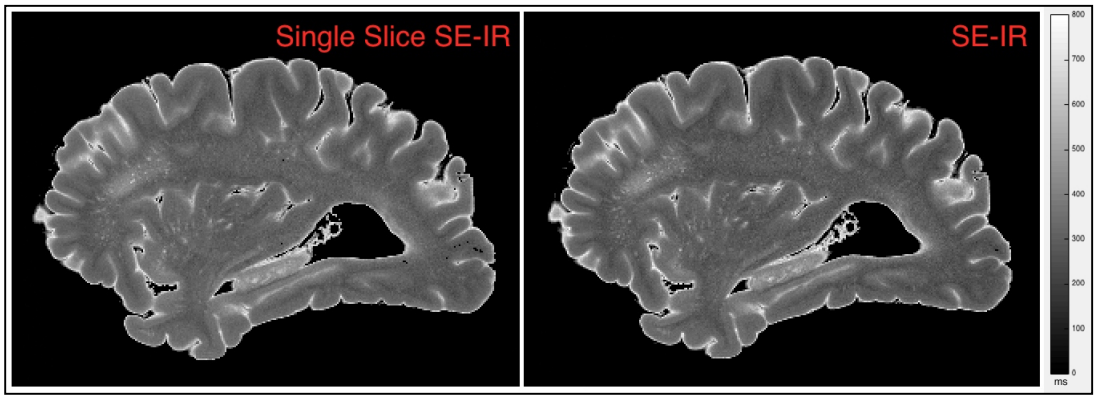

FIGURE 25: LEFT: SINGLE SLICE SE-IR SERIES WITH TI VALUES OF 50, 400, 1100 AND 2000MS. RIGHT: MULTIPLE SLICE SE-IR SERIES, CENTRE SLICE, WITH TI VALUES OF 50, 400, 1100 AND 2000MS.

The T_1 maps produced by the single slice SE-IR and the multiple slice SE-IR are visually identical.

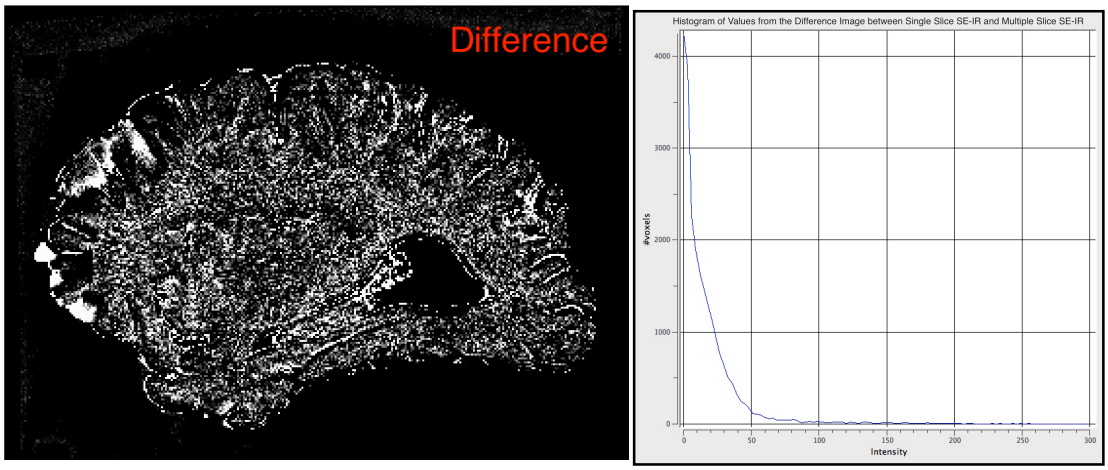

FIGURE 26: THE DIFFERENCE IMAGE BETWEEN SINGLE SLICE SE-IR AND THE MULTIPLE SLICE SE-IR T1 MAPS AND THE HISTOGRAM OF THE DIFFERENCE VALUES

The difference image shows little structure. There does seem to be some high values around the sulci. This is likely due to pockets of formalin caught in these areas. The high T_1 value of the formalin, equivalent to free water, is likely to be more difficult to ascertain with the TI values used with higher noise in the image acquisitions and higher error in the fitting method. This gives a large difference between the two methods at these points.

6.1.2 USING A TURBO SPIN-ECHO (TSE) SEQUENCE FOR IR IMAGING

Next the viability of using a Turbo Spin Echo (TSE-IR) inversion recovery sequence was tested. This is the only way that this sequence can be used *in-vivo*, as otherwise to obtain enough time points in the curve will take approximately two hours to acquire. While much work has been performed at 3T in the *in-vivo* brain, there seems to be very little work on values on the *post-mortem* brain. Therefore, the exact sequences must be tested *in-vivo* and compared with published literature. If the values match, then the method has been validated.

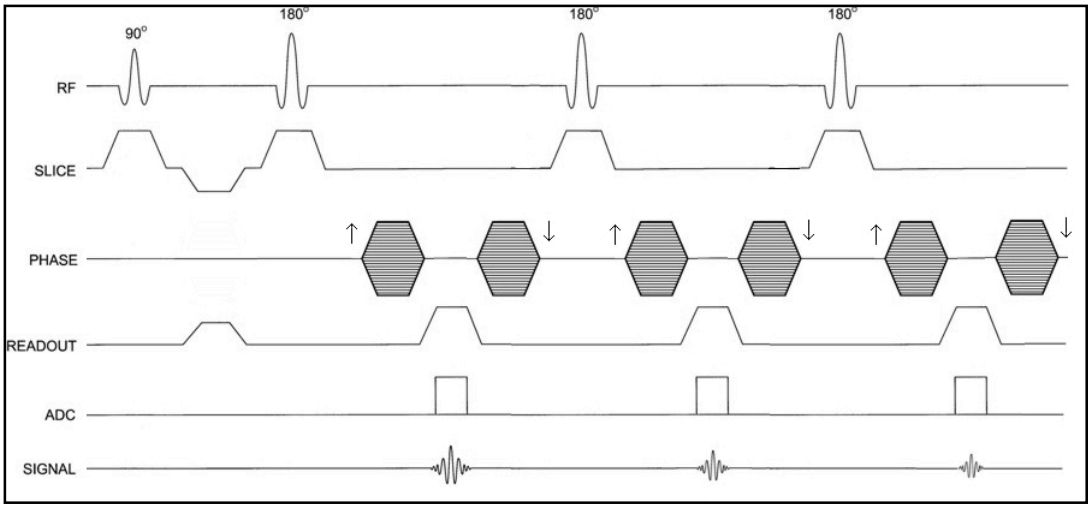

FIGURE 27: TURBO SPIN ECHO SEQUENCE DIAGRAM

The 33 slice TSE-IR sequence was acquired of the control brain C56 with TIs of 50, 400, 1100 and 2000ms. The TE was 15ms, TR was still set at 5000ms with a time of acquisition of approx. 27min for all data points with an echo train length (ETL) of 7.

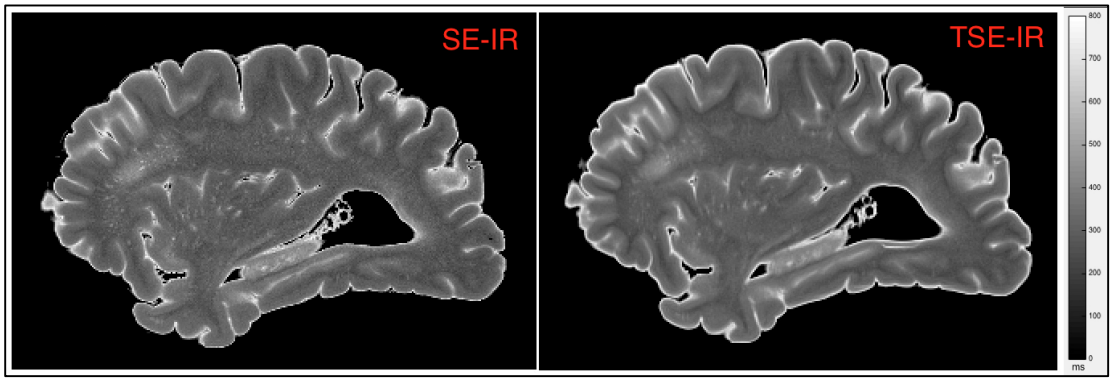

FIGURE 28: LEFT: SINGLE SLICE SE-IR SERIES WITH TI VALUES OF 50, 400, 1100 AND 2000MS. RIGHT: MULTIPLE SLICE TSE-IR SERIES, CENTRE SLICE, WITH TI VALUES OF 50, 400, 1100 AND 2000MS.

However, there are subtle differences in this image compared to the gold standard SE-IR sequence. Although the resolution matrix remains the same at 384×384, the image detail seems slightly degraded. This is due to the fact that not all lines of k-space are filled on echo unlike the SE-IR sequence, but this is paid for by the longer image acquisition time for SE-IR imaging.

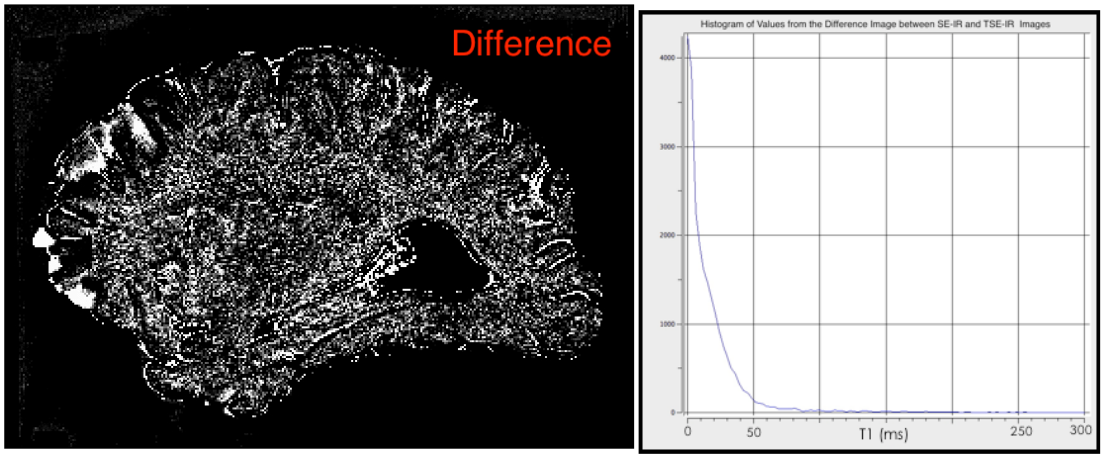

FIGURE 29: THE DIFFERENCE IMAGE BETWEEN SE-IR AND TSE-IR T1 MAP AND THE HISTOGRAM OF THE DIFFERENCE VALUES

The difference image shows little structure. There are again some high values around the sulci, which are again likely due to the pockets of formalin trapped as stated before in section 6.1.1. However, as the objective is T_1 values in white and grey matter, not free water, and image quality is less important, it is considered that using the TSE-IR method is reasonable.

6.1.3 *IN-VIVO* T_1 MAPPING IN A CONTROL BRAIN

I acquired an *in-vivo* T_1 map. As this was *in-vivo*, the image size was reduced to 128×128 with a FoV of 160×160 to reduce the time of acquisition to prevent movement artefacts. The TE was 15ms, TR was still set at 5000ms with a time of acquisition of approx. 12min. The matrix size was 128×128 with a FoV of 160×160mm with 15 coronal images taken through the centre of the head.

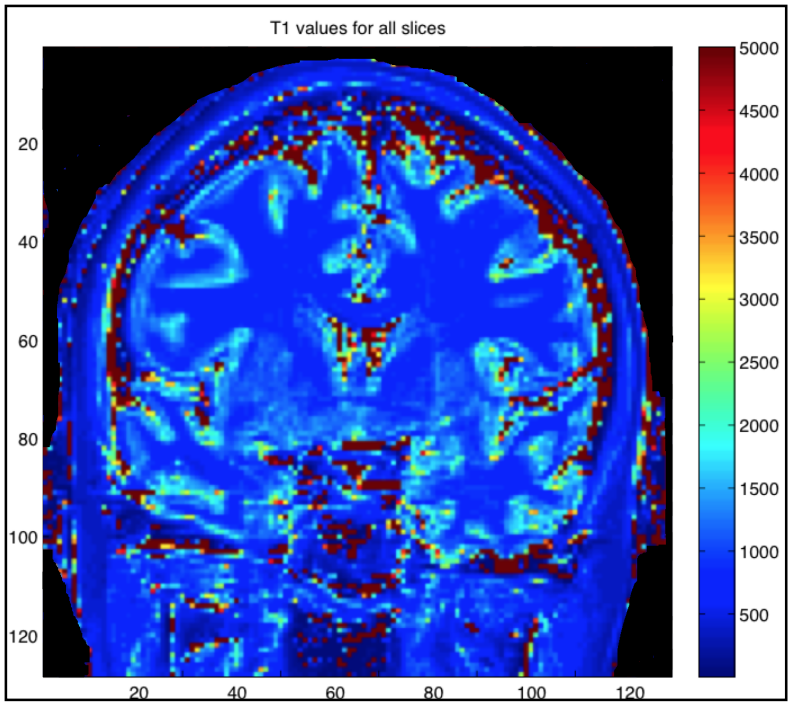

FIGURE 30: T_1 MAP OF AN IN-VIVO BRAIN, TI VALUES 50, 300, 900, 1300

6.1.4 RESULTS

Regions of interest were taken in the white and grey matter.

T_1 values (ms)	WM	GM
Post-mortem Brain	179 ± 22	234 ± 28
In-vivo Brain	822 ± 39	1234 ± 91

TABLE 4: SE-IR SEQUENCE T_1 VALUES

The results of the *post-mortem* studies did not correlate as well as might be hoped with the literature. Pfefferbaum et al.[93] found relaxation times of 426 ± 18 and 375 ± 33ms for WM and GM respectively at 1.5T in one *post-mortem* brain. The healthy status of this brain was uncertain as the patient was a known heavy drinker. The value of T_1 should increase with field strength, so it expected that 3T T_1 values would be greater. However, it is a matter of discussion how the WM value was larger than the GM in their *post-mortem* results when they found *in-vivo* T_1 values of 1138 ± 53ms for WM and 1581 ± 108ms for GM. The *in-vivo* values I found correlated well with other groups.

WM and GM values in-vivo (ms)			
Author	Field Strength	WM	GM
Henderson 1999 [146]	1.5T	613 ± 26	1226 ± 69
Steinhoff 2001 [147]	1.5T	560 ± 10	1109 ± 18
Shah 2001 [148]	1.5T	600 ± 25	1000 ± 90
Deichmann 1999 [149]	2T	682 ± 4	1268 ± 29
Clare 2001 [150]	3T	860 ± 20	1310 ± 60

TABLE 5: IN-VIVO T_1 VALUES IN HEALTHY VOLUNTEERS MEASURED BY MORE THAN ONE METHOD

6.2 T_1 MAPS IN A MS HEMISPHERE USING THE TSE-IR SEQUENCE

A T_1 map using the TSE-IR in a MS brain was acquired on the Philips scanner in order to compare the values with the DESPOT1 T_1 values acquired in section 6.5. The parameters were TE 16ms, TR 5000ms, matrix size 240 × 240, 50 slices, IR values of 50, 100, 150, 200, 300, 400, 600, 800, 1000, 1500 and 2000ms and a ETL of 7.

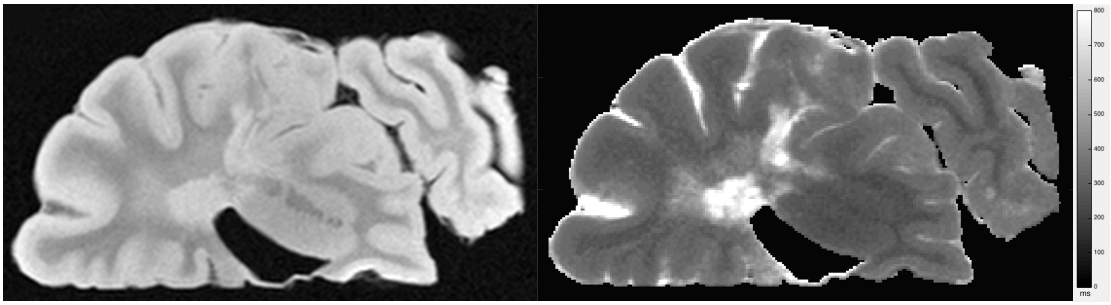

FIGURE 31: ON THE LEFT A PD-WEIGHTED IMAGED OF MS436R, ON THE RIGHT, A T_1 MAP OBTAINED USING A TSE-IR SEQUENCE, IR VALUES OF 50, 100, 150, 200, 300, 400, 600, 800, 1000, 1500 AND 2000MS

A histogram is shown below of the T_1 values found in the same slice as the T_1 map shown above.

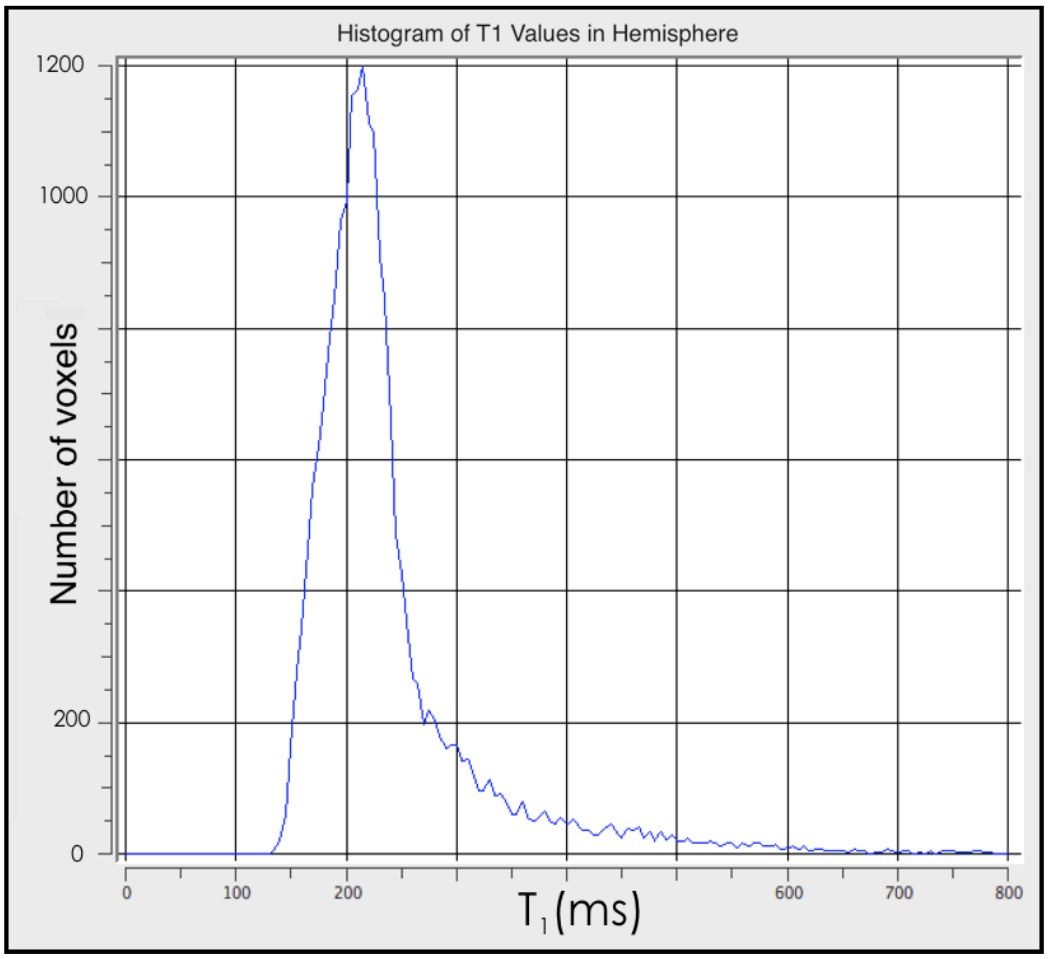

FIGURE 32: T1 VALUES IN THE HEMISPHERE SHOWN IN THE FIGURE ABOVE

The median intensity in the TSE-IR is 215ms. There are higher T_1 values between the sulci due to trapped formalin.

6.3 T_1 MAPS IN THE SPINAL CORD USING THE SE-IR SEQUENCE

Once the methodology was considered to be sound, T_1 maps were acquired in the spinal cord. The T_1 maps in Fig. 33 were acquired in the Siemens Verio 3T scanner and 32-channel head coil (see section 5.5). Approximately 10 cm sections of spinal cord were placed into sample tubes in formalin. The images were passed into the OSIRIX program for display, free on the web at http://www.osirix-viewer.com. The magnitude or PD-weighted images (and the T_1 maps) in the figure are scaled identically, and it can be seen that some areas have a higher signal than others in the PD-weighted images.

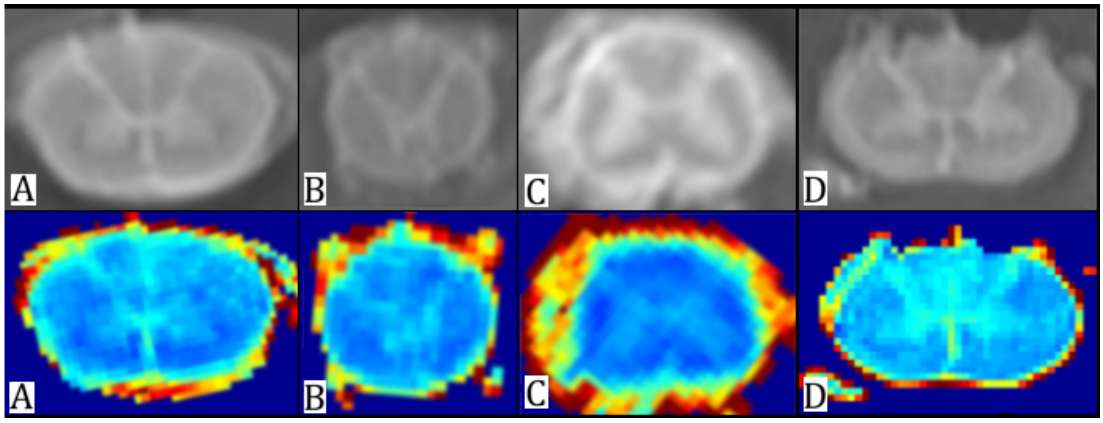

FIGURE 33: MAGNITUDE IMAGES OF THE POST-MORTEM SPINAL CORD TE/TR= 16/16000MS, TI 2000MS (TOP ROW) AND T_1 MAPS (BOTTOM ROW) OF POST MORTEM MS SPINAL CORD AT THREE DIFFERENT LEVELS, (A) CERVICAL, (B) THORACIC AND (C) LUMBAR SPINAL CORD AND POST MORTEM SPINAL CORD OF A HEALTH CONTROL (D). T1 MAPS ARE SCALED BETWEEN 0 - 800MS.

Figure 34 below shows a T_1 map of a lesion. The values in the lesion are higher than white and grey matter due to the lower myelin content and higher free water content.

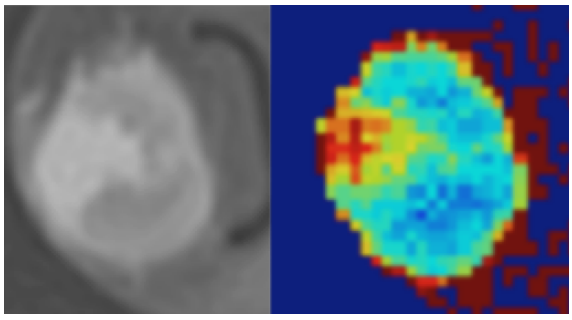

FIGURE 34: T_1 MAP OF A LESION IN THE CERVICAL MS SPINAL CORD. T1 MAP IS SCALED BETWEEN 0 – 800MS.

The T_1 values in these maps were qualitatively assessed to identify the pixels associated with WM and GM, sampling more than 10 pixels and averaging. As the spinal cord is a small

structure, typically 2cm in diameter and the pixel size was 0.5mm, there are approximately 40 voxels across the diameter. This meant that the partial volume effect was problematic. In the thoracic area for example, especially in the thin posterior grey matter horns, which were often only one voxel in diameter or an average of two. Careful decisions had to be made over whether a voxel was a true measure of one single tissue type. Care was taken to avoid the edges of the grey matter and the edges of the spinal cord for white matter values. Lesional areas were more easily identified due to higher T_1 values than the white and grey matter. White matter was more easily identified in the cervical region, grey matter in the lumbar area. The results are given in the graph below.

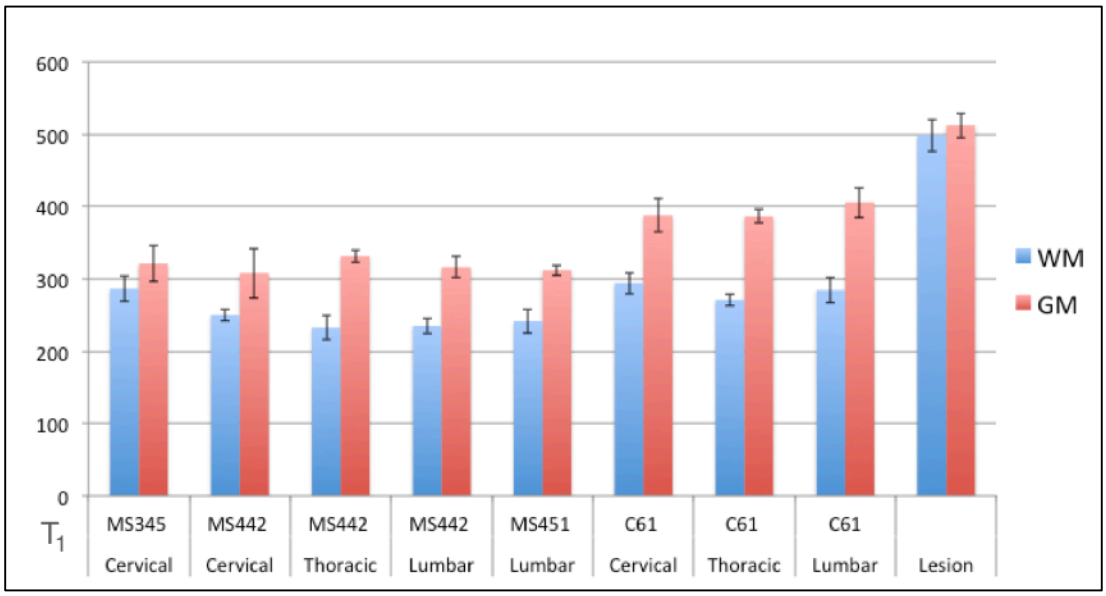

FIGURE 35: GRAPH OF T1 VALUES AT DIFFERENT LEVELS IN MS AND CONTROL SPINAL CORD. ERROR BARS SHOW THE STANDARD DEVIATION.

The average values in the MS cords were 249 ± 32 ms in white matter and 318 ± 46 ms. These values can be compared to the *in-vivo* results in the spinal cord by Smith et al[151].

	Lateral column	Dorsal column	SC GM
IR T_1 (ms)	863 ± 23	900 ± 17	972 ± 36

TABLE 6: IN-VIVO T1 VALUES IN THE SPINAL CORD FROM SMITH ET AL [151]

It is interesting to note that the difference in values of T_1 in the WM and GM in-vivo is smaller than that in brain tissue. The structure of the spinal cord WM is noted in the Smith paper as being most similar to WM found in the internal capsule and corpus callosum rather than the less dense frontal WM, and the GM most similar to the deep GM of the basal ganglia and putamen. However, when they compared the T_1 values of the structures mentioned with the spinal cord, they were not similar, finding 721 ± 68ms in the corpus callosum WM and 1102 ± 40ms in the putamen GM. It may not be possible to extrapolate spinal cord T_1 values from brain values and they must be measured separately.

6.3.1.1 Discussion

The method has been validated in first the brain and then sufficient quality images of the spinal cord were acquired using the head coil and short sections of the spinal cord.

6.4 COMPARISON WITH T_1 VALUES FROM IR-TSE MAPS WITH POST-MORTEM DELAY AND FIXATION TIME

There seemed to be some small variation in T_1 values found in different spinal cords. It was considered that this may be due to different lengths of fixation or different time periods between death and the start of fixation (post-mortem delay). Therefore, regions of interest were taken in the cervical white matter. This area was chosen as the spinal cord has a larger diameter at this point with a larger proportion of white matter. This meant that the region could be drawn with certainty that the voxels were in white matter and with the region boundaries at a distance from other tissue types to avoid partial volume effect.

This analysis was performed on the spinal cords C58, C60, MS436, MS493, MS475, MS484, MS454, MS453, MS451, MS442, MS345, MS232, MS455, MS464 and MS471.

6.4.1 RESULTS

The graph of T_1 versus fixation time is shown in Figure 36 below. The Spearman P-value is 0.97.

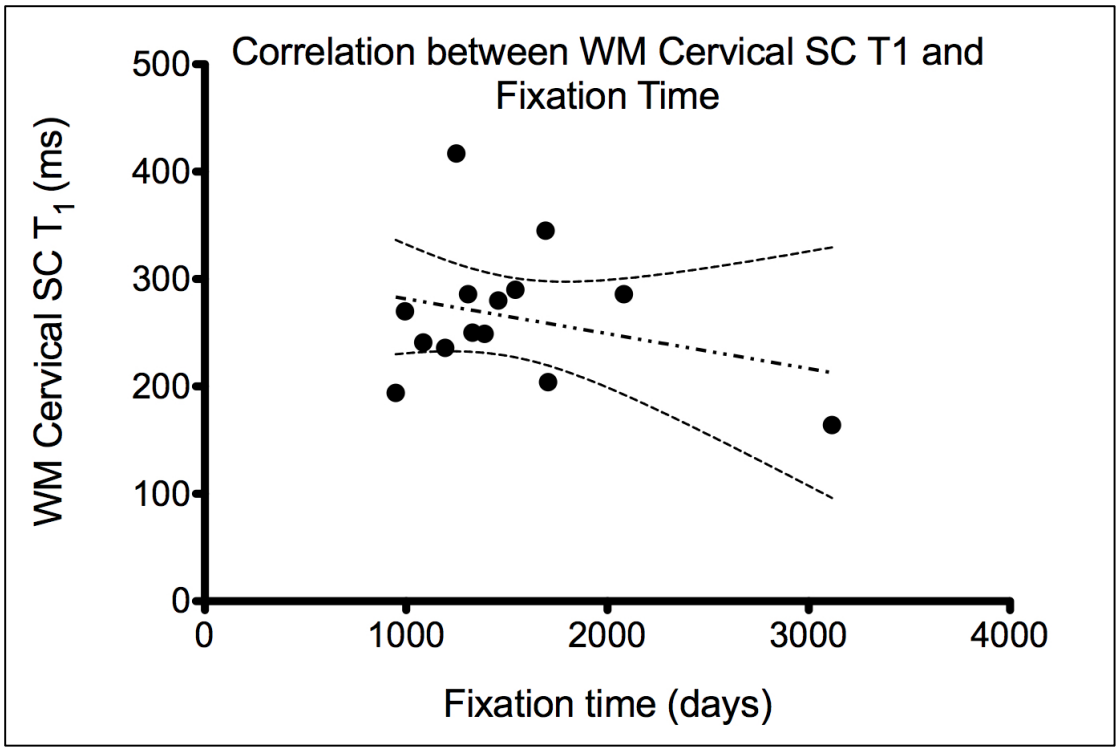

FIGURE 36: GRAPH OF T_1 VALUES IN THE CERVICAL WHITE MATTER VERSUS FIXATION TIME IN POST-MORTEM SPINAL CORDS

The graph of T_1 versus post-mortem delay is shown in Figure 37 below. The Spearman P-value is 0.74.

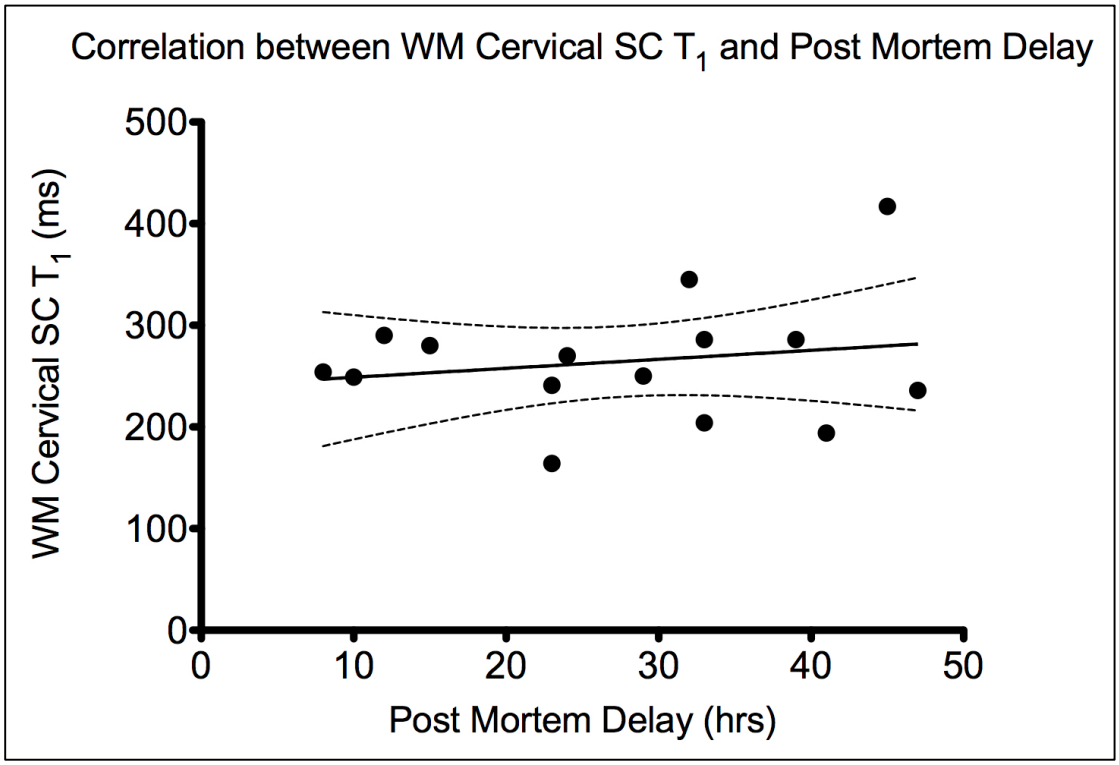

FIGURE 37: GRAPH OF T1 VALUES IN THE CERVICAL WHITE MATTER VERSUS THE POST-MORTEM DELAY IN POST-MORTEM SPINAL CORDS

6.4.2 DISCUSSION

There is no correlation between cervical white matter T_1 values in the post-mortem spinal cord and either fixation time and post-mortem delay. This implies that the variation in appearance and T_1 values in the fixed cords is due to differences in disease course. Therefore, it can be assumed that the process of removal from the cadaver and the fixation process has not affected the cords in a manner that would stop us from being able to draw conclusions about the differences in the spinal cords caused by the disease of MS itself.

6.5 T_1 MAPPING USING DESPOT1

The DESPOT1 method of T_1 map calculation is described in detail in section 2.4.6.1. The DESPOT1 fitting algorithm was provided by Tobias Wood and can be found at https://github.com/spinicist/QUIT. The DESPOT1 algorithm uses the iterative fitting Linear Least Squares (LLS) algorithm, with options for weighted-LLS and Nonlinear-LLS (described in section 2.8). The fit type that most closely matched the SE-IR derived T_1 values found in section 6.2 above is also evaluated. The default iteration number was 15. DESPOT1 is acquired as a 3D acquisition, so can be viewed in all orientations. The best orientation at acquisition can be chosen to optimise the parameters such as matrix size, TR and TE.

6.6 DESPOT1 IN THE POST-MORTEM BRAIN

6.6.1 WORK ON A 3T CLINICAL SCANNER

The performance of the three algorithms supplied with the DESPOT1 code, LLS, WLLS and NLLS was evaluated using a brain hemisphere.

6.6.1.1 Methods

The right hemisphere of MS436R was imaged with values of TE 4.6ms, TR 10ms, NSA 2, matrix size 224 × 224 with a pixel size of 0.8×0.8×0.8mm reconstructed as 0.5×0.5×0.5mm. The flip angles for the acquisitions were 3, 6, 9, 12, 15, 18, 21, 24, 27, 30, 33, 36. The brain hemisphere is surrounded by perfluorpolyether, a liquid

without hydrogen thus giving no MR signal with the coil used on the Philips Achieva 3T.

6.6.1.2 Results - Linear Least Squares Algorithm

The LLS algorithm is a procedure to find the best curve fit for a given set of points by minimising the sum of the squares of the offsets, also known as the residuals, of the points from the curve. The sum of the squares of the offsets is used in place of the offset absolute values as this allows the residuals to be treated as a continuous differentiable quantity. However, because squares of the offsets are used, outlying points can have a disproportionate effect on the fit.

A slice is shown below from the T_1 map produced by the LLS algorithm.

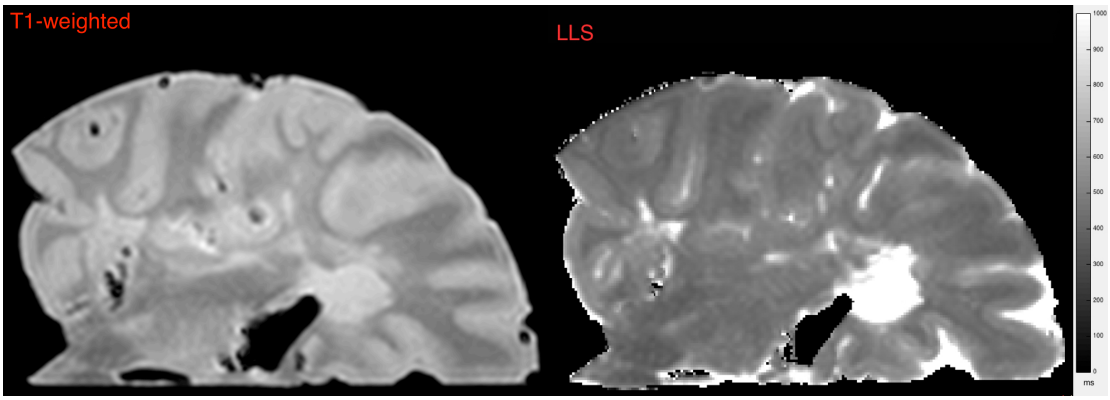

FIGURE 38: ON THE LEFT A T_1-WEIGHTED ANATOMY IMAGE, ON THE RIGHT THE T_1 MAP PRODUCED USING THE LLS ALGORITHM

6.6.1.3 WLLS

In the LLS algorithm each point is given equal weight so outliers with large noise characteristics can unduly influence the fit obtained. The weighted LLS algorithm uses the covariance matrix to give information about the quality of each point. Therefore, a point with high variance are given less weight and vice versa. It is still a minimisation problem, which converges when the residuals are minimal. The convergence of the algorithm was tested with increasing iterations. The convergence up to the default of 15 iterations against a high iteration number of 40 was also examined.

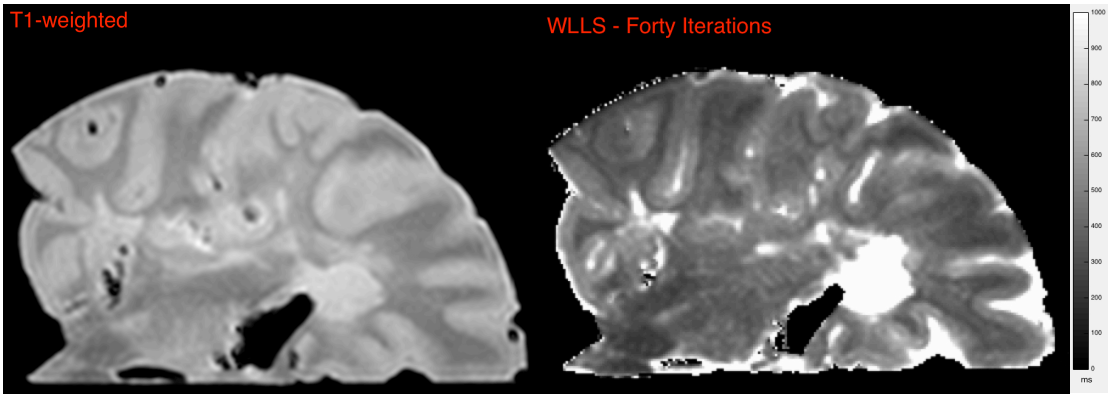

FIGURE 39: ON THE LEFT A T_1-WEIGHTED IMAGES, IN COMPARISON THE T_1 MAP PRODUCED USING 40 ITERATIONS WITH THE WLLS ALGORITHM

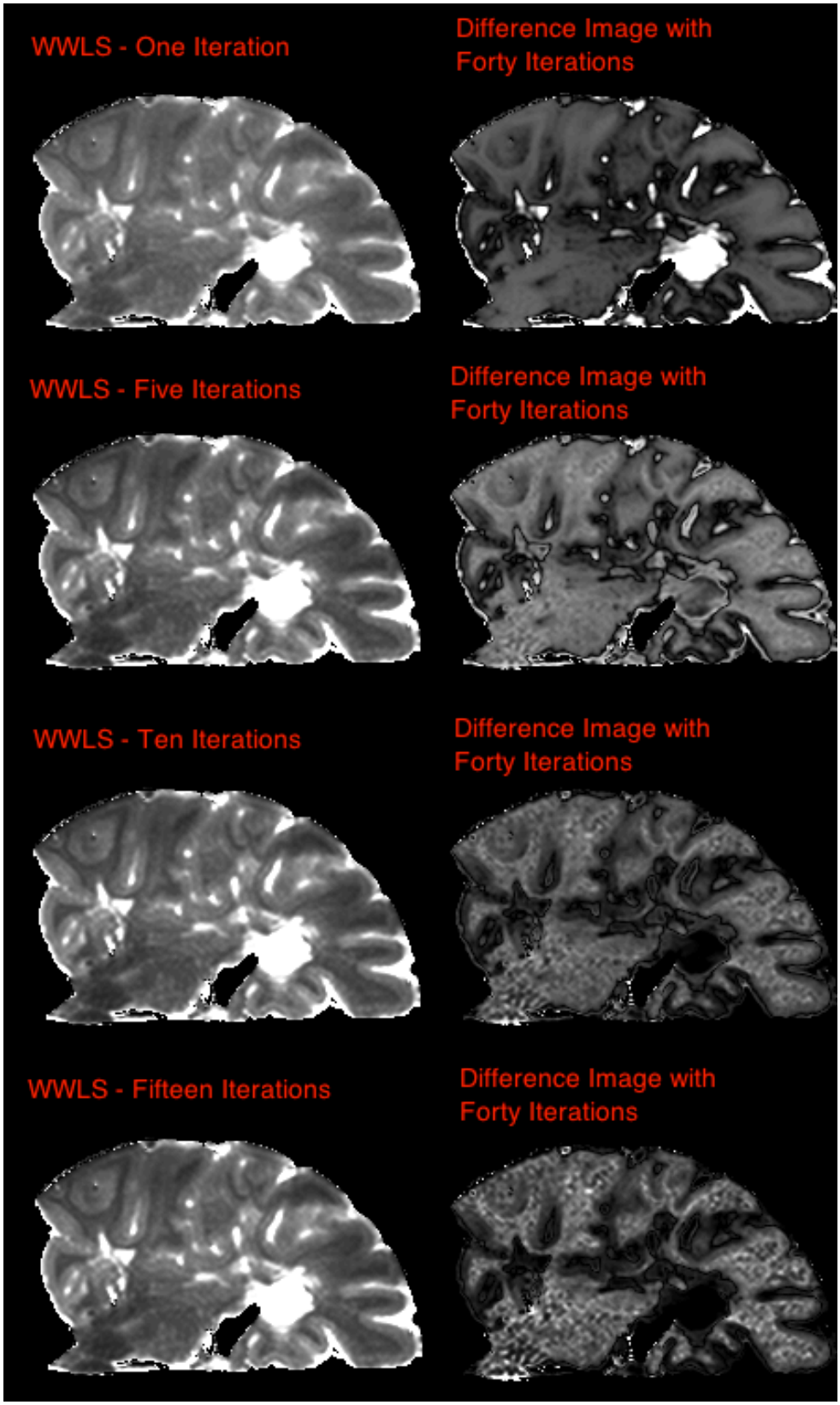

FIGURE 40: DIFFERENCE IMAGES FOR 1, 5, 10 AND 15 ITERATIONS WITH 40 ITERATIONS, PRODUCED USING THE WLLS ALGORITHM. ALL T1 MAPS ARE SCALED BETWEEN 0 AND 1000MS, AND 1, 5, 10, AND 15 ITERATIONS DIFFERENCE IMAGES BETWEEN 0 TO 200, 0 TO 10, 0 TO 0.5 AND 0 TO 0.02MS RESPECTIVELY

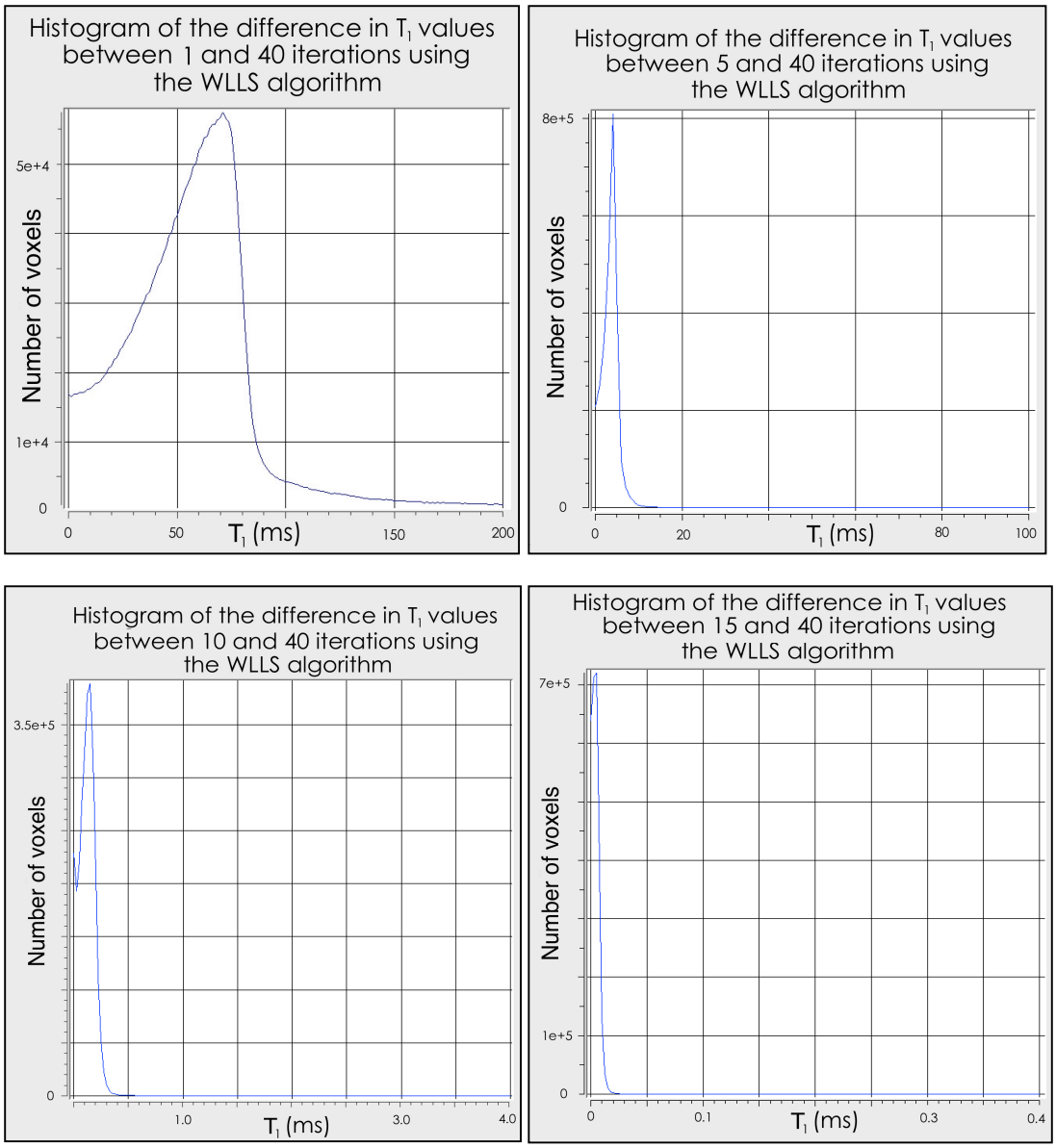

FIGURE 41: HISTOGRAMS SHOWING THE DIFFERENCE VALUES IN THE DIFFERENCE IMAGES FOR 1 ITERATION (TOP LEFT), 5 ITERATIONS (TOP RIGHT), 10 ITERATIONS (BOTTOM LEFT) AND 15 ITERATIONS (BOTTOM RIGHT). THE X AXIS HAS BEEN SCALED IN ORDER TO DISPLAY THE VALUES CLEARLY.

The difference maps show a decreasing median value with each iteration, showing that this algorithm is converging. These median values are:

Iterations	ms
1	71.25
2	36.25
4	8.75

5	4
10	0.15
15	0.005

TABLE 7: MEDIAN VALUES FOR THE WLLS ALGORITHM

6.6.1.4 NLLS Algorithm

The NLLS algorithm provides a best fit to the non-linearised version of the SPGR equation (see section 2.4.6.1). The high iteration image is shown below in comparison with the matched T_1-weighted anatomy image.

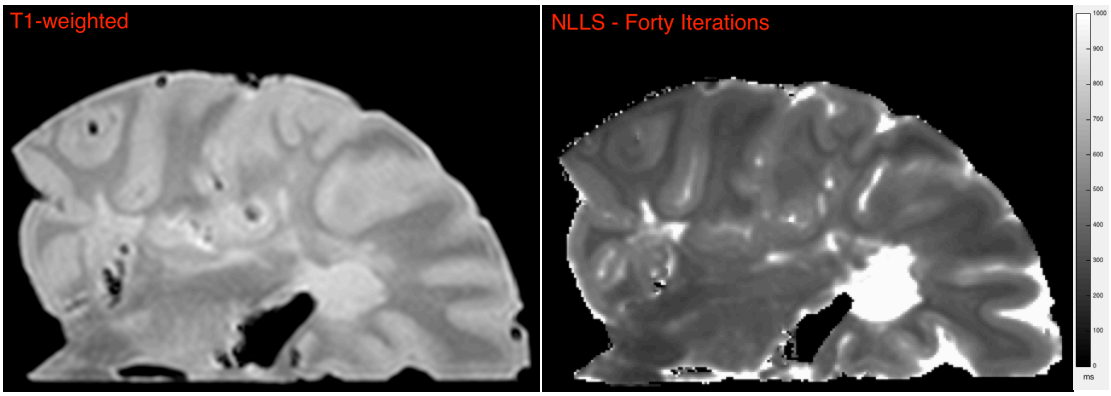

FIGURE 42: ON THE LEFT A T_1-WEIGHTED IMAGES, IN COMPARISON THE T_1 MAP PRODUCED USING 40 ITERATIONS WITH THE NLLS ALGORITHM

The results are shown below for 1, 2, 4 and 5 iterations of the NLLS algorithm of the T_1 map produced and the difference image with a high iteration value of 40 iterations.

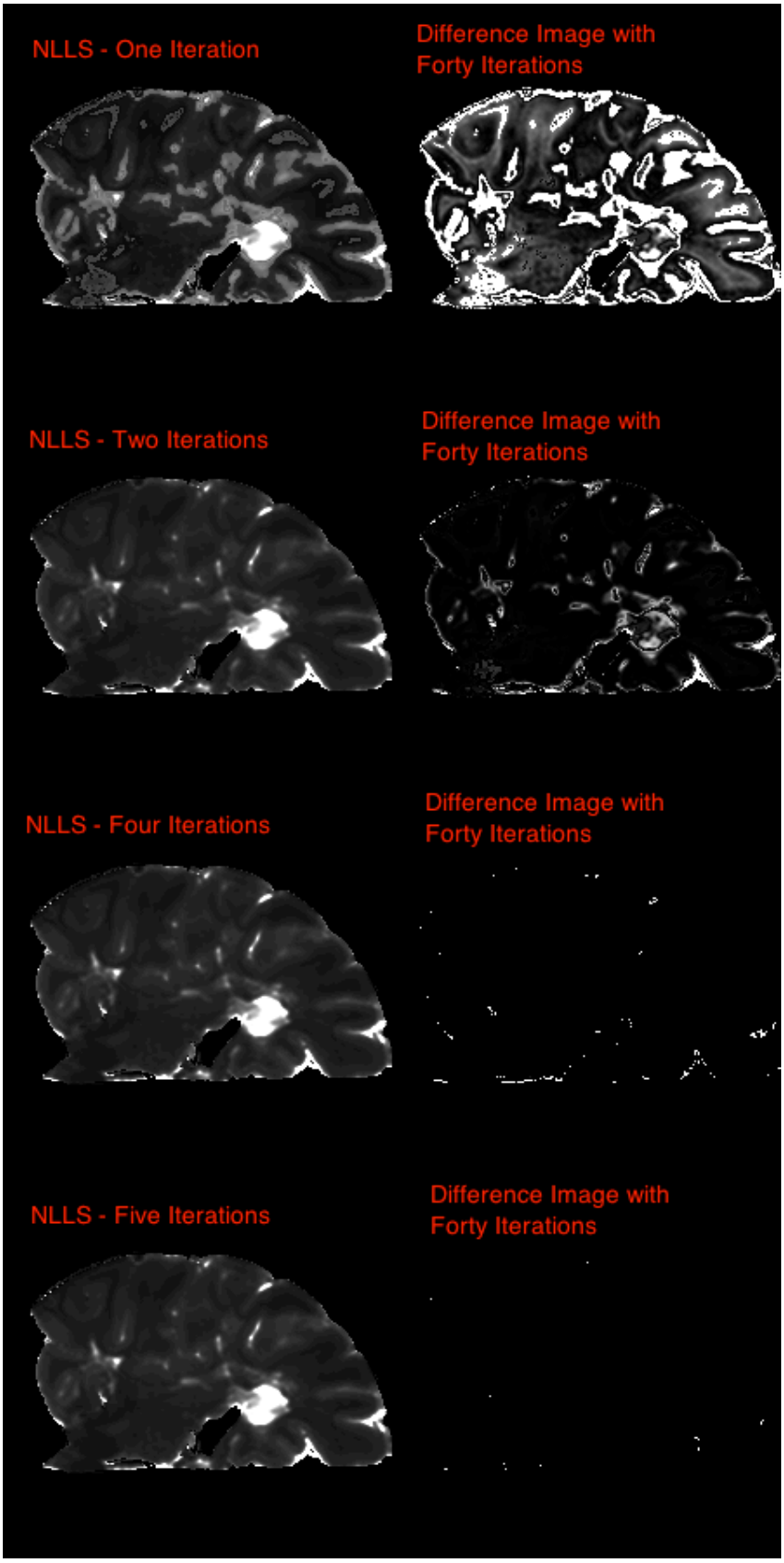

FIGURE 43: DIFFERENCE IMAGES FOR 1, 2, 4 AND 5 ITERATIONS WITH 40 ITERATIONS, PRODUCED USING THE NLLS ALGORITHM. ALL T1 MAPS ARE SCALED BETWEEN 0 AND

1000MS, AND 1, 2, 4, AND 5 ITERATIONS DIFFERENCE IMAGES SCALED BETWEEN 0 TO 100, 0 TO 10, 0 TO 0.01 AND 0 TO 0.01MS RESPECTIVELY

Shown below are the values from the difference images.

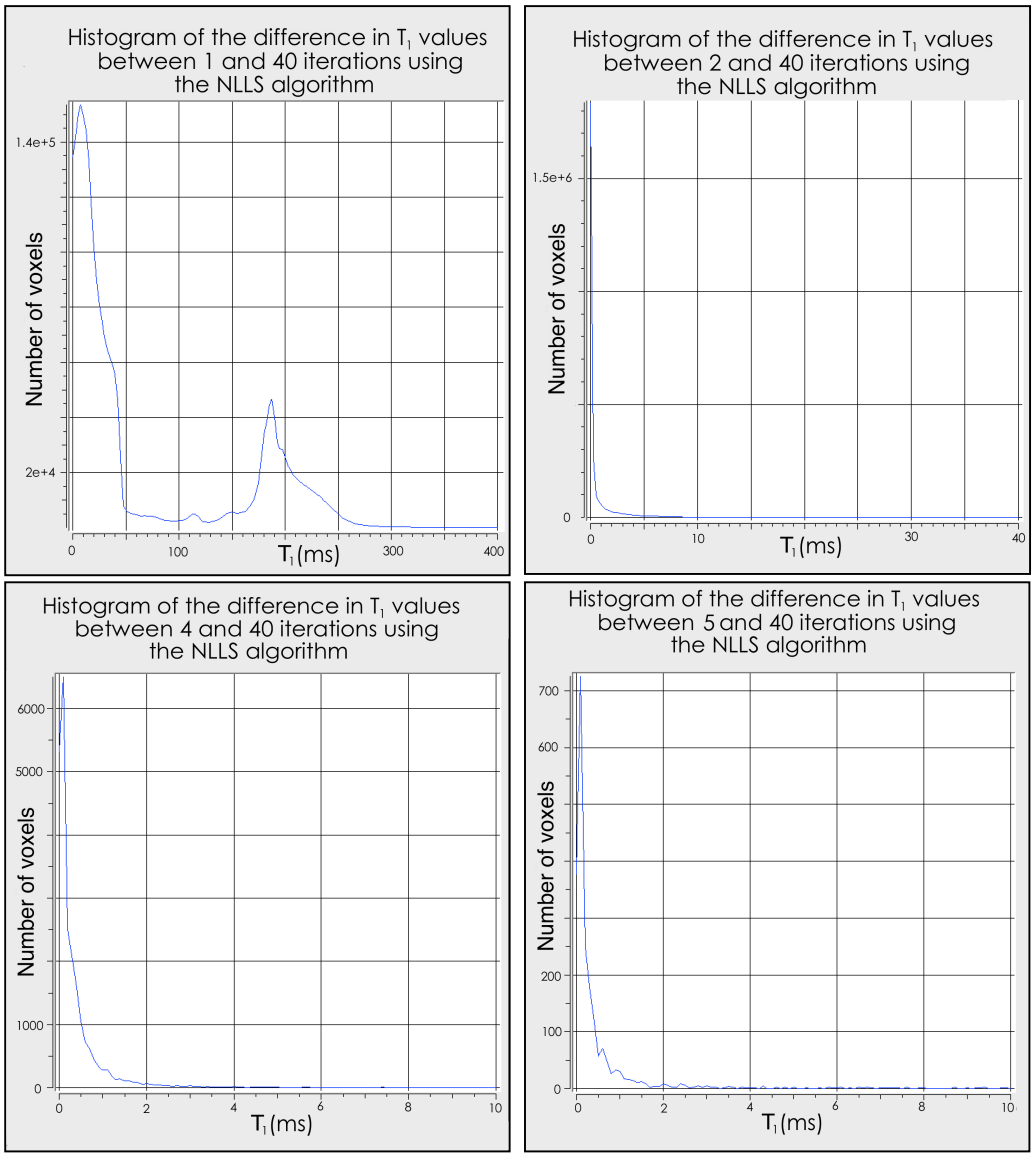

FIGURE 44: HISTOGRAMS SHOWING THE DIFFERENCE VALUES IN THE DIFFERENCE IMAGES FOR 1 ITERATION (TOP LEFT), 2 ITERATIONS (TOP RIGHT), 4 ITERATIONS (BOTTOM LEFT) AND 5 ITERATIONS (BOTTOM RIGHT). THE X AXIS HAS BEEN SCALED IN ORDER TO DISPLAY THE VALUES CLEARLY.

Iterations	ms
1	7.5
2	0.04
4	0.1
5	0.1

TABLE 8: MEDIAN VALUES FOR THE NLLS ALGORITHM. THE MEDIAN VALUE IN THE DIFFERENCE MAP OF 4 ITERATIONS IS 0.1MS IN 6499 VOXELS, 5 ITERATIONS IS THE SAME VALUE, 0.1MS, BUT 725 VOXELS.

The addition of one more iteration from 4 to 5, decreases the number of voxels that have a difference value from the high iteration image from 6499 to 725.

6.6.2 DISCUSSION

The NLLS algorithm converges more rapidly than the WLLS, within 2 iterations the difference image values are under 10ms. This proves that within the default 15 iterations all algorithm types tested will have converged.

6.7 T1 VALUES IN MAPS PRODUCED BY THE ALGORITHMS

Images are shown below of the T_1 maps produced by the three algorithms, LLS, WLLS and NLLS.

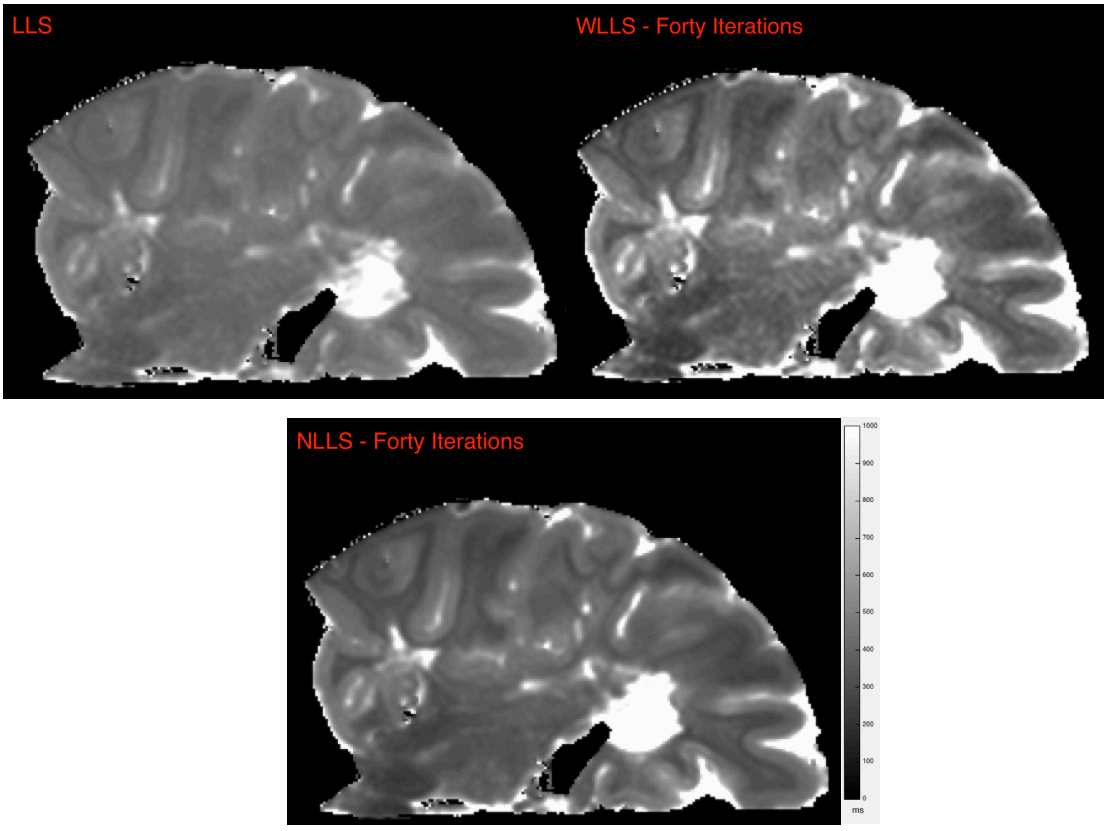

FIGURE 45: T1 MAPS PRODUCED BY THE LLS (TOP LEFT), WLLS (TOP RIGHT), AND NLLS (BOTTOM) ALGORITHMS, ALL THREE ARE SCALED TO SAME COLOUR TABLE 0-1000MS

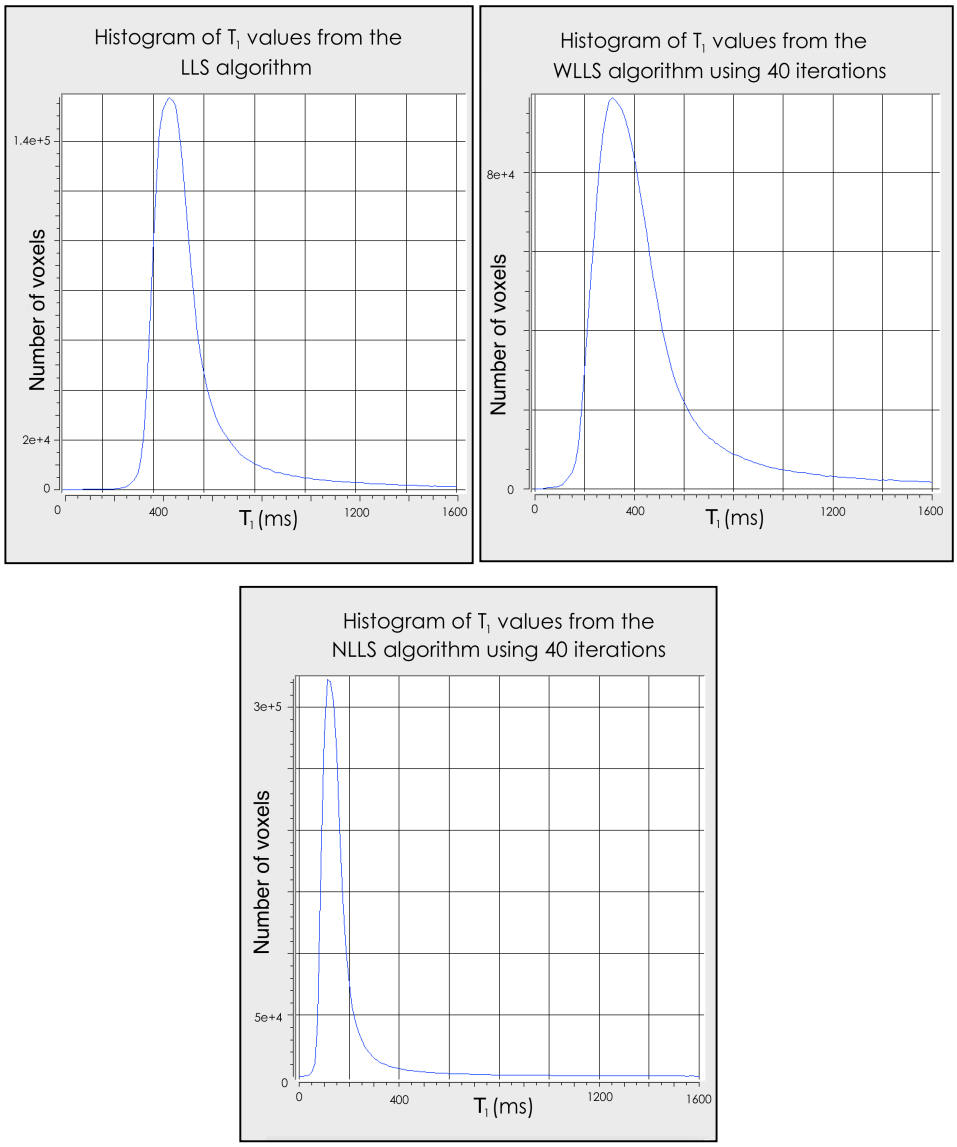

FIGURE 46: ON THE TOP LEFT A HISTOGRAM OF VALUES FROM THE LLS ALGORITHM, ON THE TOP RIGHT FROM THE WLLS ALGORITHM, THE BOTTOM IMAGE IS A HISTOGRAM OF VALUES FROM THE NLLS ALGORITHM

The LLS algorithm has high values of T_1 in the map, with little differentiation between white and grey matter. The WLLS gives lower T_1 values with the lowest T_1 values given by the NLLS algorithm. The NLLS algorithm shows good contrast between white and grey matter, with reduced noise in the image.

6.8 COMPARISON OF DESPOT1 ALGORITHM T1 VALUES WITH SE-IR T1 VALUES

The histograms of T_1 values shown in section 6.2 from a TSE-IR T_1 map acquisition, are shown below for comparison with the histogram from the slice qualitatively matched from the DESPOT1 acquisition of MS436R for all three algorithms.

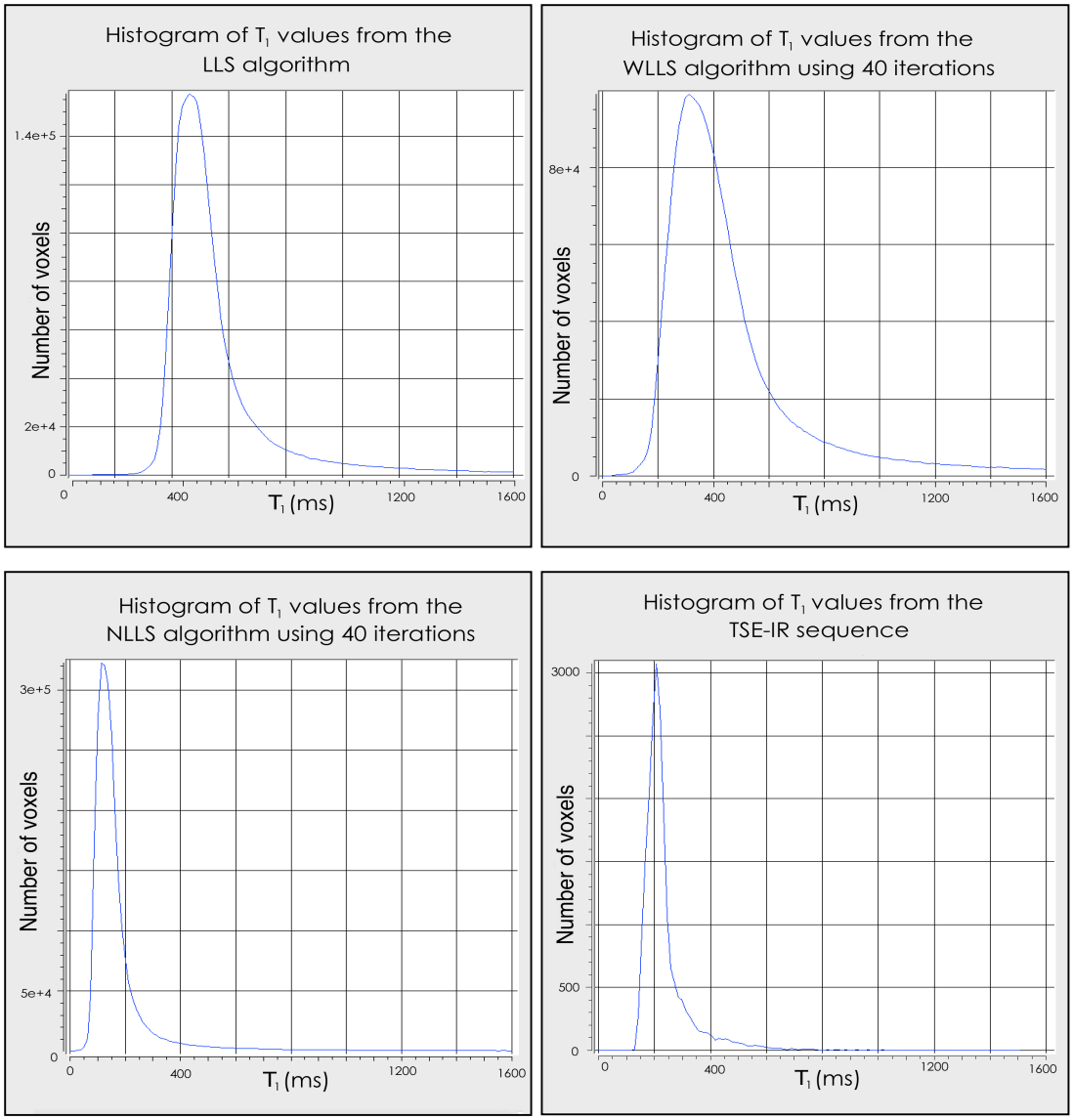

FIGURE 47: HISTOGRAMS OF THE LLS (TOP LEFT), WLLS (TOP RIGHT), NLLS (BOTTOM LEFT) ALGORITHM COMPARED TO THE TSE-IR T_1 MAP (BOTTOM RIGHT)

6.8.1.1 Discussion

It is likely that the NNLS algorithm is overfitting the data, as the non-linearised equation is complex (see section 2.8.2), and the non-linear fitting may fit to

noise in comparison to the LLS. The median value of the histogram of the NLLS algorithm is 120ms. The WLLS algorithm accounts for noise in the data with the weighting of points, but does not converge easily, the median value in its T_1 map is 312.5ms at 40 iterations and the median value of its difference image from the high iteration image is 4ms at 5 iterations, with a low value found at 15 iterations. The LLS algorithm is not useful, its median value 465ms. The median value of the TSE-IR is 215ms.

However, the NLLS algorithm gives a lower noise T_1 map than the other algorithms, and for that reason is recommended.

6.8.2 TR OPTIMISATION IN *POST-MORTEM* TISSUE

In order to optimise the DESPOT1 acquisition, it was necessary to acquire several sets of images with different TR values, as it has been proposed that the T_1 values produced by the DESPOT1 algorithm are more accurate at longer TRs[152].

6.8.2.1 Methods

The spinal cords C60, MS475, MS453, C58, MS493, MS561, MS436 and MS455 were imaged using TR values of 10, 16, 20, 24 and 30ms. All acquisitions were acquired with TE of 5.1, this was the shortest available with the shortest TR value available, 10ms. The number of signal averages (NSA) was 2, matrix size 320 × 320 with a pixel size of 0.8×0.8×0.8mm reconstructed as 0.5×0.5×0.5mm. The flip angles for the acquisitions are given in table 1. These were optimised using T_1 values of 270, 390 and 440ms using average values of T_1 found in WM, GM and lesional tissue in spinal cord and the equations given in Dr Wood's paper[153] (Improved formulas for the two optimum VFA flip-angles). Two values were calculated for each T_1 value and a set of four chosen from these.

TR (ms)	Flip angles (degrees)
10	5, 6, 30 and 36
16	6, 8, 38 and 45
20	7, 9, 41 and 43
24	8, 10, 45 and 54
30	9, 11, 50 and 59

TABLE 9: TR VALUES AND FLIP ANGLES

During the course of this thesis, the DESPOT1 algorithm was developed by Dr Wood, and had the standard LLS DESPOT1 fitting algorithm. Therefore, the TR optimisation was first performed using the LLS algorithm. Later, after the TR optimisation results from the LLS algorithm were analysed, the NLLS algorithm was added for improved performance and the data was reanalysed using the NNLS algorithm.

6.8.2.2 Results

LLS

The results of the reconstructions with the LLS algorithm are shown below, images and histograms of T_1 values in the images.

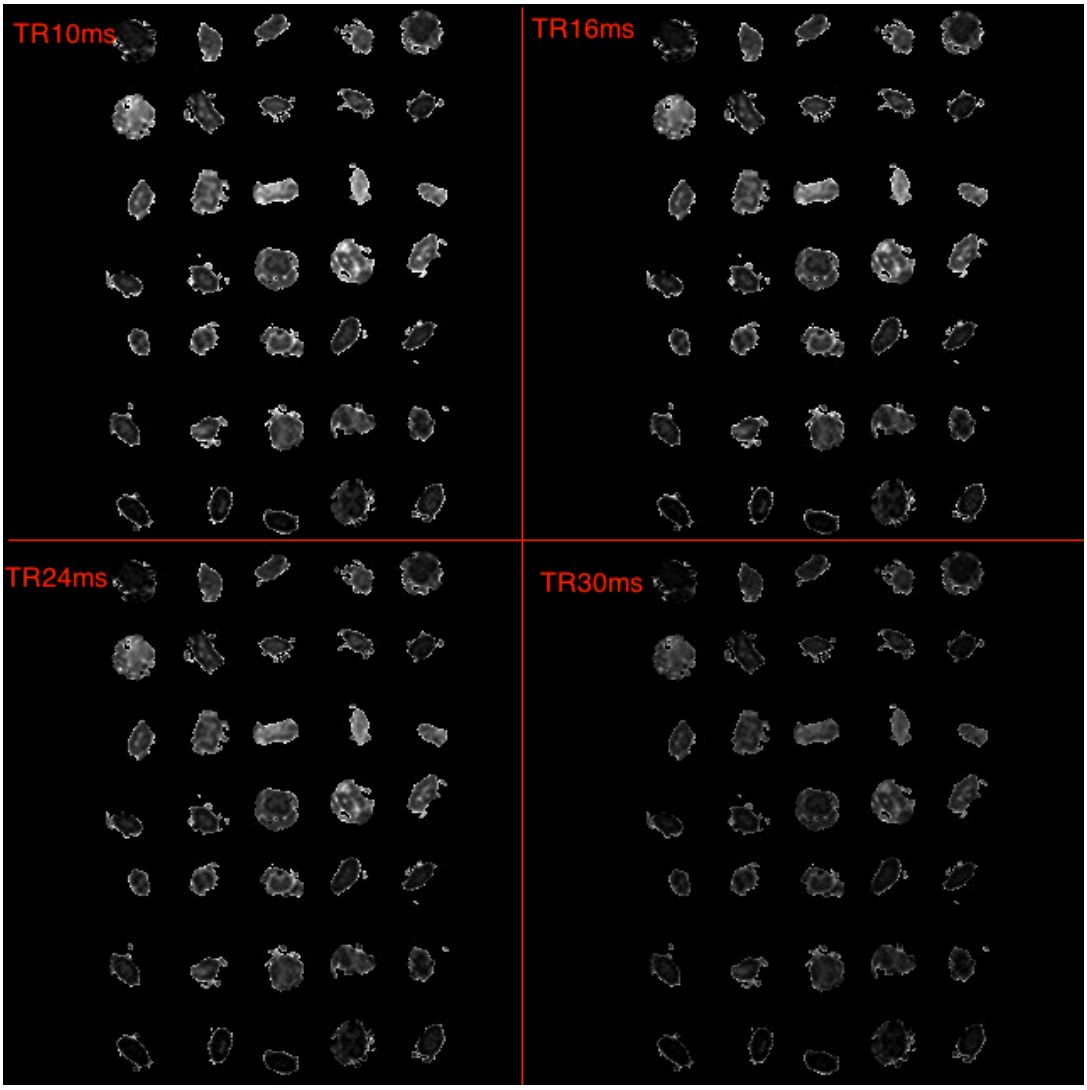

FIGURE 48: T1 MAPS CALCULATED USING THE LLS DESPOT1 ALGORITHM WITH VARYING TR VALUES IN AN EXAMPLE SLICE THROUGH SECTIONED SPINAL CORDS

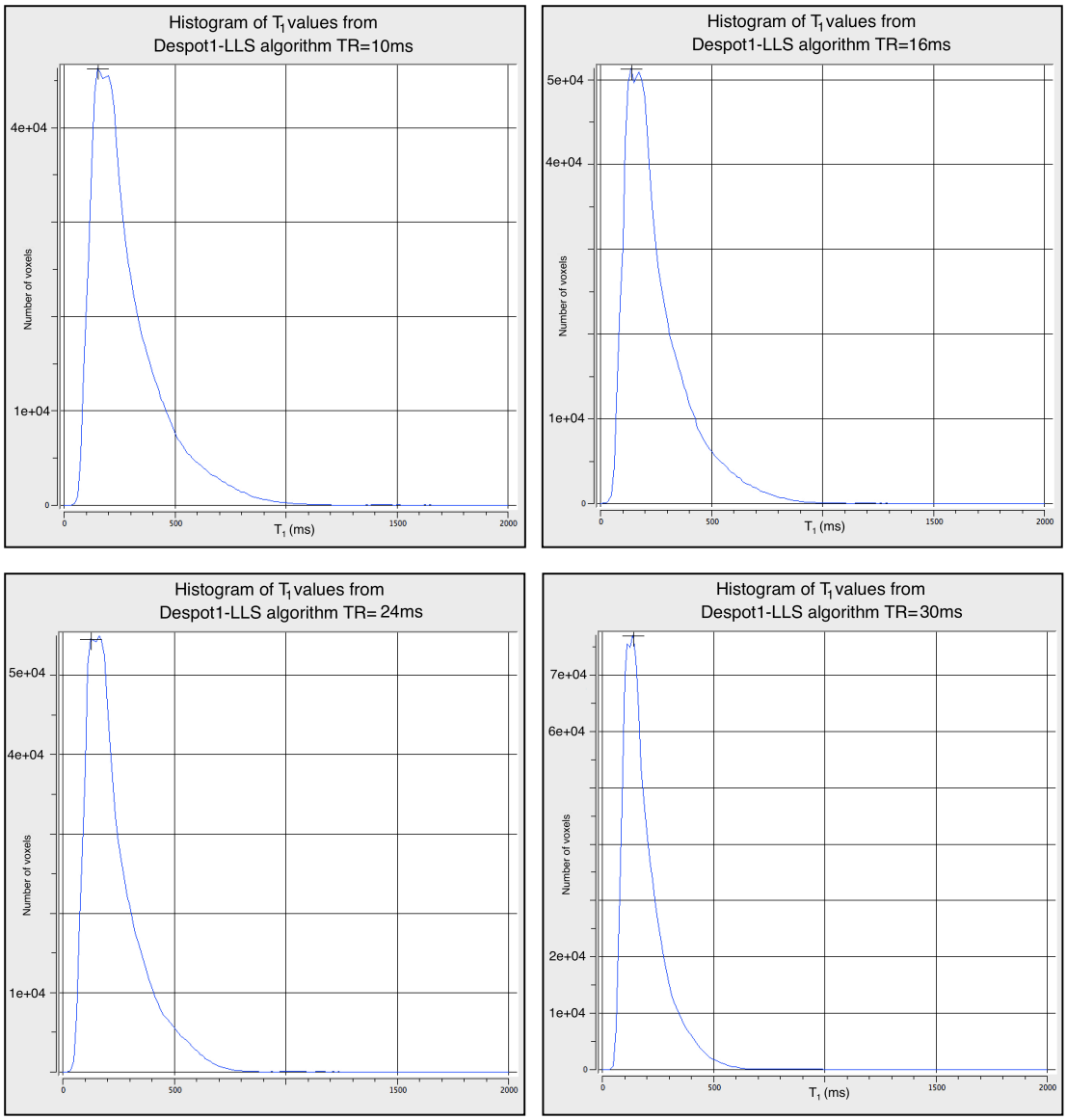

FIGURE 49: HISTOGRAMS OF VALUES IN THE DESPOT1 MAPS FROM THE LLS ALGORITHM USING TR10 (TOP LEFT), TR16 (TOP RIGHT), TR24 (BOTTOM LEFT) AND TR30 (BOTTOM RIGHT)

The median values in the histograms are:

TR (ms)	T_1 (ms)
10	150
16	137.5
20	150
24	125
30	137.5

TABLE 10: MEDIAN VALUES IN THE T1 MAPS

NLLS

The results of the T_1 map reconstructions using the NLLS algorithm are shown below in figure 50, and histograms of T_1 values in the images in figure 51.

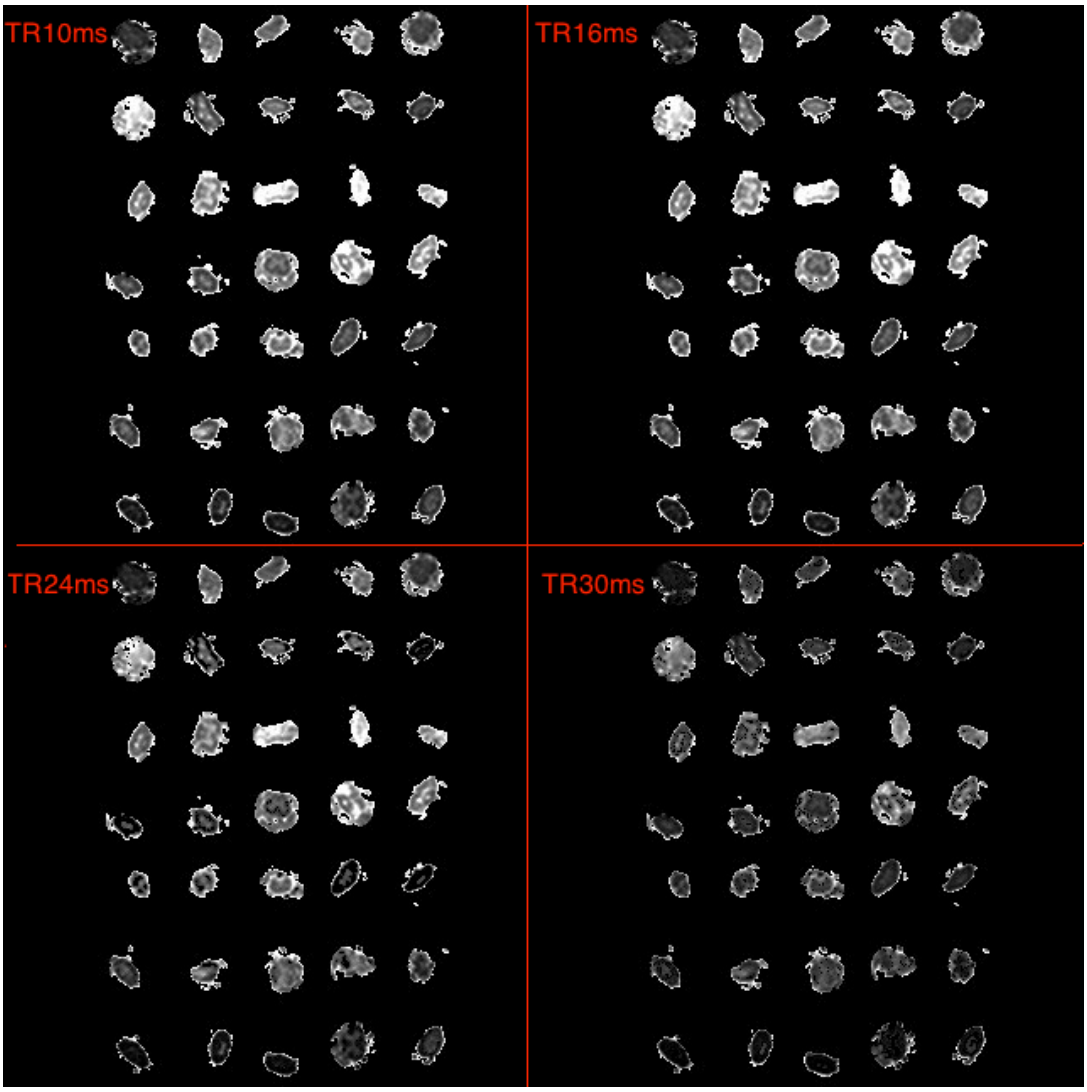

FIGURE 50: T1 MAPS CALCULATED USING THE NLLS DESPOT1 ALGORITHM WITH VARYING TR VALUES IN AN EXAMPLE SLICE THROUGH SECTIONED SPINAL CORDS

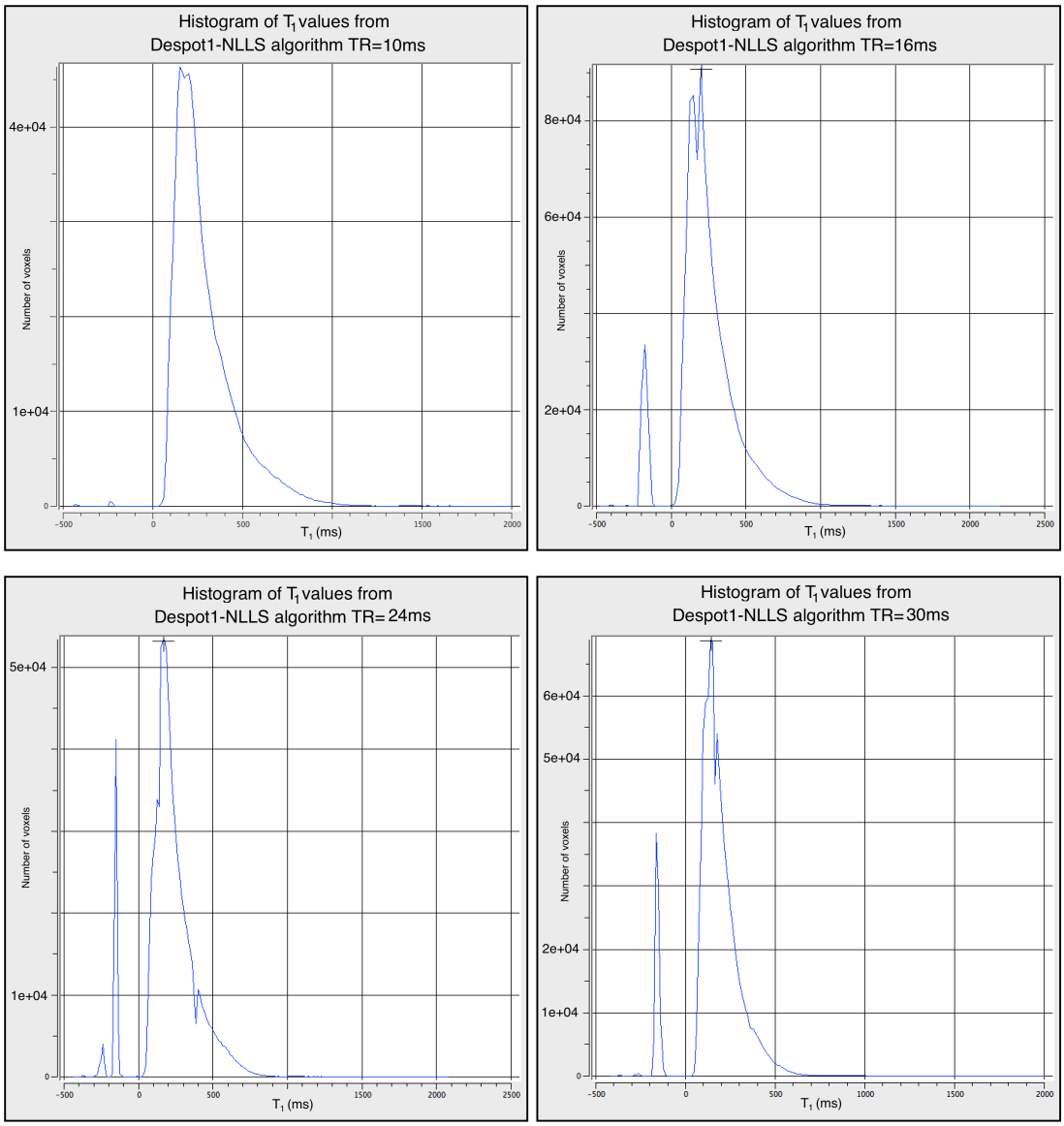

FIGURE 51: HISTOGRAMS OF VALUES IN THE DESPOT1 MAPS FROM THE NLLS ALGORITHM USING TR10 (TOP LEFT), TR16 (TOP RIGHT), TR24 (BOTTOM LEFT) AND TR30 (BOTTOM RIGHT)

The median values in the histograms are:

TR (ms)	T_1 (ms)
10	150
16	200
20	175
24	162.5
30	137.5

TABLE 11: MEDIAN VALUES IN THE T1 MAPS

6.8.2.3 Discussion

Looking at both the LLS algorithm, there is little difference between the T_1 values found with increasing TR. However, this is not the case with the NLLS algorithm where a TR of 10ms minimises the negative T_1 errors shown at higher TR values. These negative T_1 values occur in different voxels with different TR values and maybe due to noise affecting the fit when the signal has not been linearised with a small sample size of four flip angles. Increasing the sampling frequency should fully characterise the signal curve to improve non-linear fitting. In summary, whether using either the LLS or NLLS a TR of 10ms should be used. This is also in keeping with clinical practice where the TR would be kept as short as possible for patient comfort and to reduce movement.

6.9 DESPOT1 IN THE POST-MORTEM SPINAL CORD

6.9.1 WHOLE SPINAL CORDS ON A 3T CLINICAL SCANNER

6.9.1.1 Methods

The spinal cords were scanned using a DESPOT1 protocol on the Philips 3T Achieva scanner using a 15 element SENSE Spine coil (see section 5.4). An acquisition matrix 324×324, with a reconstruction pixel size of 0.5×0.5×0.5mm. A series of SPGR sequences TE/TR 3.1/11.1ms with flip angles varying from 3-36 degrees in increments of 3 degrees are acquired.

The water in the trough surrounding the glass tubes (see section 5.4 for details of the set-up) has been masked out in the processing step, leaving only the spinal cord voxels. This was performed using the 3D segmentation program provided with Osirix (http://www.osirix-viewer.com/). A region of interest is set by the user using an upper and lower threshold around the spinal cord in the transverse plane, then a 3D region of interest is grown by the program throughout the spinal cord in all slices using these threshold settings. As the cords were surrounded by the perfluorpolyether with no signal, this enabled a simple segmentation of the cords. The processing time for this operation was very short, approximately 2 minutes.

6.9.1.2 Results

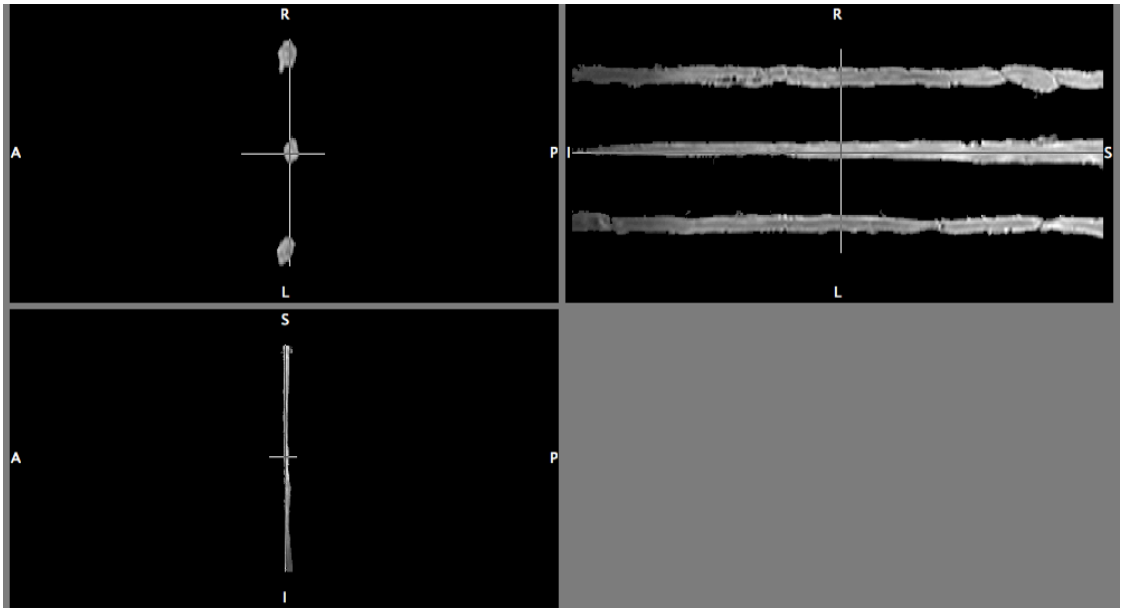

FIGURE 52: PD WEIGHTED IMAGES OF THREE SPINAL CORDS, MS471, MS454 AND MS484

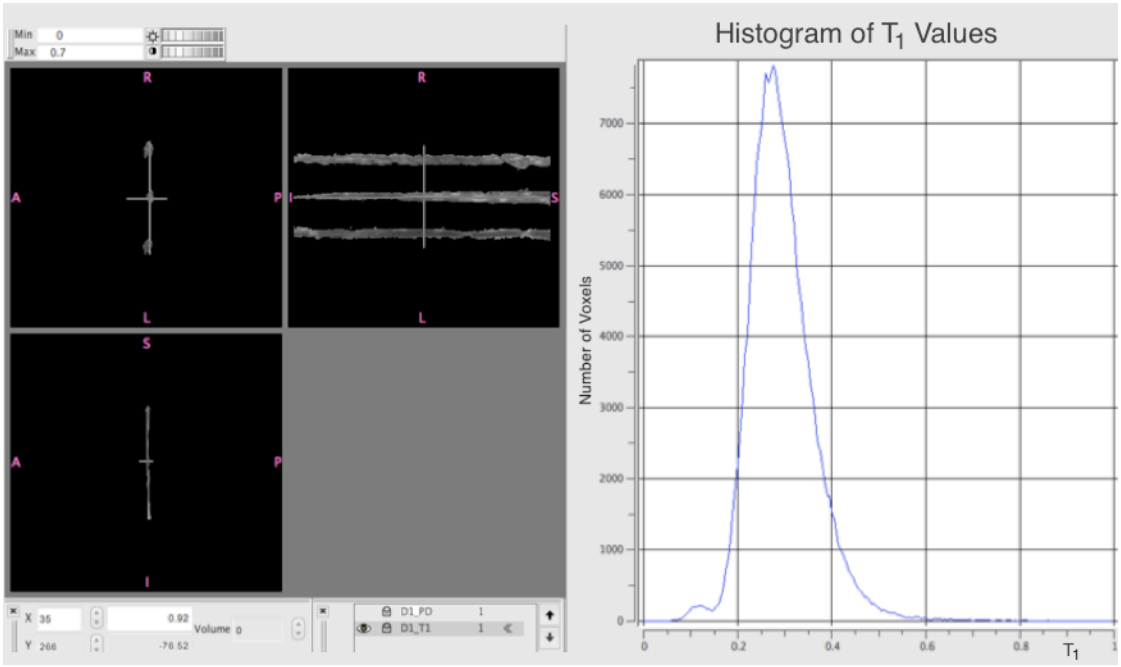

FIGURE 53: DESPOT1 T_1 MAP OF THREE SPINAL CORDS, MS471, MS454 AND MS484, LEFT. HISTOGRAM OF THE VALUES OF T_1 IN THE WHOLE IMAGE

The DESPOT1 program calculates PD images and the corresponding T_1 map shown above. The histogram of all the values in the image only includes the spinal cords. The use of the histogram was to avoid observer interpretation and variation, which can occur in a region of interest based analysis. We would wish to see distinct peaks in the histogram corresponding to white, grey and lesion

values. However, with the convergence and shortening of T_1 in post-mortem tissue, it is not surprising that we cannot distinguish white and grey matter values. It is interesting that there seems to be no distinguishable peak at lesions values of approximately 600ms (0.6 on the histogram) as found in the IR maps above. There seems to be an almost continuous spectrum of values instead. This can be compared to the obvious white and grey matter peaks shown when a brain hemisphere was scanned in the same manner as shown below.

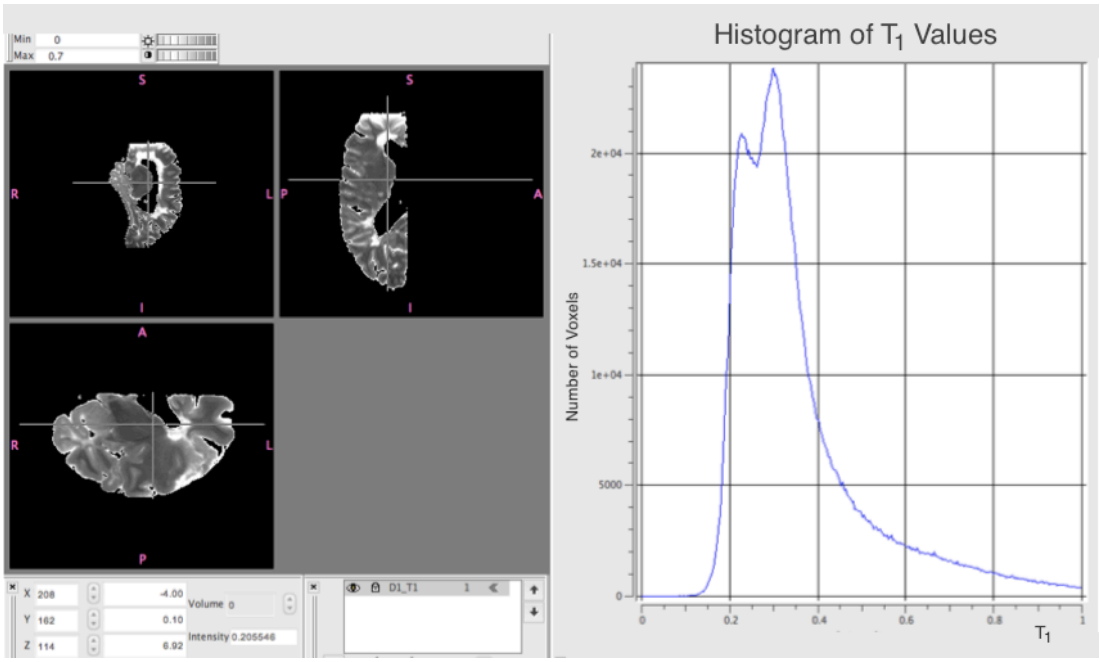

FIGURE 54: T1 MAP OF HEMISPHERE MS475R. THE PEAKS SHOWN ARE AT 227MS AND 297MS. THE LARGE PERIVENTRICULAR LESION HAS A RANGE OF VALUES ABOVE 800 MS (0.8 ON THE HISTOGRAM) AND DOES NOT PRODUCE A PEAK AT THIS POINT

6.10 WORK ON A 7T PRECLINICAL SCANNER

This work was performed during the same acquisition as the DESPOT2 work in section 7.4.2.

6.10.1 METHODS

The acquisitions performed on the 3T clinical scanner at St Bartholomew's Hospital Philips Achieva 3T scanner, were used to identify nine areas of interest on PD-weighted images. These areas were then scanned using a 7T pre-clinical scanner (Agilent Technologies DDR) and standard quadrature RF coil (Rapid

GmbH) with a field of view of 5cm by Dr Tobias Wood at King's College London. SPGR scans were acquired with parameters given in Table 1, along with an AFI scan for B1 correction[28]. The images were resampled to 150x150x300μm^3 for improved SNR. T_1 maps were processed from all flip-angles by Dr Wood. Sequence parameters are given in Table 11.

Sequence	TE/TR (ms)	Flip-Angles	Voxel Size (μm^3)	Matrix Size
SPGR	11.3/25	6,8,10,15,20,25,35,45	100x125x200	160x160x160
AFI	2.62/7.5	55	250x250x500	64x64x64

TABLE 12: PARAMETERS USED FOR THE DESPOT1 ACQUISITION ON THE 7T AGLIENT SCANNER

6.10.2 RESULTS

The images were processed by Dr. Wood using the program described above and are shown below in three orientations.

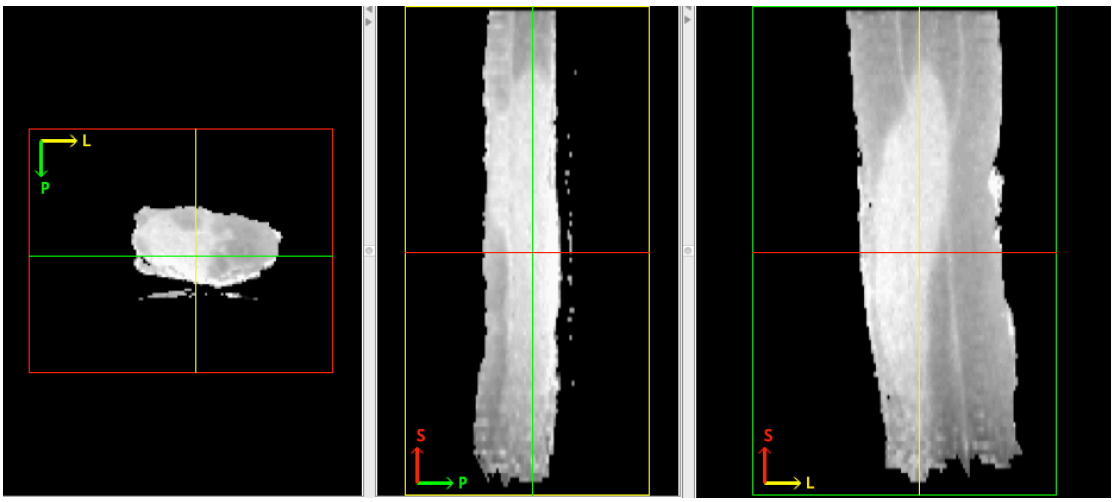

FIGURE 55: PD IMAGES OF LESION A IN THE MS471 SPINAL CORD

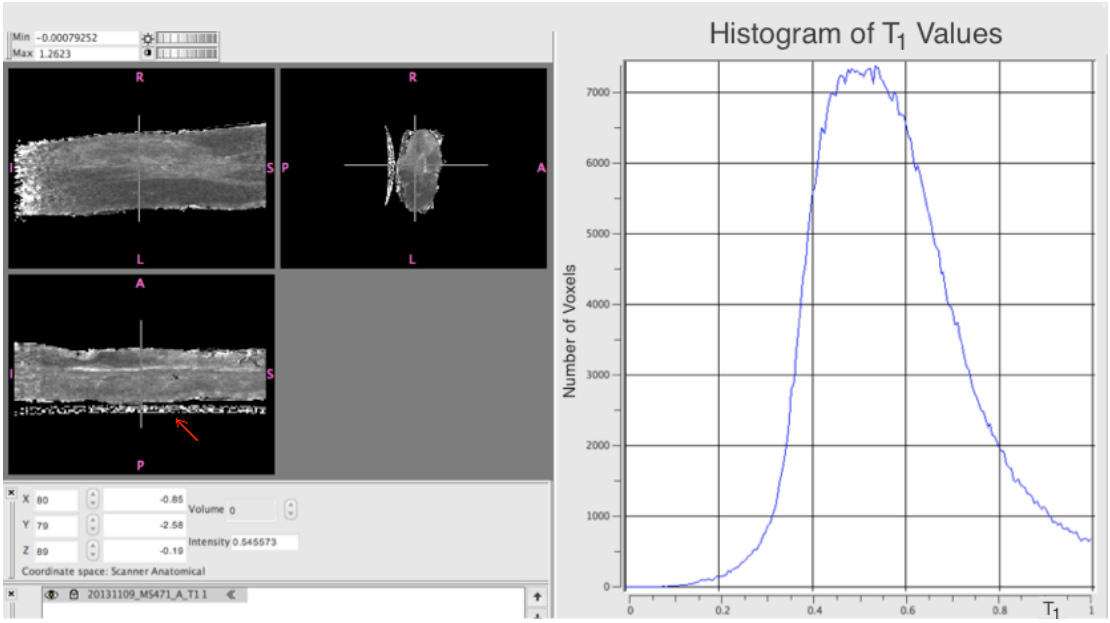

FIGURE 56: T_1 MAP AND RESULTING HISTOGRAM OF LESION A IN THE MS471 SPINAL CORD

6.10.2.1 Discussion

It is informative to note that even at a higher field strength, smaller shim volume and FoV that the T_1 values in the WM, GM and lesion still converge to the point that they cannot be distinguished in the histogram. The PD images show a great deal of contrast, with high resolution of the lesion and sharp delineation of the WM and GM (there is a RF zipper artefact at the bottom of the image, marked with an arrow). However, the T_1 map shows much reduced contrast, with the lesion and grey matter at the same grey scale value.

6.11 WORK ON A 7T WHOLEBODY SCANNER

The work on the 7T Aglient scanner shows excellent resolution, but the small bore and coil size gives image resolution advantages that are not possible in the clinical setting. In order to investigate the outcome in a more translatable setting, an opportunity to image a brain hemisphere and 6 spinal cords on a 7T Philips clinical scanner became available. The use of a clinical coil meant that the whole hemisphere could be imaged.

6.11.1 DESPOT1 MAPS IN A POST-MORTEM BRAIN HEMISPHERE

The right hemisphere of MS442R was inserted in the setup described in section 5.3, and imaged on the Philips 7T scanner at Nottingham University. The scan parameters are given in Table 12.

Sequence	TE/TR (ms)	Flip-Angles	Voxel Size (mm^3)	Matrix Size
SPGR	12/28	6, 8, 10, 15, 20, 25, 35 and 40	0.5×0.5×0.5	336×336
AFI	25/150	60	1.5×1.5×1.5	112×112

TABLE 13: PARAMETERS USED FOR THE DESPOT1 ACQUISITION ON THE 7T PHILIPS SCANNER

The B_1 map was resampled to match the resolution of the SPGR acquisition for processing. Due to the size and shape of the head coil, there was signal drop off at one end of the coil where fitting failed due to the low signal in this area.

6.11.1.1 Results

A T_1-weighted image and the corresponding DESPOT1 map are shown below. The rise in resolution seen in the T_1-weighted image is obviously noticeable between 7T and the 3T work in section 6.6.

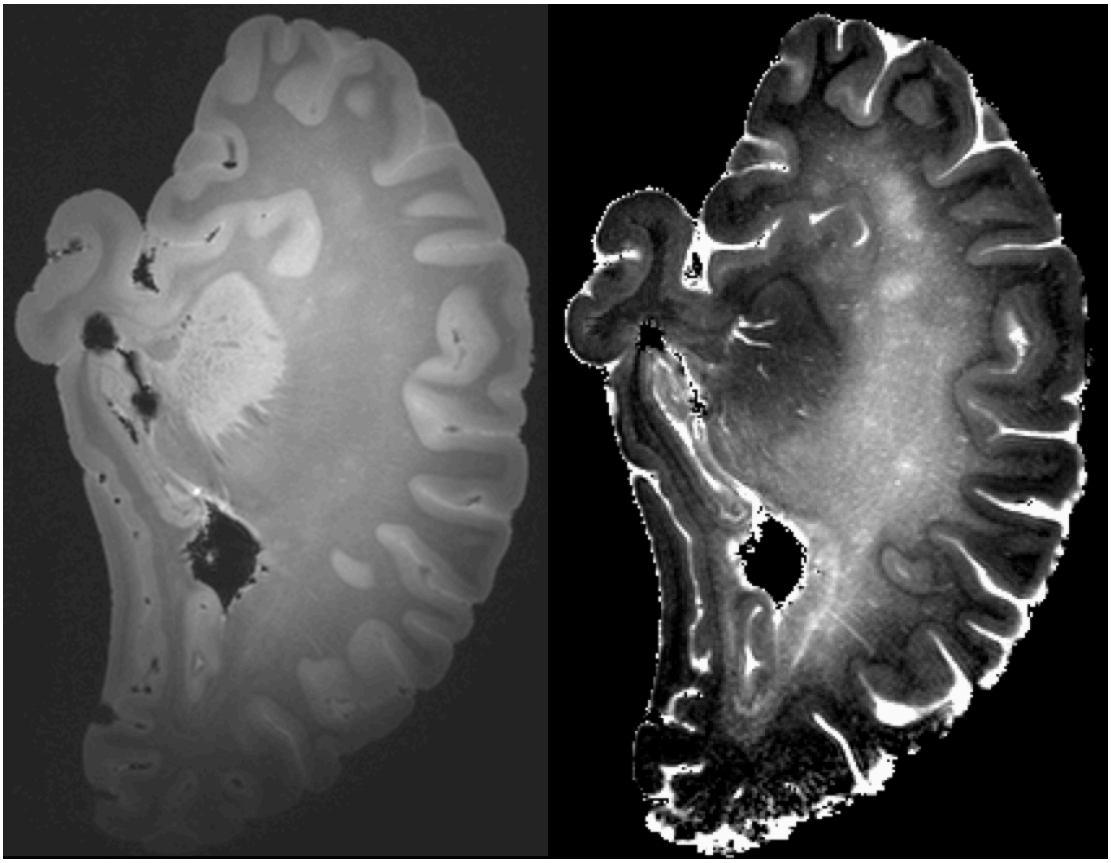

FIGURE 57: T_1-WEIGHTED IMAGE OF MS442R (LEFT), AND THE CORRESPONDING T_1 MAP (RIGHT) SHOWING INCREASED DISTINCTION OF THE LESIONS IN THE WHITE MATTER. THE T1 MAP IS SCALED BETWEEN 400 AND 1200MS.

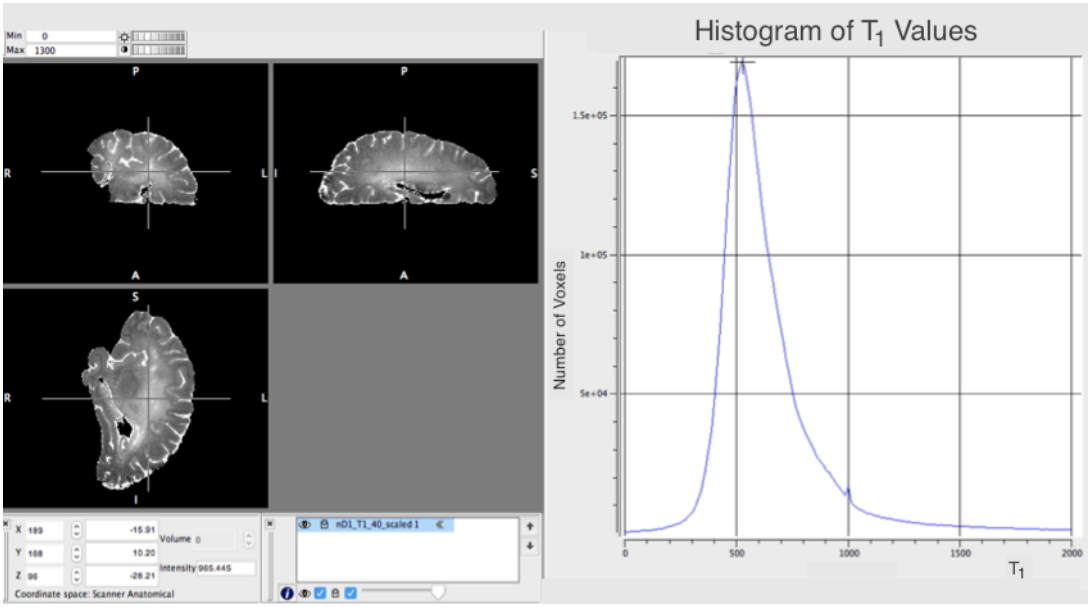

FIGURE 58: HISTOGRAM OF THE T1 VALUES FROM THE DESPOT1 ACQUISITION ON THE 7T WHOLEBODY SCANNER

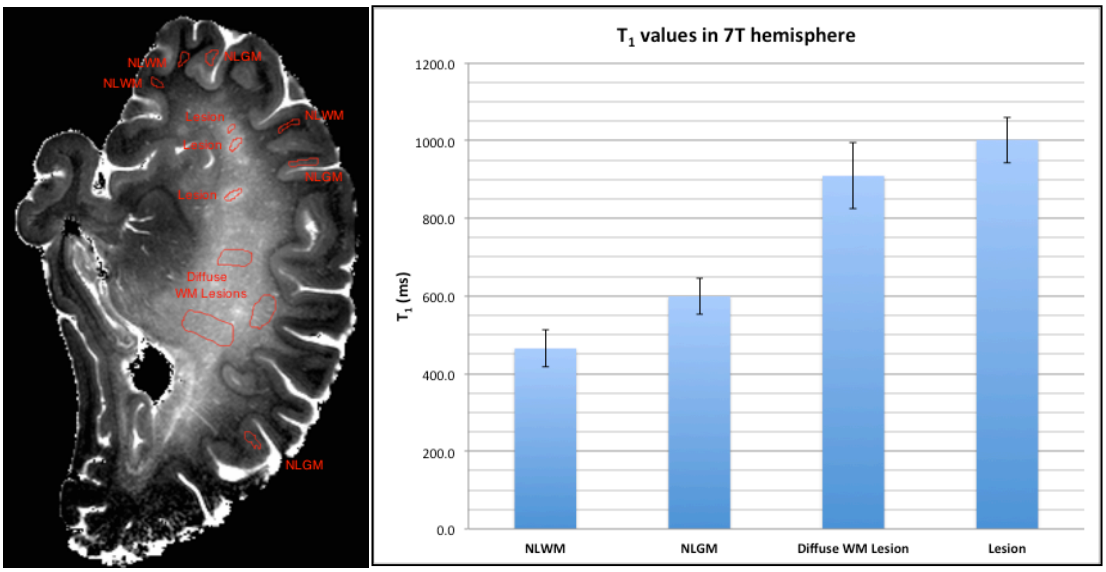

FIGURE 59: REGIONS OF INTEREST IN THE T1 MAP (LEFT). AVERAGE T_1 VALUES IN THE NON-LESIONAL WHITE MATTER (NLWM), NON-LESIONAL GREY MATTER (NLGM), DIFFUSE WM LESION AND LESIONAL AREAS OF THE RIGHT HEMISPHERE OF MS442 (RIGHT). ERROR BARS ARE THE STANDARD DEVIATION.

Studying the WM of the hemisphere, it can be seen that discerning areas that are without lesions is difficult. There is significant diffuse damage in the WM. Therefore, the central WM was designated as diffuse WM lesion with varying levels of damage. The standard deviation of the diffuse WM lesion is approximately 1.5 times that of the NLWM and NLGM, which reflects this. The NLWM was designated in the outer sulcus areas which seemed less affected by the diffuse damage.

	T_1 (ms)	SD
NLWM	464.8	47.2
NLGM	599.0	47.2
Diffuse WM Lesion	909.3	85.8
Lesion	1001.7	58.9

TABLE 14: T_1 VALUES IN MS442R

6.11.1.2 Discussion

DESPOT1 maps of the post-mortem human brain have been created successfully using a 7T clinical scanner. There was signal dropout at the back of the hemisphere in occipital lobe, due to the size of the head coil used. This has resulted in fitting failure at this location. As the meninges were not removed from the hemisphere for histological quantification, this resulted in formalin collecting in the sulci. This formalin shows as the bright white areas at the edge of the hemisphere (fig 59) due to the high T_1 values (>2000ms) in free water, even though the hemisphere had been inserted in perfluorpolyether for imaging. There have been no DESPOT1 or other T_1 mapping studies at 7T in *post-mortem* tissue to compare the T_1 values obtained. There does not seem to be a resolution of the white and grey matter into two separate peaks, but this may be due to the wide range of values found in the WM due to diffuse lesional damage.

6.11.2 CONCLUSION

DESPOT1 T_1 maps have been acquired at 3T and 7T. The processing of the images has shown that it is not possible to distinguish WM and GM easily for segmentation purposes at the resolution that can be used when imaging the whole spinal cord at 3T. Histogram analysis does not show distinct peaks at the WM and GM values even at 7T. Further work will include imaging the whole spinal cord in smaller sections at higher resolution in the head coil on the Philips scanner. This will hopefully facilitate segmentation on PD images of the tissue types to calculate T_1 values accurately.

Quantitatively, the T_1 value is not a useful index in fixed tissue. The chemical changes produced by the process of fixation shorten the T_1 values in the tissues and narrows the difference between the values. This results in T_1-weighted images having poor contrast which can be improved qualitatively by plotting the T_1 value in a map. Quantitatively, the narrow gap between the WM and GM value and the natural statistical spread of values means they are indistinguishable when spinal cord T_1 maps are plotted as histograms. This is contrary to the results found in the *post-mortem* brain but perhaps not surprising

when the *in-vivo* results of the spinal cord are examined. The paper by Smith et al.[151] already mentioned above, shows that there is a smaller difference between WM and GM values in the spinal cord than the brain *in-vivo*, and with the convergence of T_1 from fixation in the spinal cord, T_1 contrast between WM and GM is lost. However, the contrast between the normal WM and GM and lesions is retained due to the higher T_1 values in the lesions. Lesions may be relatively simple to visualise in T_1 maps of the *post-mortem* spinal cord as that difference in values is the only contrast in the image, and it will be interesting to compare the MRI results with histology.

6.12PSIR IN THE POST-MORTEM SPINAL CORD

There have been no *post-mortem* studies that examined PSIR imaging in the brain or the spinal cord and no histological verification of the technique. Therefore, *post-mortem* spinal cords were imaged on the Siemens Verio 3T scanner and 32-channel head coil with 'real' or phase-corrected reconstruction. Small sample tubes with short 10cm sections of spinal cord from patients MS345, MS232 and MS464 were used (see section 5.5). The section from patient MS232 was found to be unusable due to damage on the images.

Patient	Spinal area
MS345	Cervical
MS464	Thoracic
MS464	Lumbar
MS464	Lesion

TABLE 15: PSIR SPINAL CORD SAMPLES

A TE value of 16ms and TR of 16000ms were used as these were found to give the best white/grey matter contrast in fixed tissue. The results from the SE-IR T_1 measurements performed in the spinal cord were used to calculate reasonable TI values to null the GM, WM and lesion in the spinal cord samples, using the ideal signal curve Eqn. 69, rearranged for TI.

$$TI = \mathrm{LN}\,2 \cdot T_1 \qquad \text{EQUATION 73}$$

Null TI values for each tissue were based on an average value across all spinal cord values.

Tissue type	Calculated T_1 value (ms)	TI to null particular tissue (ms)
GM	300	200
WM	250	170
Lesion	500	350

TABLE 16: VALUES USED TO CALCULATE IMAGING PARAMETERS

6.12.1.1 Results

It was reasonably difficult to pinpoint the null point for the WM and GM tissues due to variations in shim and B_1 pulse, the narrow difference between the tissues meant if one tissue type was nulled, the other had little signal at the same time point. The graph below shows mean values for regions of interest in the GM and WM in the cervical spine, the error bars shown are SD values.

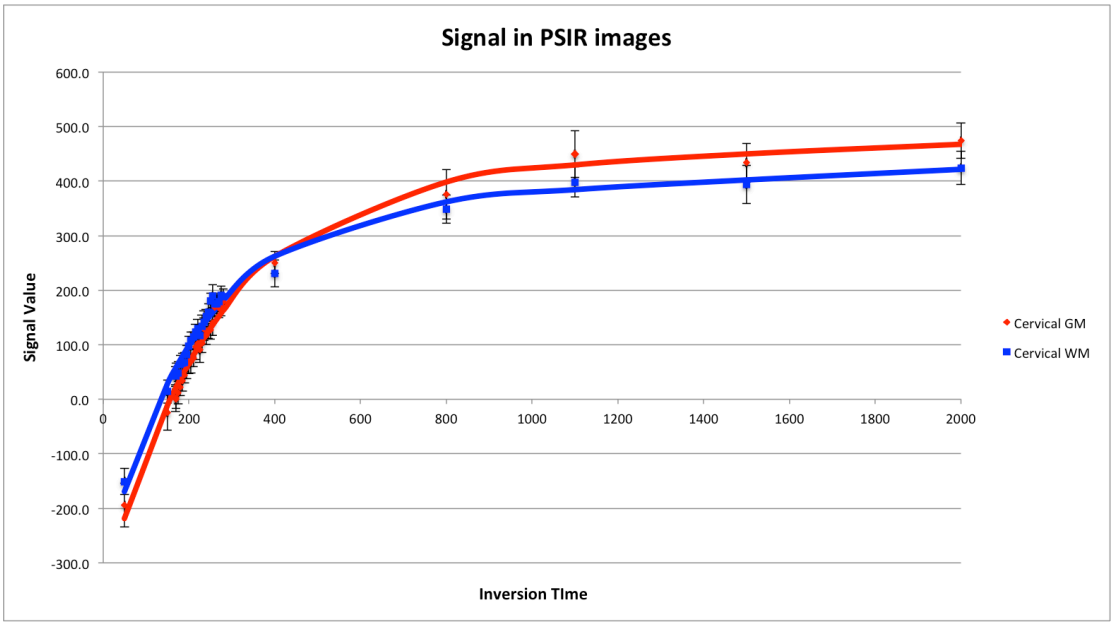

FIGURE 60: SIGNAL CURVES FROM PSIR IMAGES FROM REGIONS PLACED IN THE GM AND WM

In the central part of the curve where both the WM and GM curve cross the null point, there is little difference in signal value and therefore contrast between the two tissues. The long TI images are the same as PD-weighted images with a formalin/CSF suppressing IR pulse. It can be said that the PSIR

image may improve contrast at short TI but the main purpose is to replicate the nullification of lesions as the Sethi paper *in-vivo*. The best contrast occurred at short (50ms) and very long TI (2000ms), showing that the T_1 curves for the white and grey matter are furthest apart at both ends, i.e. the signal difference is dominated by PD differences.

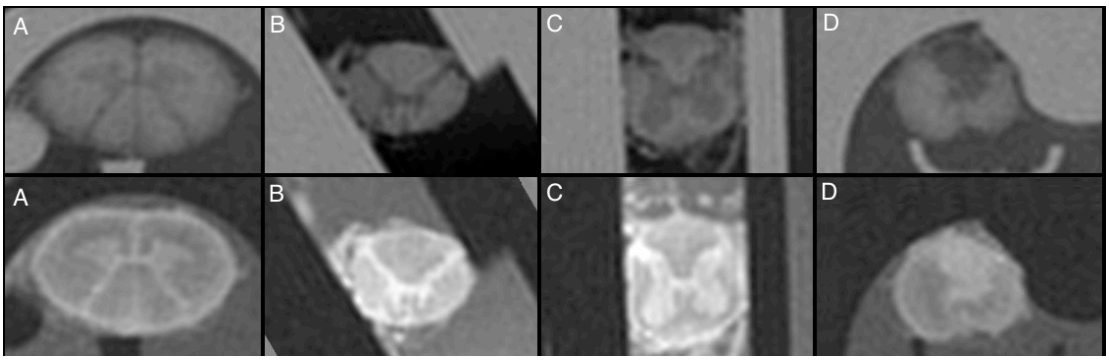

FIGURE 61: PSIR IMAGES (TE/TR 16/16000MS) OF THE *POST-MORTEM* SPINAL CORD, CERVICAL (A), THORACIC (B), LUMBAR (C) AND LESION (D). THE TOP ROW HAS A TI OF 50MS AND THE BOTTOM ROW 2000MS.

The TI was set to null grey matter in the PSIR images shown below in Fig. 62 with TE = 16 ms and TR = 16000 ms and TI = 170 ms. These can be compared to magnitude images.

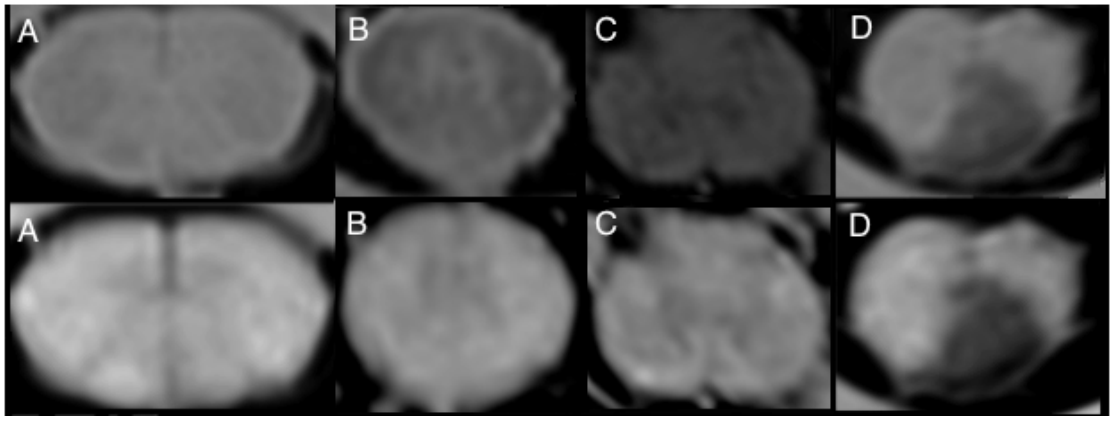

FIGURE 62: MAGNITUDE IR (TOP ROW) AND PSIR IMAGES (BOTTOM ROW) OF MS CERVICAL (A), THORACIC (B), LUMBAR (C) AND A LESION IN THE THORACIC SPINAL CORD (D).

The images shown above demonstrate the lack of added diagnostic value from PSIR images in the fixed post-mortem spinal cord in comparison to PD images. The lesion can be seen in both the magnitude and PSIR images without

any extra information. If the TI is set to null the lesion, all contrast is removed from the white and grey matter as shown below.

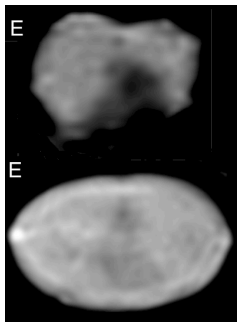

FIGURE 63: PSIR IMAGES (TE/TR 16/16000MS) OF (TOP ROW) LESION AND (BOTTOM ROW) CERVICAL SPINAL CORD WITH TI 350MS

6.12.1.2 Conclusion

PSIR images have been acquired in the *post-mortem* fixed spinal cord. The shortened and converging T_1 values found in fixed tissue result in contrast-less images when the *in-vivo* method of nulling the lesions is reproduced. No extra diagnostic information is gained by nulling the GM.

6.13 THE VISTA SEQUENCE

The Visualization of Short Transverse relaxation time component (ViSTa) sequence was first proposed in 2003[154]. It uses double inversion pulses to suppress a large range of long T_1 values corresponding to intra/extra cellular and free water to leave the only contrast in the image arising from the short T1 values hopefully corresponding to the signal from myelin water. In this sequence, the transverse magnetisation at an echo time after a 90° excitation can be written as follows:

$$M_{xy} = M_0\left(1-\left(2-\left(2-e^{-TD/T_1}\right)e^{-TI_1/T_1}\right)e^{-TI_2/T_1}\right)e^{-TE/T_2^*}$$

Where TI_1 and TI_2 are the two inversion pulse times and TD is the wait time after acquisition before the next inversion (shown in figure 64A below). M0 is the magnetisation in the z-direction before excitation.

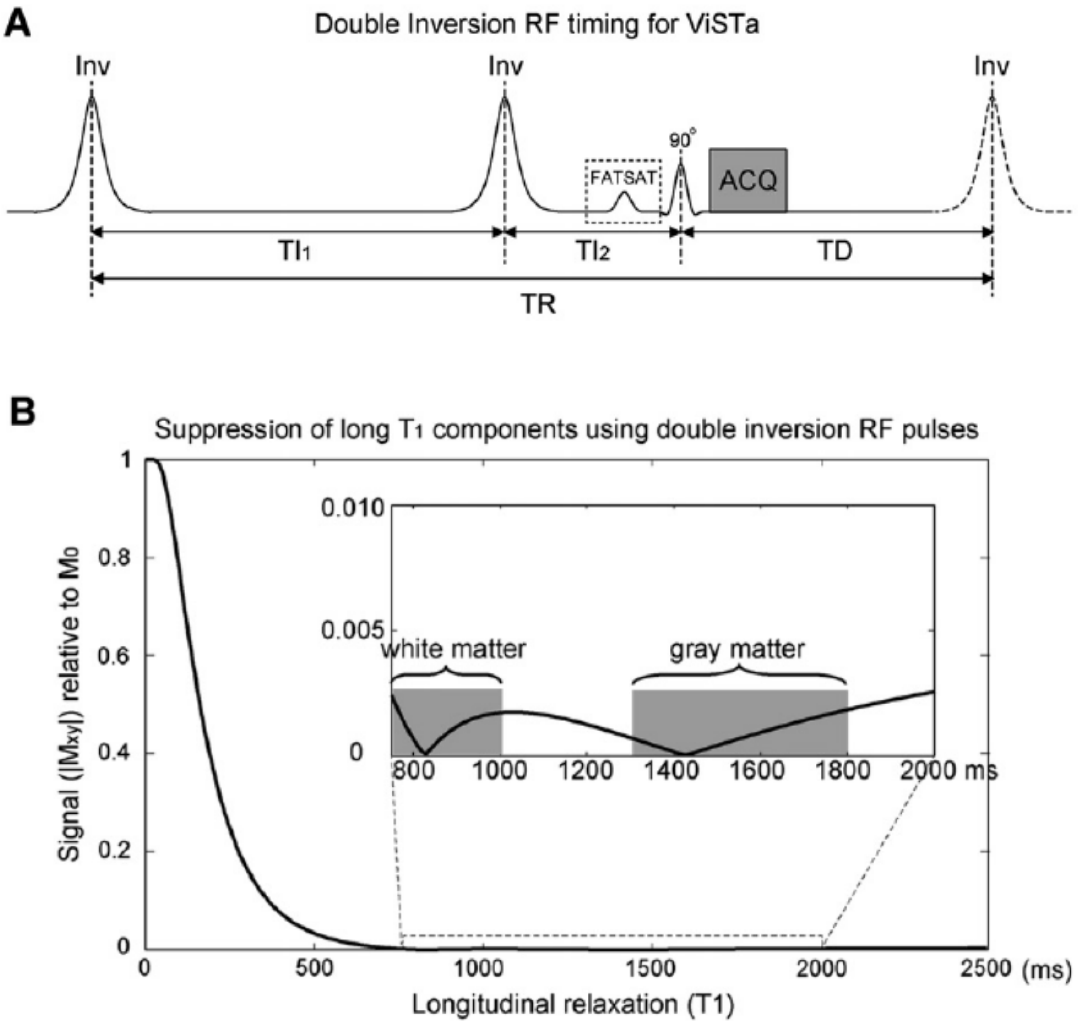

FIGURE 64: (A) DOUBLE INVERSION RF PULSE SEQUENCE FOR DIRECT VISUALIZATION OF SHORT TRANSVERSE RELAXATION TIME COMPONENT IMAGING (VISTA). THE TIMING (TI1 = 560 MS, TI2 = 220 MS, AND TD = 380 MS) WAS OPTIMIZED TO HAVE MAXIMUM SUPPRESSION IN WATER SIGNAL IN THE RANGE OF 750 ≤ T1 ≤ 5000 MS. (B) TRANSVERSE MAGNETIZATION AS A FUNCTION OF T1 IN THE VISTA SEQUENCE. THE DOUBLE INVERSION PULSE ENABLED SIGNAL SUPPRESSION OVER A WIDE RANGE OF LONG T1. REPRODUCED FROM OH ET AL[154]

It should be noted that the T_1 value of myelin water is not known, though the T_2 value has been investigated fully (20ms[110]). Direct observation of multiple T_1 components is not possible *in-vivo* due to the relative time scales of T_1 relaxation and the exchange of magnetisation between water environments[7]. As the T_1 value is greater than the mean residence time of protons in each environment, the magnetisation is a product of all before returning to thermal equilibrium, and it is difficult to isolate the signal from each. Put simply, the T_1 decay curve is mono-exponential and no information regarding cellular

structure can be extracted. The T_1 value is expected to be short however due to the restricted environment of myelin water. In the original paper, it was shown that suppression should begin at the WM and GM T_1 values, and this experiment sought to replicate this. If the T_1 values found in post-mortem brain are 179 ± 22 ms in WM and 234 ± 28 ms in GM (see section 6.1.2), we must suppress these using very short TI_1, TI_2 and TD values.

A parameter search was performed using the equation above to calculate the values of TI_1, TI_2 and TD that would be needed for post-mortem tissue. These were 80, 30 and 60ms respectively, with a total TR of 170ms. The graph of this function is shown in figure 65 below.

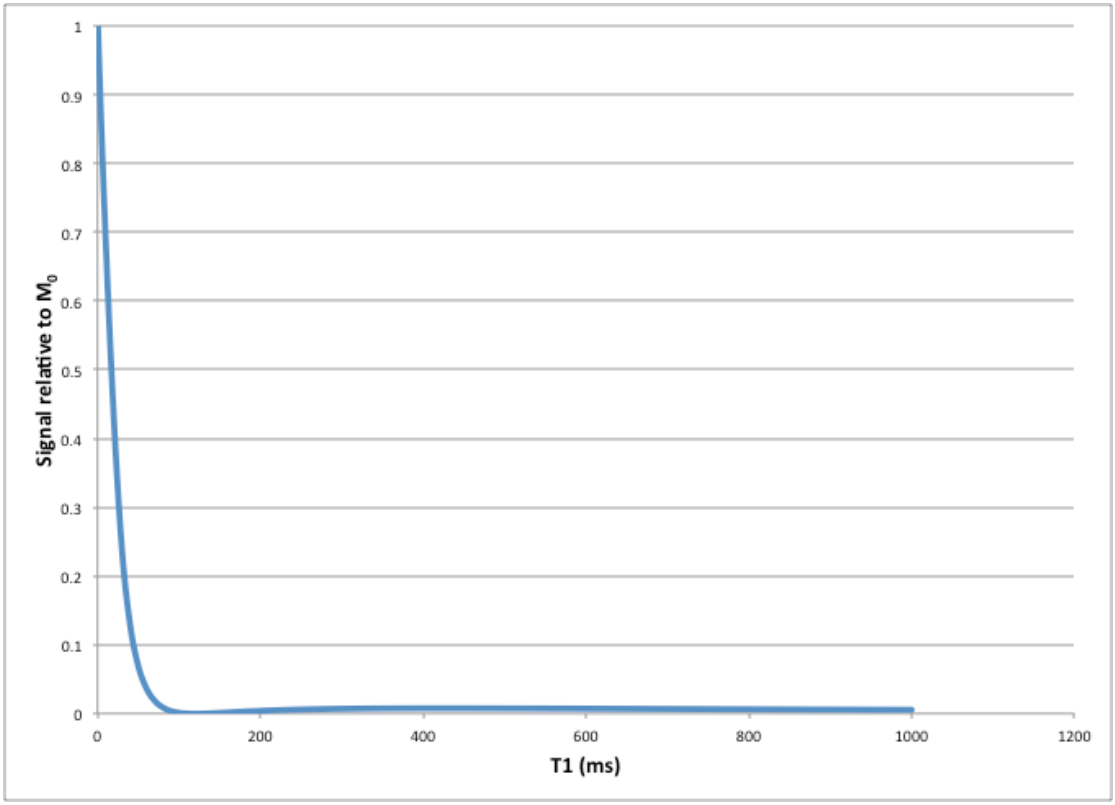

FIGURE 65: THEORETICAL SIGNAL SUPPRESSION CURVE WITH EMPIRICALLY DETERMINED VALUES

There is good suppression of all T_1 values above 100ms which should provide a myelin image using these values. In case this resulting in oversuppression of the short T_1 values an alternative was calculated given in figure 66 below.

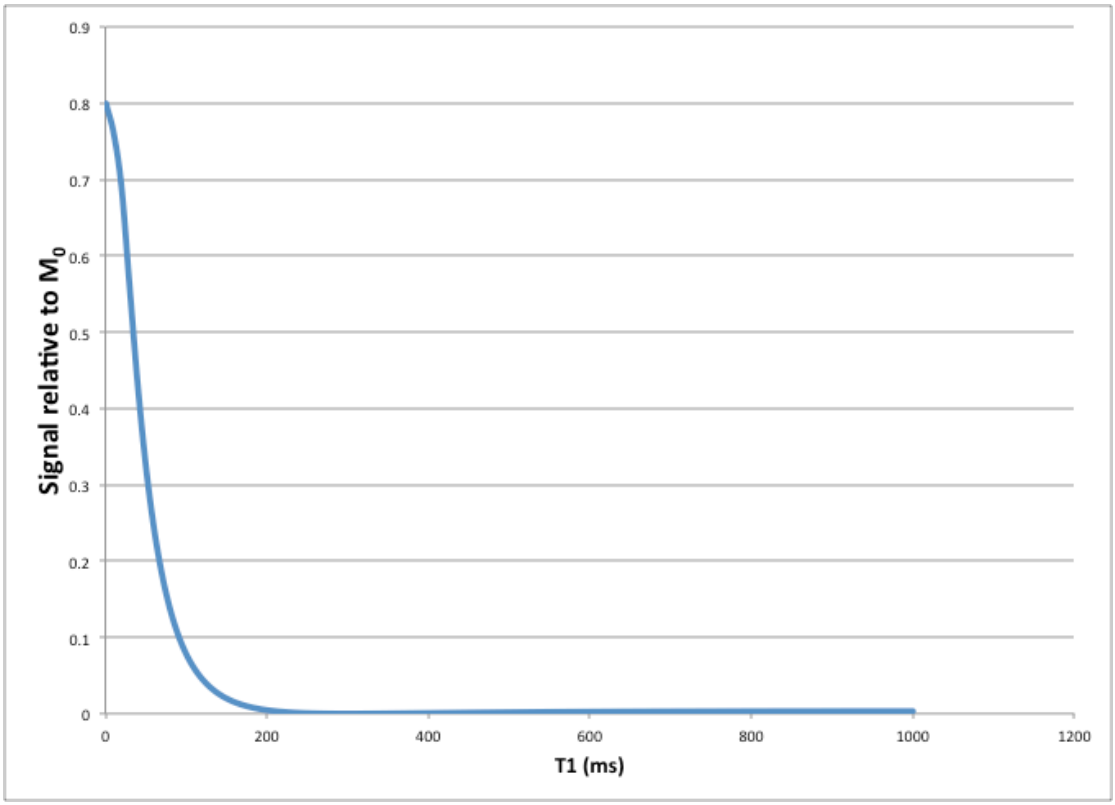

FIGURE 66: ALTERNATIVE THEORETICAL SIGNAL SUPPRESSION CURVE WITH EMPIRICALLY DETERMINED VALUES

The values of TI_1, TI_2 and TD were 150, 60 and 100ms respectively. The suppression of values below 200ms is not complete but the longer values may be able to be used on the clinical scanner.

6.13.1 RESULTS

It was not possible to replicate the exact calculated values at the scanner due to SAR constraints. The values of TI_1, TI_2 and TD were 80, 32.2 and 66ms respectively. This gave the suppression shown in the graph below (red line in Fig. 67).

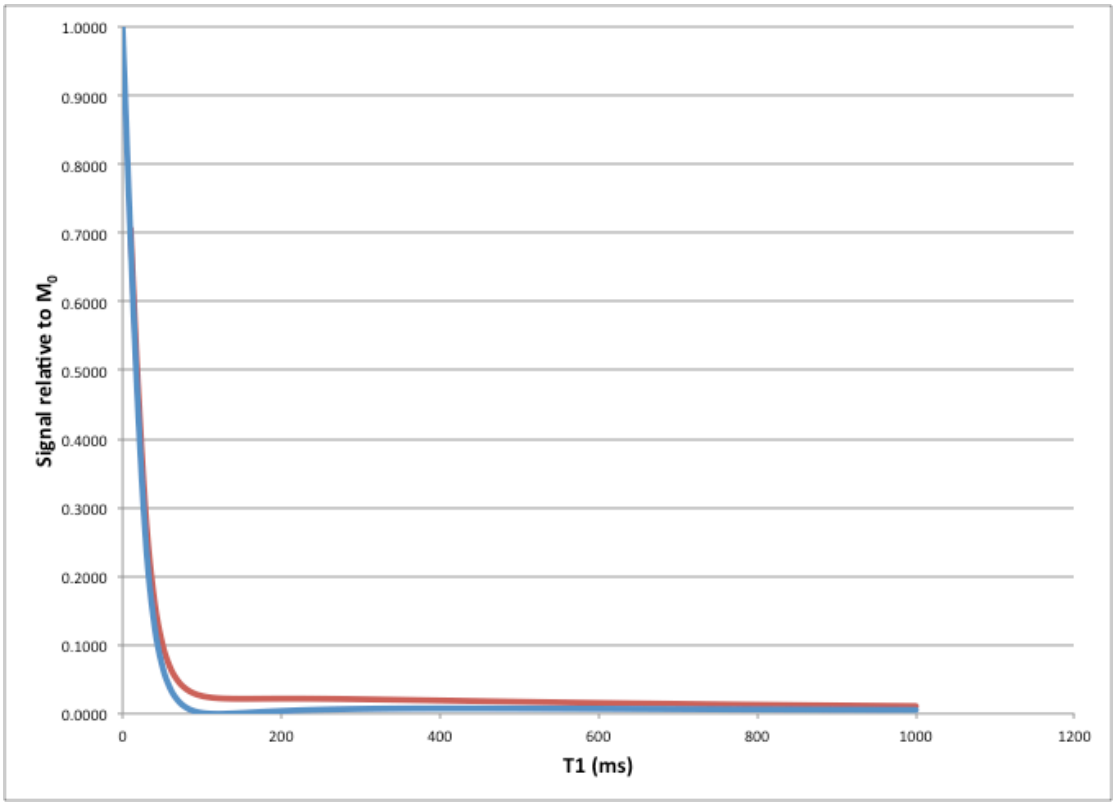

FIGURE 67: ACTUAL SIGNAL SUPPRESSION WITH THE VISTA SEQUENCE ACHIEVABLE ON THE PHILIPS SCANNER

The suppression of the T_1 values was not perfect but at 100ms was theoretically 1%. It was not possible to add a fat saturation pulse. The alternative values of 150, 60 and 100ms were possible without alteration.

The images acquired with the two sequences are shown in Figure 68 below.

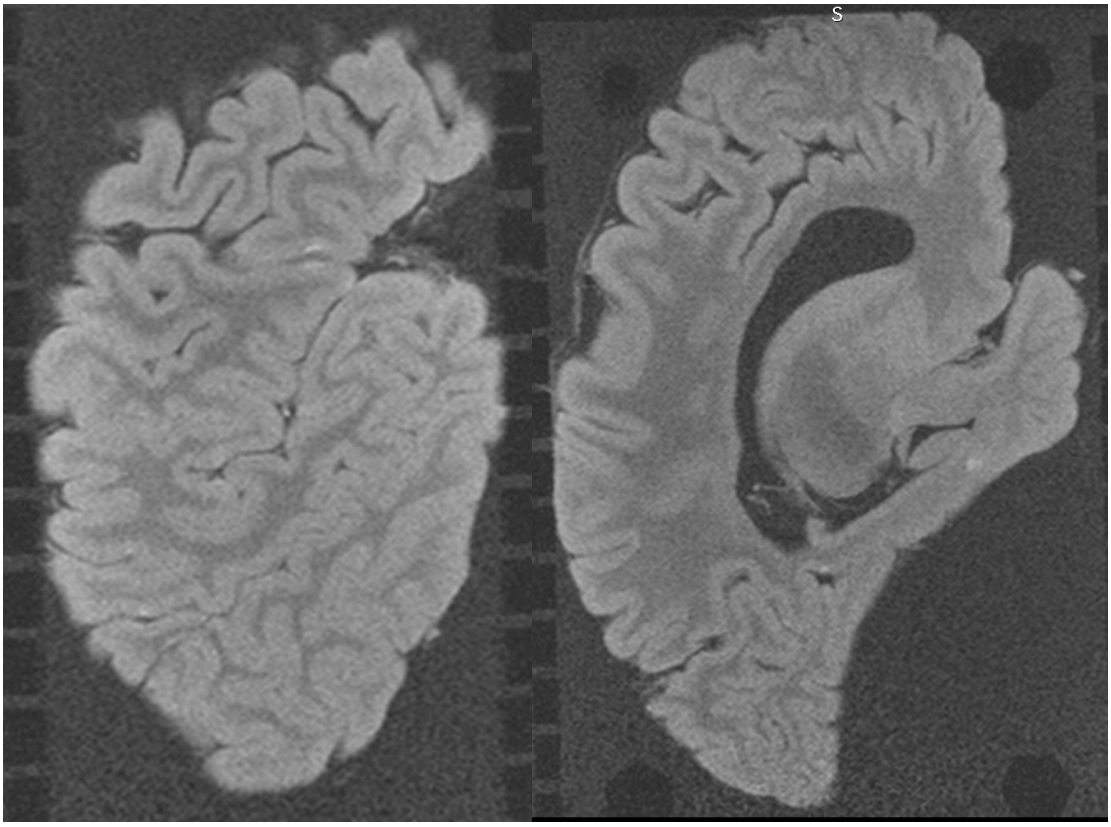

FIGURE 68: SLICES 9 AND 24 OF MS459L USING TI_1, TI_2 AND TD OF 80, 32.2 AND 66MS. TE 7.7MS, TR 206MS, NSA 5, 0.5 × 0.5 × 2MM MATRIX.

The image as acquired is not a myelin water image. White matter should obviously have a higher signal than the grey matter ribbon due to the higher myelin content.

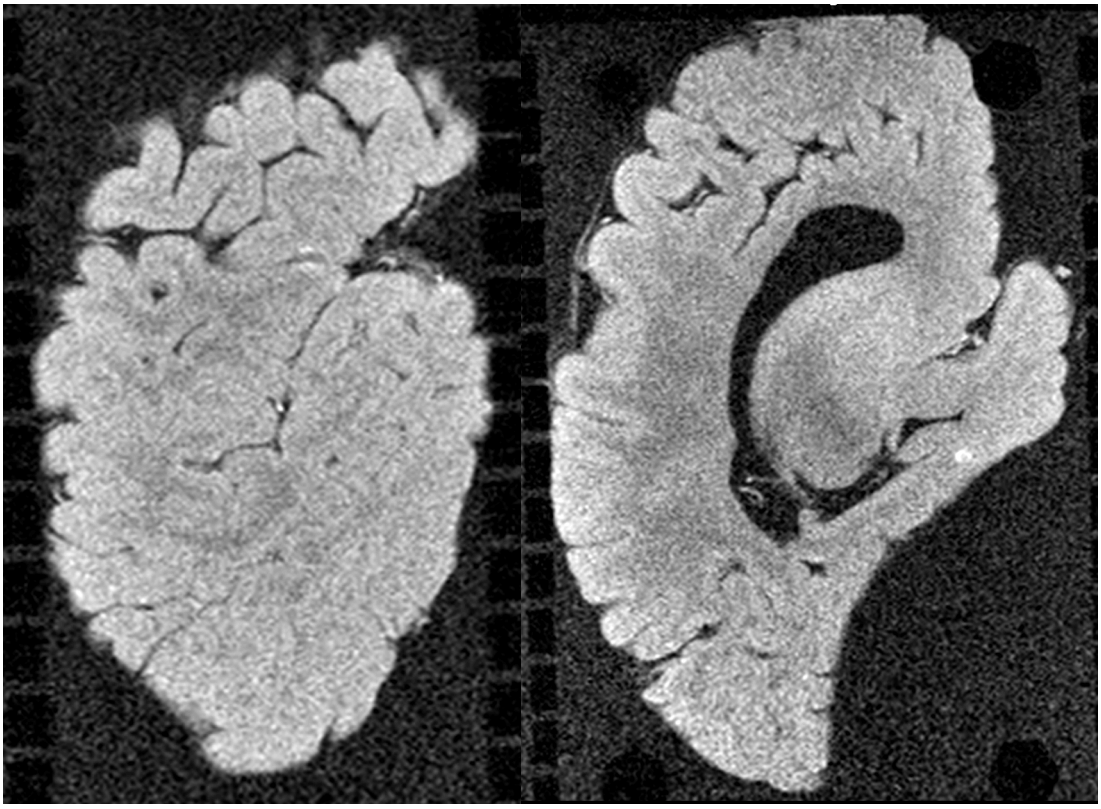

FIGURE 69: SLICES 9 AND 24 OF MS459L USING TI_1, TI_2 AND TD OF 150, 60 AND 100MS. TE 7.7MS, TR 310MS, NSA 2, 0.5 × 0.5 × 2MM MATRIX.

The change of parameters, including the reduction in averages from 5 to 2 due to time constraints has resulted in much higher noise. However, the theoretical curve predicted less suppression of the signal by the double inversions so it is surprising this has not had some mitigation on the effects of the reduction in number of signal averages. It remains obvious however, that this is not a myelin water image with the GM still showing higher signal than WM.

The extension of the selected parameters to a TI_1, TI_2 and TD of 240, 80 and 210ms increases the noise and lowers the contrast between WM and GM even further, even though the signal suppression curve is largely unchanged, as shown in the Figure 70 below.

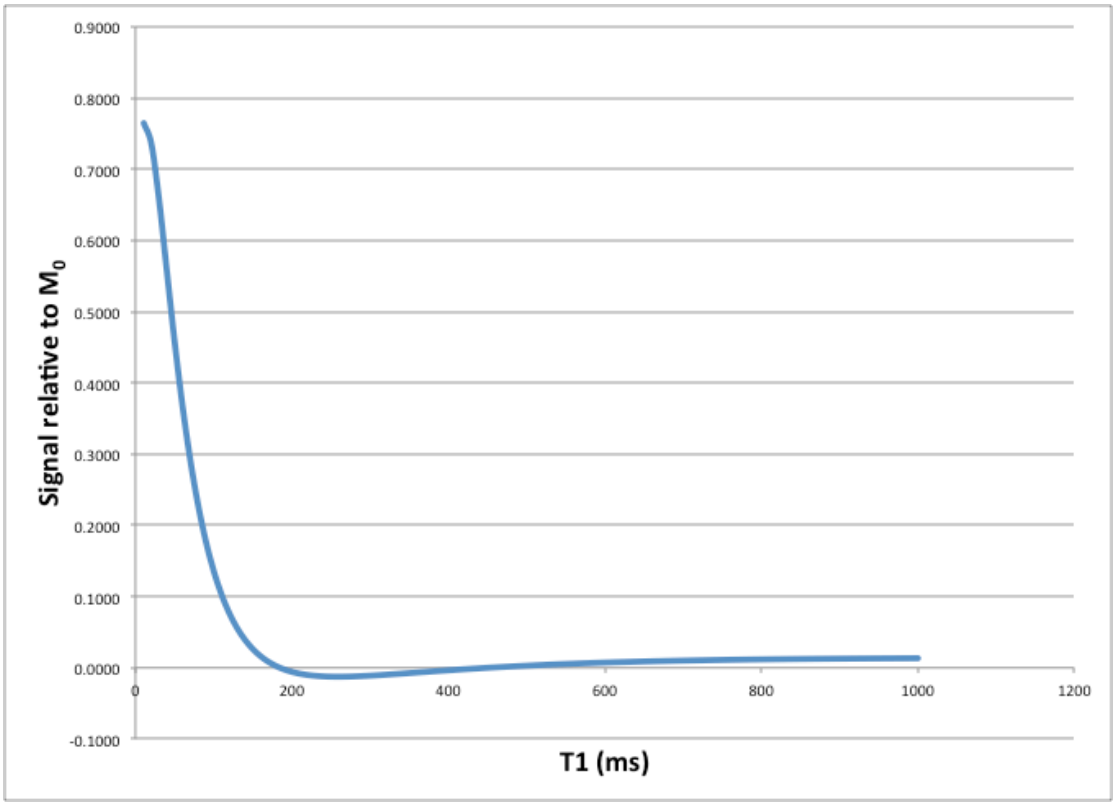

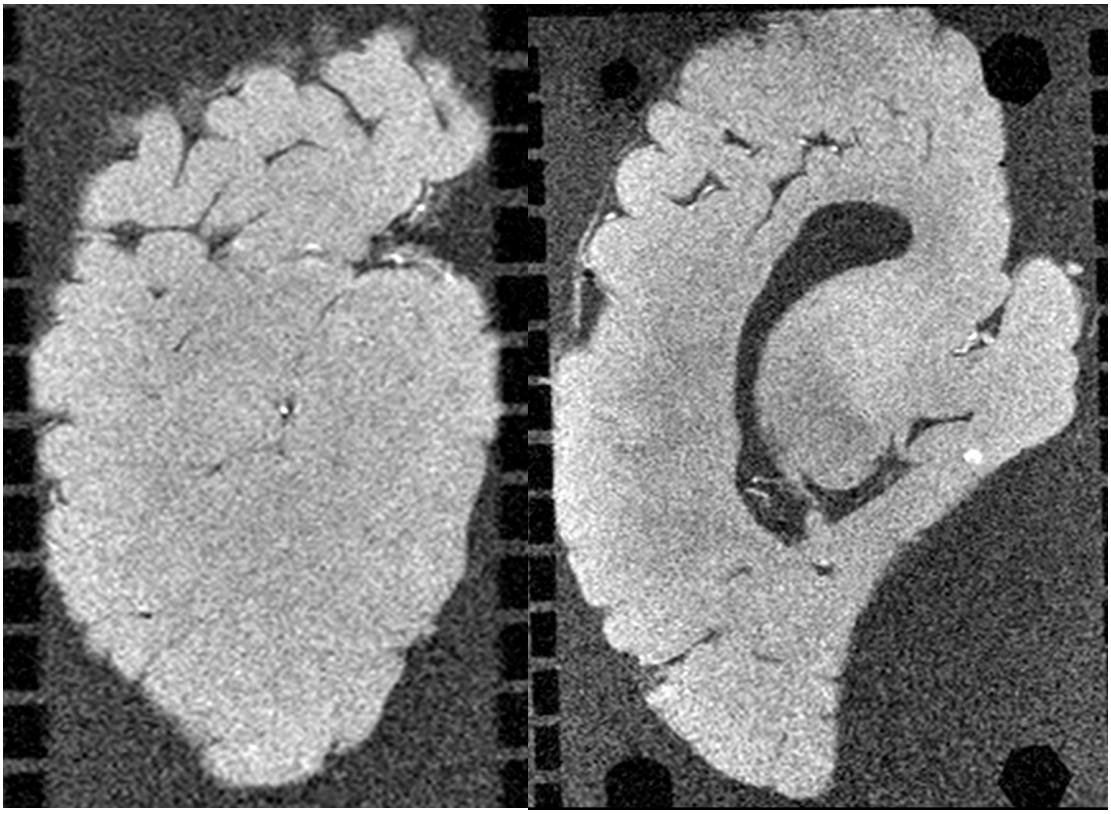

FIGURE 70: SUPRRESSION CURVE AND RESULTING IMAGES OF SLICES 9 AND 24 OF MS459L USING TI_1, TI_2 AND TD OF 240, 80 AND 210MS. TE 7.7MS, TR 530MS, NSA 2, 0.5 × 0.5 × 2MM MATRIX.

It could be that the fat saturation pulse changes the magnetisation in such a way as to obtain an image with a higher signal in the white matter, though whether an image obtained in this manner is a myelin water image is debatable.

6.13.2 DISCUSSION

Although the VISTA sequence seems to be a simple matter of determining the values which give suitable signal suppression, this does not seem to be the case in the fixed tissue situation. If the extra fat suppression pulse used *in-vivo* is added (this would need pulse programming) the sequence may be more successful. It is likely that the fat suppression pulse adds to the suppression of the *in-vivo* signal above that of just the fat signal in combination with the other IR pulses, applied in the centre as a triple IR sequence. What TI value an extra corresponding IR pulse would need to be applied at in fixed brain tissue, which doesn't contain surrounding fatty tissue, would have to be investigated.

6.14 SUMMARY

In this chapter, the gold standard method of measuring T_1 has been implemented and the results compared with published data. The *in-vivo* measurements match published data for this field strength well, and show that the protocol has been implemented correctly. The protocols were then optimised for fixed tissue measurements. There are some questions around the data that has been published for fixed tissue which may explain the discrepancies from these new results.

The SE-IR and TSE-IR sequences were compared directly, and since the differences seen between the sequences can be linked to experimental setup the TSE-IR sequences was chosen for latter measurements.

Spinal cord data were then acquired and T_1 results defined for the first time in fixed tissue. It would appear that the fixation of spinal cord has a smaller effect on T_1 values than the fixation of brain tissue.

Having validated the gold standard methods for T_1 measurement and defined baseline figures for fixed spinal cord the accuracy of T_1 measurement in fixed tissue by the DESPOT1 algorithm was investigated for the first time. This was investigated at both 3T and 7T.

After this, two T_1 inversion-recovery based imaging methods were assessed. The PSIR sequence, successful in fixed brain tissue, was not useful in fixed spinal cord tissue due to the smaller difference between white and grey matter. The VISTA sequence although seemingly technically simple, was not possible to acquire successfully due to the shortening of the T_1 values in fixed tissue and the limitations of a clinical scanner.

Determining the baseline T_1 values of fixed tissue at 3T allows for the simple implementation of research sequences in all fixed tissue work in MS and other pathologies by other groups. These are used in further work in this thesis as the T_1 values established by inversion recovery are used to decide the flip angle range required for accurate measurement of T_1 by the DESPOT1 sequence which is subsequently used in the mcDESPOT algorithm.

7 T_2 MAP ACQUISITION

7.1 SINGLE COMPONENT T_2 MAP ACQUISITION

7.1.1 WORK ON A 3T CLINICAL SCANNER IN A BRAIN HEMISPHERE

The standard method of measuring T_2 is the single component measurement of T_2. This can be performed with the CPMG sequence described in section 2.6.1 with fewer echoes acquired and less time taken. This only gives the average T_2 value for each voxel, rather than the constituent T_2 values for the mix of tissues with the voxel.

7.1.2 METHODS

A hemisphere was acquired on the Philips scanner. The sequence parameters were TE 10ms, TR 10000, slice thickness 2mm, matrix 256 × 256, echo train length 24 (TE 10 - 240ms, in steps of 10ms). The odd echoes were discarded during calculation in order to avoid stimulated echo effects in the fitted curve (see section 2.6.1). The Fiji MRI Analysis Calculator was used to calculate the T_2 values (http://imagej.net/Fiji). This program uses a simplex algorithm to fit the curve to the single T_2 equation.

7.1.3 RESULTS

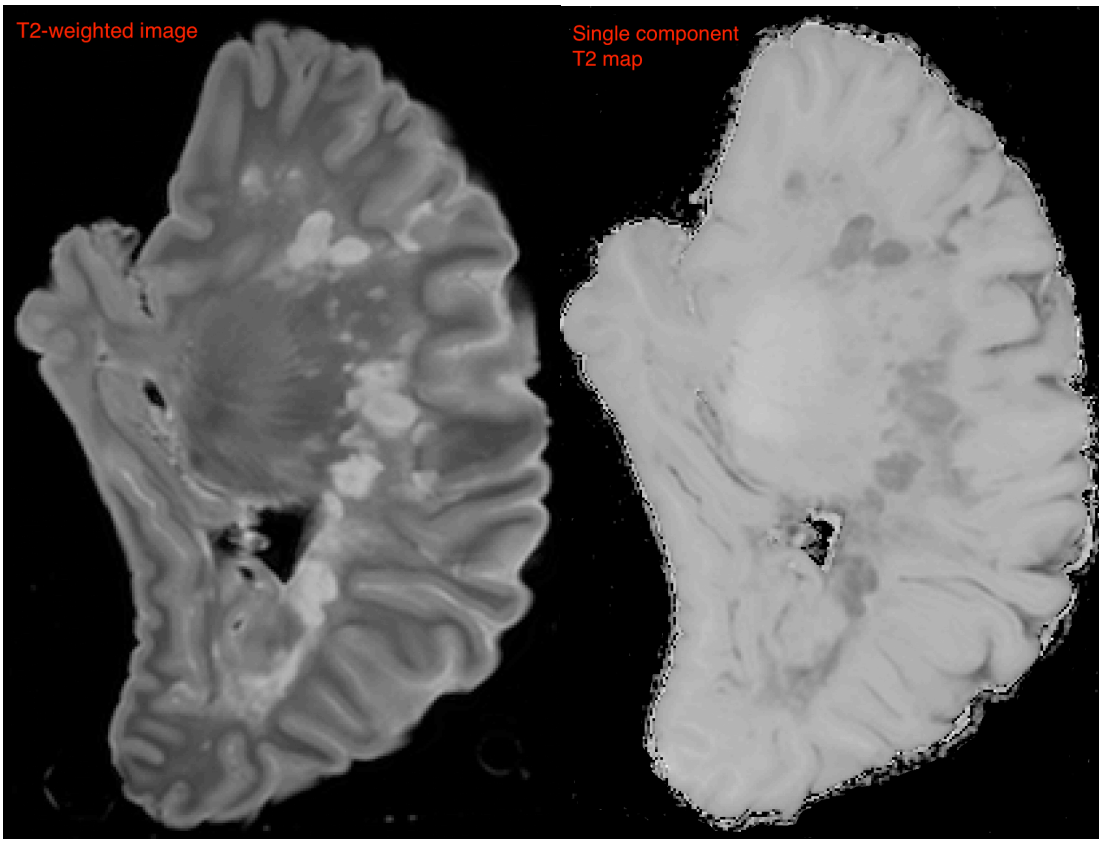

FIGURE 71: SAGITTAL T2-WEIGHTED IMAGE (TE 40, TR 10000MS) OF HEMISPHERE MS436R SHOWING SEVERE DEMYELINATION IN THE WHITE MATTER AND THE CORRESPONDING T2 MAP (MASKED). THE T2 MAP IS DISPLAYED BETWEEN 0 AND 100 MS

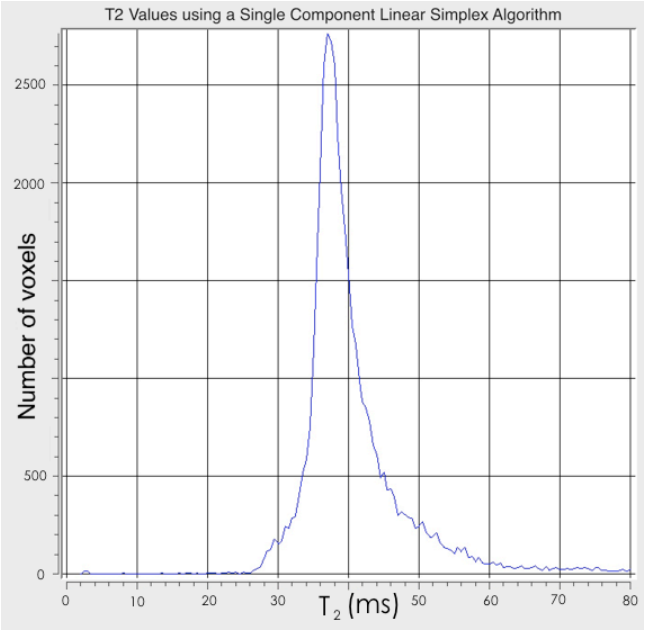

FIGURE 72: HISTOGRAM OF THE T_2 VALUES FOUND IN THE HEMISPHERE MS436R USING A SINGLE EXPONENTIAL FITTING ALGORITHM

The median value of T_2 found in this map is 37 ms. There is little differentiation between the white and grey matter, the lesions are reasonably well delineated but the diffuse white matter damage seen in the T_2-weighted image is difficult to discern.

7.2 DESPOT2 T_2 MAP ACQUISITION IN A BRAIN HEMISPHERE

7.2.1 WORK ON A 3T CLINICAL SCANNER

The acquisition of DESPOT2 maps was found to be very challenging. The early acquisitions were found to show unexpected jumps in the centre frequency determination between acquisitions. To try to address this, a patch was acquired from Philips to stop the preparation steps (detailed in section 5.1) updating. All acquisitions should be identical except for the change in flip angle and RF phase. This patch sets a preparation option of 'same prep' and this is used after the first scan in the bSSFP acquisition, the first scan being set to 'auto' so that appropriate factors are used. The first scan in the set is also the highest flip angle, as this sets the gain appropriately for the rest of the flip angles. As the prep steps including the receiver gain are not updated after this point, the data must be acquired from the highest flip angle first to the lowest flip angle or there will be a signal overflow artefact, meaning that the data cannot be used.

Due to various factors, this patch was not available until 2.5 years into the project and this gave a short timescale for the acquisition of data. Also at this point the spinal cords had been dissected into 10cm pieces for other projects and so a successful acquisition is not available of the whole spinal cords on the spinal coil.

The TR chosen in these experiments is the shortest possible in order to minimise the banding artefacts found in this sequence[20]. The TE value is set by the TR as a balanced sequence by its nature means that the TE must be half of the TR. The flip angles acquired were 7, 14, 21, 28, 35, 42, 49 and 56 degrees. This was a truncated number of flip angles, with the intention at first to acquire at 63, 40, 77 and 84 degrees also. However, even with the same prep patch applied

during the acquisition, the bands still moved at the higher flip angles even though acquired with the same phase increment. This is likely to be due to variable rate RF pulses used with the bSSFP sequence to lower SAR deposition. These variable rate RF pulses are applied over a longer time period in order to lower the maximum amplitude to reduce the SAR, which means higher flip angles can be used. The RF pulse is applied in conjunction with a slice selection gradient. The time dilation of the RF pulse increases with flip angle. The TE and TR are adjusted to remain the same but the dB/dt and the time the magnetisation will take to reach the transverse plane changes. This can be seen by the parameters from an example DESPOT2 acquisition in Table 16. Little change is shown in the dB/dt values at lower flip angles and then larger steps at higher flip angles.

FA	TE	TR	Acquisition Duration	dB/dt
84	4.001	8.10000038146972	512.171142578125	69.802850853528
77	4.001	8.10000038146972	512.171142578125	52.341895429911
70	4	8.10000038146972	512.171142578125	43.271342173583
63	4	8.10000038146972	512.171142578125	38.720462217021
56	4	8.10000038146972	512.171142578125	35.873781436124
49	4	8.10000038146972	512.171142578125	33.922757376778
42	4	8.10000038146972	512.171142578125	33.006543174358
35	4.001	8.10000038146972	512.171142578125	32.201124088188
28	4.001	8.10000038146972	512.171142578125	31.460507568234
21	4.001	8.10000038146972	512.171142578125	30.792323009300
14	4.001	8.10000038146972	512.171142578125	30.510501542183
7	4.001	8.10000038146972	512.171142578125	30.510501542183

TABLE 17: EXAMPLE PARAMETERS COPIED FROM THE DICOM HEADERS OF THE FILES FOR A DESPOT2 ACQUISITION

The banding artefact is caused by how much phase the transverse magnetisation accumulates away from on-resonance at 0°. This is why short TR values are used to minimise the banding as that minimises the time for the magnetisation to accumulate significant phase away from 0°. So it would be expected that the same TR would give the same phase accumulation. However, when the RF pulse length is adjusted, the magnetisation will spend different amounts of time on the transverse plane accumulating phase, as there will be differing amounts of time before the rotation is complete. This means each acquisition will have differing phase accumulation and differing

banding artefacts. The effect is more pronounced at higher flip angles. This is clinically irrelevant, but means that when acquiring individual scans, it is not possible to make them identical in this respect. Therefore, it is not possible to remove the banding artefact and higher flip angles cannot be used.

The solution to these problems would be to fix the RF pulse length to that required for the highest flip angle (it would be expected to affect the minimum TR available). This would need to be programmed as part of the sequence, which was not available without a research agreement with Philips.

While the sequences were acquired with a 4 RF phase cycling scheme (0, 90, 180, 270), due to the fact that as standard, the default 0° is actually 180° as this gives the maximal signal. Therefore, if 0, 90, 180, 270 is acquired, the actual values are 180, 90, 0, 270. A Philips representative stated that the 90 and 270 angles were as labelled.

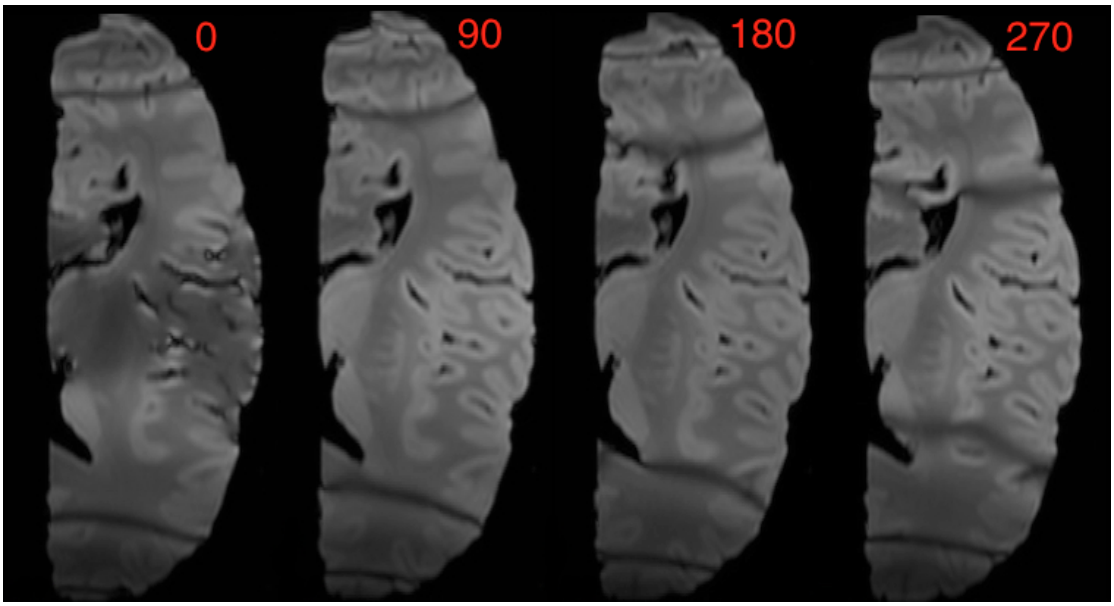

FIGURE 73: A DESPOT2 DATASET FROM MS422L SHOWED CORRESPONDING IMAGES FROM 0, 90, 180 AND 270 RF PHASE CYCLING ACQUISITIONS. THE 0 DEGREE ACQUISITION SHOULD HAVE SUPPRESSED SIGNAL ACROSS THE HEMISPHERE BUT AS THE RF PULSE IS NOT IDEAL THIS IS ONLY SEEN IN THE CENTRAL SECTION.

There was a concern that the long acquisition time (~5 hours) without the prep steps being run and the values adjusted may have caused the image to drift, but it can be seen in figure 73 above that this is not an issue. The dataset from 0° and 270° (which were approximately 3.5 hours apart in acquisition) were

subtracted from each other. If there had been any drift in image position this would have resulted in a halo of high signal pixels. However, although within the hemisphere the banding is intensified, there is no halo.

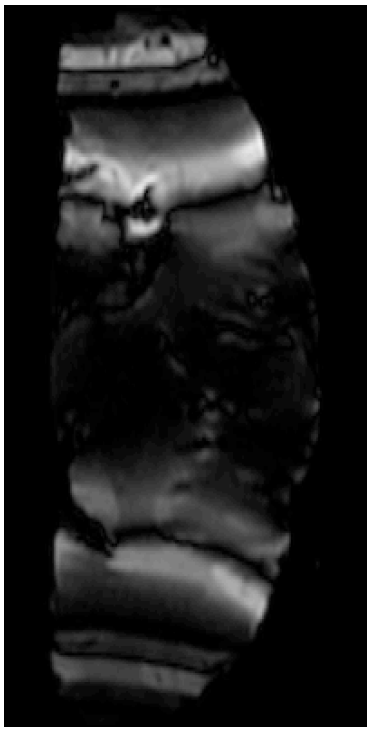

FIGURE 74: SUBTRACTION OF THE 0 DEGREE AND 270 DEGREE PHASE CYCLING SET TO EXAMINE ANY POSITIONAL DRIFT DUE TO LONG IMAGING TIME WITHOUT SCANNER PREPARATION STEPS BEING RUN

7.2.2 METHODS

Two algorithms are used with the DESPOT2 code, the 2 step Levenberg-Marquardt (LM) and the Broyden-Fletcher-Goldfarb-Shanno algorithm. These were combined with the T_1 maps produced by the NLLS algorithm with 15 iterations chosen for DESPOT1 (see section 6.6.1).

7.2.3 RESULTS

Results for the two algorithms with the standard phase cycling of 0° and 180° are shown below. It can be seen that although the RF phase cycling has moved the bands considerably, the banding is still seen in the T_2 map.

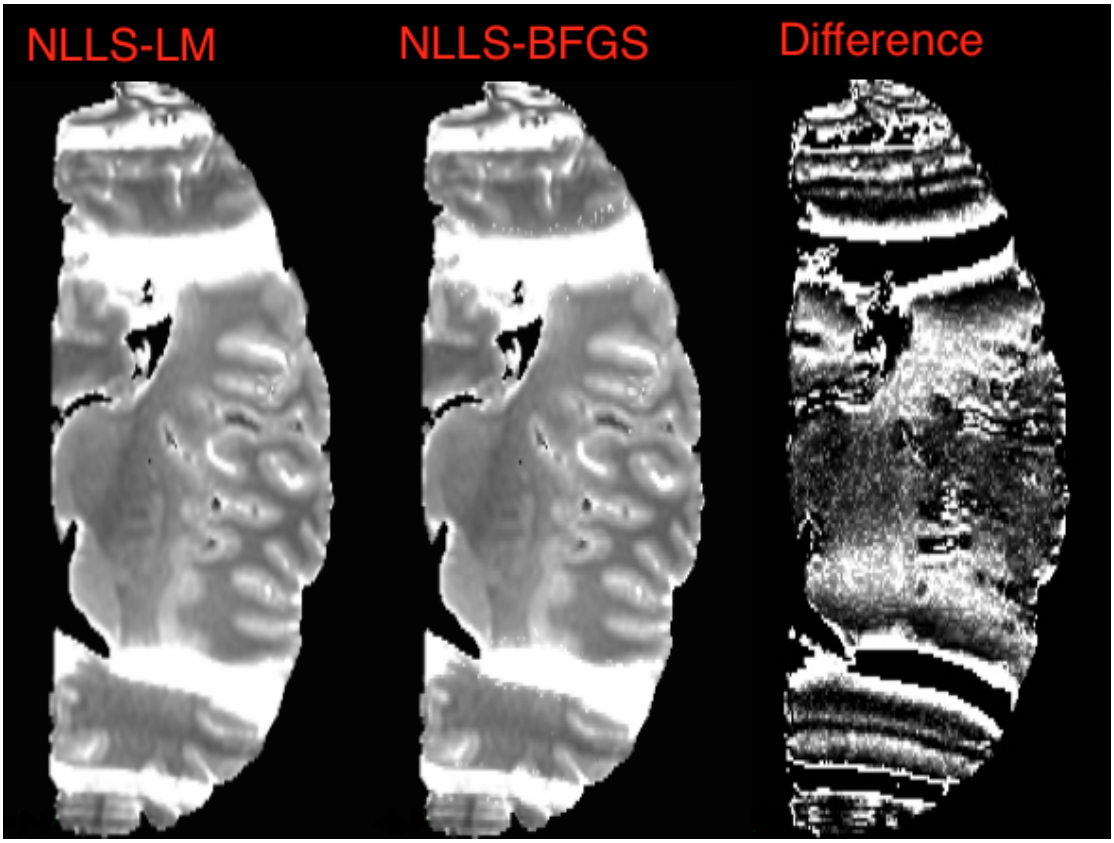

FIGURE 75: T_2 MAPS CALCULATED BY THE LM ALGORITHM (LEFT) AND THE BFGS ALGORITHM (MIDDLE) USING THE NLLS PRODUCED T_1 MAP AND A PHASE CYCLING SCHEME OF 0/180 WITH A DIFFERENCE IMAGE (RIGHT). THE T1 MAPS ARE DISPLAYED BETWEEN 0 AND 200MS

However, not only is there banding in the images, the BFGS algorithm shows pixels where the fitting has failed around the artefacts. This is shown below in Fig. 76.

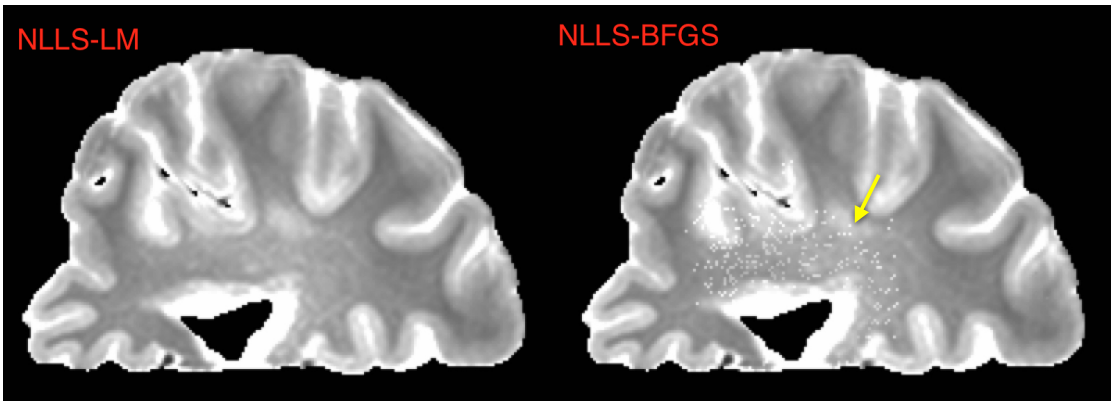

FIGURE 76: LM (LEFT) AND BFGS (RIGHT) ALGORITHM WITH THE BFGS ALGORITHM SHOWING FITTING FAILURES NEAR BAND BOUNDARIES. THE T1 MAPS ARE DISPLAYED BETWEEN 0 AND 200MS

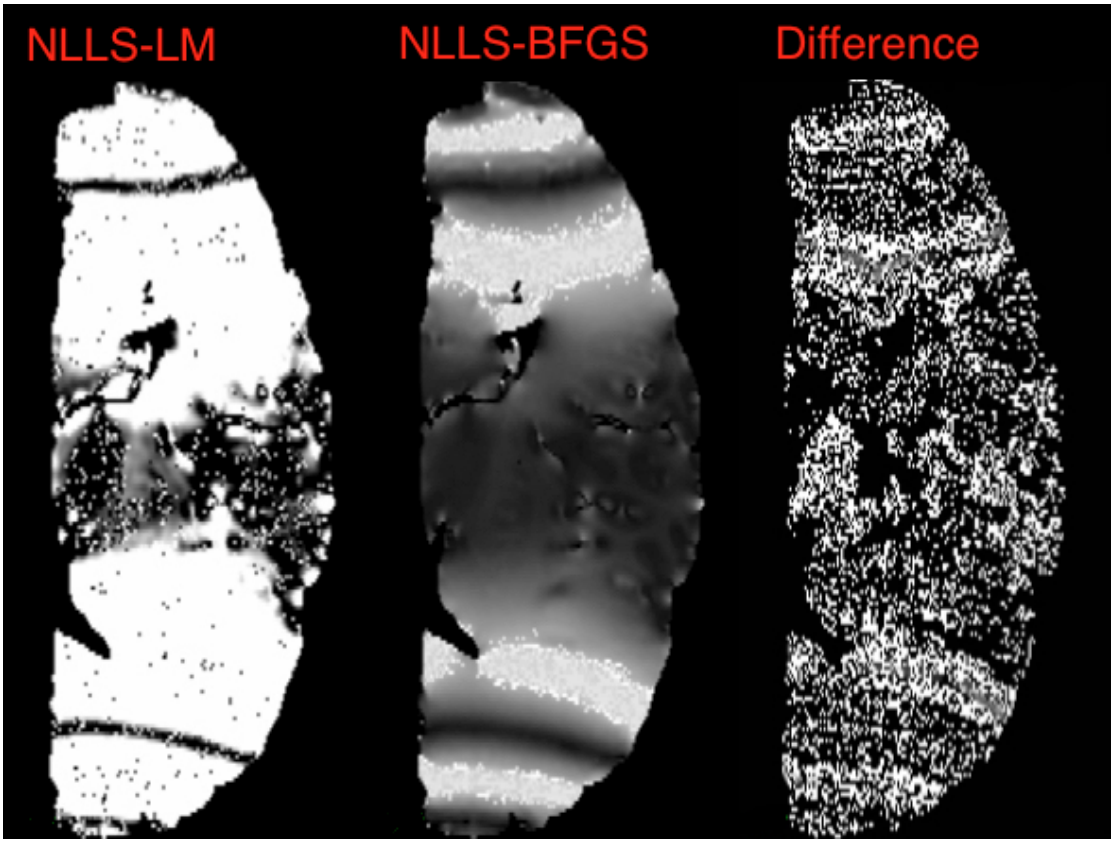

FIGURE 77: OFF-RESONANCE FREQUENCY MAPS PRODUCED BY THE LM (LEFT) AND BFGS (RIGHT) ALGORITHM AND A 0/180 RF PHASE CYCLING SCHEME. THE OFF-RESONANCE MAPS ARE SCALED BETWEEN 0 AND 2π

A good off-resonance frequency f0 map would show little variation of off-resonance across the image. In these f0 images we see banding or what appears to be wrapping. This can be explained by referring to the original paper by Deoni et al.[22], in which they say "due to the periodic and repeating nature of $\sin(\theta_{RF} + \omega TR)$ and $\cos(\theta_{RF} + \omega TR)$, i.e. $\sin(0) = \sin(2\pi)$ and $\cos(0) = \cos(2\pi)$, ωTR need only be investigated between the limits of 0 and 2π. As we are not concerned with finding the exact absolute value of ωTR, but only its relative value, we choose the minimum of the ωTR estimates". This can be seen within the off-resonance map produced by the BFGS algorithm where the map has wrapped between 0 and 2π. The LM algorithm shows uniform sections outside of the central area and noise in the central area. This in contrast to the BFGS algorithm, with more uniform values in the central area.

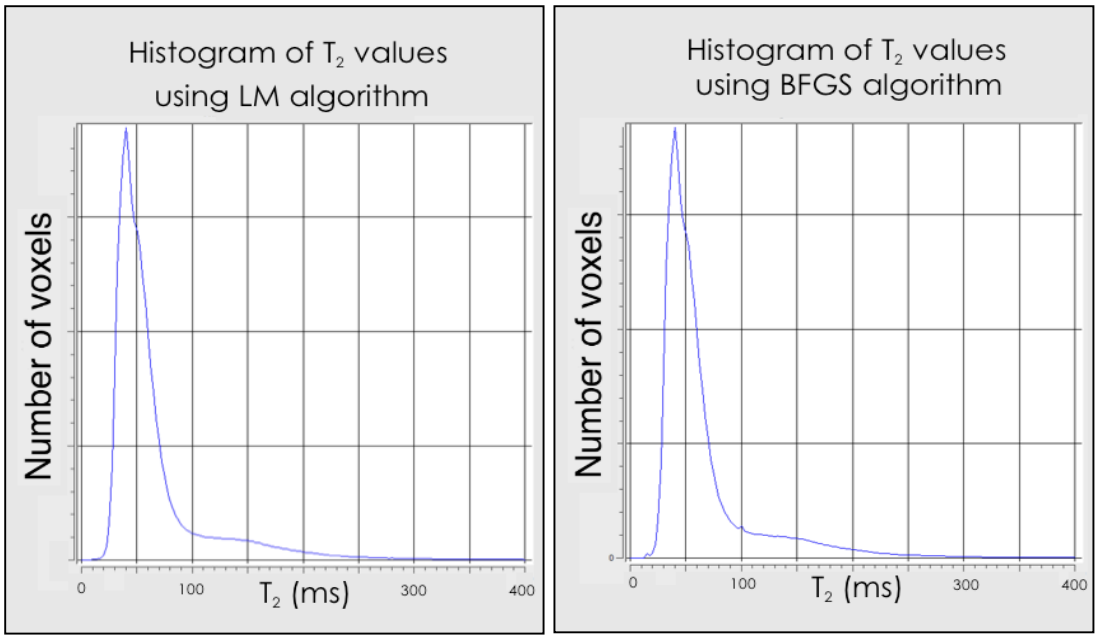

FIGURE 78: HISTOGRAMS OF THE T_2 VALUES IN THE T_2 MAPS PRODUCED FROM THE LM (LEFT) AND BFGS (RIGHT) ALGORITHMS WITH THE 0/180 PHASE CYCLING SCHEME

The histograms for the T_2 maps are shown above in figure 78. While the T_2 maps have differences and the f0 maps are very definitely different, the actual values produced by the two different algorithms are very similar. The median value for both maps is 40ms and the median of the difference values is 0.00016. The actual time of reconstruction for the BFGS algorithm was 10111 seconds and the LM algorithm was 2263 seconds, a difference of 4.5 times more processing time for BFGS.

A RF phase cycling scheme of 0°, 90°, 180° and 270° was reconstructed using the same hemisphere.

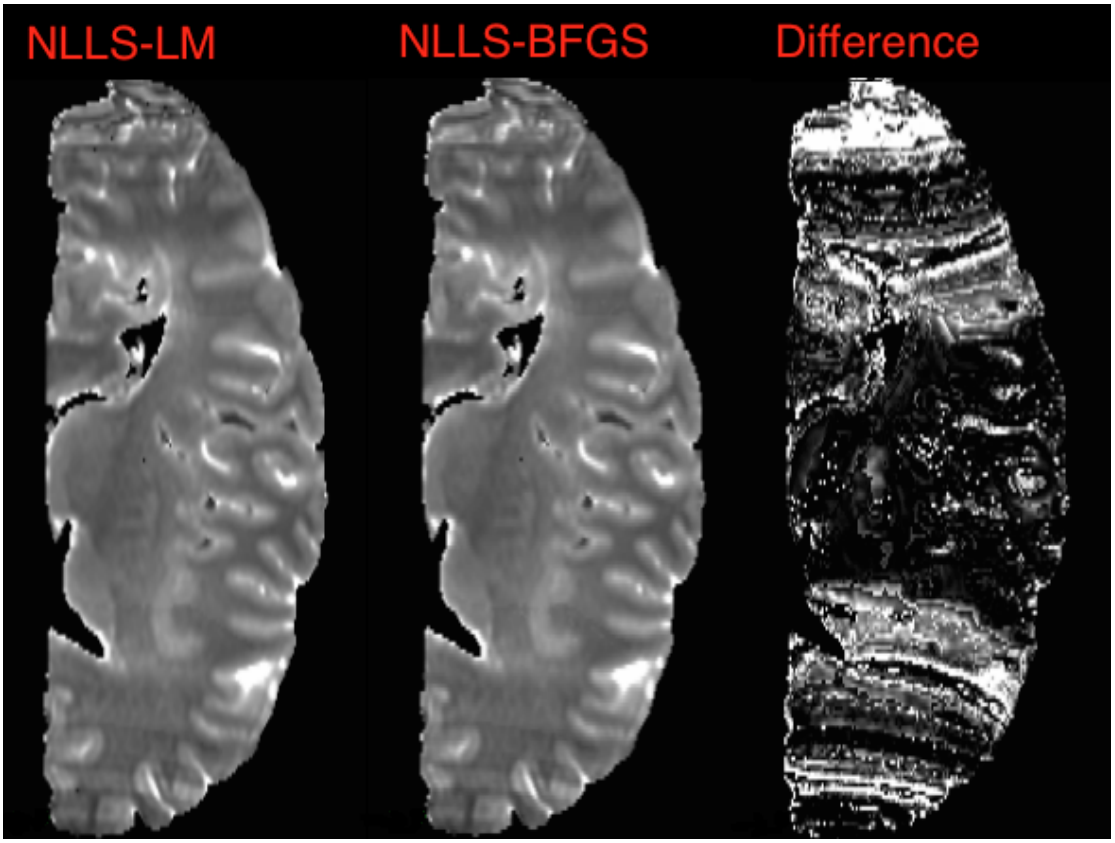

FIGURE 79: T_2 MAPS CALCULATED BY THE LM ALGORITHM (LEFT) AND THE BFGS ALGORITHM (MIDDLE) USING THE NLLS PRODUCED T_1 MAP AND A PHASE CYCLING SCHEME OF 0/90/180/270 WITH A DIFFERENCE IMAGE (RIGHT). THE T1 MAPS ARE DISPLAYED BETWEEN 0 AND 200MS

The T_2 maps still retain some residual banding artefacts but using this RF scheme is obviously more successful than the two-phase scheme for removing the banding. Although the two maps from the algorithm look equivalent, the difference image shows that in the areas where banding is problematic, at the top and bottom of the image, there are differences. These can be considered negligible though, as the median of the difference map values is 0.0001ms.

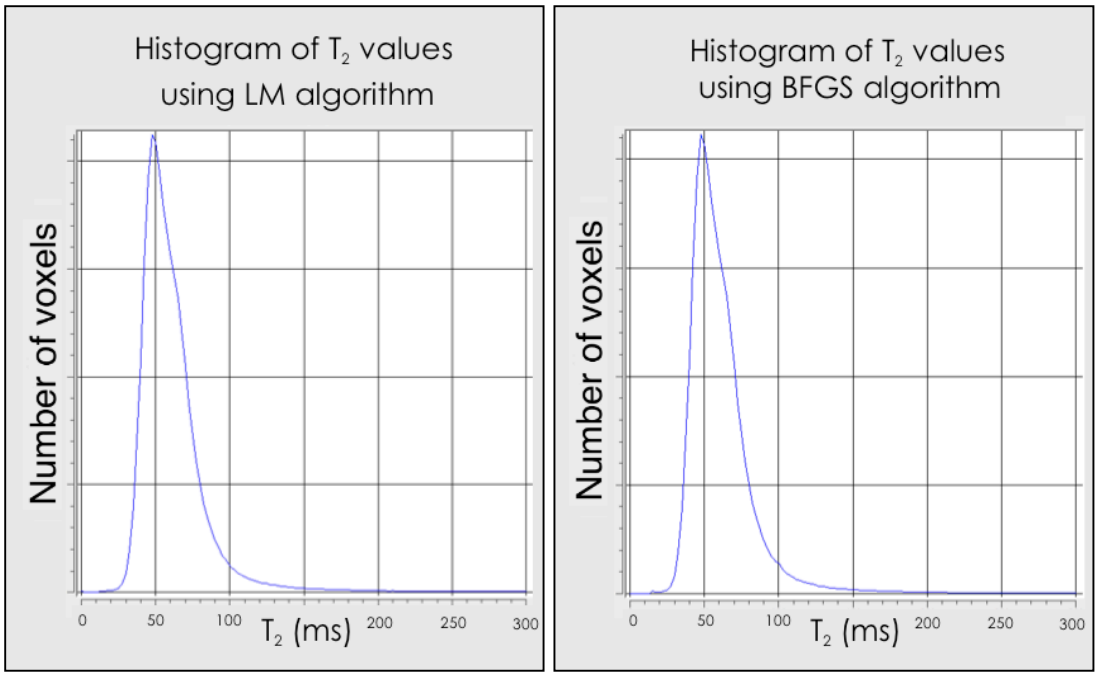

FIGURE 80: HISTOGRAMS OF THE T_2 VALUES IN THE T_2 MAPS PRODUCED FROM THE LM (LEFT) AND BFGS (RIGHT) ALGORITHMS WITH THE 0/90/180/270 PHASE CYCLING SCHEME

The histograms for the T_2 values in the T_2 maps for the 0/90/180/270 phase cycling scheme are shown above. The histograms are very similar with the median value for each 47.5ms. The reconstruction time for the LM algorithm was 6030 seconds and the BFGS algorithm was 35887 seconds, approximately six times the reconstruction time.

The off-resonance frequency maps f0 are shown below in figure 81 for each algorithm. With the full 0/90/180/270 phase cycling scheme, the off-resonance is fitted between -2π and 2π.

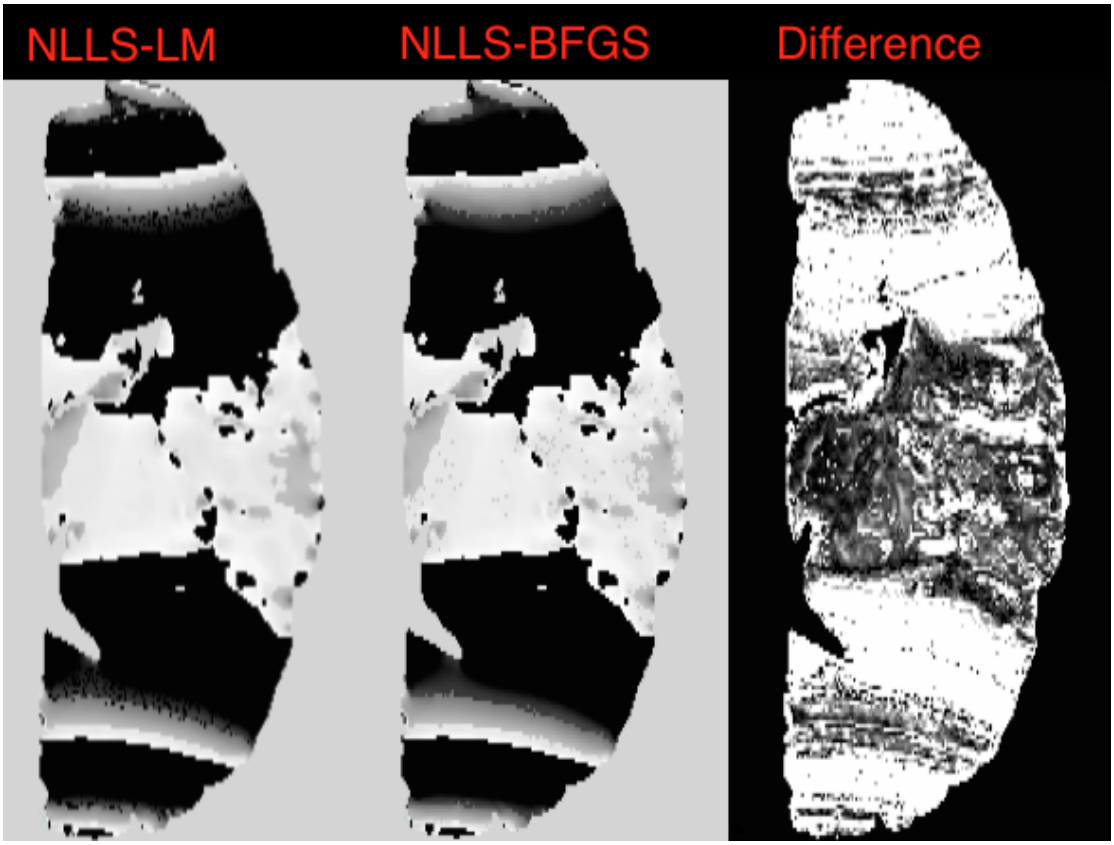

FIGURE 81: OFF-RESONANCE FREQUENCY MAPS F0 PRODUCED BY THE LM (LEFT) AND BFGS (RIGHT) ALGORITHM AND A 0/90/180/270 RF PHASE CYCLING SCHEME. . THE OFF-RESONANCE MAPS ARE SCALED BETWEEN 0 AND 2π

With this RF phase scheme the f0 maps are similar, the wrapping artefact is shown in Figure 82 below.

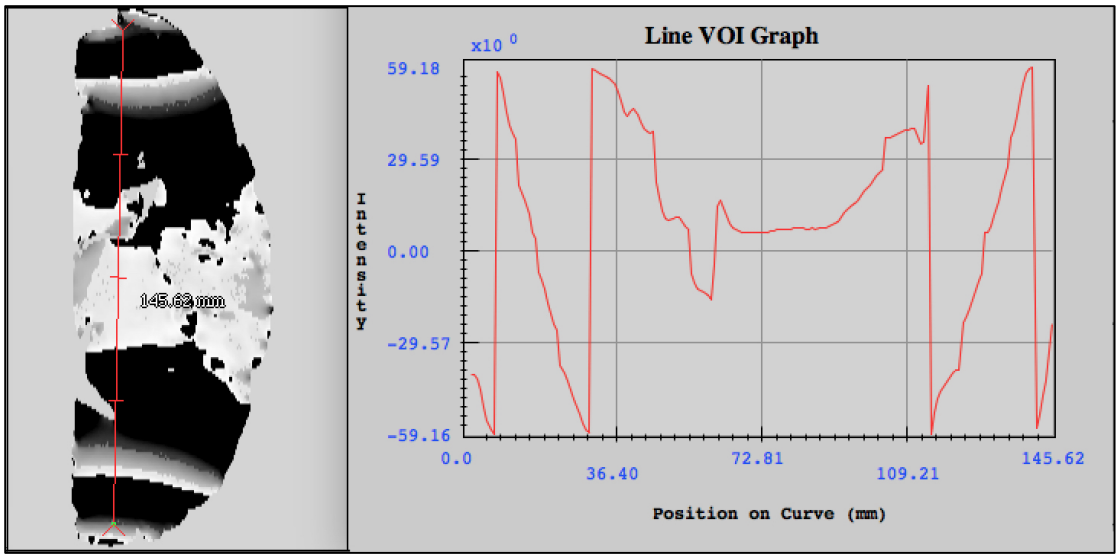

FIGURE 82: OFF-RESONANCE FREQUENCY LINE GRAPH SHOWING FREQUENCY (HZ) WRAP AND A Z^2 SHAPE DUE TO B_0 INHOMOGENEITY

The line graph shows a Z^2 shape, looking at this we can make inferences about the B_0 field as B_0 field inhomogeneities cause higher phase precession. The B_0 field has a small homogeneous area in the centre with higher inhomogeneity at either end. This would correspond with the position of the hemisphere in the head coil, with the ends of the hemisphere positioned at either end of the coil.

The different algorithms have some failures to evaluate the f0 value in some pixels in different areas depending on the algorithm. This is demonstrated by the figure below.

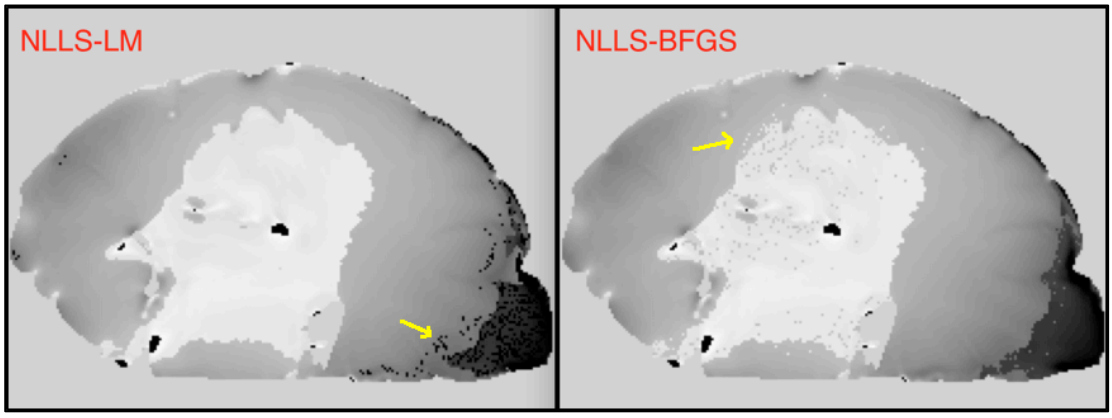

FIGURE 83: ON THE LEFT THE LM ALGORITHM WHERE ON THE RIGHT SIDE OF THE IMAGES THERE ARE FAILURES IN THE FITTING IN THE DARKER AREA WHERE PIXELS SWITCH FROM MINUS TO PLUS VALUES, RESULTING IN LARGE DIFFERENCES IN OFF-RESONANCE FREQUENCY VALUES. ON THE RIGHT THE BFGS ALGORITHM WHERE IN THE CENTRE LIGHT AREA, THE VALUES AGAIN SWITCH FROM MINUS TO PLUS VALUES THOUGH NOT SUCH LARGE DIFFERENCE VALUES

7.2.4 DISCUSSION

The T_2 values from both algorithms are comparable from both algorithms using both RF phase cycling schemes. To make a decision between the algorithms when using a 0/180°, the f0 maps from the algorithms were examined. The BFGS algorithm shows similar smooth f0 values in the central region, whereas the LM algorithm has failed to fit the off-resonance correctly. However, T_2 maps with banding are not useful so the two-phase cycle scheme is not recommended in this situation. The 4 phase RF cycling scheme gives non-banded T_2 images, the f0 are as expected with large B_0 homogeneity found in a large sample in a clinical scanner. There does not seem to be any significant difference in the

two algorithms with the four-phase cycling scheme, therefore if time constraints were an issue, the 2-step LM algorithm could be used as it has a shorter reconstruction time.

7.3 COMPARISON OF DESPOT2 WITH SINGLE COMPONENT T2 MAP ACQUISITION

A comparison was made with the single component T_2 map and the DESPOT2 T_2 NLLS-LM map. These methods are similar as they are both fit equations for a single T_2 value. However, it should be noted that both maps are not optimum. It is known that the T_2 curve is multi-exponential, indeed 32 echo train length CPMG acquisitions are used for short T_2 myelin water imaging, which decomposes the curve into components corresponding to myelin water and intra/extra cellular water as described in section 4.4.

The DESPOT2 acquisition contains an amount of banding that made visual matching of the slices difficult between it and the single exponent T_2 map. The best matched slice is shown below. There was also some slight difference in plane between the two acquisitions.

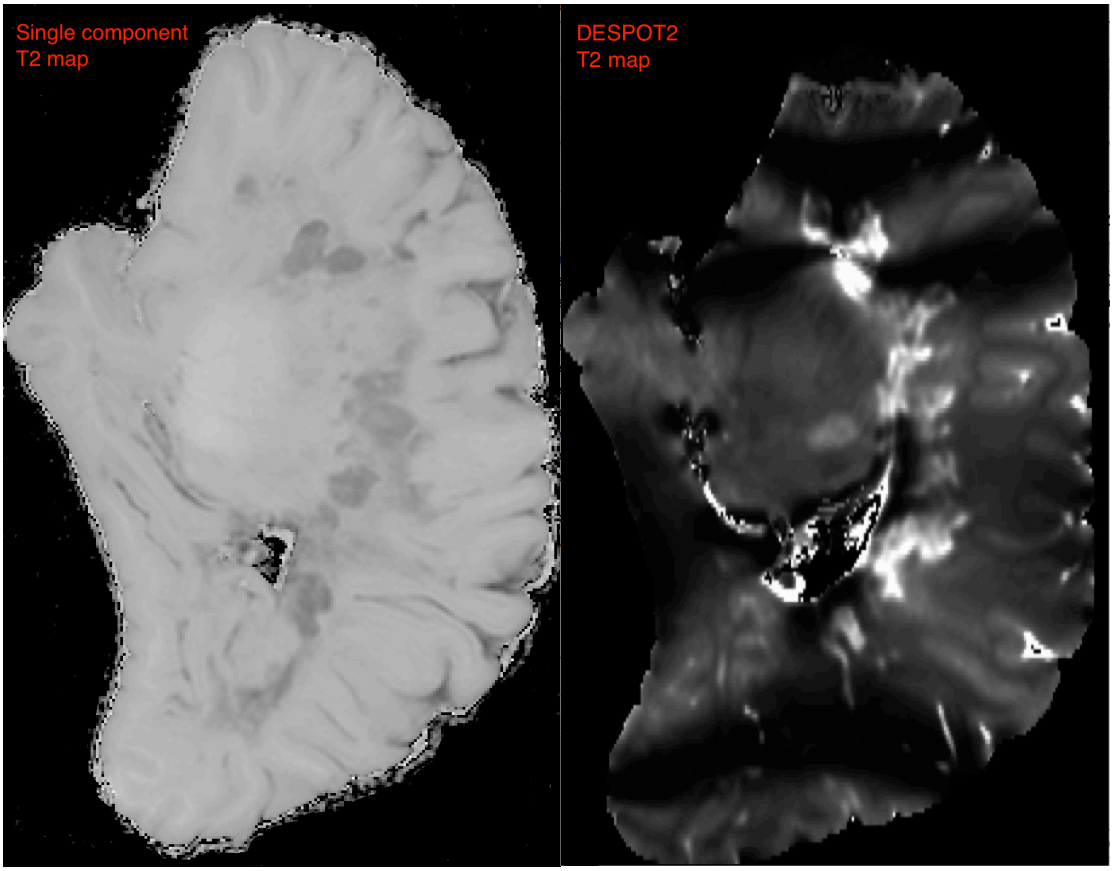

FIGURE 84: SINGLE COMPONENT T2 MAP (LEFT) AND DESPOT2 T2 MAP FROM MS436R. THE T1 MAPS ARE DISPLAYED BETWEEN 0 AND 200MS

The histogram of T_2 values from the single exponential T_2 map and those from the DESPOT2 algorithm are shown below in figure 85.

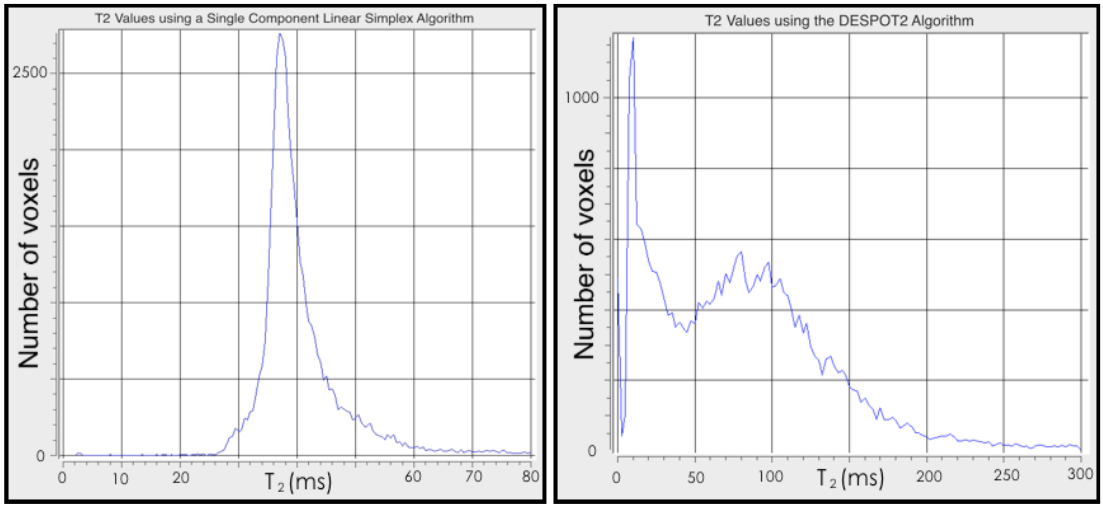

FIGURE 85: T2 VALUES FROM THE SINGLE EXPONENTIAL (LEFT) AND DESPOT2 ALGORITHM (RIGHT)

The values in the T_2 map from the DESPOT2 algorithm show a higher variance than those from the single exponential calculation and also from the DESPOT2 MS442L T_2 maps shown in section 7.2 above. The median value in the histogram from MS436R is 10 ms, there is also a second peak at 80 ms.

With the amount of severe lesional tissue seen in the hemisphere, as well as the diffuse white matter damage, it is likely there should be a higher range of T_2 values in this hemisphere. The narrow peak seen in the single exponential T2 map seems less likely with little differentiation between white and grey matter. The banding however affects the DESPOT2 map severely even with the full phase cycling.

7.4 DESPOT2 IN THE POST-MORTEM SPINAL CORD

7.4.1 WORK ON A 3T CLINICAL SCANNER

7.4.1.1 Methods

Acquired immediately after the DESPOT1 acquisition and using the same B_1 map, the same spinal cords were scanned using a DESPOT2 protocol on the Philips 3T Achieva scanner using a 15 element SENSE Spine coil (see section 5.5).

Regions of interest in the spinal cords on the DESPOT2 T2 maps were drawn using MIPAV (http://mipav.cit.nih.gov/). Regions were only drawn where the observer could be definite that only that tissue type (e.g. WM or GM) were present.

7.4.1.2 Results

A magnitude image and the corresponding slice from the T_2 map are shown below. The T_2 values in each section of spinal cord change dependent on spinal cord not location.

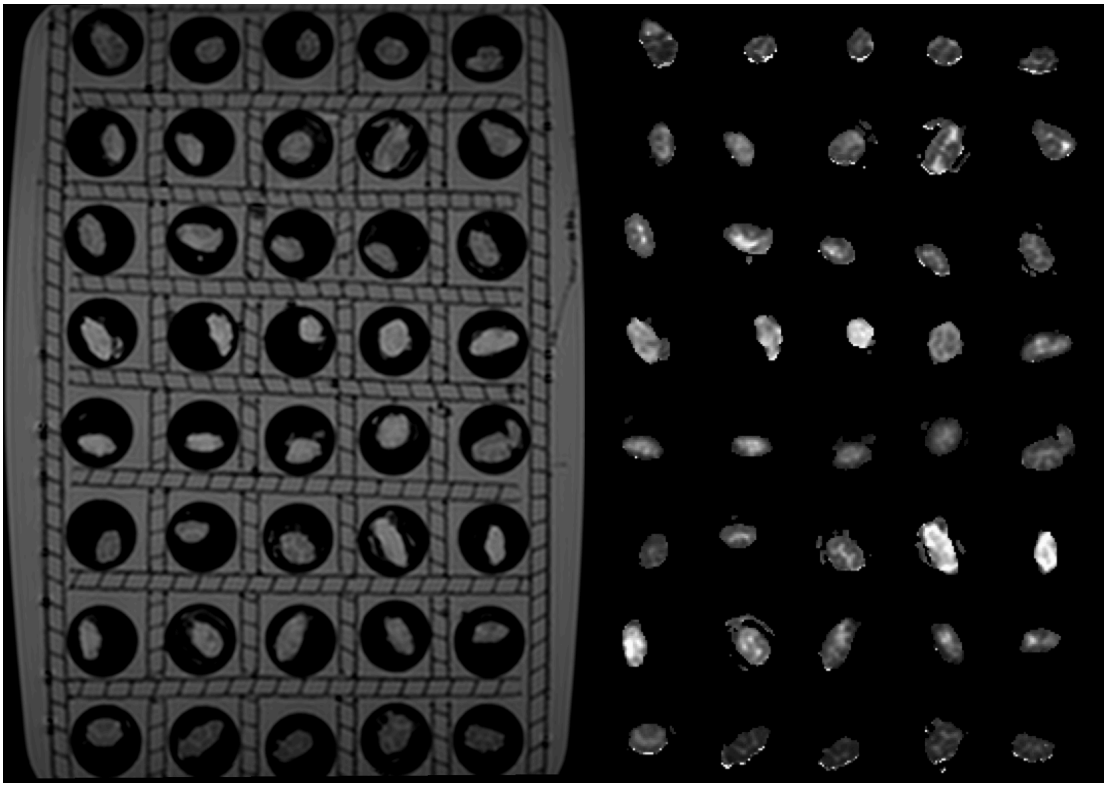

FIGURE 86: MAGNITUDE IMAGE (LEFT) FROM THE SPGR IMAGE (FA 3) SHOWN WITH THE CORRESPONDING SLICE FROM THE T2 MAPS FROM DESPOT2 (RIGHT). T2 MAPS ARE SCALED BETWEEN 0 AND 150MS

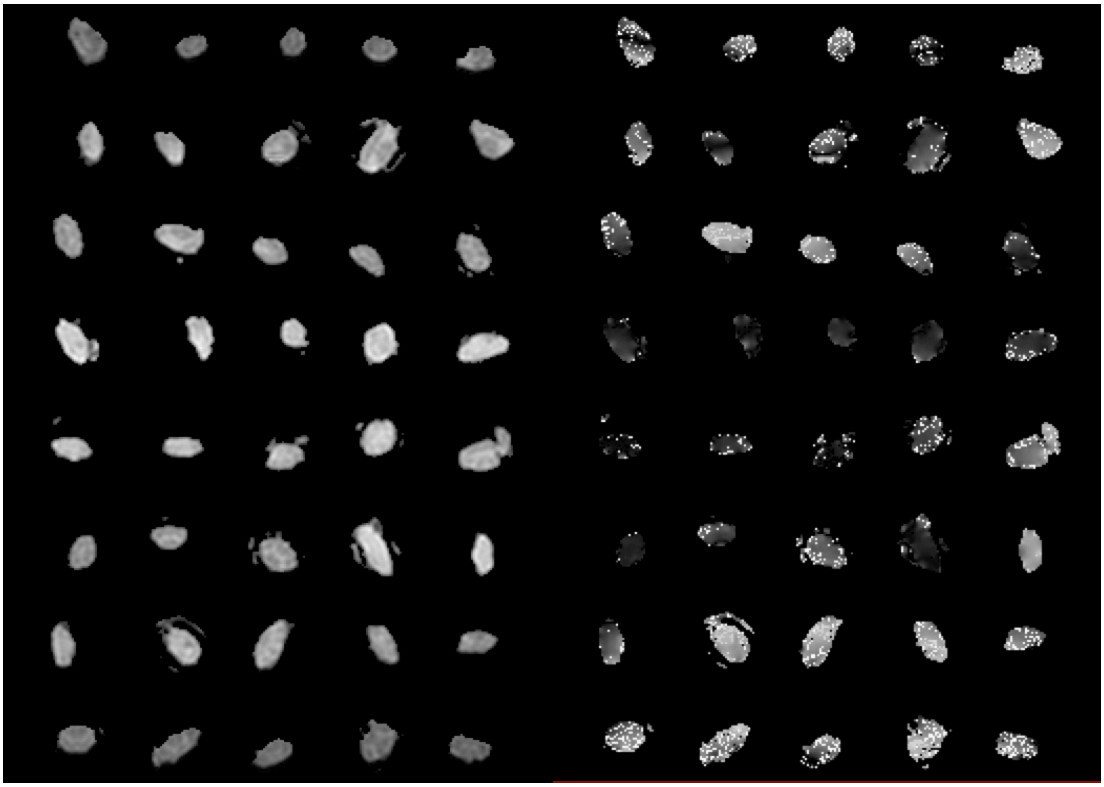

FIGURE 87: PD MAPS (LEFT) FOR THE SLICE SHOWN ABOVE, GENERATED BY THE DESPOT2

CODE AND THE CORRESPONDING OFF-RESONANCE F0 MAP (LEFT). OFF-RESONANCE MAPS ARE SCALED BETWEEN 0 AND 2π

The image above shows spinal cord sections acquired after removing all of the bSSFP images that showed movement in the bands even after using the 'sameprep' patch. This left only 7 flip angles in the calculation (7, 14, 21, 28, 35, 42, and 49). However, the DESPOT2 calculation is successful, example sections are shown below with corresponding magnitude images.

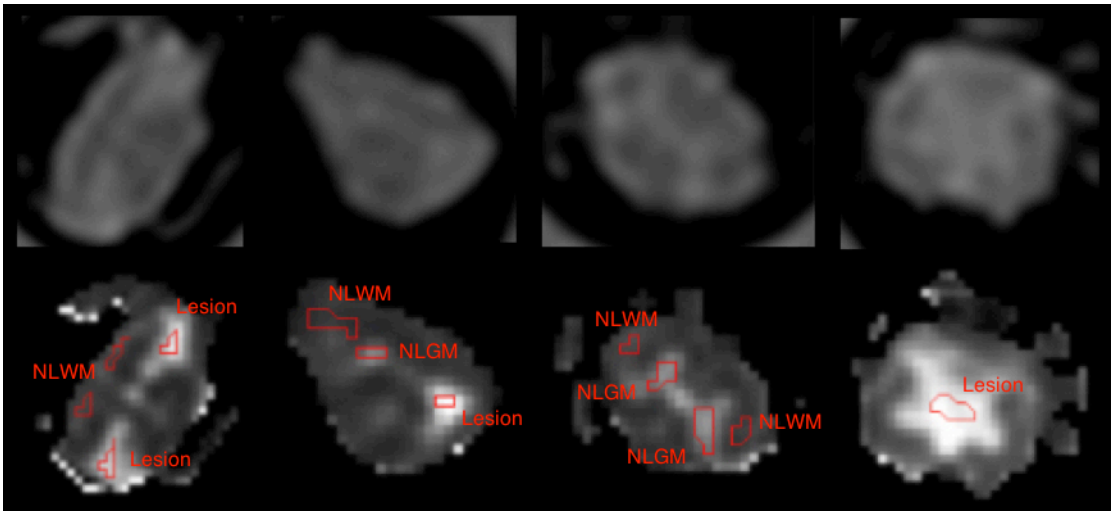

FIGURE 88: SECTIONS FROM THE ACQUISITION SHOWN ABOVE WITH EXAMPLE ROIS IN THE T_2 MAP. MAGNITUDE IMAGES ARE SHOWN ABOVE AND T_2 MAPS BELOW. T2 MAPS ARE SCALED BETWEEN 0 AND 150MS

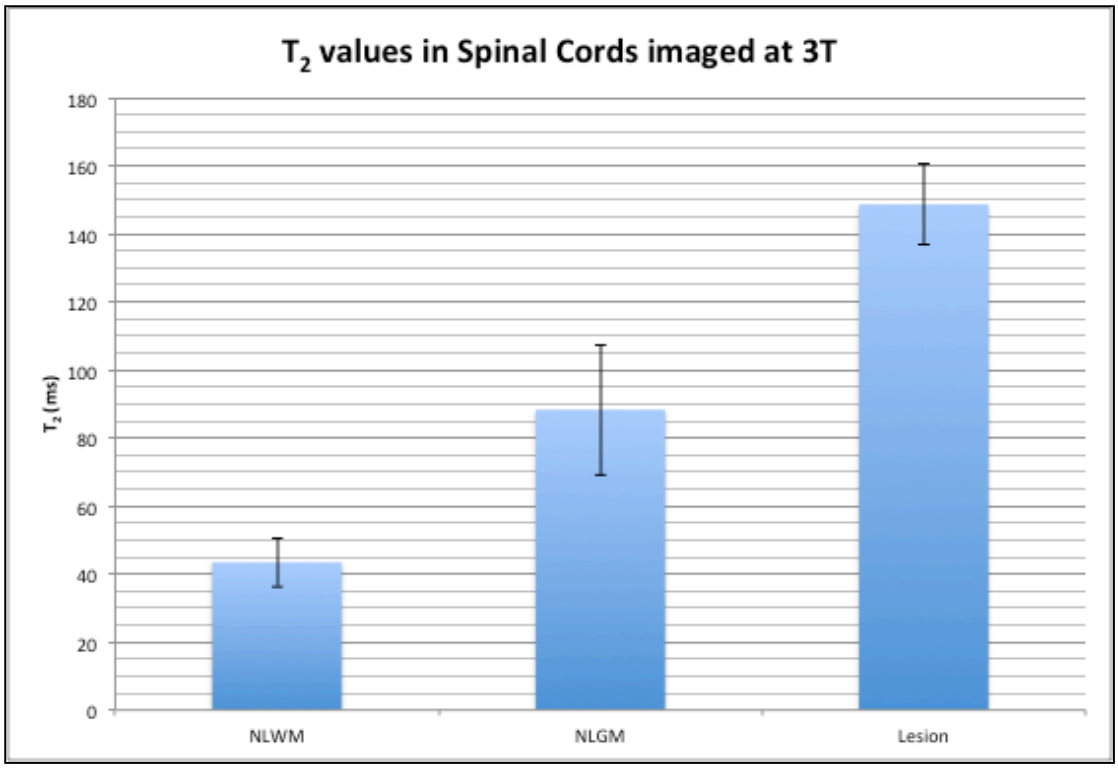

FIGURE 89: AVERAGE T2 VALUES IN THE NLWM, NLGM AND LESIONAL AREAS. ERROR BARS ARE THE STANDARD DEVIATION.

The resolution of these scans at 3T is not sufficient to confidently identify and separate lesional grey and white matter. It is in fact difficult to identify pixels that can be confidently identified as white and grey matter without partial volume effects, and so these were combined.

7.4.1.3 Discussion

T_2 maps using the DESPOT2 algorithm have been acquired with the use of a software patch supplied by Philips. This patch was not completely successful in preventing the movement of the off-resonance banding artefact, which is likely due to variation of the RF pulse duration at high flip angles.

The T_2 values found in the DESPOT2 maps show good separation between T_2 values in non-lesional WM, non-lesional GM and lesion. However, this may have been prejudiced by the decision to only draw ROIs in areas where the observer could be definite about tissue type, which would occur in a high contrast situation. Other cord sections shown in Figure 86 show little contrast, and are difficult to segment into tissue type even when using the PD maps for reference.

These cords may show severe diffuse WM damage, leaving little difference in myelination, which would be best confirmed by histology.

7.4.2 WORK ON A 7T PRECLINICAL SCANNER

This work was performed during the same acquisition as the DESPOT1 work in section 6.8.2.

7.4.2.1 Methods

The acquisitions performed on the 3T clinical scanner at St Bartholomew's Hospital Philips Achieva 3T scanner, were used to identify nine areas of interest on PD-weighted images. These areas were then scanned using a 7T pre-clinical scanner (Agilent Technologies DDR) and standard quadrature RF coil (Rapid GmbH) with a field of view of 5cm by Dr Tobias Wood at King's College London. bSSFP (with 2 RF phase-cycles) scans were acquired with parameters given in Table 16, along with an AFI scan for B_1 correction[28]. The images were resampled at 150x150x300μm^3 for improved SNR. T_2 and PD maps were processed from all flip-angles.

Sequence	TE/TR (ms)	Flip-Angles	Voxel Size (μm^3)	Matrix Size
bSSFP	2/4	14,17,20,25,35,50,65	100x125x200	160x160x160
AFI	2.62/7.5	55	250x250x500	64x64x64

TABLE 18: SEQUENCE PARAMETERS USED FOR ACQUISITION AND PROCESSING WITH THE 7T AGILENT SCANNER

7.4.2.2 Results

The results were processed by Dr. Wood using the same program described above in section 6.8.2 and the results are shown below.

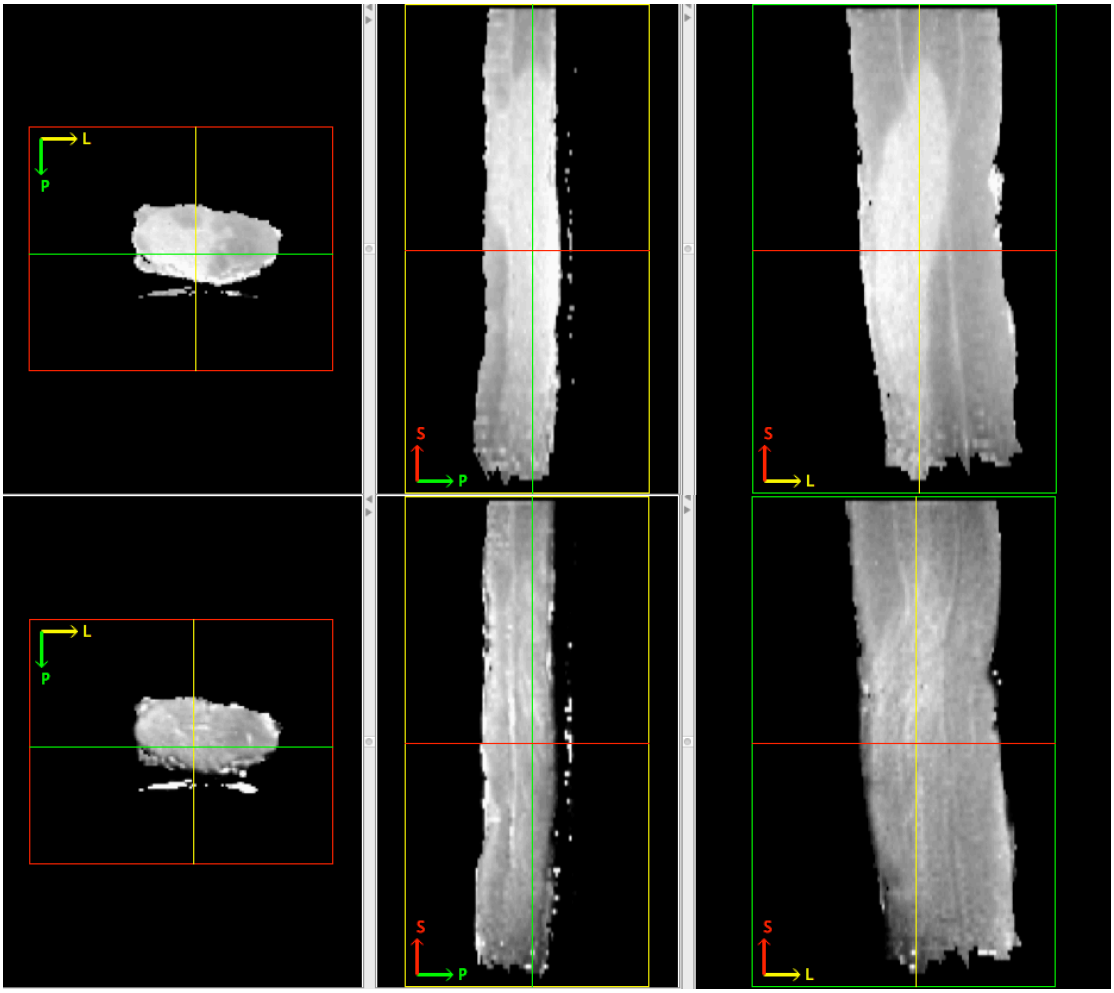

FIGURE 90: PD MAP (TOP) AND T2 MAP (BOTTOM) OF LESION A IN THE MS471 SPINAL CORD

The histogram of and PD and T_2 values is shown is Figure 91 below

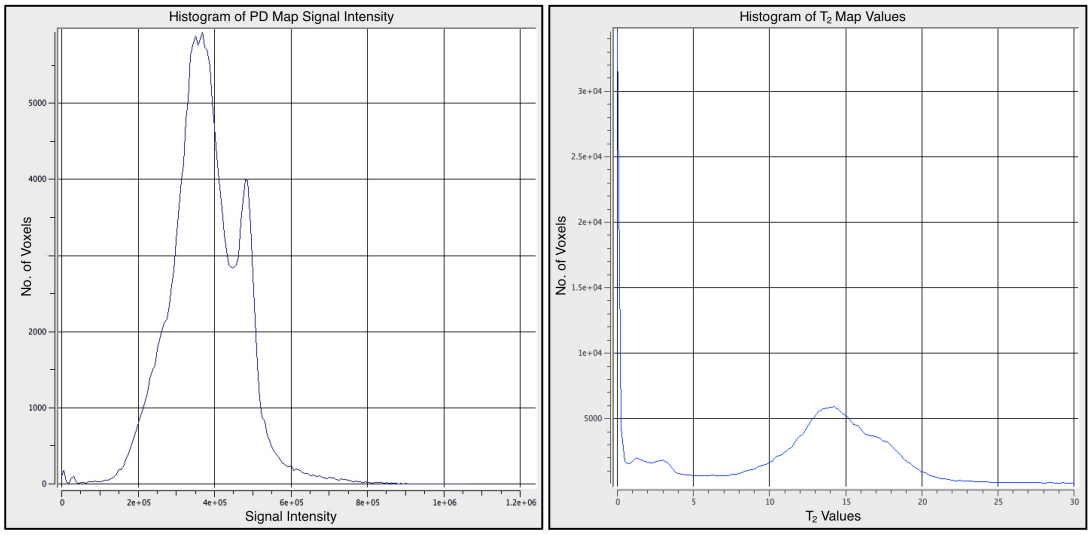

FIGURE 91: HISTOGRAMS OF PD MAP (LEFT) AND T2 MAP VALUES (RIGHT)

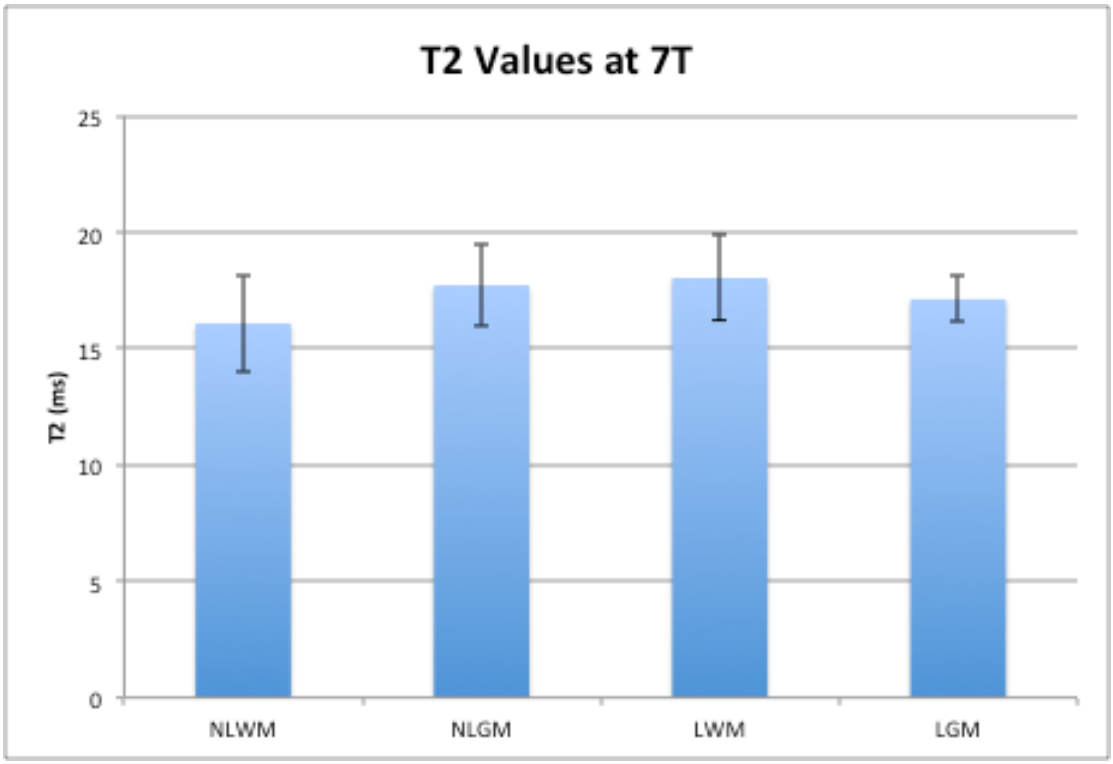

FIGURE 92: GRAPH OF T2 VALUES FOUND USING THE 7T PRECLINICAL SCANNER IN NON-LESIONAL WHITE MATTER, NON-LESIONAL GREY MATTER AND LESIONAL WHITE AND GREY MATTER. THE ERROR BARS SHOW THE STANDARD DEVIATION

7.4.2.3 Discussion

On examining the T_2 maps there is very little contrast between the white, grey and lesional areas even though the situation is the ideal experimental setup with higher field strength, small bore and small imaging volume where it is possible to achieve a good shim volume.

7.5 WORK ON A 7T WHOLEBODY SCANNER

7.5.1 METHODS

As described before in section 6.11, the right hemisphere of MS442R was imaged on the Philips 7T scanner at Nottingham University. The scan parameters were as shown in the table below to match those acquired on the Agilent scanner in section 7.4.2.

TE (ms)	TR (ms)	bSSFP FA
4.4	9	7, 10, 14, 17, 20, 25, 35 and 50

TABLE 19: SEQUENCE PARAMETERS USED FOR ACQUISITION AND PROCESSING WITH THE 7T WHOLEBODY SCANNER

Due to the size and shape of the head coil which is designed for brain imaging and gives better images at the top of the coil, there was signal drop off at one end of the coil. Curve fitting failed in this area due to the low signal.

7.5.2 RESULTS

The magnitude images from each phase increment at a flip angle of 20 degrees are shown below.

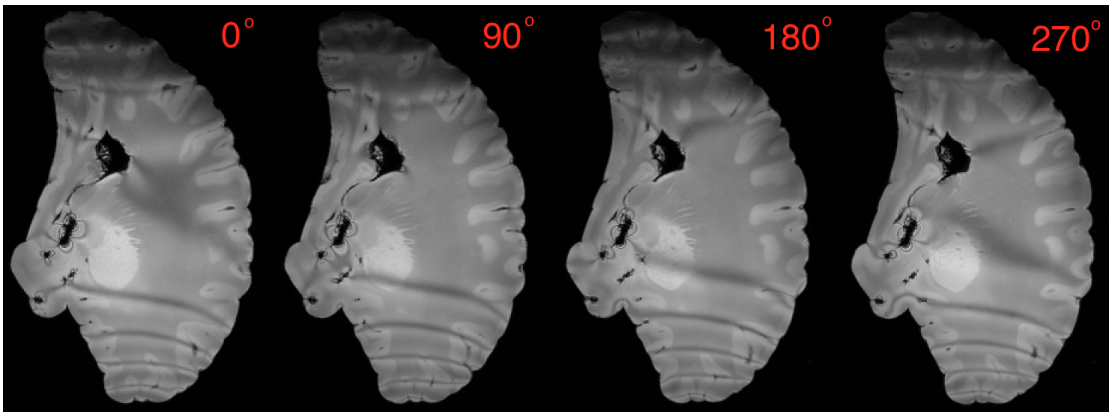

FIGURE 93: A DESPOT2 DATASET FROM MS422R SHOWED CORRESPONDING IMAGES FROM 0, 90, 180 AND 270 RF PHASE CYCLING ACQUISITIONS AT 20°. THE 0 DEGREE ACQUISITION SHOULD HAVE SUPPRESSED SIGNAL ACROSS THE HEMISPHERE BUT AS THE RF PULSE IS NOT IDEAL, ESPECIALLY PROBLEMATIC AT HIGH FIELD STRENGTHS, THERE IS ONLY A SMALL SECTION IN THE CENTRE OF THE HEMISPHERE.

Again, the standard RF cycling method of 0° and 180° was used initially for reconstruction of T_2 maps.

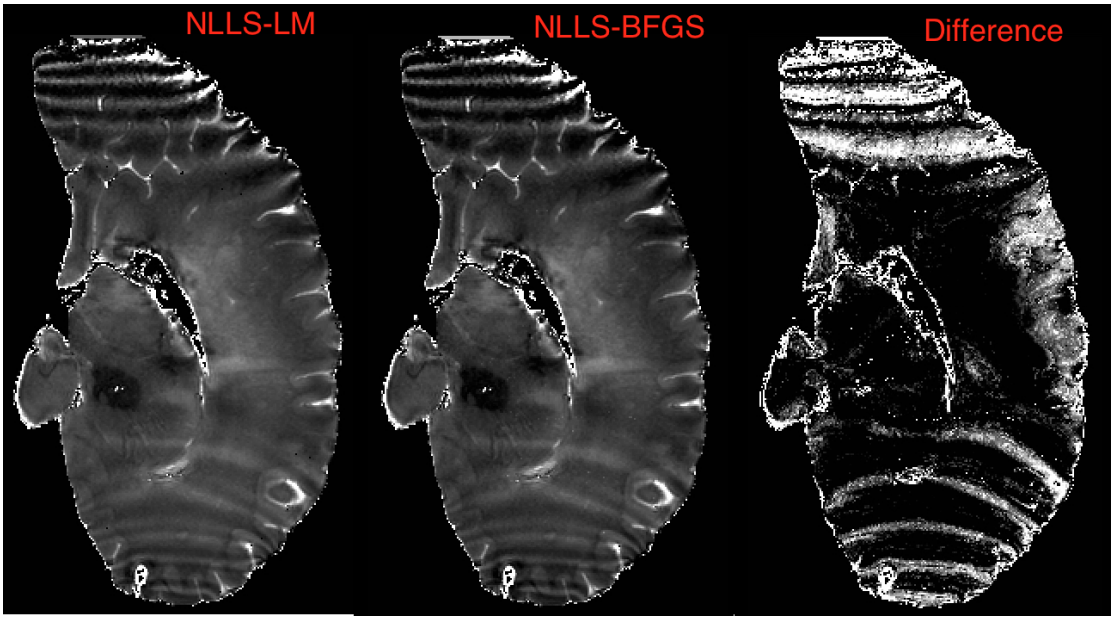

FIGURE 94: MAPS OF T_2 VALUES CALCULATED BY THE LM ALGORITHM (LEFT) AND THE BFGS ALGORITHM (RIGHT) USING THE NLLS PRODUCED T_1 MAP AND A PHASE CYCLING SCHEME OF 0/180. T2 MAPS ARE DISPLAYED BETWEEN 0 AND 100MS.

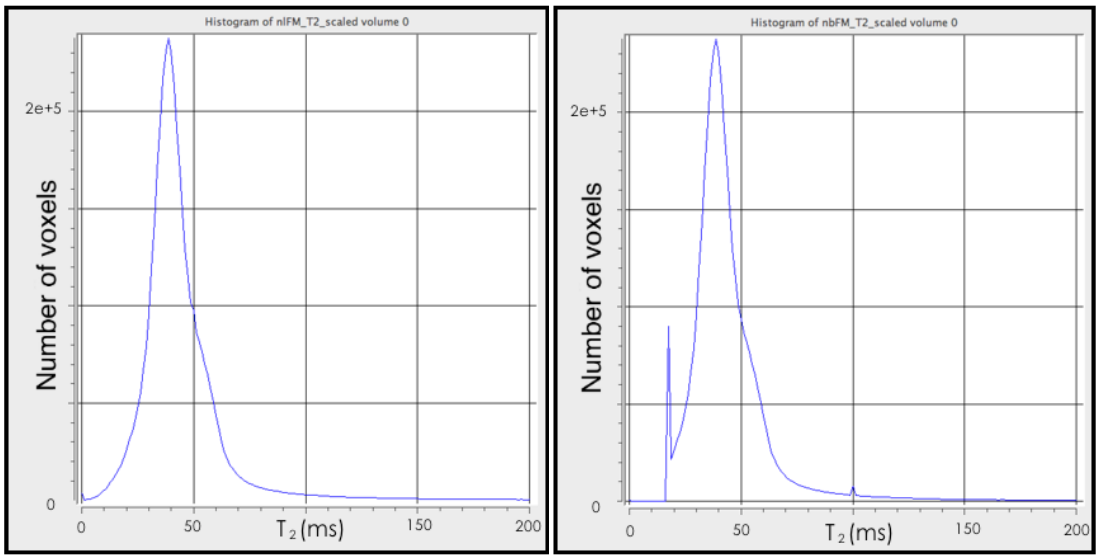

FIGURE 95: HISTOGRAM OF T_2 VALUES CALCULATED BY THE LM ALGORITHM (LEFT) AND THE BFGS ALGORITHM (RIGHT) USING THE NLLS PRODUCED T_1 MAP AND A PHASE CYCLING SCHEME OF 0/180

The median values were identical at 38.75ms for both algorithms, however the BFGS algorithm shows peaks at 17.5 and 100ms. The peak at 17.5ms seems to be as a result of a cut-off value at 16.25, with all values which are found below this value in the LM algorithm placed at a false value just after this cut-off. The BFGS algorithm is also shows greater banding than the LM algorithm, which can

be seen in the difference image. The median value of the difference histogram is 0.001, indicating little difference between the values except these peaks.

The same hemisphere was then processed using the full phase cycle scheme of 0°, 90°, 180° and 270°.

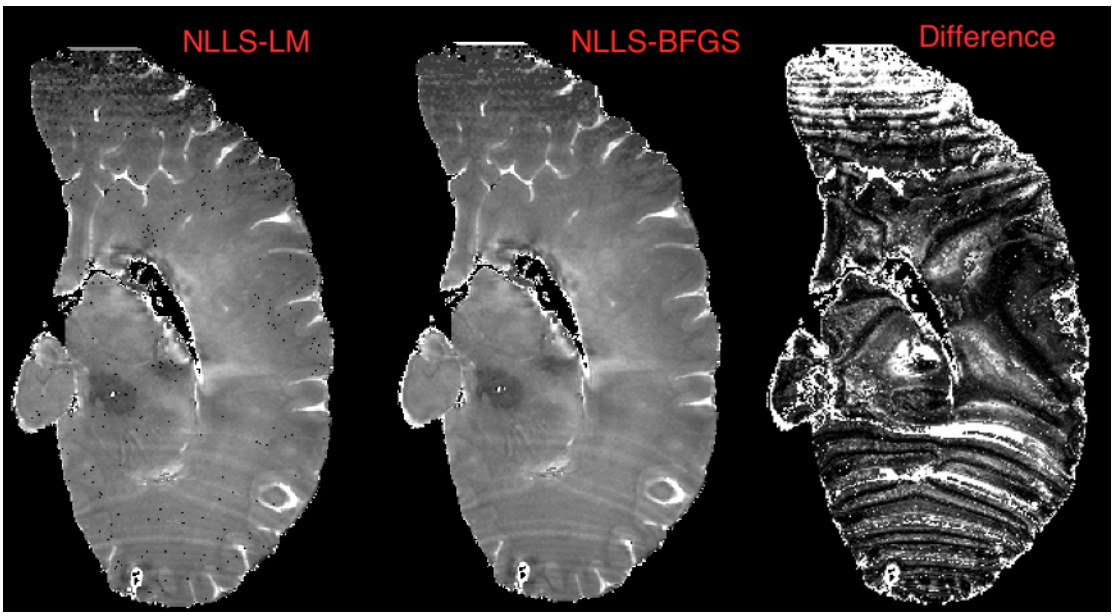

FIGURE 96: MAPS OF T_2 VALUES CALCULATED BY THE LM ALGORITHM (LEFT) AND THE BFGS ALGORITHM (RIGHT) USING THE NLLS PRODUCED T_1 MAP AND A PHASE CYCLING SCHEME OF 0/90/180/270. T2 MAPS ARE DISPLAYED BETWEEN 0 AND 100MS.

Again, there is some residual banding left but again the full phase cycling scheme is more successful as removing the banding artefacts.

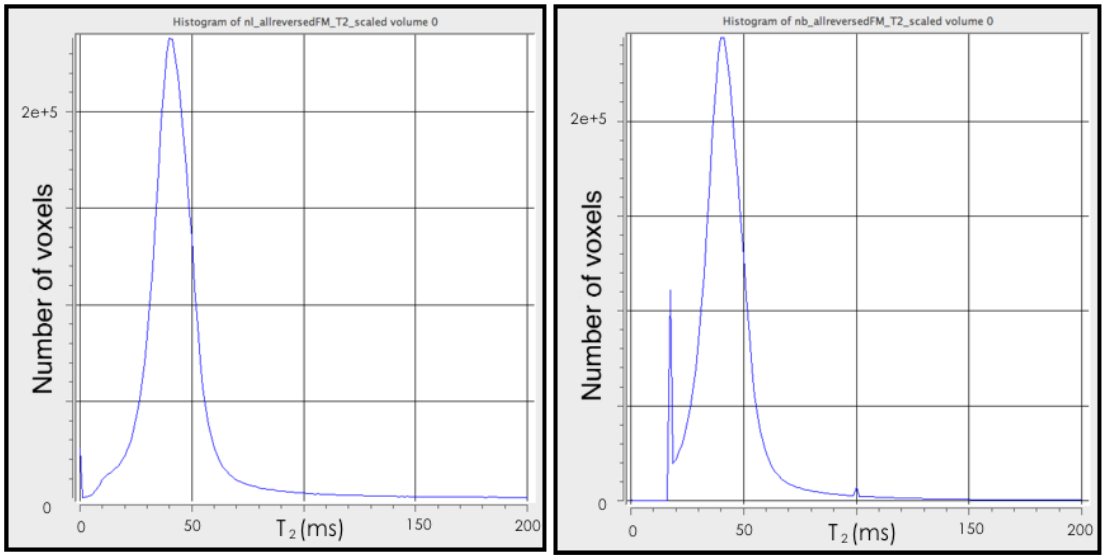

FIGURE 97: HISTOGRAM OF T_2 VALUES CALCULATED BY THE LM ALGORITHM (LEFT) AND

THE BFGS ALGORITHM (RIGHT) USING THE NLLS PRODUCED T_1 MAP AND A PHASE CYCLING SCHEME OF 0/90/180/270

The median value was again identical at 40ms for both algorithms. The BFGS algorithm again shows a cut-off of 16.25 with a peak at 17.5, and a small peak at 100ms. The LM algorithm result has fitting failures across the field of view where the result is zero, as shown in the zoomed areas taken from figure 95 and shown in figure 98 below.

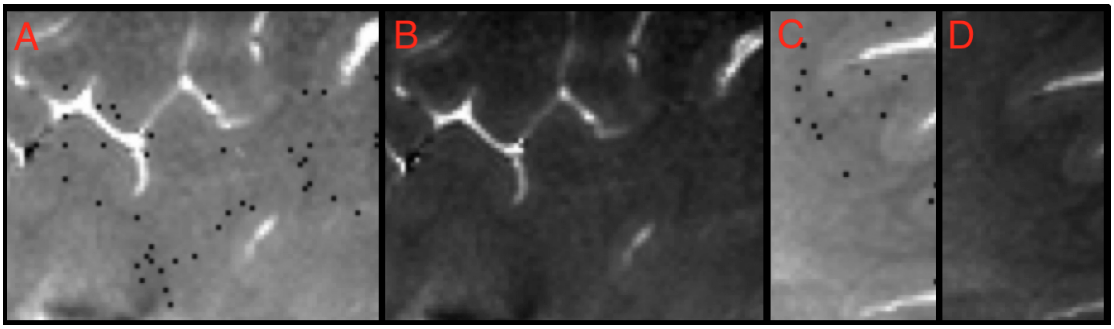

FIGURE 98: CLOSE UPS OF EXAMPLE AREAS FROM THE T_2 MAPS SHOWN IN FIGURE 95 WHERE FITTING FAILURES HAVE OCCURRED. A AND C ARE FROM THE LM ALGORITHM AND B AND D ARE FROM BFGS ALGORITHM

The off-resonance frequency images for both algorithms are shown below. The same fitting failures are visible in the f0 map for the LM algorithm.

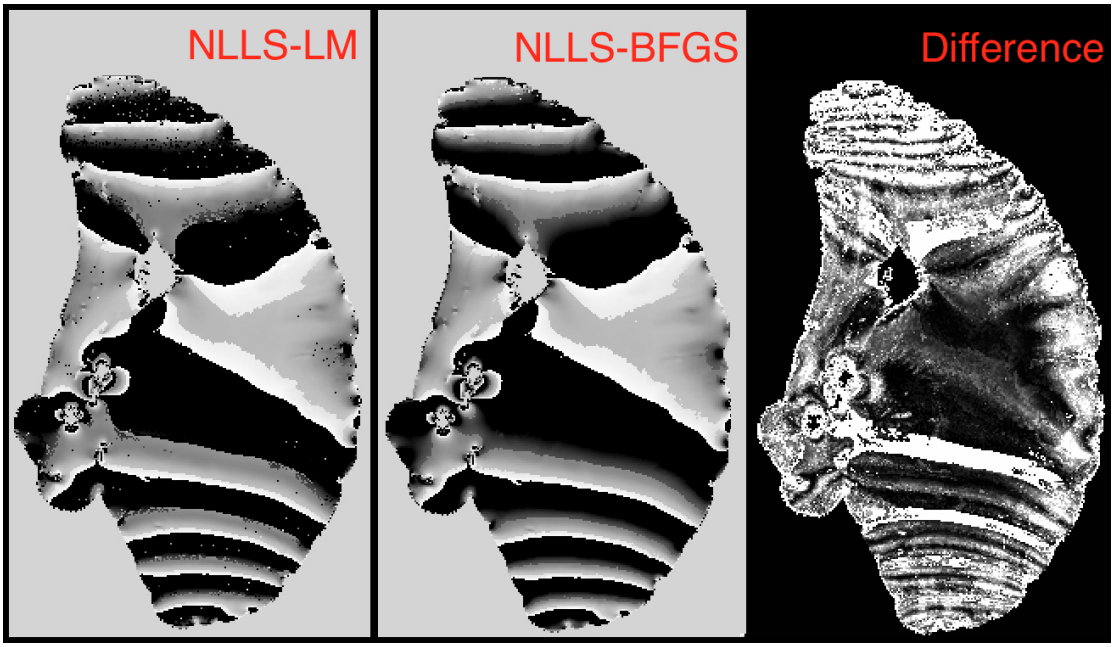

FIGURE 99: MAPS OF OFF-RESONANCE FREQUENCY F0 PRODUCED BY THE LM (LEFT) AND BFGS (RIGHT) ALGORITHM AND A 0/90/180/270 RF PHASE CYCLING SCHEME.

Both algorithms show multiple f0 bands especially at the ends of the hemisphere. This is reflected in increased banding in the images in comparison to the 3T images in section 7.4.1.

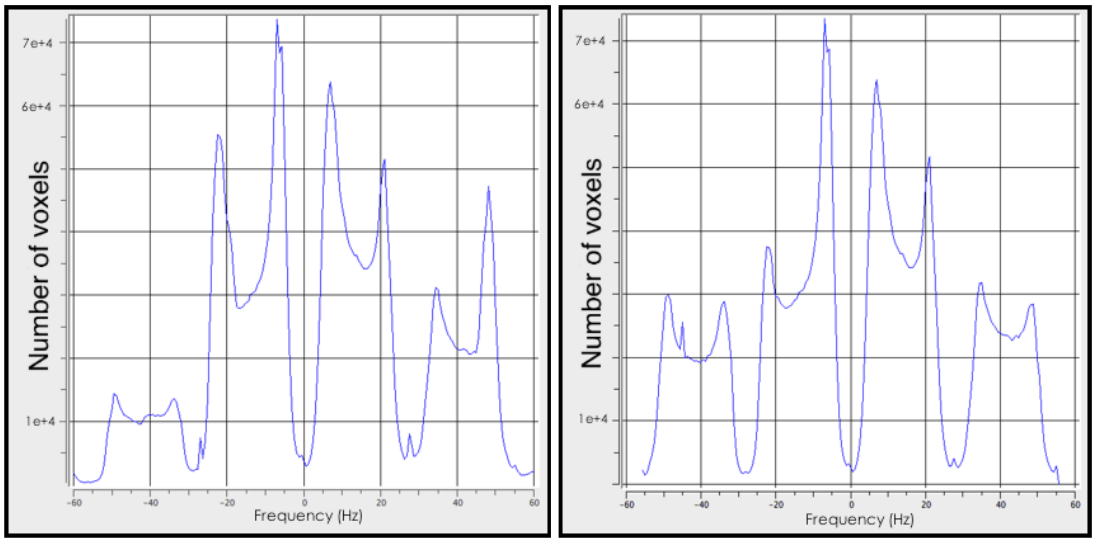

FIGURE 100: HISTOGRAMS OF OFF-RESONANCE FREQUENCY F0 VALUES IN THE MAPS SHOWN IN THE FIGURE ABOVE PRODUCED BY THE LM (LEFT) AND BFGS (RIGHT) ALGORITHM AND A 0/90/180/270 RF PHASE CYCLING SCHEME

The great inhomogeneity across the images causes large off-resonance effects which is shown in the maps above. The inhomogeneity in the B_1 map in shown in Figure 101 below.

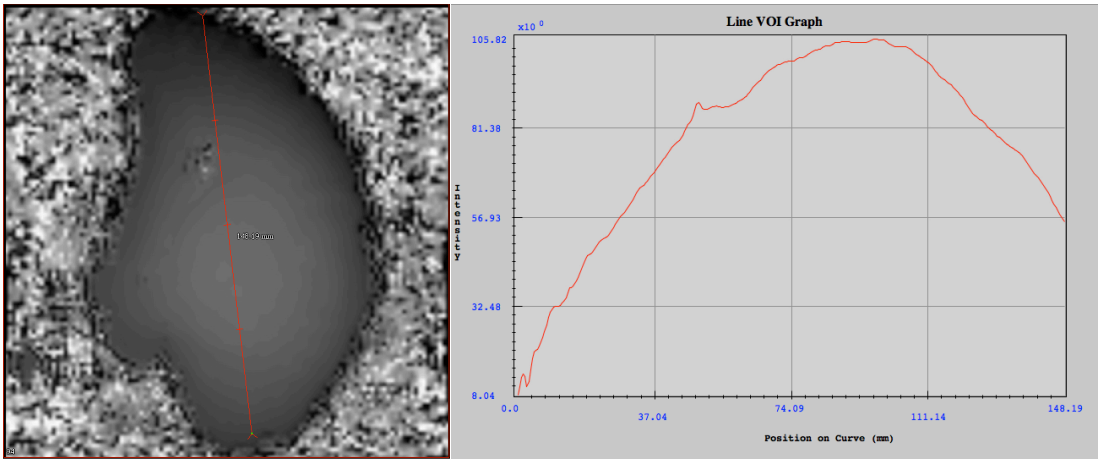

FIGURE 101: LINE GRAPH OF B1 VALUE (RIGHT) FROM LINE SHOWN ON B1 MAP IMAGE (LEFT). THE TOP OF THE LINE AT THE TOP OF THE IMAGE CORRESPONDS TO POSITION 0 ON THE LINE GRAPH

7.5.3 DISCUSSION

T_2 maps have been successfully reconstructed at 7T using both algorithms. The maps show greater banding artefacts with large jumps in off-resonance frequency across the image between minus and plus values. This is due to the large field inhomogeneity at higher field strengths causing large off-resonance effects. One solution to this problem may be to image smaller sections of post-mortem tissue to provide a more uniform shim across the sample.

7.5.4 CONCLUSION

Using a truncated flip angle scheme, DESPOT2 T_2 maps were successfully acquired. Further work here would be to use pulse programming to constrain the RF pulse duration to one value. This may resolve the issue at higher flip angles of shifting of the banding artefact.

7.6 SUMMARY

In this chapter, the measurement of T_2 in fixed tissue was examined. The T_2 of fixed spinal cord at 3T was measured for the first time using a single exponential method. This could not be considered the gold standard as it is well known that there are multiple water compartments in tissue[155]. However, it was used to compare values with DESPOT2 as this also gives a single T_2 value for each voxel.

Parameters to be used with the DESPOT2 algorithm were optimised. DESPOT2 values in fixed brain and spinal cord tissue at 3T and 7T were examined for the first time. However, the acquisition using the wholebody 7T scanner was not successful with severe banding artefacts. The 3T spinal cord acquisition was most successful, due to the better shim achieved over the small spinal cord section.

The results for the single exponential and DESPOT2 T_2 values in a brain hemisphere at 3T did not match. However, as neither of the methods were optimal with banding in the DESPOT2 image and the aforementioned single exponential T_2 measurement it is difficult to draw a conclusion.

The DESPOT2 was successful in providing a large range of T_2 values in fixed tissue. This is more likely to correspond to the actual situation as it has been shown there is a wide range of T_2 values (10ms-100ms at 1.5T) in fixed tissue[110]. It was not possible to segment the image into the three tissue types of white, grey and lesion which would correspond to the three myelin states due to the images. With pulse programming to fix the RF pulse length, which would enable the algorithm to fit the off-resonance values successfully, therefore removing the banding artefact, and this would give a clearer idea of whether the T_2 values found by DESPOT2 were correct.

Determining the baseline T_2 values of fixed spinal cord tissue at 3T allows for the informed implementation of research sequences in all fixed tissue work in MS and other pathologies as the T_1 values. The optimisation of the DESPOT2 sequence will be used further in this thesis for the mcDESPOT algorithm.

8 MYELIN WATER IMAGING USING THE CPMG SEQUENCE

Myelin water imaging uses a 32-echo Carr-Purcell-Meiboom-Gill (CPMG) spin-echo sequence and involves the separation of the signal from different water environments within a voxel based on their transverse relaxation times. However, the 180° refocusing pulses are not perfect leading to stimulated echoes which must be corrected. The programs for data fitting were written at University of British Columbia, Vancouver, British Columbia, Canada by Thomas Prasloski[32] (please see section 2.8.4 for details). The myelin water fraction is defined here as the amount of signal in the short T_2 peak attributed to myelin relative to the total signal in the T_2 distribution.

8.1 T2 MAPS IN THE POST-MORTEM BRAIN USING THE CMPG SEQUENCE

8.1.1 WORK ON A 3T CLINICAL SCANNER

The CPMG method has been histologically validated in the brain at both 1.5T and 7T but at 3T has only been applied *in-vivo*. There was a small section of fixed MS brain that was examined with a single slice acquisition in Kolind et al. paper[112] but with little detail or an image as sequence development was the main aim of the paper. A hemisphere was imaged at 3T using the CPMG sequence to examine the sequence parameters that would be most successful at 3T.

8.1.2 PARAMETER EXAMINATION

One hemisphere was imaged on the Philips scanner. The Matlab programs for analysis of CPMG data contain a GUI fronted program that can calculate the MWF and other parameters immediately in a single voxel or region of interest. This was used to examine the data, and decide upon suitable values for component T_2 values for MWF creation.

8.1.2.1 White Matter

It can be seen that the hemisphere contains a large amount of diffuse white matter damage. The darkest parts of the white matter have a good separation between the myelin water fraction, intra/extra-cellular and free water as shown below in Fig. 102.

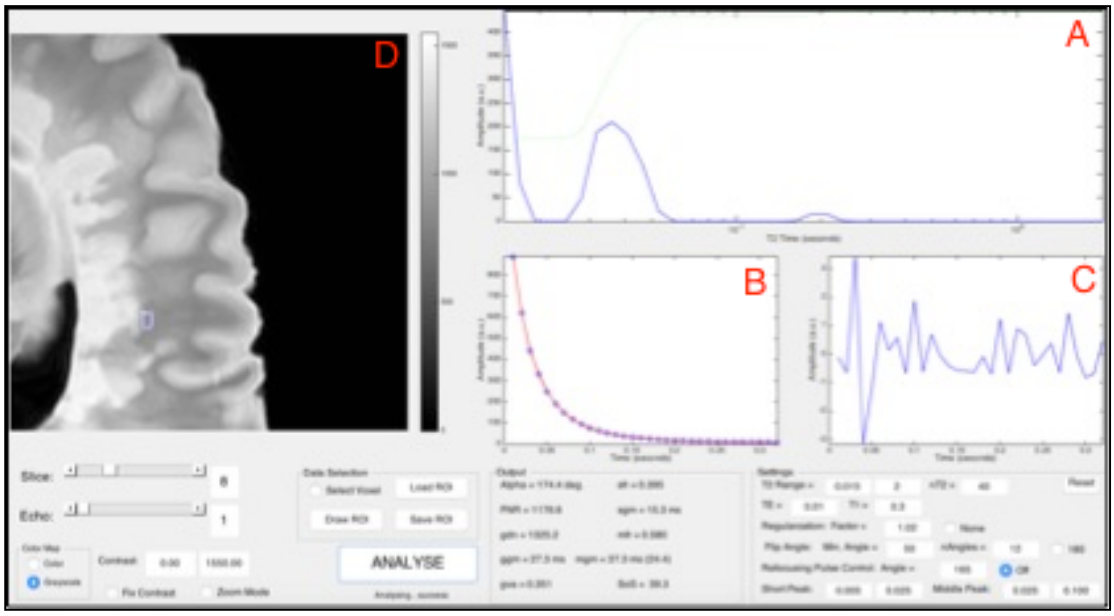

FIGURE 102: AN EXAMPLE T2 DISTRIBUTION IN THE WHITE MATTER (A). THE SHORT MYELIN PEAK IS BETWEEN 0.005 AND 0.025, INTERMEDIATE PEAK BETWEEN 0.025 AND 0.100 AND THE FREE WATER PEAK ABOVE 0.100 SECONDS. B SHOWS THE FIT THROUGH THE 32 ECHOES WITH C THE RESIDUALS OF THIS FIT. D SHOWS THE ROI IN THE IMAGE

In the more diffusely damaged white matter, the two peaks of myelin and intra/extra-cellular are more difficult to separate as shown below in Fig. 103.

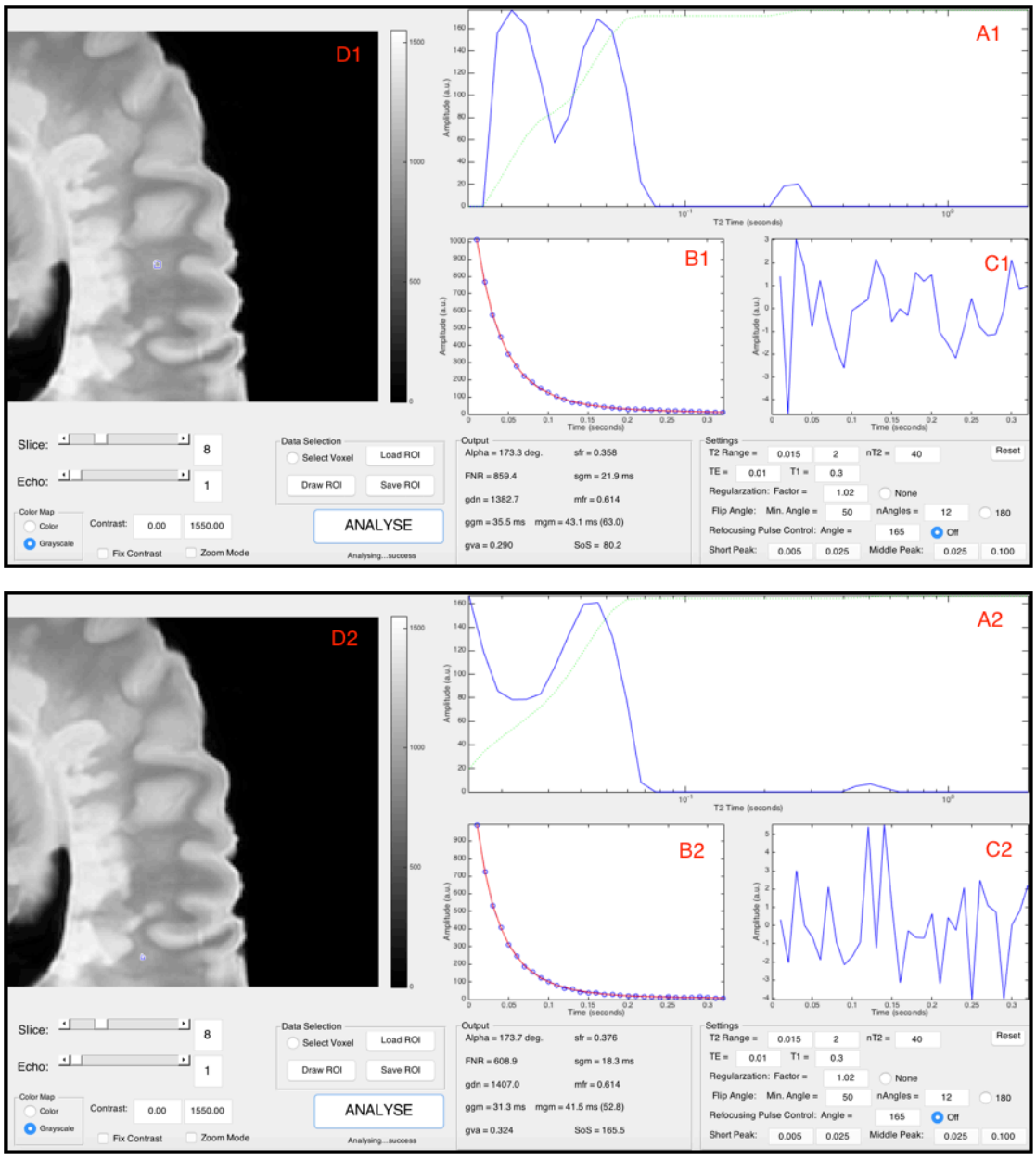

FIGURE 103: EXAMPLES OF T2 DISTRIBUTIONS FOUND IN PIXELS IN TWO AREAS OF DIFFUSELY DAMAGED WM (D1, D2) WITH POOR SEPARATION OF THE MYELIN WATER AND INTRA/EXTRA CELLULAR WATER COMPONENTS (SEEN IN A1 & A2) WITH THE FITTING SHOWN IN (B1 & B2) AND RESIDUALS IN (C1 & C2)

8.1.2.2 Grey Matter

Unfortunately, with the echo time that was available on our scanner, the grey matter myelin component was not discernable from the intra/extra-cellular component. It can be seen in figure 104 below that there is no short T_2 component that would correspond to myelin, the intra/extra cellular

component remains at the same position in the distribution at approximately 30-40ms.

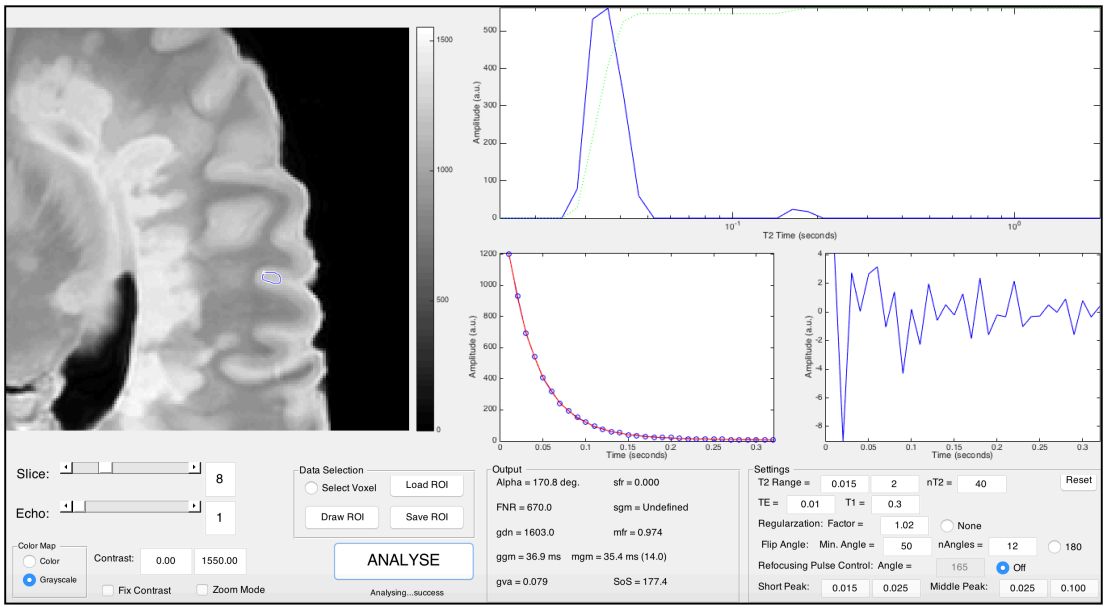

FIGURE 104: AN EXAMPLE OF A T2 DISTRIBUTION IN THE GREY MATTER DEMONSTRATING THE LACK OF A SHORT MYELIN PEAK WITH ONLY THE INTRA/EXTRA CELLUAR AND FREE WATER PEAK LEFT IN THE DISTRIBUTION. THE SIMILARITY OF THE POSITIONS OF THE PEAKS MAY BE COMPARED IN FIG. 101

8.1.2.3 Lesion

Figure 105 below shows the T_2 distribution in a lesion. This distribution shows a large spread of values, which implies a spread of water environments in this ROI. This is in contrast to the sharp myelin peak which would correspond to the laminar water environment that would be reasonably unvarying. The distribution is also wider than the intra/extra cellular component, and would imply a chaotic cellular structure in the scar tissue of the lesion with many water environments.

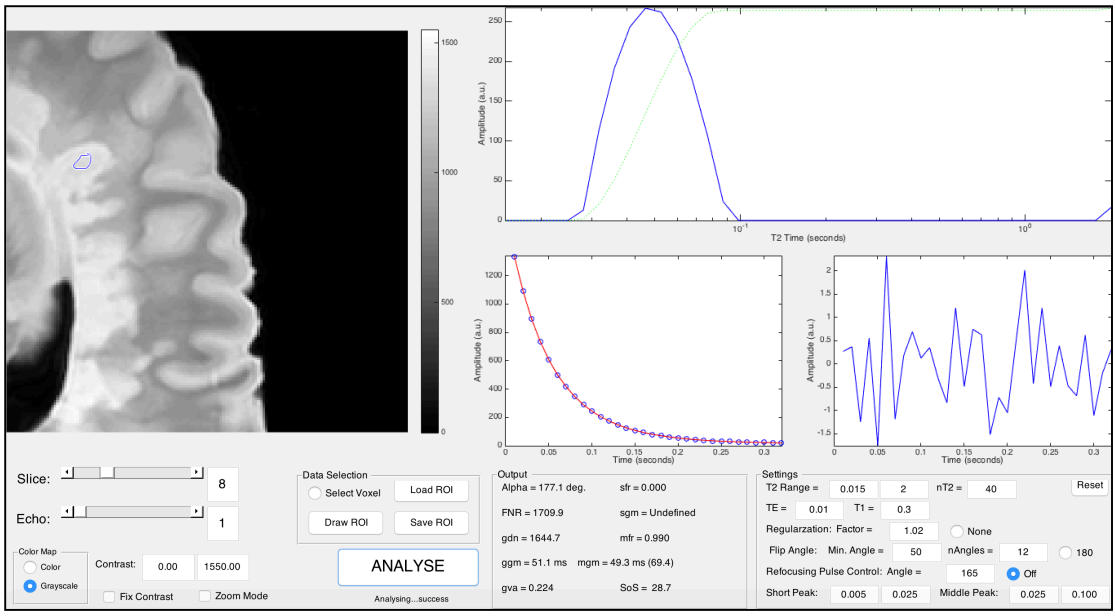

FIGURE 105: AN EXAMPLE OF A T2 DISTRIBUTION IN A LESION SHOWING A WIDER SINGLE PEAK IN THE REGION OR SLIGHTLY HIGHER OF THE INTRA/EXTRA CELLULAR PEAK SEEN IN FIGS. 101-103

8.1.3 RESULTS

The image intensity is proportional to the logarithm of the myelin water fraction. The MWF is given as a fraction of the total water.

Matching T_2 and Myelin Water fractions are shown below in Fig. 106.

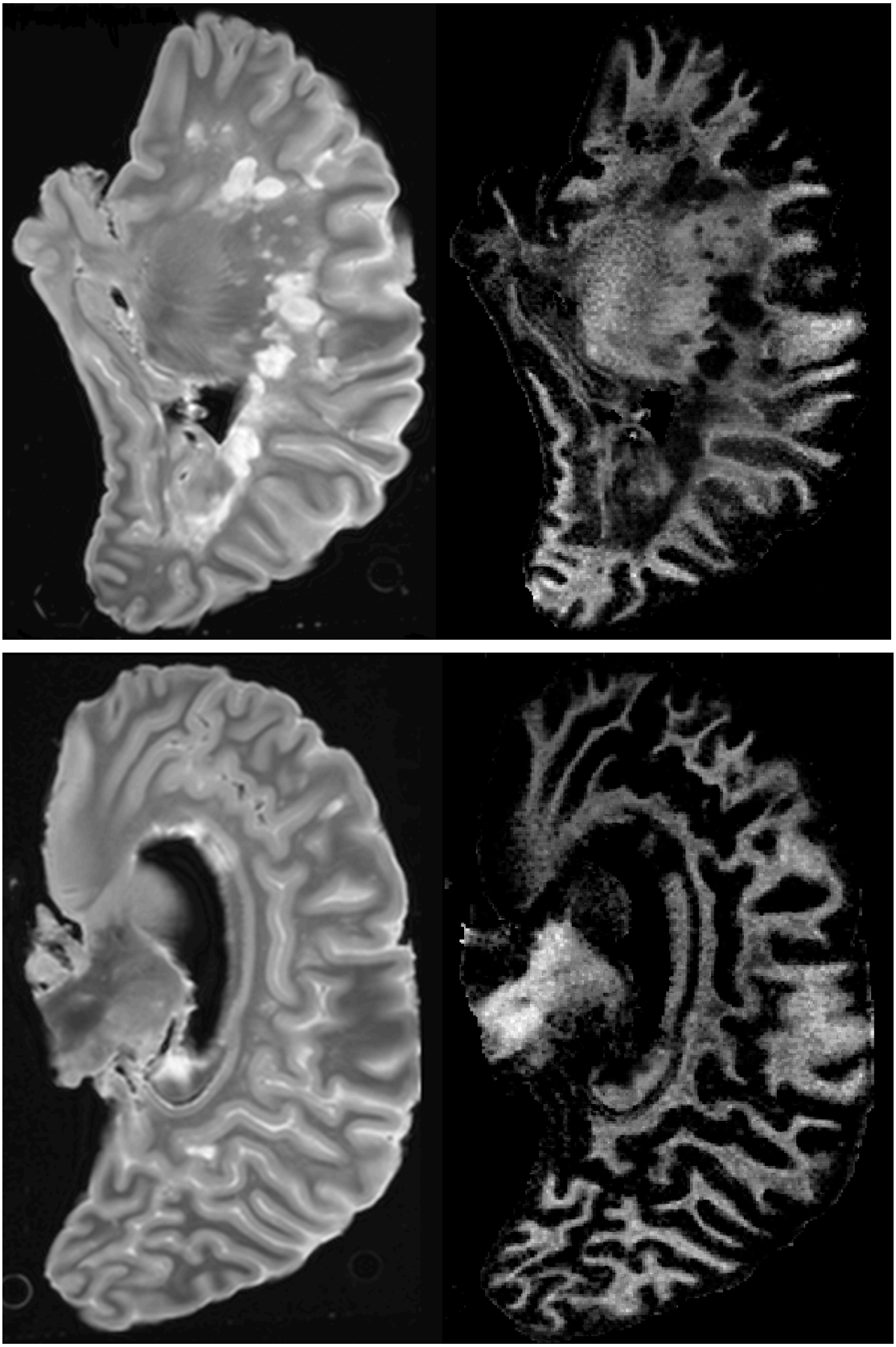

FIGURE 106: TWO EXAMPLE MATCHING PD-WEIGHTED IMAGES (TE 40, TR 3000, ON THE LEFT) AND MWF MAPS (ON THE RIGHT) IN MS436R. MWF MAPS ARE DISPLAYED BETWEEN 0 AND 0.9

Example regions of interest are shown below in Fig 107 for normal appearing white matter (NAWM), diffusely damaged white matter (DDWM) and lesional white matter (LWM).

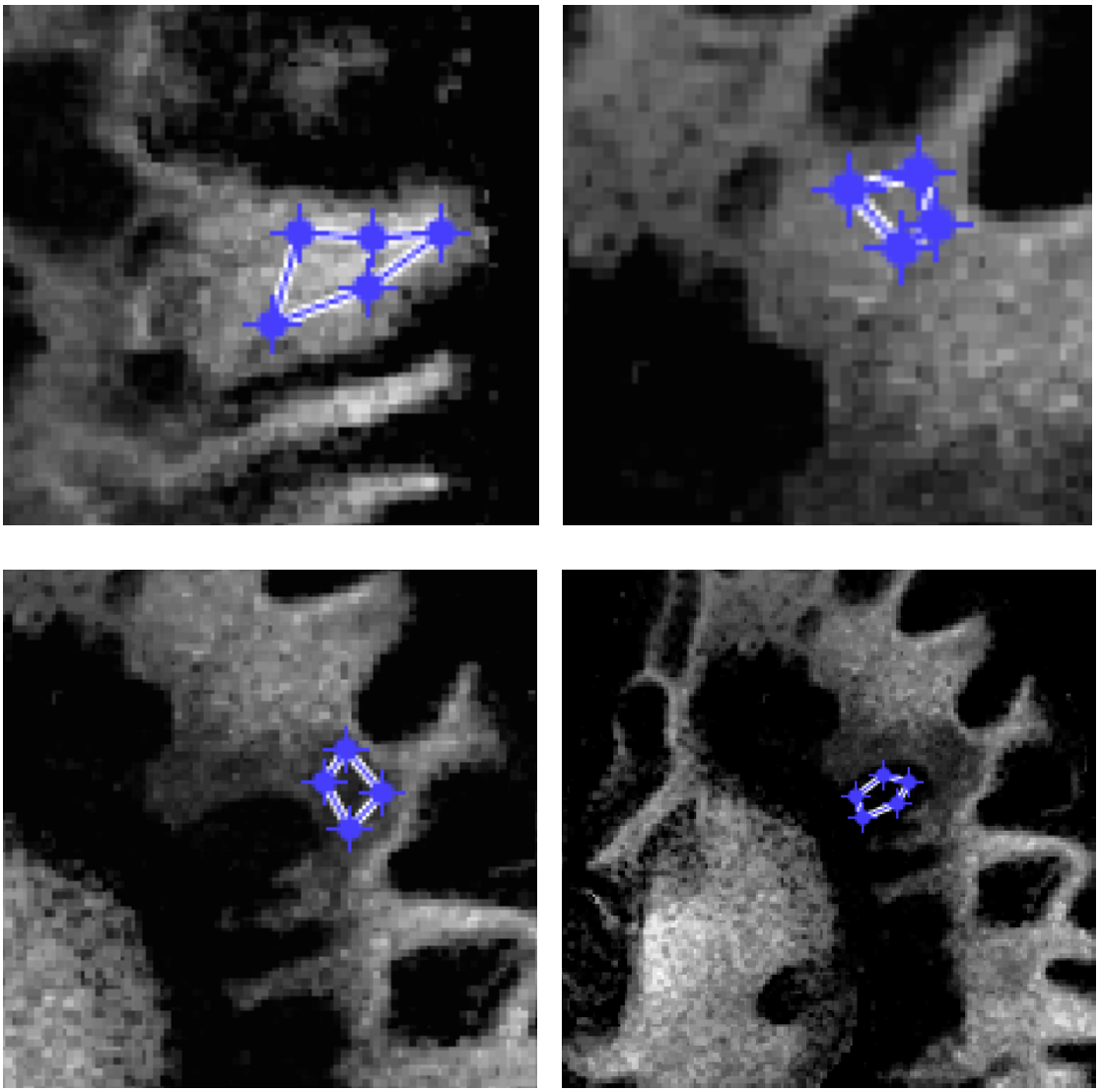

FIGURE 107: EXAMPLE ROIS IN THE NAWM (TOP LEFT AND TOP RIGHT), DDWM (BOTTOM LEFT) AND LWM (BOTTOM RIGHT) IN MS436R

A graph showing the values of MWF in NAWM (0.46±0.09), DDWM (0.15±0.04) and LWM (0.005±0.006) white matter is shown below in Fig. 108.

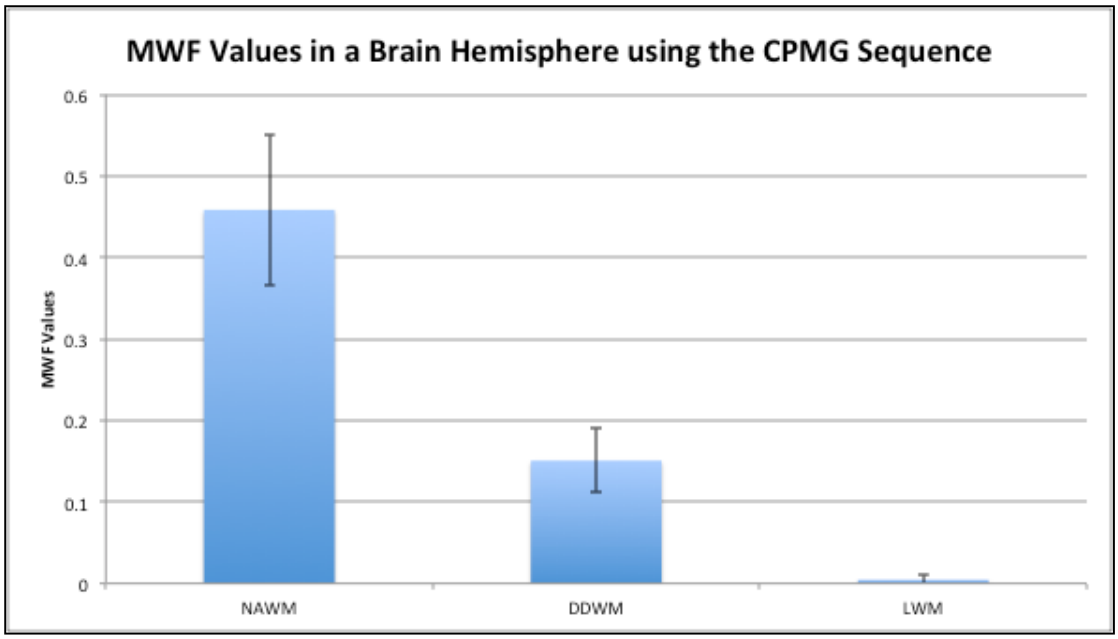

FIGURE 108: MWF VALUES IN NAWM, DDWM AND LWM FROM MS436R. THE ERROR BARS ARE STANDARD DEVAITION VALUES

This value is similar to the MWF value in WM given in Kolind et al.[112] of approximately 0.43 (the value is given in a bar chart so is slightly imprecise). It is unclear whether the value in that paper is in normal-appearing or diffusely-damaged tissue. However, it is likely to be in the NAWM.

8.1.4 DISCUSSION

This shows that the parameters selected above produce acceptable short myelin fraction maps in the white matter of the brain. The maps shown above seem comparable to the *post-mortem* maps of the brain in other publications such as Moore et al.[109] at 1.5T and Laule et al.[111], the maps from their papers are shown below. Although a comparison of printed images, the work at 7T using a 30cm bore Bruker scanner seems to have better resolution and was able to separate the short myelin and intra/extra-cellular signal in grey matter.

Due to the increase of resolution at higher field strengths, there seems to be better delineation of lesions and less noise in the 3T maps in comparison to the1.5T images from Moore et al. The lower noise may be due to the longer T_2 values, possibly giving a better separation of components. The better separation of components at higher field strengths in certainly evident in the 7T

work, which was able to resolve the myelin component in grey matter, where both the work in this thesis at 3T and the work by Moore et al. at 1.5T failed. These maps are shown below in Figure 109 and 110 for comparison.

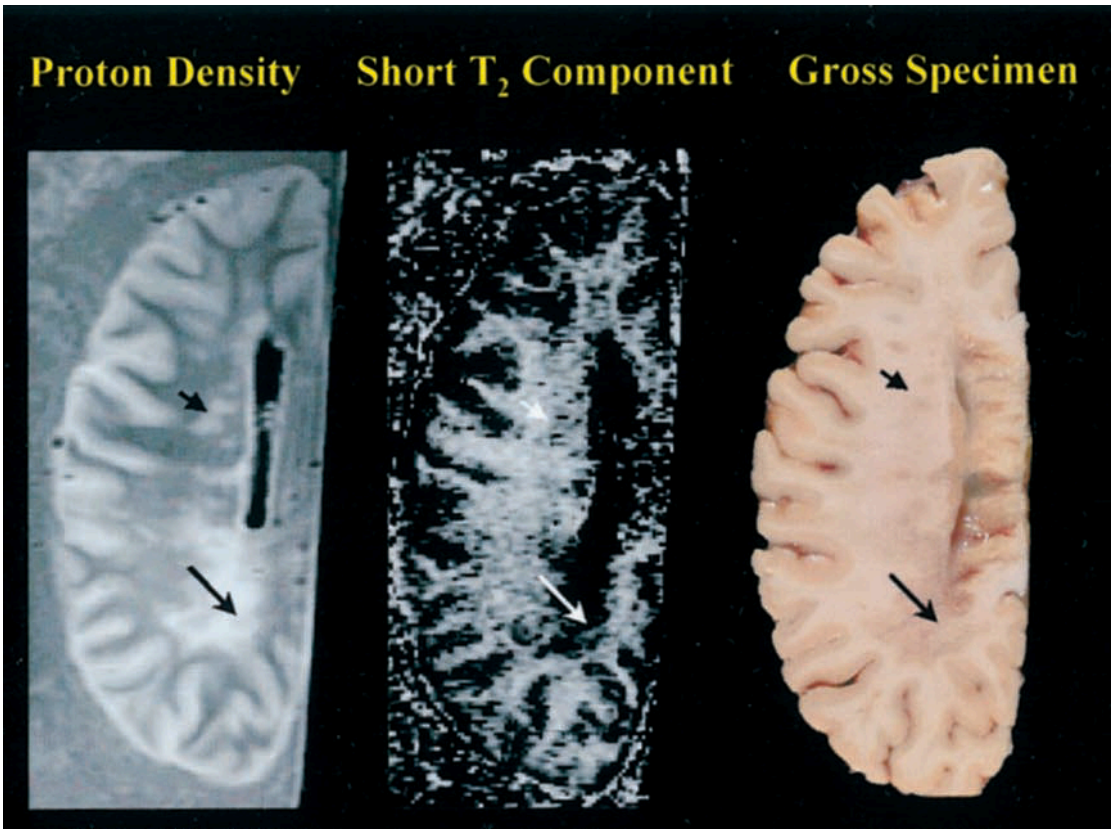

FIGURE 109: FIGURE REPRODUCED FROM MOORE ET AL.[109] SHOWING A PROTON-DENSITY IMAGE (LEFT), MWF IMAGE (CENTRE), AND SPECIMEN (RIGHT). ARROWS SHOW CORRESPONDING LESIONAL AREAS

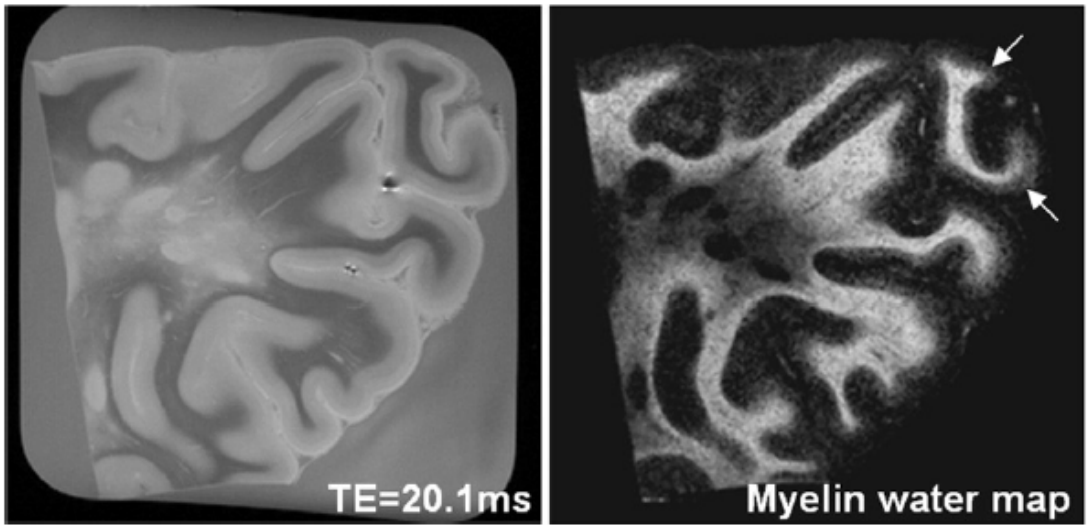

FIGURE 110: MWF MAP (RIGHT) IN A SECTION OF BRAIN AT 7T, AND A PD-WEIGHTED IMAGE (LEFT) REPRODUCED FROM LAULE ET AL.[111]

8.2 T_2 MAPS IN THE POST-MORTEM SPINAL CORD USING THE CMPG SEQUENCE

The CPMG sequence was acquired in 3D due to the problem of magnetisation transfer outside of the FoV with 2D sequences (see section 2.6.1 on CPMG above). One of the disadvantages of the CPMG sequence is how time consuming it is. Using a TR of 3000ms, NSA of 2, a small number of slices such as 10 and a relatively low in-slice acquisition resolution of 0.6x0.6mm the whole sequence takes 5 hours and 49 minutes. This means that the mcDESPOT and CPMG sequence short myelin water maps were unable to be acquired at the same time and the slices compared directly. Therefore, comparison of the maps was done by the identification of lesions as landmarks within the spinal cord. The 2mm slice thickness of the CPMG acquisitions (if 0.5mm slice width were used only 5mm of spinal cord could be imaged, even with the long acquisition time and a 3D acquisition which can achieve a shorter TE than the 2D sequence for thinner slices) is not directly comparable to the 0.5mm 3D voxel of the whole brain mcDESPOT map.

8.2.1 WORK ON A 3T CLINICAL SCANNER

The first CPMG sequence was acquired using the same spinal cords as were used in the Kings 7T Aglient small animal scanner, MS471, MS454, MS484. The first control C61 was found to be unsuitable for use as a control and later a new control C58 was acquired using the similar parameters on the Aglient scanner. The first C58 scan was acquired the same parameters but there was a signal loss in the centre of the acquisition, found in all acquisitions at that time, which was later found to be a transmit coil problem. This artefact seemed mild but when the images were processed, the signal values were found to be unusable. Unfortunately, C58 had been processed for histology when this was established and so couldn't be repeated to match exactly. Therefore, a slightly different sequence was used for comparison.

8.2.1.1 Methods

Three complete formalin fixed spinal cords from pwMS (1 male, 2 females; age 67-87 years; disease duration 8-44 years; duration of fixation 995-1309 days) and one control (male; age 89; duration of fixation 1320 days) were imaged using the set-up for sectioned cords (see section 5.5).

The pwMS spinal cords were imaged on a Philips Achieva 3T using a 3D CPMG sequence (32 echoes, TE n × 10.26ms, TR 1000ms, 0.6×0.6×2.0mm^3 matrix, 20 slices, in conjunction with a 16-element head-coil) and the control cord (32 echoes, TE n × 10ms, TR 3000ms, 0.6 x 0.6 x 2.0mm^3 matrix, 21 slices). The MWF water maps were calculated using the NNLS algorithm, using bounds of 5 – 30ms for short T2 and 30 – 300ms for intermediate T2 values. The bounds used were altered compared to typical in-vivo values (short T2, 10 – 30ms, intermediate T2, 70 – 1000ms[111]) due to the shortened T2 relaxation time found in fixed tissue. Cords were dissected throughout into blocks of 5mm thickness, processed for embedding in paraffin, and sections stained for Myelin Basic Protein (MBP). Focal areas of complete myelin loss were identified as demyelinated lesions in the white (LWM) and grey matter (LGM).

Sections that were identified as matching on the MR images and MBP stained sections were then stained with LFB. This stain can be used to obtain a

quantitative myelin measure if all sections are stained using the same concentration of LFB at the same time point. The stained sections are then scanned and a very high resolution jpeg image of each section obtained. The image is then set to a grey scale between 0 and 256, and then regions of interest are taken with a mean grey value. The histological sections were matched to the MRI slices by calculating the location of the histological section from the end of the piece of the spinal cord and then calculating the MRI slice corresponding to that physical location. The correspondence of the histological section and MRI slice was then checked qualitatively by a collaboration of histopathologist, radiologist and physicist. The ROIs were then drawn on the MR slices and qualitatively matched on the jpeg images. These ROIs were then again checked by a collaboration of histopathologist, radiologist and physicist

8.2.1.2 Results

Figure 110 shows an example curve of the signal decay in one pixel as a function of the echo time. Although the distribution of T_2 values showed shortened values relative to previous *in-vivo* measurements, the two components associated with myelin and intra/extracellular water are resolved, as shown in Figure 111. Figure 112 shows example matched MBP stained histological section, T_2-weighted MR images and MWF maps.

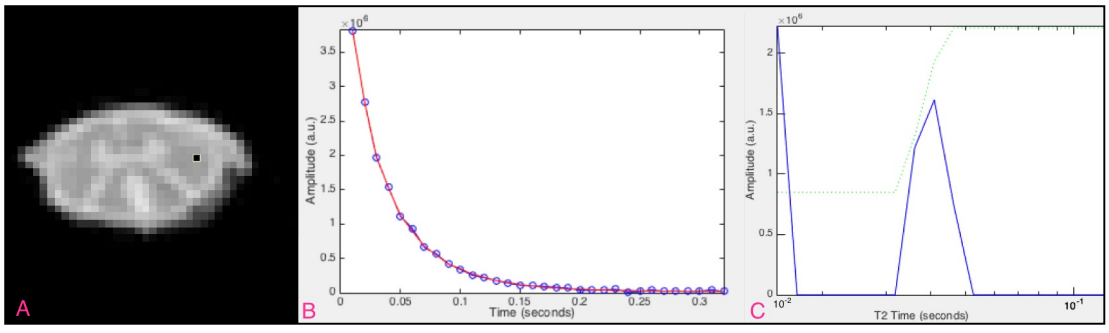

FIGURE 111: AN EXAMPLE SIGNAL CURVE IN WM (BLACK DOT) AND THE TWO SEPARATE SIGNAL PEAKS OF SHORT AND INTERMEDIATE T_2 VALUES. THE DOTTED GREEN LINE SHOWS CUMULATIVE T_2 VALUES. NOTE THE COMPRESSION OF THE T_2 VALUES AGAINST THE Y-AXIS DUE TO FIXATION BUT THE TWO NORMAL DISTRIBUTIONS CAN BE RESOLVED

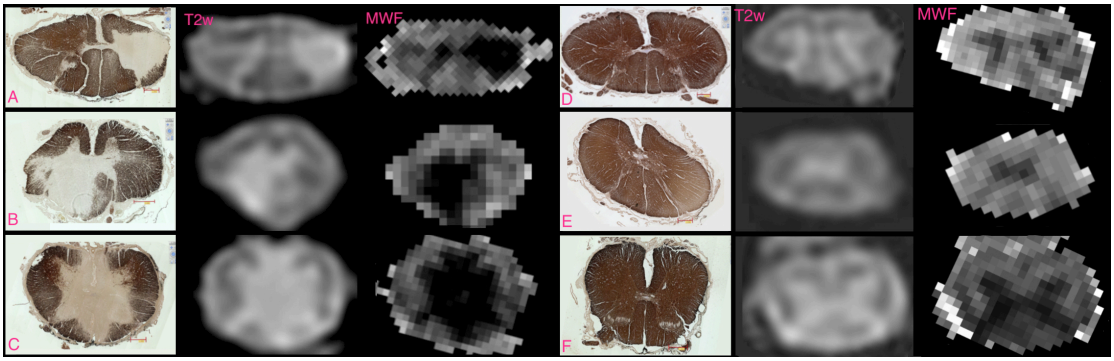

FIGURE 112: MATCHED EXAMPLE MBP, T_2-WEIGHTED MR IMAGES AND MWF MAPS FROM DIFFERENT SPINAL CORD LEVELS. AN EXAMPLE PWMS SPINAL CORD, C7 (A), T5 (B) AND L3 (C) ON THE LEFT AND CONTROL CORD C8 (D), T8 (E) AND L5 (F) ON THE RIGHT. MWF MAPS ARE DISPLAYED BETWEEN 0 AND 0.9

Regions of interest were taken throughout the myelin maps produced by the algorithm; not all of the areas had matching histological sections. Regions were taken wherever tissue types had voxel values that were thought to be only one tissue type. With such a small structure as the spinal cord (cross-sectional area of one or two cm), and the low-resolution scans obtainable with a clinical 3T scanner, often a region of interest that may confidently obtained as one tissue type avoiding partial volume effects, is one voxel only. In the lumbar area, which has a large grey matter component, it is difficult to identify white matter and in the thoracic area, where the grey matter is thinner, it is difficult to identify grey matter voxels.

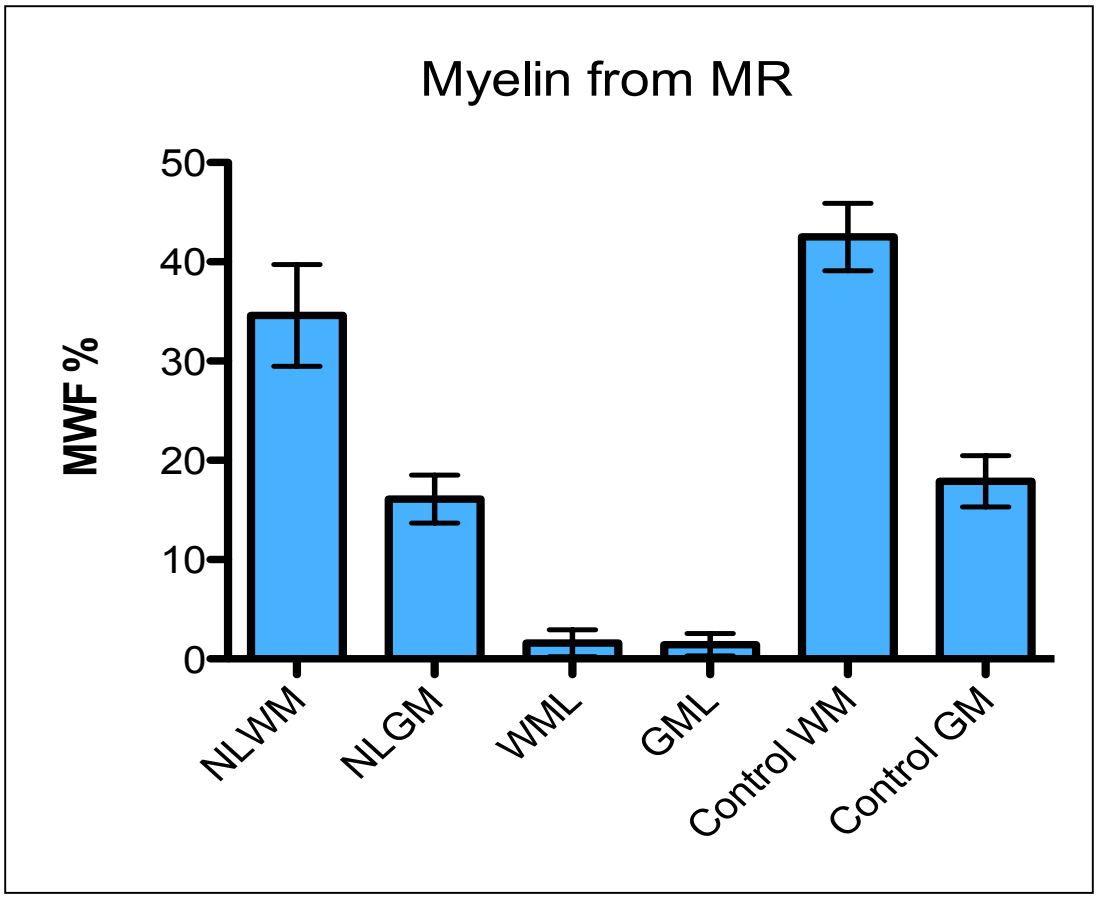

FIGURE 113: MR MYELIN WATER FRACTION VALUES IN THE NLWM, NLGM, WML, GML, CONTROL WM AND CONTROL GM

It is known that MS causes diffuse damage in the non-lesional white matter[156], therefore it is to be expected that there is difference in myelination values between NLWM in MS cords and WM in control cords. Although it has been shown that the extent of damage in the grey matter does not always correlate with the extent of white matter damage[156], it may also be hypothesised that there would also be a difference in myelination between control GM and NLGM. Therefore, the correlation between control and non-lesional tissue in WM and GM was calculated as shown in Table 18. These calculations were made using GraphPad Prism using a non-parametric Spearman correlation and a two-tailed P value.

Correlation of Control White Matter and Non-lesional White Matter	
Number of XY Pairs	10
Spearman r	-0.5228
P value (two-tailed)	0.12
Correlation of Control Grey Matter and Non-lesional Grey Matter	
Number of XY Pairs	8
Spearman r	0.4762
P value (two-tailed)	0.24

TABLE 20: CORRELATION COEFFICIENTS FROM A COMPARISON OF VALUES IN CONTROL WM AND NLWM AND THE VALUES IN CONTROL GM AND NLGM

As the myelin phospholipids increases within the sample, the level of staining increases and hence optical density value increases from 0 to 100%. This corresponds to 0 to 256 grey values in the scanned microscope image. Since all of the samples were processed at the same time, under the same conditions and using the same batch of reagents, this proportionality should extend across all samples. Whilst not an absolute quantity, the OD value should give a linear relationship with myelin phospholipid concentration. In the MR measure of myelin, the myelin water fraction is a volume fraction of the water in a voxel as a fraction of everything else contained in the voxel (intra/extracellular or free water). Therefore, the two measures are not directly relatable as one is proportional to the phospholipid concentration and the other a measure of myelin water fraction. However, both values should be proportional to the amount of myelin and hence should be well correlated. In order to compare these two methods of myelin measure, the correlation between the two values is examined.

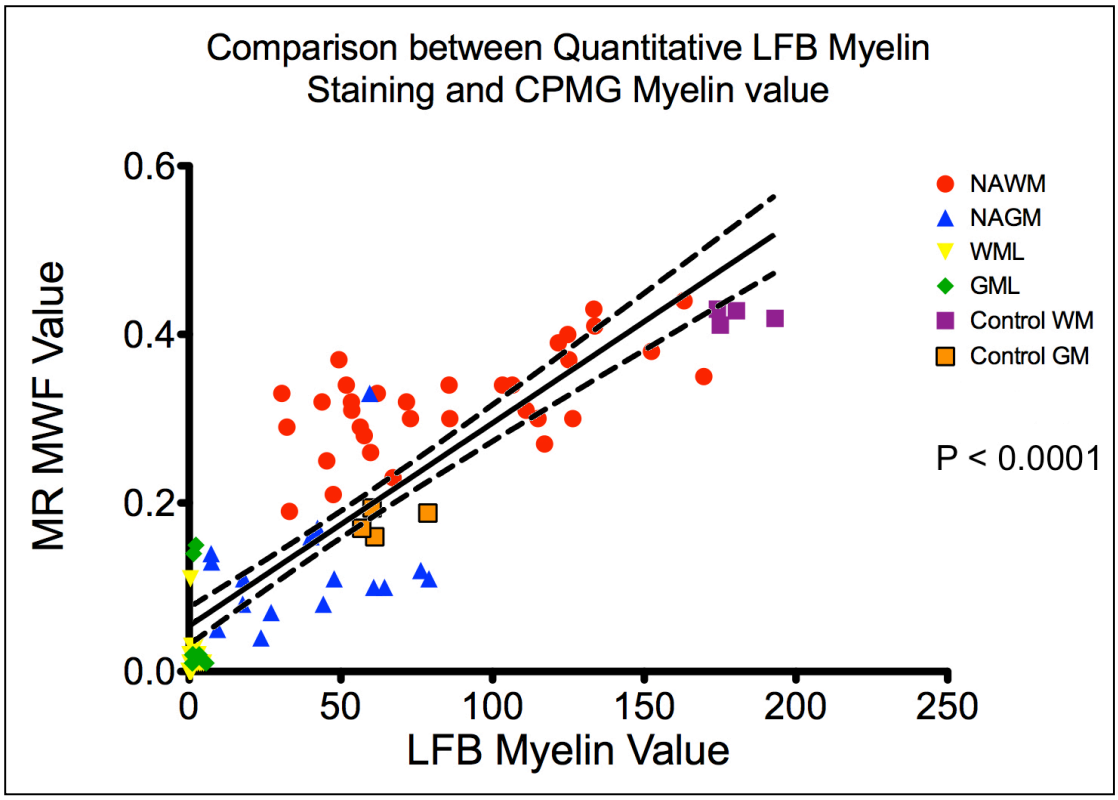

FIGURE 114: COMPARISON BETWEEN LFB STAINING OPTICAL DENSITY VALUE AND THE MR MWF VALUE. THE LINEAR REGRESSION LINE IS SHOWN AS THE MEAN AND ERROR BARS OF THE 95% CONFIDENCE INTERVAL

The Pearson correlation coefficient was 0.86 with a 95% confidence interval of 0.80 to 0.91 with a P-value of <0.001. When only control data was analysed (Control WM and Control GM) the Pearson correlation coefficient was 0.989 (95% confidence interval 0.94-0.998, P<0.0001).

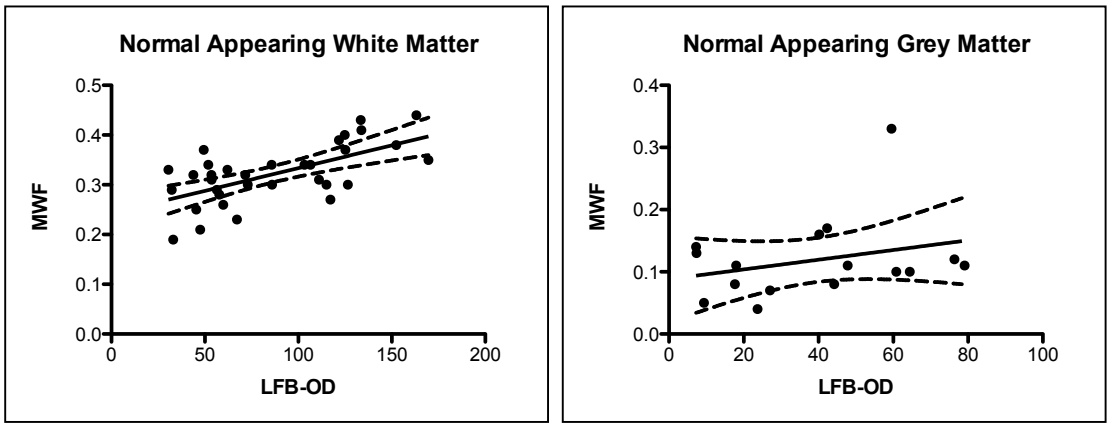

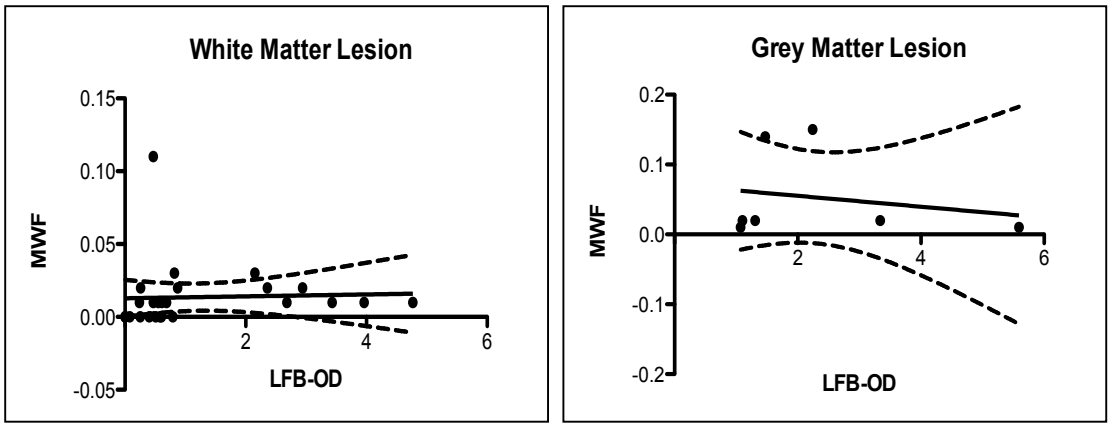

FIGURE 115: INDIVIDUAL GRAPHS OF COMPARISON OF LFB-OD AND MWF IN THE NAWM, NAGM, WML AND GML. THE LINEAR REGRESSION LINE IS SHOWN AS THE MEAN AND ERROR BARS OF THE 95% CONFIDENCE INTERVAL

There is modest correlation in the NAWM with a correlation coefficient of 0.63. The correlation in the NAGM, WML, and GML is poor with correlation coefficients of 0.28, 0.04 and -0.2 respectively.

8.2.1.3 Discussion

A good visual match was found between MBP staining and myelin water maps. Calculated MR myelin volume fraction values are shown in Figure 113. Average values in the white and grey matter of the control cord were 41.9±3.8 and 17.9±2.6 respectively. There was no significant difference between NLWM and control WM (P-value 0.12) and no significant difference between NLGM and control grey matter (P-value 0.24). However, in a larger sample, from examination of the data with a larger range in the NLWM, it is probable that the known difference in myelination between NLWM and control WM would be significant[156]. It is difficult to say if this would also be true in the grey matter.

8.2.1.4 Conclusions

Myelin water imaging was successfully applied to fixed post mortem MS spinal cord. Good correspondence was detected between myelin water fraction maps and the myelination status in non-lesional white matter, non-lesional grey matter, lesional grey matter and lesional white matter.

8.3 SHORT T_2 MYELIN FRACTION AT 3T IN NON-FIXED TISSUE

8.3.1 WORK ON A 3T CLINICAL SCANNER

As part of the PSIR work (section 6.12), some non-fixed tissue sections were acquired from the MS Tissue Bank. As part of the acquisition protocol for these samples, 32-echo CPMG myelin water imaging was acquired. Due to the nature of fresh tissue this was not always successful. The non-fixed spinal cord was arriving from a distance and had often been removed from the cadaver in such a manner as to render it unusable. This meant, although five sections of non-fixed tissue were acquired, only MS595 produced usable images.

As well as the physical damage to the tissue, it was found that the water content was quite large, with a small myelin fraction in the white matter and even lower in the grey matter, almost zero.

8.3.1.1 Methods

The pwMS spinal cords were imaged on a Philips Achieva 3T using a 3D CPMG sequence (32 echoes, TE n × 10.26ms, TR 3000ms, 0.6×0.6×2.0mm^3 matrix, 20 slices, using a 16-element head-coil). The set-up was the same as fixed tissue (box filled with water with plastic waffle holder for the 1.5 diameter tubes, see section 5.5) with the non-fixed tissue sample in the centre of the field of view. The MWF water maps were calculated using the NNLS algorithm, using bounds of 5 – 40ms for short T_2 and 40 – 1000ms for intermediate T_2 values.

8.3.1.2 Results

The multi component analysis of example pixels in the white and grey matter are shown below. The white matter analysis shows a short and intermediate component, whereas the grey matter shows a very small short component, around 10 times smaller than the white matter. There was no long T_2 water component found.

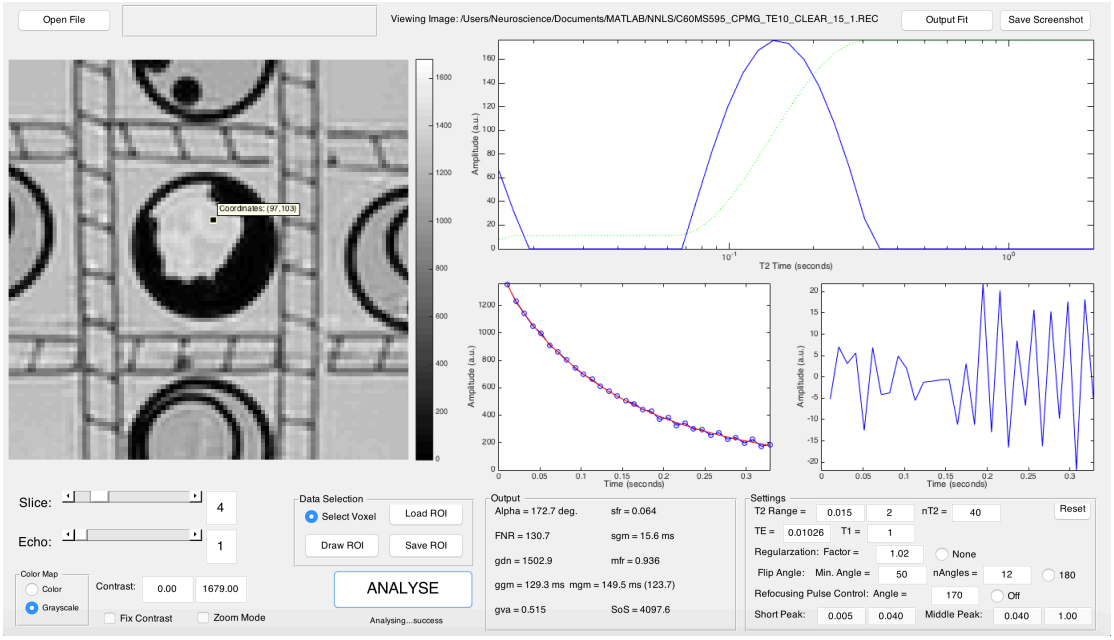

FIGURE 116: COMPONENT ANALYSIS IN THE WHITE MATTER IN NON-FIXED TISSUE. THE SHORT MYELIN PEAK IS BETWEEN 0.005 AND 0.004, INTERMEDIATE PEAK BETWEEN 0.04 AND 0.100. THE SHORT COMPONENT CORRESPONDING TO MYELIN HAS A VOLUME FRACTION OF 0.064, THE INTERMEDIATE HAS 0.936.

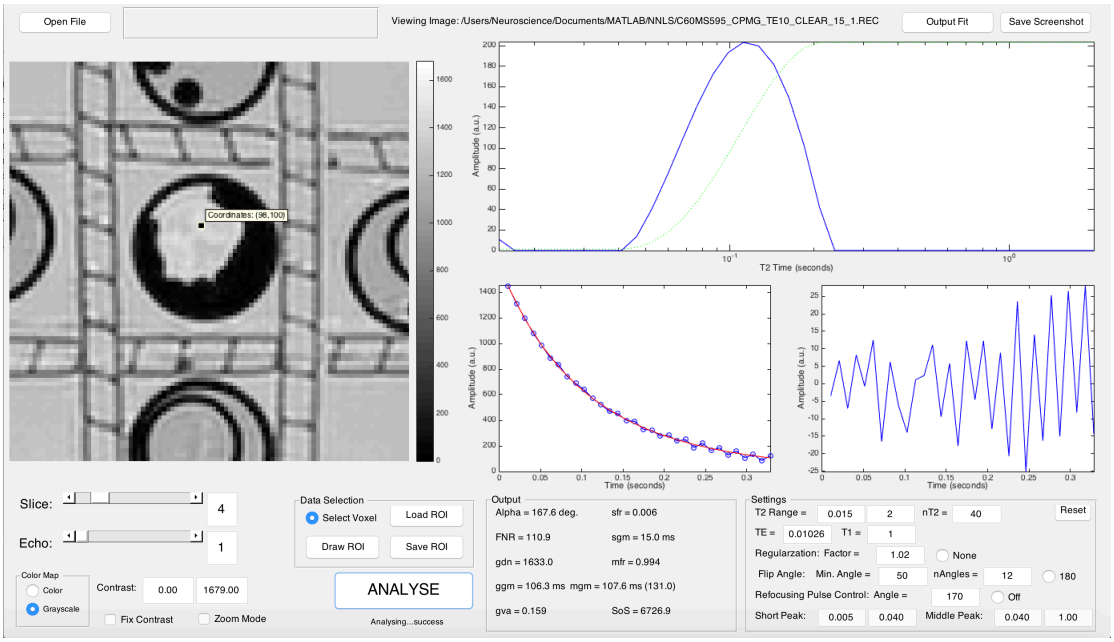

FIGURE 117: COMPONENT ANALYSIS IN THE GREY MATTER IN NON-FIXED TISSUE. THE BOUNDARIES WERE SET THE SAME AS THE WHITE MATTER ABOVE.

A PD-weighted image and its corresponding myelin water fraction map is shown below in figure 118.

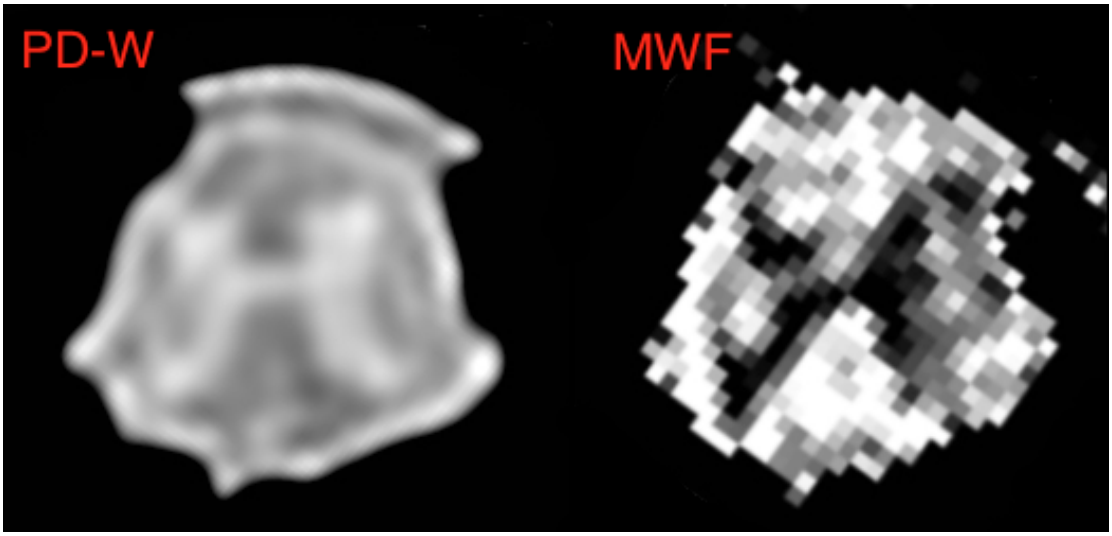

FIGURE 118: A PD-WEIGHTED IMAGE (LEFT, TE 10.262MS, TR 3000MS) SHOWN WITH ITS CORRESPONDING SHORT MYELIN WATER FRACTION (RIGHT).

The myelin water volume fraction values in the white matter areas of the anterior and posterior columns in the map shown above was 0.0994 with a standard deviation of 0.0175. In the grey matter, the short component was often not resolved as seen in the totally black areas in the MWF map shown above corresponding to a value of 0. When it was successful, in a total of four pixels with certainty (avoiding partial volume effects), the myelin water volume fraction was 0.03 with a standard deviation of 0.008.

8.3.1.3 Discussion

In the same manner as the fixed brain hemisphere detailed in section 8.1, it was not always possible to detect the myelin water component in grey matter in non-fixed tissue. However, the multi-component analysis was able to successfully resolve a short myelin component in the white matter.

8.4 DISCUSSION

The MWF values for fixed brain were much higher than *in-vivo* MWF values. This apparent increase is likely due to dehydration in the fixed brain, which is expected to occur preferentially for the intra- and extracellular compartments as more energy is required to extract the water trapped between the myelin bilayers. Evidence of dehydration is also apparent from the lower normalized standard deviations of residuals as the RF coil was better able to tune with less

water present[112]. Higher than *in-vivo* values were also found in Kolind et al.[112] with white matter values of 0.18 *in-vivo* and 0.43 in *post-mortem*.

Current limitations on the signal-to-noise ratio available for *in-vivo* T_2 relaxation studies are likely responsible for the difficulty involved in separating the intra/extra-cellular water peak. There have been indications of a prolonged T_2 component in heavily myelinated white matter structures and in MS lesions[17].

8.5 SUMMARY

The short T_2 CPMG myelin water fraction method has been fully explored in an MS brain hemisphere at 3T and compared to published work at 1.5T and 7T. Results were satisfactory with values comparing well to published work. It has been shown that cortical grey matter myelin water fraction value is difficult to determine at 3T.

The short T_2 CPMG method was then applied in fixed spinal cord at 3T for the first time. It was then compared with quantitative Luxol fast blue myelin staining. This method has been used before to quantify myelin histologically and validate the CPMG method in brain hemisphere at 1.5T and 7T. The CPMG technique was shown to be successful in predicting myelin content in the spinal cord.

The short T_2 CPMG sequence was applied in non-fixed spinal cord tissue for the first time. Only one sample was successfully acquired but the results were promising. Values were much lower in non-fixed tissue than in fixed but this was also found with lower values *in-vivo* than fixed post-mortem brain in Kolind et al. paper, if it can be assumed that non-fixed tissue is similar in properties to *in-vivo* tissue.

The CPMG sequence has been validated at 3T, and the likely result of the myelin quantification at this field strength on a clinical scanner examined in both the brain and spinal cords. This informs the use of this sequence in the clinical setting, showing that it is likely to be successful in the white matter and deep grey matter in the brain, but may not give all the information required for cortical lesion myelin quantification. It has been shown that this sequence will

be successful in quantifying the myelin in the spinal cord clinically, from its success in both fixed and non-fixed tissue.

9 VALIDATION OF MULTICOMPONENT DRIVEN-EQUILIBRIUM SINGLE-PULSE OBSERVATION OF T_1 AND T_2 IN POST-MORTEM TISSUE

9.1 WORK ON A 3T CLINICAL SCANNER IN POST-MORTEM BRAIN

The mcDESPOT sequence has mostly been used in the brain *in-vivo* in MS patients[126,127] and tracking myelin development in children[121,123,125]. In order to compare more easily with this previous work, a post-mortem hemisphere was acquired with the mcDESPOT sequence. The hemisphere MS436 was imaged on the Philips MR scanner.

9.1.1 METHODS

The right hemisphere of MS436 was inserted in the custom-made holder, immersed in perfluorpolyether. It was imaged on the Philips Achieva Scanner in the SENSE Neurovascular coil as described before in section 5.3.

TE (ms)	TR (ms)	SPGR FA	bSSFP FA
4.779	10	3, 6, 9, 12, 15, 18, 21, 24, 27, 30, 33, 36	
4	8.1		7, 14, 21, 28, 35, 42, 49, 56, 63, 70, 77, 84

TABLE 21: ACQUISITION PARAMETERS AT 3T ON THE PHILIPS ACHIEVA SCANNER WITH THE MS436R HEMISPHERE

The hemispheres were reconstructed using the mcDESPOT algorithm supplied by Dr. Tobias Wood at https://github.com/spinicist/QUIT. The algorithm allows some reconstruction values to be set with the option –t u. As fixed tissue has very different values to the default *in-vivo* values supplied, the range of starting values of each parameter or bounds, needed to been evaluated. T1_m and

T2_m are the range of T_1 and T_2 values that are considered to be associated with myelin in the voxel, T1_ie and T2_ie are associated with intra/extra-cellular water, T1_csf and T2_csf are associated with CSF or free water. The bounds for T_2 were informed by the values found using the CPMG algorithm. The three other parameters are tau_m, the residence time of the myelin compartment, f_m, the fraction of the voxel that is considered to be myelin, and f_csf, the fraction of the voxel that is CSF or free water. The off-resonance frequency f_0 and B_1 bounds are automatically set by the algorithm. The myelin fraction maps f_m shown in the results section have unitless fraction voxel values between the two values set in the f_m bounds in the tables associated with the figures. All images are displayed between these two values e.g. if the f_m bounds are 0.001 and 0.35, this corresponds to the minimum and maximum myelin water fraction value.

9.2 CHOICE OF ALGORITHM

The mcDESPOT algorithm is provided with options on the model and algorithms used, as detailed in the table below. There are also options for the number of iterations. Again, default parameters were available for both 3T and 7T options but these are optimised for in-vivo images.

Model	Switch	Algorithm	Switch
1 component	-M 1	Use Uniform distribution for Region Contraction	-a S
2 component	-M 2	Use Gaussian distribution for Region Contraction	-a G
2 component; no exchange	-M 2nex	Use BFGS algorithm	-a b
3 component	-M 3		
3 component; no exchange	-M 3 nex		

TABLE 22: OPTIONS PROVIDED WITH THE MCDESPOT ALGORITHM

For this analysis, all flip angles were used and only a slice in the central area of the brain was reconstructed.

9.2.1 RESULTS

All images were made with the bounds shown below in Table 23. These bounds were informed by the T_1 and T_2 values established in the previous sections. The myelin water T_2 bounds are known and established in 3T in Chapter 8. The total or average T_1 values found in the IR-TSE work were found to be 234ms in GM and 179ms in WM. These were averaged and since the myelin water component is expected to be the shortest T_2 component, it was expected to be below this value. It was difficult to decide the lower bound of the T_1 as there have been no studies on this in fixed *post-mortem* tissue, but since T_1 is greater than or equal to T_2 and the T_2 of myelin water is between 10 and 30ms is unlikely that any T_1 value found below 10ms is accurate and likely to be noise. Therefore, the lower bound was set at 10ms. The optimised IE bounds were not investigated here but were set by the upper bound of the myelin water in the T_1 and T_2, and in T_2 the IE bound found before. The optimised CSF or FWF bounds were also not investigated but kept long in both T_1 and T_2 to correspond to values for free water.

Bounds	PD	T1_m	T2_m	T1_ie	T2_ie	T1_csf	T2_csf	tau_m	f_m	f_csf	f0	B1
Lower	1	0.01	0.001	0.3	0.03	1.0	0.11	0.025	0.001	0.001	-61.73	4.3e-311
Upper	1	0.3	0.02	0.8	0.1	5	3.5	0.6	0.35	0.999	61.73	1.5e-154

TABLE 23: BOUNDS SET WITH ALL ALGORITHMS USED

9.2.1.1 Default Region Contraction Algorithm (Gaussian distribution)

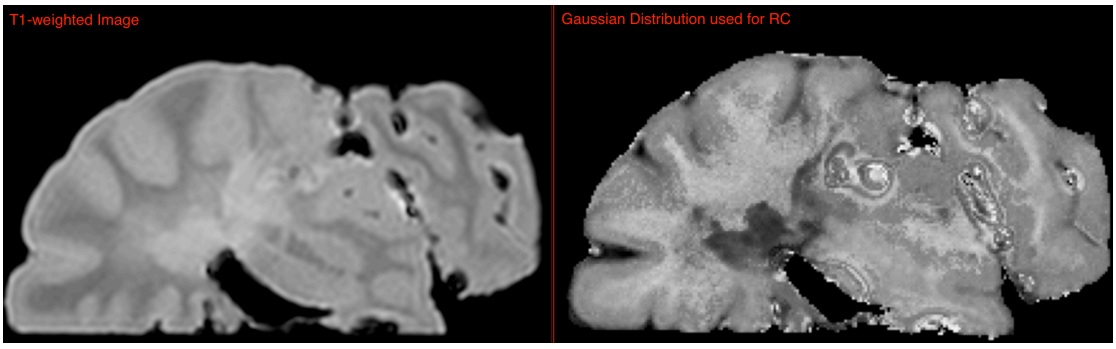

FIGURE 119: T_1 WEIGHTED IMAGE OF AN EXAMPLE SLICE AND THE RECONSTRUCTED MCDESPOT MYELIN WATER FRACTION MAP AT THIS SLICE USING A GAUSSIAN DISTRIBUTION

The Gaussian distribution shows modest correlation with white matter and grey matter anatomy in some parts of the brain. However, there were large susceptibility artefacts at air boundaries.

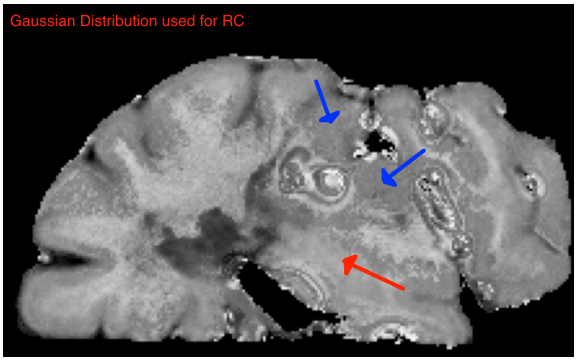

FIGURE 120: THE MWF MAP FROM FIG. 118 WITH ARROWS SHOWING LOCATION OF UNRESOLVED AREAS OF MYELIN DISTRIBUTION

Some areas of the deep grey matter, such as the substantia nigra (as shown with the arrow on the left) are unresolved when compared to the T_1-weighted image. This is possibly due to the susceptibility artefact at the boundary between the perfluorpolyether and the ventricle area causing the fitting to fail. This is also seen in areas surrounded by susceptibility artefacts (blue arrows) where the white matter is decreased in signal.

9.2.1.2 Uniform distribution used with the Region Contraction Algorithm

The results found using the region contraction algorithm with the assumption that the probability distribution of the myelin values is uniformly distributed within the initial bounds set is shown below.

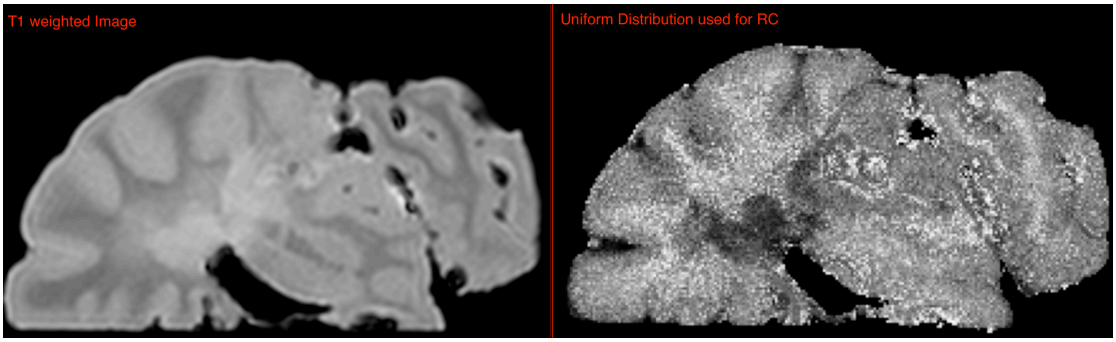

FIGURE 121: T_1-WEIGHTED IMAGE OF SLICE 130 (LEFT) AND THE RECONSTRUCTED MCDESPOT MYELIN IMAGE AT THIS SLICE USING A UNIFORM DISTRIBUTION (RIGHT)

This shows a reduced resolution of the myelin distribution in the hemisphere. There is some difference between white, grey and lesional matter but this is obscured by the noise in the map. It is not as successful as the algorithm using a Gaussion probability distribution.

9.2.1.3 Broyden-Fletcher-Goldfarb-Shanno (BFGS) algorithm

The results found using the region contraction algorithm and the BFGS algorithm are shown below.

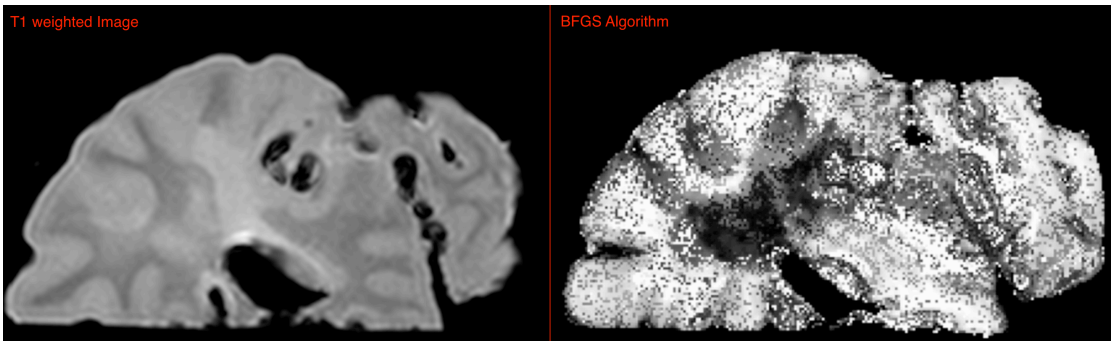

FIGURE 122: T1 WEIGHTED IMAGE OF SLICE 130 AND THE RECONSTRUCTED MCDESPOT MYELIN IMAGE AT THIS SLICE USING A BFGS ALGORITHM

The BFGS algorithm shows even poorer results than the uniform distribution, and seems unsuitable for this situation. There are multiple pixel failures, resulting in a very noisy appearing image. The lesional area has little signal as expected, but there is little differentiation between white and grey matter, though it is not straightforward to comment on this with the number of failed pixels

9.2.2 DISCUSSION

The region contraction algorithm using a uniform distribution is the default algorithm used by Deoni when this technique was first proposed. In this situation, resolving the myelin component in fixed post-mortem tissue, using the assumption that the values are distributed in a Gaussian distribution is superior. The BFGS algorithm should not be used in this situation.

The Gaussian distribution fitting is most successful in areas where there are no susceptibility artefacts, which underlines the sensitivity of the mcDESPOT algorithm to these artefacts. This is made especially difficult in large sample post-mortem scanning, as even drying the sample before insertion into Perfluorpolyether and with gentle agitation once in Perfluorpolyether, there may be some air still trapped due to the nature of the sample. In order to minimise this problem, it might be appropriate to scan smaller samples. In this

case, a set-up which gives adequate coil loading in a clinical scanner will have to be designed.

9.3 NUMBER OF FLIP ANGLES REQUIRED

In the previous section on DESPOT2 (section 7.2), the off-resonance precession was found to change between flip angles due to the variable RF pulse. Therefore, only a subset of the acquired flip angles between 7° and 56° were found to be useable, producing images with a reasonably stable banding artefact that could be removed with processing. The bSSFP images using only these flip angles were entered into the mcDESPOT algorithm.

All images were made with the bounds shown below in table 24.

Bounds	PD	T1_m	T2_m	T1_ie	T2_ie	T1_csf	T2_csf	tau_m	f_m	f_csf	f0	B1
Lower	1	0.01	0.001	0.3	0.03	1.0	0.11	0.025	0.001	0.001	-61.73	4.3e-311
Upper	1	0.3	0.02	0.8	0.1	5	3.5	0.6	0.35	0.999	61.73	1.5e-154

TABLE 24: BOUNDS USED TO INVESTIGATE THE NUMBER OF FLIP ANGLES REQUIRED TO CONSTRUCT MCDESPOT IN FIXED TISSUE

9.3.1.1 Results

The results from this reconstruction are shown below.

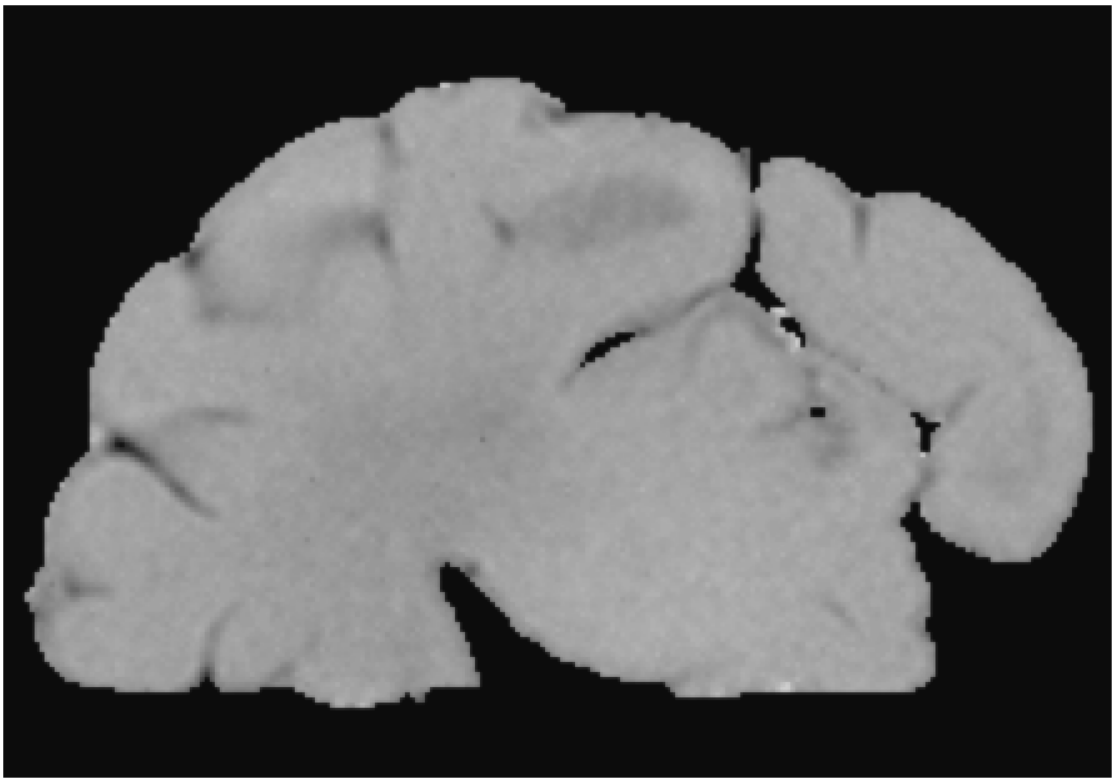

FIGURE 123: A SLICE THROUGH A MYELIN MAP PRODUCED BY THE MCDESPOT ALGORITHM WHEN BSSFP IMAGES WITH FLIP ANGLES THROUGH 7° TO 56° (SEE TABLE 19)

Using only the reduced number of flip angles, the algorithm completely fails with no definition in white or grey matter, just a uniform signal value across the slice.

However, there is an option to insert a f0 map, which removes one of the free parameters to be determined by the algorithm. If an all zero value f0 map is used, this simulates an excellent shim situation. Although this is simulated, it may be close to the truth in the centre of the hemisphere as seen in the off-resonance frequency maps in section 7.2. However, this cannot be used to give a quantitative myelin water estimation with simulated f0 values. The results are shown below.

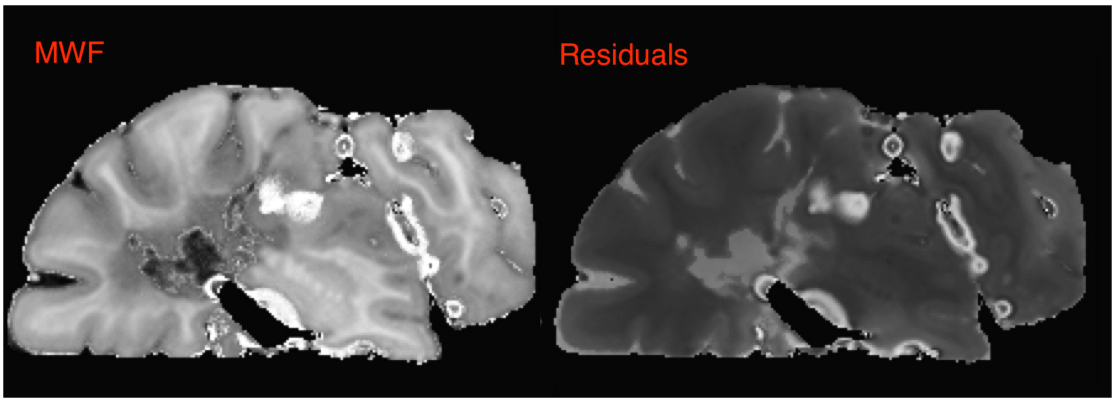

FIGURE 124: A CENTRAL SLICE THROUGH A MYELIN MAP PRODUCED BY THE MCDESPOT ALGORITHM WHEN AN ARTIFICIALLY CONSTRUCTED OFF-RESONANCE FREQUENCY F0 MAP OF ZEROS IS USED AS A PARAMETER

All the flip angles that were first acquired could be used (up to the 84 degrees), and if the banded area at the ends of the hemisphere is avoided, a good myelin map is achieved. The lesional areas next to the ventricles are more heterogeneous than expected, but it is difficult to say if this is erroneous as this image has been artificially created with the simulated zero f0 map and there is no quantitative histology available. There seems to be further decrease in signal around the more obvious lesional areas. However, this may correspond to the diffuse damage seen in the non-lesional white matter in multiple sclerosis. The susceptibility artefacts have very high values, but this is not surprising as a susceptibility artefact causes signal drop-out and the mcDESPOT algorithm would fail to determine the true value. This is shown by the corresponding high values in the residual error map.

9.4 CHOICE OF COMPARTMENT BOUNDS

The banding artefacts at the ends of the hemisphere were not removed in any of the reconstructions attempted. An example image is shown below.

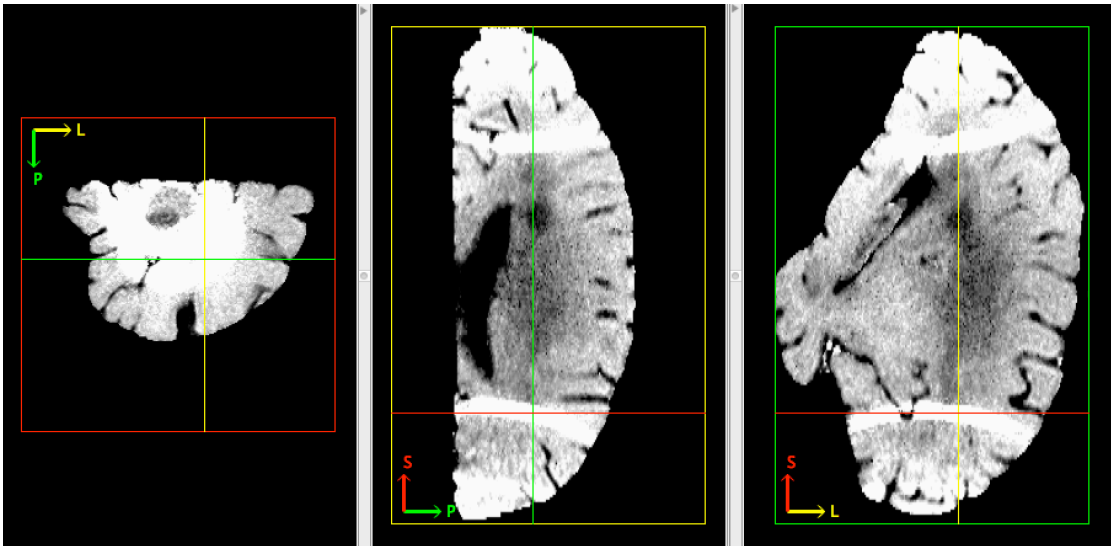

FIGURE 125: HEMISPHERE RECONSTRUCTED SHOWING BANDING ARTEFACTS AT THE ENDS OF THE HEMISPHERE

As these reconstructions were not successful in removing the banding, and the banding may affect the myelin fraction values across the field of view, the reconstructions are not considered quantitative.

However, we can still examine the central area where the banding artefacts are fewer in a qualitative manner. The bounds used for the compartment can be examined for myelin signal contrast. For this purpose, the hemisphere was reconstructed with a range of different bound values.

9.4.1 RESULTS

The bounds used and the resulting mcDESPOT myelin images are shown below. All bound values are in seconds. All the flip angles that were acquired were used for the curve fitting in the algorithm. However, as the banding is present the image was not considered quantitatively reliable for myelin water fraction.

Bounds 1	PD	T1_m	T2_m	T1_ie	T2_ie	T1_csf	T2_csf	tau_m	f_m	f_csf
Lower	1	0.01	0.005	0.5	0.04	1.5	1	0.025	0.001	0.001
Upper	1	0.4	0.03	0.8	0.15	5	3.5	0.6	0.35	0.999

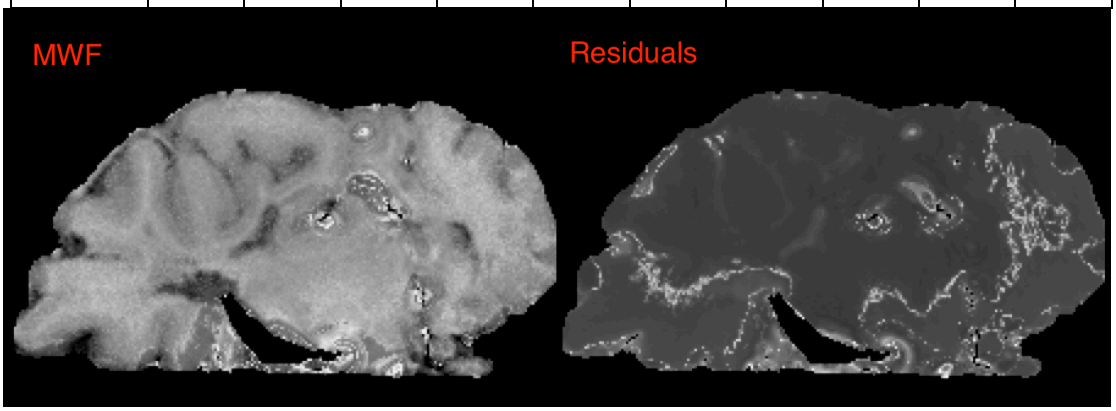

FIGURE 126: AN EXAMPLE SLICE THROUGH THE HEMISPHERE WITH THE BOUNDS USED IN THE TABLE

The myelin image, while there is slightly higher signal in the white matter, which would be correct with the higher myelin content in white matter, the definition between white and grey matter is poor. There are also susceptibility artefacts at boundaries between the hemisphere and the perfluorpolyether.

As the T_1 values are expected to be shorter due to fixation from the previous work in this thesis, the T_1 upper bound was then changed to reflect this. The lower T_2 bound was increased to 0.01 to avoid noise.

Bounds 2	PD	T1_m	T2_m	T1_ie	T2_ie	T1_csf	T2_csf	tau_m	f_m	f_csf
Lower	1	0.01	0.01	0.4	0.04	1.5	1	0.025	0.001	0.001
Upper	1	0.3	0.03	0.8	0.15	5	3.5	0.6	0.35	0.999

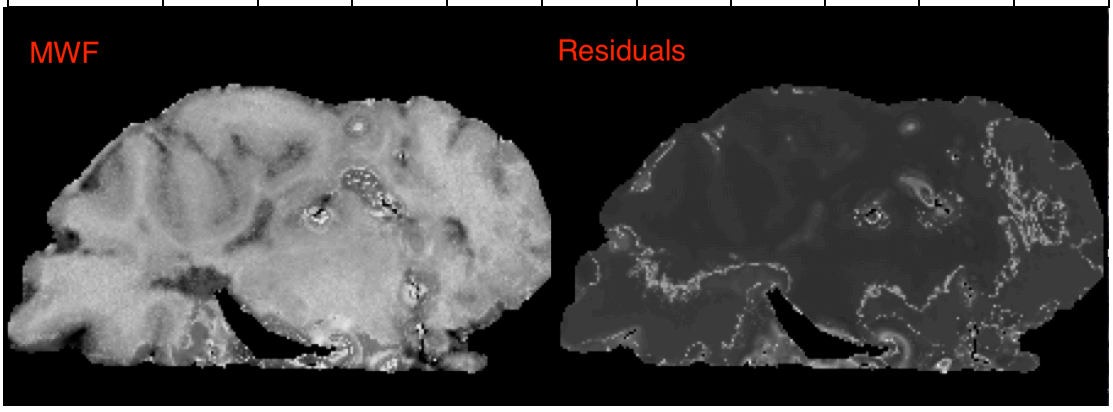

FIGURE 127: EXAMPLE SLICE THROUGH THE HEMISPHERE WITH THE BOUNDS USED IN THE TABLE

Neither of these changes made little difference to the myelin image. Therefore, in order to locate the lower T_1 bound, this was changed to 100ms.

Bounds 3	PD	T1_m	T2_m	T1_ie	T2_ie	T1_csf	T2_csf	tau_m	f_m	f_csf
Lower	1	0.1	0.01	0.4	0.04	1.5	1	0.025	0.001	0.001
Upper	1	0.3	0.03	0.8	0.15	5	3.5	0.6	0.35	0.999

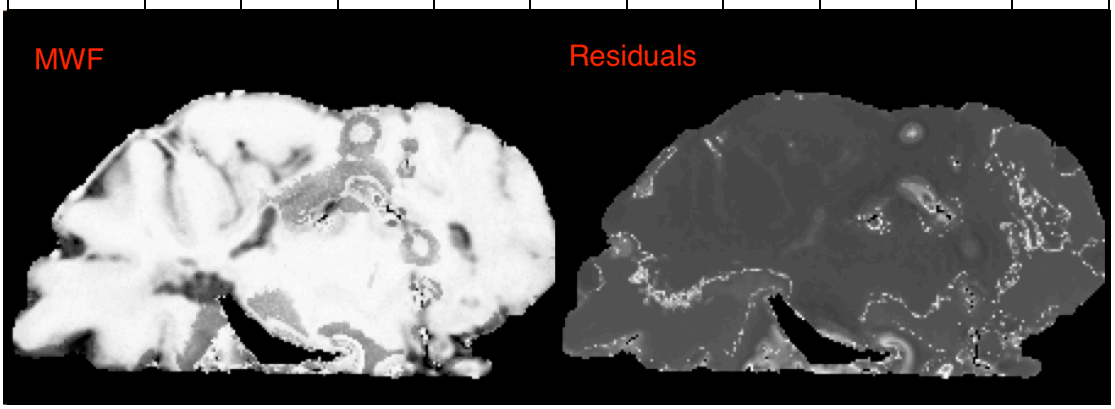

FIGURE 128: EXAMPLE SLICE THROUGH THE HEMISPHERE WITH THE BOUNDS USED IN THE TABLE

When the lower T_1 bound of myelin is set above 100ms, all myelin contrast is lost. This result implies that the T_1 of myelin must be below this value. Whether the myelin water value could be determined by the stochastic region contraction was tested by reducing the upper myelin water bound until the best contrast between WM, GM and lesion was found. This was found at 0.03s or 30ms. The results of this final reconstruction are shown below.

Bounds 4	PD	T1_m	T2_m	T1_ie	T2_ie	T1_csf	T2_csf	tau_m	f_m	f_csf
Lower	1	0.01	0.001	0.3	0.03	1.5	1	0.025	0.001	0.001
Upper	1	0.03	0.025	0.8	0.15	5	3.5	0.6	0.35	0.999

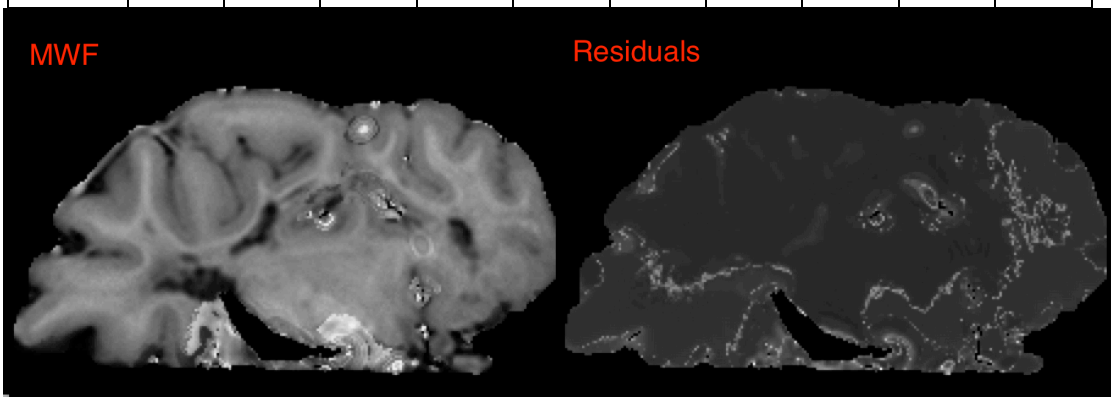

FIGURE 129: EXAMPLE SLICE THROUGH THE HEMISPHERE WITH THE BOUNDS USED IN THE TABLE

9.4.2 DISCUSSION

The best myelin map contrast was found by setting the bounds to between 0.01-0.03s. The narrow scope of these bounds imply that the search algorithm was failed to find the solution with the wider bounds used in bound set 1, even though the myelin water values were contained in these wider bounds. The residual images are similar for every bound set; this is likely due to large residual values from banding artefacts obscuring any smaller value change from bound set differences. These off-resonance artefacts are removed in the reconstruction from section 9.3.1.1 in the centre of the hemisphere when the off-resonance f0 map is forced to zero, and the residual image shows the fitting error corresponding to myelin proportion (high error at low myelin values).

9.5 NUMBER OF ITERATIONS REQUIRED

As the RC used with the Gaussian distribution provided superior results, only the improvement gained by increasing the number of iterations with this algorithm was tested. The algorithm was run with slice 130 and the number of iterations increased from one to ten.

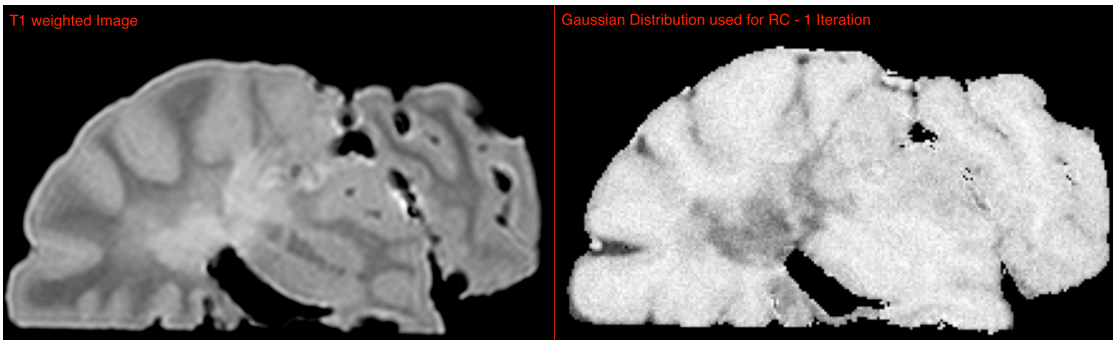

FIGURE 130: ONE ITERATION MCDESPOT RECONSTRUCTION OF SLICE 130 IN MS436R

The time taken for one iteration of one slice was 2140 seconds.

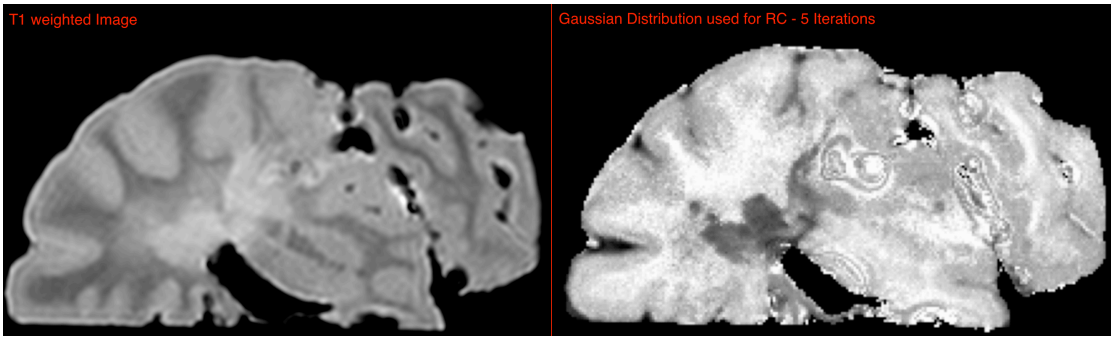

FIGURE 131: FIVE ITERATION MCDESPOT RECONSTRUCTION OF SLICE 130 IN MS436R

The time taken for five iterations of one slice was 10412 seconds.

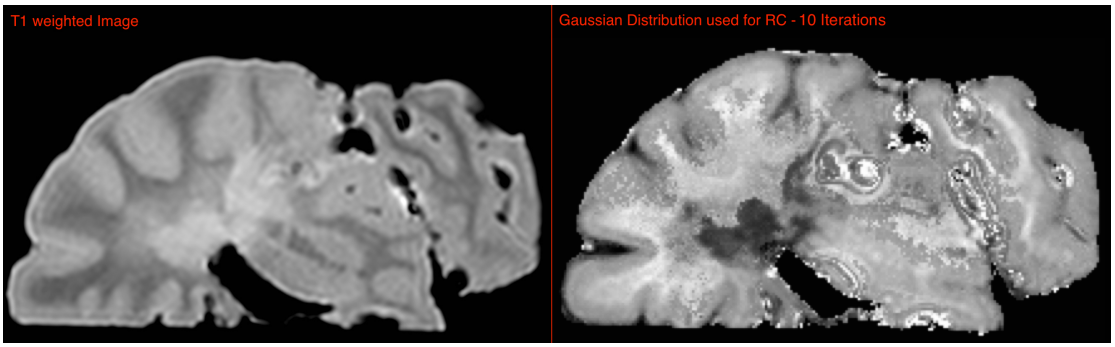

FIGURE 132: TEN ITERATION MCDESPOT RECONSTRUCTION OF SLICE 130 IN MS436R

The time taken for ten iterations of one slice was 40810 seconds.

9.5.1 DISCUSSION

There is a marked increase in distinction of structure between one and five iterations, and an approximately fivefold increase in processing time. The increase in distinction of structure between five and ten iterations is not greatly increased but the processing time between one and ten iterations is increased by twenty-fold. The later iterations have a higher processing time that does not add comparable structure distinction. Therefore 5 iterations were used for subsequent reconstructions.

9.6 WORK ON A 3T CLINICAL SCANNER IN POST-MORTEM SPINAL CORDS

The parameters used are shown below in table 25, as before.

TE (ms)	TR (ms)	SPGR FA	bSSFP FA
4.779	10	3, 6, 9, 12, 15, 18, 21, 24, 27, 30, 33, 36	
4	8.1		7, 14, 21, 28, 35, 42, 49, 56, 63, 70, 77, 84

TABLE 25: ACQUISITION PARAMETERS AT 3T ON THE PHILIPS ACHIEVA SCANNER WITH FIXED POST-MORTEM SPINAL CORDS

The images obtained were analysed for movement of the banding artefact. As, at higher flip angles, there was movement of the bands and therefore only flip angles up to 49° were used for reconstruction. The bSSFP images from 49° to 84° at a phase cycle value of 180° are shown below in figure 133.

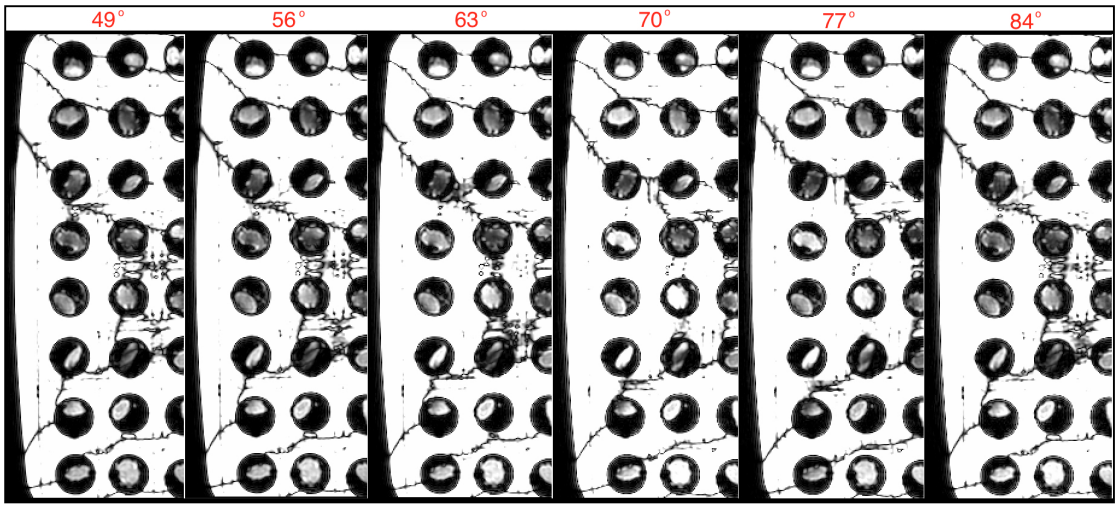

FIGURE 133: BSSFP IMAGES ACQUIRED OF MS453, MS495, MS493, MS570, MS455, MS436, MS556, MS561, MS475 AND C60

The movement of the banding can be seen in the images above especially in the centre area of the image in the surrounding water.

Using the bSSFP data with flip angles from 7 to 49°, the mcDESPOT algorithm was then used to reconstruct the data along with the SPGR data with flip angles from 3 to 36°. Four phase angles of 0, 90, 180 and 270° were used for image reconstruction.

9.6.1 RESULTS

The result of the reconstruction is given below. The bounds used were informed by those that were successful in the hemisphere in section 9.4.

Bounds	PD	T1_m	T2_m	T1_ie	T2_ie	T1_csf	T2_csf	tau_m	f_m	f_csf
Lower	1	0.01	0.001	0.3	0.03	1	0.11	0.025	0.001	0.001
Upper	1	0.03	0.02	0.8	0.1	5	3.5	0.6	0.35	0.999

TABLE 26: BOUND SET USED FOR RECONSTRUCTION OF MCDESPOT MYELIN MAPS AT 3T IN SPINAL CORDS

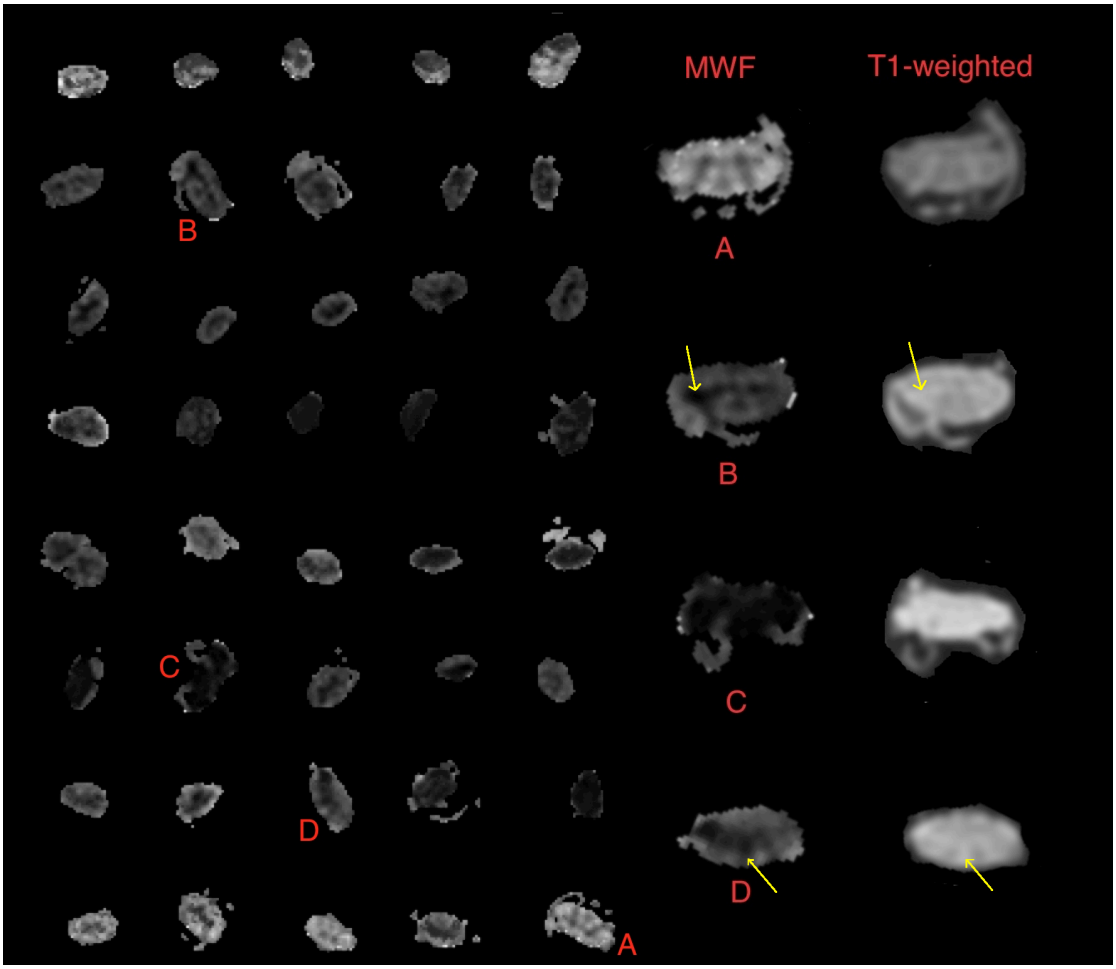

FIGURE 134: AN EXAMPLE SLICE FROM A RECONSTRUCTION USING THE MCDESPOT ALGORITHM SHOWING MYELIN WATER FRACTION IN CONTROL AND MULTIPLE SCLEROSIS SPINAL CORDS

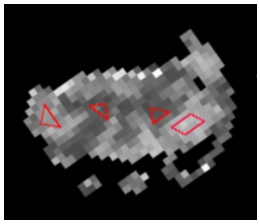

FIGURE 135: ROI IN CONTROL MS SC

Figure 134 above shows an example slice from the MWF image. Example sections from the cervical area in four spinal cords where the algorithm was most successful are shown on the right. The other thoracic and lumbar areas and other cords show some white matter/grey matter differentiation. A is from the cervical control cord, which was the overall most successful section, showing the best differentiation between WM, GM and lesion.

The accuracy of the myelin quantification in this one small region is questionable. However, regions of interest were placed in this area as shown in Figure 134. The average MWF fraction in white matter was 0.20±0.03 and 0.07±0.01 in grey matter.

B, C and D are other cervical cord areas that have either partially or completely failed to differentiate white and grey matter. However, in B and D, it is possible with comparison to the T_1-weighted images to suggest a reduction in signal in the lesional area on the MWF (shown by arrows). The lesional areas are seen as areas of increased signal on the T_1-weighted images (also shown by arrows). Image C is difficult to interpret without histology. The areas without signal imply a lack of myelin, but may be due to failure of the algorithm in this area.

Shown below in figure 136 are the histograms for control (A) and multiple sclerosis (B) sections.

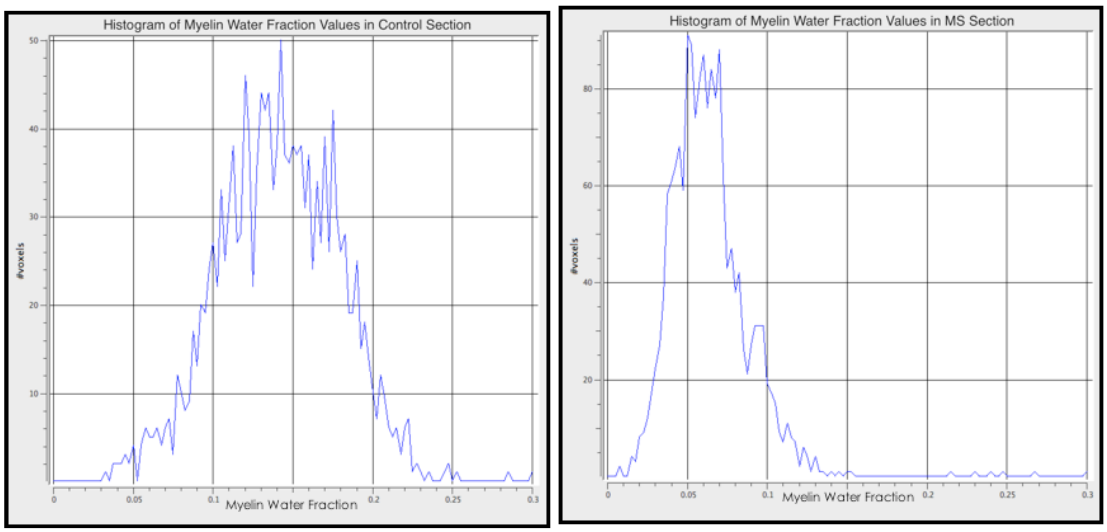

FIGURE 136: HISTOGRAMS OF THE CONTROL AND MS SPINAL CORD SECTIONS SHOWN IN FIG. 132 FOR THE BOUND SET GIVEN IN TABLE 24

9.6.2 DISCUSSION

Using the restricted bounds that were the most successful in the hemisphere, the mcDESPOT algorithm was partially successful in post-mortem fixed spinal cord. The algorithm is most successful in larger diameter cervical sections in control cord. In smaller cord sections, such as the thoracic area, the success of the algorithm in discerning structure is unsure. Histological sections of these cords would allow comparison of myelination with these images. However, from inspection, there does seem to be a measure of structure within the images.

The values of MWF in control white matter (0.20±0.03) and grey matter (0.07±0.01) are low in comparison to CPMG discerned MWF values (0.42±0.009 and 0.18±0.0016 for control WM and control GM respectively). There is a decrease in MWF values in the multiple sclerosis cord from those in the control cord as seen in the histograms of these sections, which would match the assumed clinical situation. However, there remains the question of accuracy of these values, as dependent on the upper bound set, these values change as seen in the hemisphere in section 9.4. Boundaries are chosen by the operator matching the expected structure in the spinal cords in the resulting images rather than the algorithm discerning the minima without intervention.

9.7 WORK ON A 7T PRECLINICAL SCANNER

9.7.1 METHODS

Complete formalin-fixed spinal cords of 3 pwMS (1 male, 2 female; age 67-87 years; disease duration 8-44 years; duration of fixation 1127-1441 days) were placed on a Perspex frame, inserted in glass tubes and immersed in perfluoropolyether. The whole cords were first imaged on a Philips Achieva 3T scanner using a 15 element SENSE Spine coil, allowing nine areas of interest for scanning at 7T to be identified on PD-weighted images. These areas were then scanned using a 7T pre-clinical scanner (Agilent Technologies DDR) and standard quadrature RF coil (Rapid GmbH) with a field of view of 5cm by Dr Tobias Wood at King's College London. SPGR and bSSFP (with 2 RF phase-cycles) scans were acquired with parameters given in Table 27, along with an AFI scan for B_1 correction[28].

Sequence	TE/TR (ms)	Flip-Angles	Voxel Size (μm^3)	Matrix Size
SPGR	11.3/25	6,8,10,15,20,25,35,45	100x125x200	160x160x160
bSSFP	2/4	14,17,20,25,35,50,65	100x125x200	160x160x160
AFI	2.62/7.5	55	250x250x500	64x64x64

TABLE 27: ACQUISITION PARAMETERS USED ON THE AGLIENT SCANNER FOR THE MCDESPOT SEQUENCE

The images were resampled at 150x150x300μm^3 for improved SNR. T_1, T_2 & PD maps were processed from all flip-angles by Dr Wood. The spinal cords were processed with the mcDESPOT algorithm also by Dr Wood using a uniform distribution for region contraction. As shown before in section 6.1 and in the literature[89,90], the standard sequence parameters used *in-vivo* are not suitable for fixed *post-mortem* tissue due to the changes in relaxation indices following fixation as T_1 values for grey matter (GM) and white matter (WM) appear to converge, resulting in a reduction of contrast available from T_1-weighted scans. Due to this, shorter T_1 and T_2 ranges than *in-vivo* were required to produce the MWF, IEWF & FWF maps (Table 28). These bounds were determined by Dr Wood.

Pool	MWF	IEW	FWF
T_1 (ms)	50-200	250-600	650-2000
T_2 (ms)	1-12	15-30	50-500

TABLE 28: BOUNDS USED FOR PROCESSING ACQUISITIONS FROM THE 7T AGLIENT SCANNER

MR maps were then matched with histology by comparing positional information from the 3T whole cord scans and 7T scans. ROIs were outlined on PD maps (Figure 138) produced from DESPOT2 and transferred using MIPAV to all other maps for calculation of signal value. Cords were dissected throughout into blocks of 5mm thickness, processed for embedding in paraffin, and sections stained for Haematoxylin & Eosin (H&E), Myelin Basic Protein (MBP) and SMI by Ms Natalia Petrova. Focal areas of complete myelin loss were identified as demyelinated lesions in the white (WML) and grey matter (GML). Cellularity and axonal counts were determined by counting the number of cells in four square ROIs (size: 120×120μm^2) cast onto WML and non-lesional white matter (NLWM) on H&E and SMI stained sections, and expressed as cells/mm^2 (as seen in Figure 137) also performed by Ms Petrova.

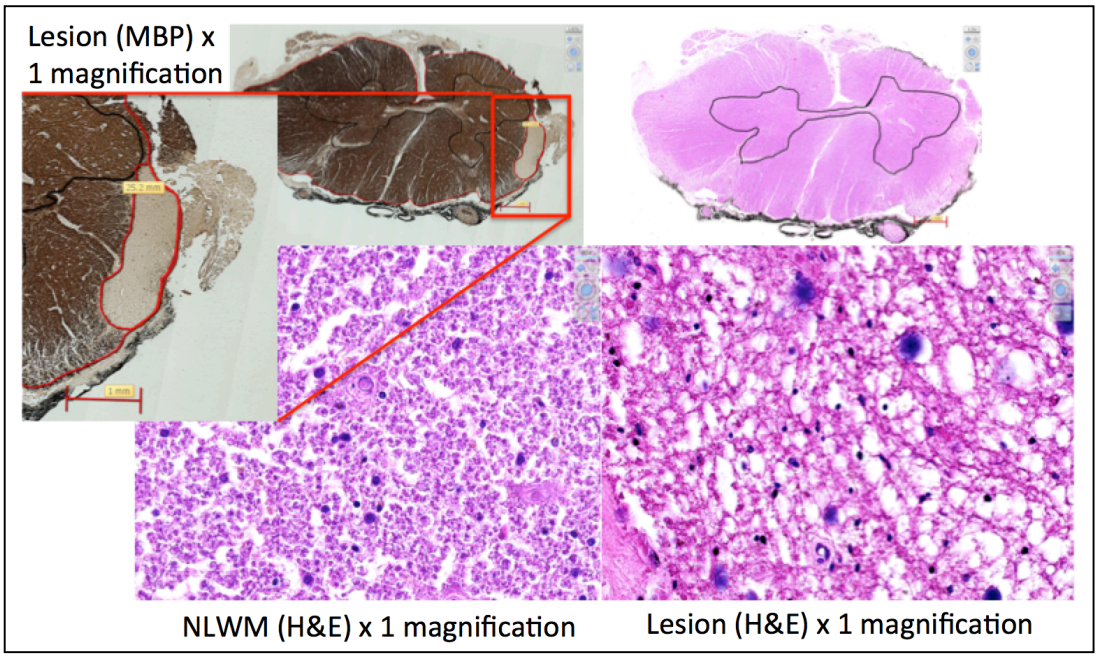

FIGURE 137: TOP LEFT IMAGE SHOWING MAGNIFICATION OF A MBP STAINED SECTION FROM THE SPINAL CORD MS471 SHOWING A LESION IN THE LATERAL COLUMN. THE H&E STAINING OF A SECTION MS471 ON THE BOTTOM LEFT SHOWS DENSE CELLULARITY IN THE NLWM WHILE THE H&E STAINING OF THE LESION AREA SHOWS SPACE BETWEEN THE CELLS WHICH COULD CONTRIBUTE TO A FREE WATER FRACTION COMPONENT

9.7.2 RESULTS

Figure 138 shows matched histology and quantitative MR index maps of three MS spinal cords.

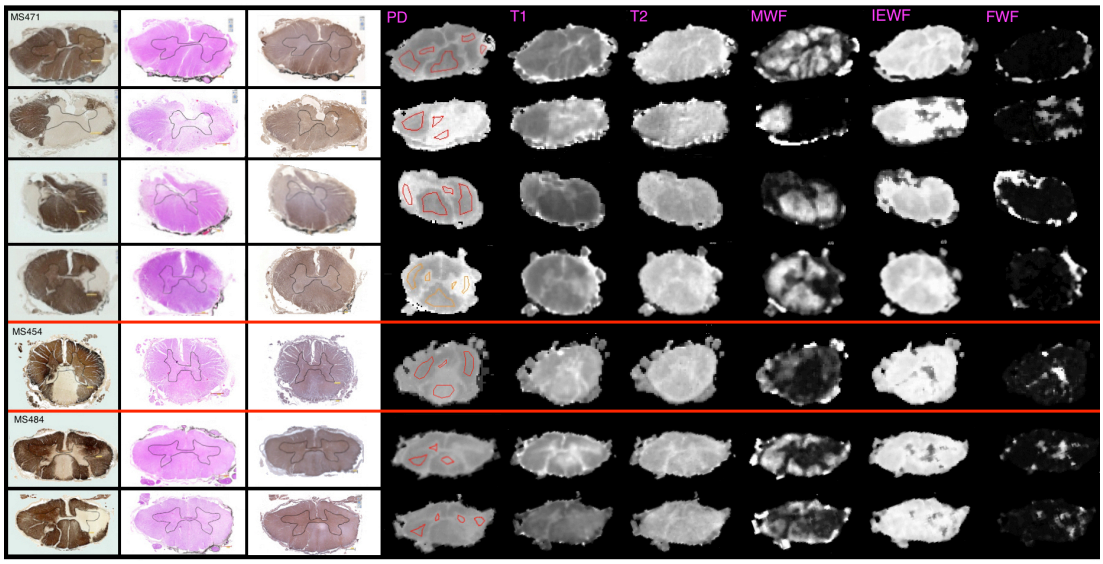

FIGURE 138: HISTOLOGICAL SECTIONS STAINED FOR MBP AND H&E, AND CORRESPONDING QUANTITATIVE MR MAPS FOR MS471, MS454 AND MS484 SPINAL CORDS

An excellent visual match was achieved between histology and PD maps, showing good anatomical detail and therefore was used to plan regions of interest. The histological slides stained with MBP, H&E and SMI at the level of each lesion found are shown next to T1, T2, MWF, IEF and FWF maps at the same level as matched by the method above. Numerical values for T1, T2, MWF%, IEF% and FWF% are shown below in Table 29.

	NLWM	NLGM	WML	GML
T_1(ms)	473±88	571±97	604±72	641±42
T_2(ms)	16±2	18±2	18±2	17±1
MWF%	10±9	9±6	2±1	3±2
IEF%	85±10	86±18	82±16	80±18
FWF%	4±2	10±18	15±16	17±18

TABLE 29: AVERAGE VALUES OF T1, T2, MWF%, IEWF% AND FWF% ACROSS ALL SPINAL CORDS

ROI	NLWM (Nuclei/mm^2)	Lesion (Nuclei/mm^2)
MS471 C8	1858	1736
MS471 T3	2546	1458
MS471 T5	1944	1892
MS471 T11	2778	2760
MS454 C7a	1615	1215
MS454 C7b	1389	1233
MS484 T11	2135	2170

TABLE 30: ABSOLUTE COUNTS OF NUCLEI IN REGIONS OF INTEREST SHOWN ON THE PD MAPS IN FIGURE 138

9.7.3 DISCUSSION

The lack of contrast shown in the T_2 maps obtained from the DESPOT2 sequence might imply that, as the MWF obtained from the mcDESPOT sequence is considered to be derived from the short T_2 component, that the MWF map would also show reduced contrast. However, this was found not to be the case, with the MWF maps showing good definition of the white, grey and lesional tissue within the spinal cord with high myelin content in the normal appearing white matter and very low myelin content in the lesions. This would suggest that there may be an influence of a short T_1 component on the derived MWF. Deoni et al.[7] hypothesised that a "direct observation of multiple T_1 components is confounded by the relative time scales of T_1 relaxation and intra-compartment exchange". In the shortened T_1 values of fixed tissue however, the T_1 values are more comparable to T_2 values *in-vivo*, and a reduced time scale for T_1 may be considered. Also, a reduced exchange of magnetisation between proton pools in fixed tissue during the T_1 recovery, due to cross-linking of molecular bonds caused by the fixation process, may enable separate T_1 components to be observed. The same paper also states that "components may be distinguished on account of unique T_1 values, unique T_2 values, or both" in the mcDESPOT analysis. Due to the processes described above caused by fixation unique T_1 values may be distinguished by the mcDESPOT analysis. This could explain why this technique reveals such good tissue contrast despite shortened relaxation times.

The IEWF maps do not hold useful information, and quantitatively in this small sample size there does not seem to be any difference between lesional tissue and NLWM/control tissue.

Some of the lesions show a significant free water component, with all lesional sections showing an increase of the FWF compared to control tissue. This may be a more reliable indicator of cellular loss, and was investigated using the H&E and SMI stained sections. Lesions that show free water have a greater amount of decellularisation on these stains, which is somewhat confirmed by the absolute count of nuclei (Table 30), though it is difficult to say in this sample size.

This implies more space in larger cells and between the cells in these areas, which would explain a larger free water component.

9.8 PRELIMINARY WORK ON A 7T WHOLEBODY SCANNER

From the DESPOT1 and 2 data used in sections 6.11 and 7.5, myelin water maps were reconstructed using the mcDESPOT algorithm. The opportunity to scan on the 7T wholebody scanner at the Magnetic Resonance Centre in Nottingham was only available for one mcDESPOT acquisition. The results of this preliminary acquisition are detailed here.

9.8.1 METHODS

The right hemisphere of MS442 was inserted in the custom-made holder, immersed in perfluorpolyether. It was imaged on the 7T Philips Achieva Scanner in the SENSE Neurovascular coil as described before in section 5.2. The flip angles were chosen to match the values used on the 7T Agilent scanner as these had been successful at isolating the myelin signal at 7T previously.

TE (ms)	TR (ms)	SPGR FA	bSSFP FA
12	28	6, 8, 10, 15, 20, 25, 35 and 40	
4.4	9		7, 10, 14, 17, 20, 25, 35 and 50

TABLE 31: ACQUISITION PARAMETERS USED FOR THE MCDESPOT SEQUENCE ON THE 7T WHOLEBODY SCANNER

9.8.2 RESULTS

The hemisphere was reconstructed with all four phase cycles with the parameters below (matched to the bounds used in the 7T work in the small animal scanner) using a 3-compartment model.

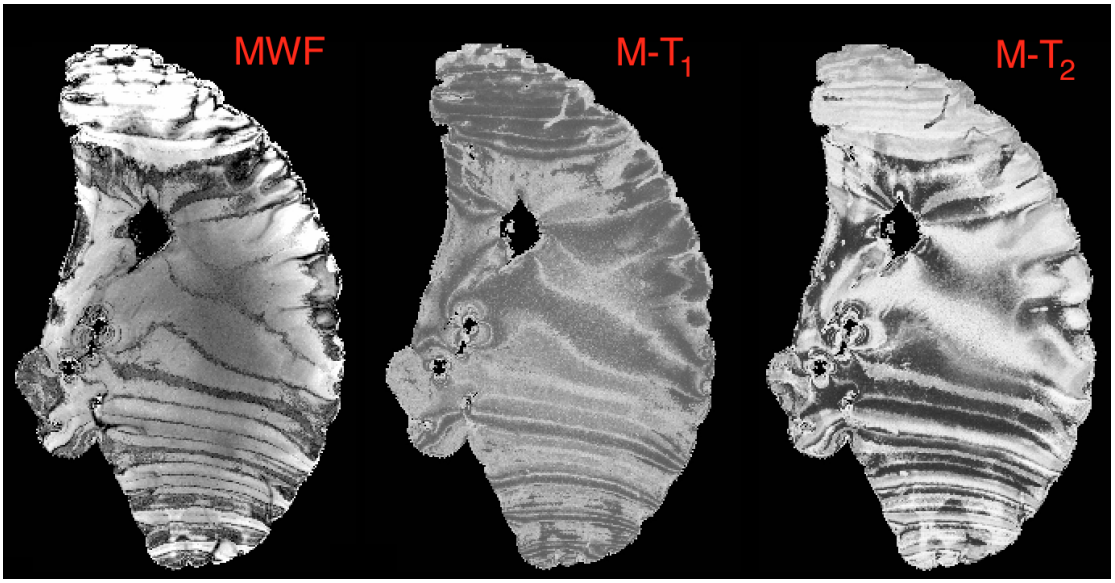

FIGURE 139: MYELIN MAP (LEFT) USING THE MCDESPOT ALGORITHM AND ALL FOUR PHASE CYCLES

Figure 139 above, shows a map of myelin water fraction and maps of the T_1 and T_2 values associated with myelin.

9.8.3 DISCUSSION

Unfortunately using the preliminary data acquired, the reconstruction was not successful. The reconstructed images show severe banding artefacts throughout the hemisphere. Most, if not all structure is obscured, with the most severe banding at either end of the hemisphere. This is caused by the large signal variation across the field of view in the 7T scanner causing such severe banding artefacts that even with RF phase cycling with four different images, the signal could not be recovered. The bands occur so close together that there is no spatial location between them that is not affected by the bands. The algorithm takes the maximal signal at each voxel between the RF phase with high signal and the RF phase containing low signal in the banding artefact, recovering the true signal across the image. In this case, the maximal signal is never sampled as the bands move with RF phase cycling, as the voxel is always within a banding artefact. This means the true signal for that voxel can never be recovered.

The worse the B_0 inhomogeneity, the higher the added phase precession and more frequent and closer together the off-resonance banding artefact

appears. With the inhomogeneity seen in the whole hemisphere, it would be recommended that the acquisition should be repeated using smaller sections of brain tissue for better B_0 homogeneity across the sample. If the TR is also kept as short as possible, this may lead to an acquisition where the banding artefact can be removed. The nature of the bSSFP sequence, being sensitive to off-resonance effects and B_0 inhomogeneity (which is pronounced at higher field strengths) will make it difficult to acquire this sequence successfully at 7T.

9.9 LESION CASE STUDY

A lesion was documented using the 7T Aglient scanner that was visible on the PD and MWF map but was not on the MBP staining. However, this lesion was visible on the LFB, showing that the MRI was able to visualise when there is myelination but the phospholipids are disturbed.

FIGURE 140: SAGITTAL PD MAP SHOWING THE TWO LESIONS VISUALISED IN THE LUMBAR AREA

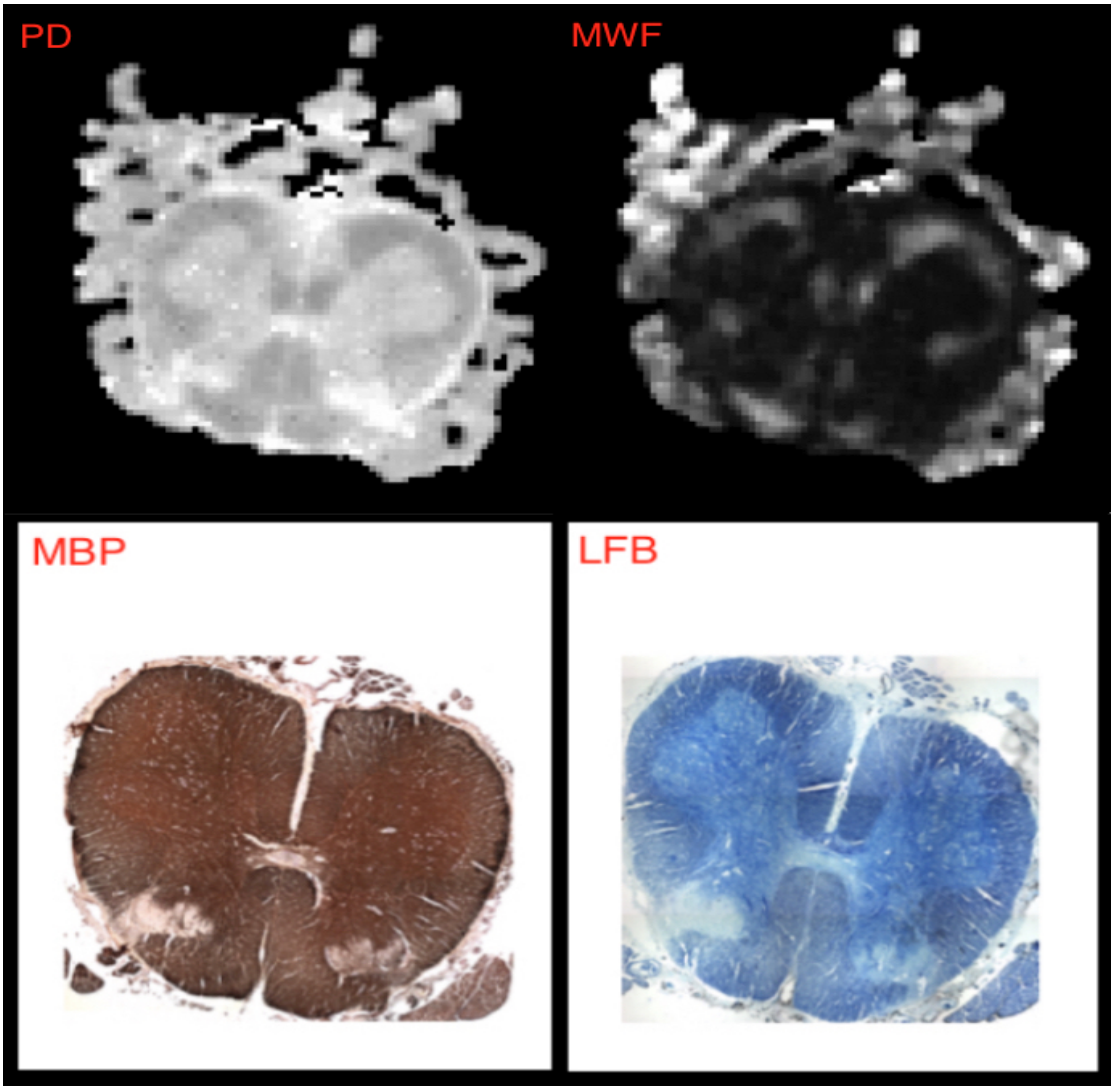

FIGURE 141: FIGURE SHOWING A MR DERIVED PD MAP (TOP LEFT), A MYELIN WATER FRACTION MAP (TOP RIGHT), AND HISTOLOGICAL MBP (BOTTOM LEFT) AND LUXOL FAST BLUE (BOTTOM RIGHT) STAINING. THE LESION IS CLEARLY VISABLE IN THE MR IMAGES AND THE LBF STAIN BUT THERE IS NO CORRESPONDING LOSS IN THE MBP STAIN

9.10 SUMMARY

The mcDESPOT algorithm has been applied in post-mortem fixed tissue for the first time. The parameters of the algorithm for best use in fixed tissue were first examined. As detailed in the DESPOT2 chapter, the acquisition sequences were restricted by the clinical scanner at 3T, which constrained the success of the algorithm, as the algorithm can only separate the myelin water fraction component with a successful DESPOT2 acquisition. This limited the conclusions which can be drawn about the algorithm in this situation. However, these

limitations have been examined and the solution provided of use of fixed length RF pulses which would be expected to provide a successful acquisition at 3T. The clinical acquisition at 7T is deeply affected by the inhomogeneous B_0 field, possibly more affected than can be corrected with a successful RF phase cycling scheme even with accurate f_0 determination.

The mcDESPOT algorithm has been histologically validated in the spinal cord at 7T. These results have shown that in ideal imaging conditions (small imaging volume, narrow bore, and high field strength) the myelin water fraction determined by the mcDESPOT algorithm is proportional to myelin content.

This validation of the mcDESPOT sequence is a validation of the sequence in a high signal situation, such as those published by Deoni et al. *in-vivo*. However, the results in this thesis show that the success of mcDESPOT algorithm in a low signal situation requires a different search algorithm, such as Bayesian methods. This may improve the results *in-vivo* also, though this is beyond the scope of this thesis. The results in this chapter inform users of the mcDESPOT algorithm of the accuracy of the myelin measurements in the published literature.

10 DISCUSSION

In this thesis, T_1, T_2, and myelin water fraction mapping has been examined in fixed post-mortem tissue. Relative to in-vivo, fixed tissue has limiting factors of reduced T_1 and T_2 values, which were confirmed with TSE-IR T_1 mapping and single-exponential CPMG T_2 mapping. The added reduction of myelination by the diffuse damage caused by MS, when it is considered that contrast in the brain and spinal cord originates from myelin, causes signal distinction between white and grey matter to be low. These factors result in a low-contrast, low-signal imaging situation.

The agreement of the fast steady-state DESPOT1 T_1 map and DESPOT2 T_2 map values with gold standard methods of TSE-IR T_1 mapping and single-exponential CPMG T_2 mapping has been investigated. The CPMG sequence was acquired with an echo train length of 32, which allowed extra pre-processing to deconvolve the data into multi-exponential components and separate the short T_2 component of water which is thought to correspond to myelin content. As this method has been histologically validated, it was considered the gold standard for myelin water quantification. Using the DESPOT1 and DESPOT2 data in combination, the mcDESPOT algorithm was used to reconstruct myelin water maps.

The fast DESPOT1 T_1 mapping method was evaluated in fixed post-mortem tissue. The DESPOT1 SPGR fitting algorithms (LLS, WLLS and NLLS) have not been evaluated and compared before in this context and constitute original work. The NLLS algorithm was found to provide T_1 values closest to the TSE-IR T_1 values. It should be noted that the DESPOT1 algorithm was acquired with 12 flip angle values for further myelin water data reconstruction. It is more usually acquired with two optimised flip angles around the Ernst angle for solely T_1 value determination. The excess of data points should increase the accuracy of the fit. In further work, it would be interesting to evaluate the difference in values between these two acquisitions.

The DESPOT2 bSSFP data fitting algorithms (2-step LM and BFGS) were evaluated and the LM algorithm was found to provide T_2 values closest to the

single-exponential values derived from the CPMG sequence. Again it should be noted that DESPOT2 is usually acquired with two flip angles. The reconstruction was also impeded by the banding artefacts, which are common to bSSFP images. Here the bands were unable to be removed from the data, even with RF phase cycling, without access to pulse programming with a research license. This reduced the number of flip angles that could be used for fitting.

The CPMG sequence was successful in the fixed post-mortem brain hemisphere and spinal cord. Original data of the CPMG sequence used at 3T was acquired with both brain hemisphere and spinal cord. There has been one other case report using the CPMG on MS spinal cord with only one MS sample[113]. Here, three fixed whole spinal cord samples and a fixed whole control cord sample have been imaged and compared to histology. There has also been preliminary work with non-fixed MS spinal cord.

High MWF values were found from the CPMG myelin water fraction maps, relative to *in-vivo* values. The cause of this may be the reduced water in the samples after fixation but may also be due to slower exchange between compartments, as the samples are imaged at room temperature where exchange is slower[114] and also the slowing of exchange due to the cross-linking of bonds due to the fixation process.

The mcDESPOT algorithm shows partial success in fixed tissue with more promising results in the brain hemisphere and cervical control spinal cord. The stochastic region contraction algorithm was only successful when the bounds for T1 attributed to myelin were set with the narrow range of 20ms. When other bound range were used, still covering the narrower range that showed partial success, the algorithm was unable to converge to the results that gave the partial success.

Converging on other incorrect minima is a known limitation of the stochastic region contraction algorithm[128]. The initial bound set passed to the algorithm affects the result and must be chosen carefully or in this case with very narrow limits. However, If the search space was limited any further than the bounds set

for T_1 value of the myelin component that was found to be successful in this thesis, it would make a search for a solution by algorithm unnecessary.

Bouhrara et al.[157] found that even for the simplest two-pool signal model consisting of MWF and non-myelin-associated water, the dimensionality of the parameter space for obtaining MWF estimates was high. They suggest the use of Bayesian methods instead of the stochastic region contraction implementation of NLLS algorithm to improve MWF estimation. Further work in this area would be to implement Bayesian methods to investigate any improvement in the low contrast situation of fixed MS tissue.

However, the unsuccessful results for the mcDESPOT sequence reported in this thesis could be due to the limited number of flip angles used. With the option of sequence programming available on the Philips scanner, enabling the sequence to be acquired correctly with a fixed TR resulting in stationary banding at all flip angles in the bSSFP images, the algorithm may be more successful. The use of variable rate RF pulses is necessary as fixed RF pulses cannot produce the higher flip angles without breaching SAR limits with the same sequence timing. The stretching of the RF pulses, keeping the maximum amplitude under SAR limits, mean that the full curve can be sampled at higher flip angles rather than being limited to lower flip angles and lower information gained for full curve fitting for T_2. The same effect could be achieved by lengthening the fixed RF pulse time until the SAR limits were not breached. This would affect the length of the acquisition sequences, though this would be a reduced problem in post-mortem work.

A limitation of this project is that a large simulation was not undertaken at the start, which may have shown that the mcDESPOT sequence would have been unsuccessful in the circumstances it was finally acquired under. However, the mcDESPOT sequence had been shown to be successful in obtaining what are ostensibly myelin water images *in-vivo* in multiple publications, and the mcDESPOT sequence was been successful in separation of the myelin water fraction in fixed spinal cord in the initial acquisitions at King's College London on the 7T pre-clinical scanner. Therefore, it was expected that the application of this sequence to *post-mortem* tissue at 3T would require only the optimisation

of acquisition parameters, much like the approach needed for the CPMG sequence in earlier work. Once it was discovered that the higher flip angles could not be obtained without the variable rate pulses, and the pulse length could not be set to a fixed length without sequence programming permissions, the intent was to obtain this from the manufacturer. This was not possible, and the final acquisitions were not acquired with optimal parameters. Before any other acquisitions are made in fixed tissue on a clinical 3T scanner, it would be useful to simulate the acquisitions with the proposed changes to check whether they would be successful, as the sequence in these circumstances has been found to be challenging.

Another effect on the mcDESPOT sequence is magnetisation transfer which is the exchange of spin magnetisation between free water protons and macromolecular protons. As the magnetisation relaxation time in the macromolecular protons is so short, magnetisation transferred to this pool can no longer be detected, meaning that this exchange process causes a loss of signal. This process is inherent to all steady-state measurements on biological systems[158] and will affect the measurement precision of short T_1[131] and T_2[159] values. The use of very short RF pulses per repetition time reduces banding artefacts and minimises finite RF pulse effects, but this will lead to considerable MT effects because MT scales as the square of the pulse amplitude[159]. The converse of using prolonged RF pulses per repetition time to minimise MT effects leads to increased finite pulse effects. Boulant et al.[160] implemented a correction for finite pulse effects into the Bloch equations to compensate for relaxation and MT effects during excitation. Using finite pulse effect correction in the algorithm would mean that RF pulse duration could be increased to minimise MT effects; this would be balanced by the increased banding artefact with longer TR. However, phase cycling may be successful in correcting the banding artefact once the RF pulse length is fixed. The interplay between all these factors requires optimisation at higher field strengths and in fixed tissue, and sequence programming capability would be required to set the RF pulse length.

11 CONCLUSION

The determination of the relaxation parameters T_1 and T_2 and their role in monitoring myelin in demyelinating diseases has been shown in this work. The shortening of T_1 in fixed tissue reduced its ability to differentiate white and grey matter and was found not to be useful. The multi-exponential nature of T_2 in the brain and spinal cord has been found to be very useful in the short T_2 CPMG sequence to separate the myelin water fraction. In this thesis, the success of the short T_2 CPMG sequence was examined at 3T and was shown to be successful in the white matter and deep grey matter, but was found to be unsuccessful in cortical grey matter. This finding demostrates the expected success of this sequence and algorithm *in-vivo* and its utility in disease monitoring at this field strength. The fast steady-state sequence mcDESPOT can be also used to determine myelin water fraction in clinically acceptable times, in comparison to the short T_2 CPMG sequence. However, it has not been histologically evaluated in the literature to determine if the myelin measure produced is accurate. Therefore, fixed post-mortem tissue that could be imaged and then histologically assessed and compared with MR imaging was used. This brought challenges as fixation causes chemical changes that affect the imaging parameters. Unfortunately, there were also some other imaging challenges, as sequence programming was not available to fully optimise the sequences. However, these limitations have been identified, and with the changes to the sequences detailed in this thesis added, imaging fixed post-mortem tissue with the mcDESPOT sequence should be successful. In further work, applying the mcDESPOT sequence successfully in fixed tissue, especially in a larger fixed brain hemisphere, using a clinical scanner will fully verify the sequence. To do this will require access to the balanced SSFP sequence code and possibly the use of a different search algorithm, such as a Bayesian method.

12 REFERENCES

1. Bernstein MAK, K.F.; Zhou, X.J. Handbook of MRI Pulse Sequences: Elsevier; 2004.
2. Tofts PS. Quantitative MRI of the Brain: Wiley; 2003.
3. Brown RY-C, N.; Cheng, E.; Haacke, M.; Thompson, M.; Venkatesan, R.;. Magnetic Resonance Imaging: Physical Principles and Sequence Design, Second Edition. 2014.
4. Elster ADB, J.H. Questions and answers in Magnetic Resonance Imaging. Second Edition ed: Mosby; 2001.
5. Farahani K, Sinha U, Sinha S, Chiu LC, Lufkin RB. Effect of field strength on susceptibility artifacts in magnetic resonance imaging. *Computerized medical imaging and graphics : the official journal of the Computerized Medical Imaging Society* 1990; **14**(6): 409-13.
6. Ludeke KM, Roschmann P, Tischler R. Susceptibility artefacts in NMR imaging. *Magnetic resonance imaging* 1985; **3**(4): 329-43.
7. Deoni SC, Rutt BK, Arun T, Pierpaoli C, Jones DK. Gleaning multicomponent T1 and T2 information from steady-state imaging data. *Magnetic resonance in medicine* 2008; **60**(6): 1372-87.
8. Zur Y, Wood ML, Neuringer LJ. Spoiling of transverse magnetization in steady-state sequences. *Magnetic resonance in medicine* 1991; **21**(2): 251-63.
9. Barral JK, Gudmundson E, Stikov N, Etezadi-Amoli M, Stoica P, Nishimura DG. A robust methodology for in vivo T1 mapping. *Magnetic resonance in medicine* 2010; **64**(4): 1057-67.
10. Wang HZ, Riederer SJ, Lee JN. Optimizing the precision in T1 relaxation estimation using limited flip angles. *Magnetic resonance in medicine* 1987; **5**(5): 399-416.
11. Fram EK, Herfkens RJ, Johnson GA, et al. Rapid calculation of T1 using variable flip angle gradient refocused imaging. *Magnetic resonance imaging* 1987; **5**(3): 201-8.
12. Homer J, Beevers M. Driven-Equilibrium Single-Pulse Observation of TI Relaxation. A reevaluation of a rapid new method for determining NMR spin lattice relaxation times. *Journal of Magnetic Resonance* 1985; **63**: 287-97.
13. Deoni SC, Rutt BK, Peters TM. Rapid combined T1 and T2 mapping using gradient recalled acquisition in the steady state. *Magnetic resonance in medicine* 2003; **49**(3): 515-26.
14. Kellman P, Arai AE, McVeigh ER, Aletras AH. Phase-sensitive inversion recovery for detecting myocardial infarction using gadolinium-delayed hyperenhancement. *Magnetic resonance in medicine* 2002; **47**(2): 372-83.
15. Meiboom S, Gill D. Modified Spin - Echo Method for Measuring Nuclear Relaxation Times. *Review of Scientific Instruments* 1958; **29**(8): 688-91.
16. Carr HYaP, E. M. Effects of Diffusion on Free Precession in Nuclear Magnetic Resonance Experiments. *Phys Rev* 1954; **94**(3): 630-8.
17. MacKay A, Laule C, Vavasour I, Bjarnason T, Kolind S, Madler B. Insights into brain microstructure from the T2 distribution. *Magnetic resonance imaging* 2006; **24**(4): 515-25.

18. Yang QX, Wang J, Zhang X, et al. Analysis of wave behavior in lossy dielectric samples at high field. *Magnetic resonance in medicine* 2002; **47**(5): 982-9.
19. Scheffler K, Hennig J. Is TrueFISP a gradient-echo or a spin-echo sequence? *Magnetic resonance in medicine* 2003; **49**(2): 395-7.
20. Deoni SC, Ward HA, Peters TM, Rutt BK. Rapid T2 estimation with phase-cycled variable nutation steady-state free precession. *Magnetic resonance in medicine* 2004; **52**(2): 435-9.
21. Perkins TG, Wehrli FW. CSF signal enhancement in short TR gradient echo images. *Magnetic resonance imaging*; **4**(6): 465-7.
22. Deoni SC. Transverse relaxation time (T2) mapping in the brain with off-resonance correction using phase-cycled steady-state free precession imaging. *Journal of magnetic resonance imaging : JMRI* 2009; **30**(2): 411-7.
23. Hargreaves BA. Fast Gradient Echo Sequences Including Balanced SSFP. http://mrsrl.stanford.edu/www/studygroup/2/Files/Hargreaves_ISMRM.pdf2016).
24. Spencer RG, Fishbein KW. Measurement of spin-lattice relaxation times and concentrations in systems with chemical exchange using the one-pulse sequence: breakdown of the Ernst model for partial saturation in nuclear magnetic resonance spectroscopy. *Journal of magnetic resonance (San Diego, Calif : 1997)* 2000; **142**(1): 120-35.
25. Deoni SC, Rutt BK, Jones DK. Investigating exchange and multicomponent relaxation in fully-balanced steady-state free precession imaging. *Journal of magnetic resonance imaging : JMRI* 2008; **27**(6): 1421-9.
26. Deoni SC, Matthews L, Kolind SH. One component? Two components? Three? The effect of including a nonexchanging "free" water component in multicomponent driven equilibrium single pulse observation of T1 and T2. *Magnetic resonance in medicine* 2013; **70**(1): 147-54.
27. Berger MF, Silverman HF. Microphone array optimization by stochastic region contraction. *Signal Processing, IEEE Transactions on* 1991; **39**(11): 2377-86.
28. Yarnykh VL. Actual flip-angle imaging in the pulsed steady state: a method for rapid three-dimensional mapping of the transmitted radiofrequency field. *Magnetic resonance in medicine* 2007; **57**(1): 192-200.
29. Gupta RK. A new look at the method of variable nutation angle for the measurement of spin-lattice relaxation times using fourier transform NMR. *Journal of Magnetic Resonance (1969)* 1977; **25**(1): 231-5.
30. Hennig J. Multiecho imaging sequences with low refocusing flip angles. *Journal of Magnetic Resonance* 1988; **78**(3): 397-407.
31. Whittall KP, MacKay AL. Quantitative interpretation of NMR relaxation data. *Journal of Magnetic Resonance (1969)* 1989; **84**(1): 134-52.
32. Prasloski T, Madler B, Xiang QS, MacKay A, Jones C. Applications of stimulated echo correction to multicomponent T2 analysis. *Magnetic resonance in medicine* 2012; **67**(6): 1803-14.
33. Marquardt DW. An algorithm for least-squares estimation of nonlinear parameters. *Journal of the society for Industrial and Applied Mathematics* 1963; **11**(2): 431-41.
34. Levenberg K. a method for the solution of certain nonlinear problems in least squares. *Quart Appl Math 2* 1944; **164**: 164-8.

35. Compston AM, I.R.; Noseworthy, J.; Lassman, H.; Miller, D.H.; Smith, J.K.; Wekerle, H.; Confavreux, C.;. McAlpine's Multiple Sclerosis. 4th ed: Elsevier; 2005.
36. Mackenzie IS, Morant SV, Bloomfield GA, MacDonald TM, O'Riordan J. Incidence and prevalence of multiple sclerosis in the UK 1990-2010: a descriptive study in the General Practice Research Database. *Journal of neurology, neurosurgery, and psychiatry* 2014; **85**(1): 76-84.
37. Society MS. About MS. 2014. http://www.mssociety.org.uk/what-is-ms/information-about-ms/about-ms.
38. Purves D. Neuroscience. Fourth Edition ed: Sinauer Associates; 2008.
39. Squire L, Bloom FE, Spitzer NC, et al. Fundamental Neuroscience: Elsevier Science & Technology; 2008.
40. Compston A, Coles A. Multiple sclerosis. *Lancet (London, England)* 2008; **372**(9648): 1502-17.
41. Yong VW, Marks S. The interplay between the immune and central nervous systems in neuronal injury. *Neurology* 2010; **74 Suppl 1**: S9-S16.
42. Frohman EM, Racke MK, Raine CS. Multiple Sclerosis — The Plaque and Its Pathogenesis. *New England Journal of Medicine* 2006; **354**(9): 942-55.
43. Thomalla G, Glauche V, Koch MA, Beaulieu C, Weiller C, Rother J. Diffusion tensor imaging detects early Wallerian degeneration of the pyramidal tract after ischemic stroke. *NeuroImage* 2004; **22**(4): 1767-74.
44. Poloni G, Minagar A, Haacke EM, Zivadinov R. Recent developments in imaging of multiple sclerosis. *The neurologist* 2011; **17**(4): 185-204.
45. Popescu V, Agosta F, Hulst HE, et al. Brain atrophy and lesion load predict long term disability in multiple sclerosis. *Journal of neurology, neurosurgery, and psychiatry* 2013.
46. Polman CH, Reingold SC, Banwell B, et al. Diagnostic criteria for multiple sclerosis: 2010 revisions to the McDonald criteria. *Annals of neurology* 2011; **69**(2): 292-302.
47. Bergers E, Bot JC, De Groot CJ, et al. Axonal damage in the spinal cord of MS patients occurs largely independent of T2 MRI lesions. *Neurology* 2002; **59**(11): 1766-71.
48. Bot JC, Blezer EL, Kamphorst W, et al. The spinal cord in multiple sclerosis: relationship of high-spatial-resolution quantitative MR imaging findings to histopathologic results. *Radiology* 2004; **233**(2): 531-40.
49. DeLuca GC, Ebers GC, Esiri MM. Axonal loss in multiple sclerosis: a pathological survey of the corticospinal and sensory tracts. *Brain : a journal of neurology* 2004; **127**(Pt 5): 1009-18.
50. DeLuca GC, Williams K, Evangelou N, Ebers GC, Esiri MM. The contribution of demyelination to axonal loss in multiple sclerosis. *Brain : a journal of neurology* 2006; **129**(Pt 6): 1507-16.
51. Ganter P, Prince C, Esiri MM. Spinal cord axonal loss in multiple sclerosis: a post-mortem study. *Neuropathology and applied neurobiology* 1999; **25**(6): 459-67.
52. Agosta F, Absinta M, Sormani MP, et al. In vivo assessment of cervical cord damage in MS patients: a longitudinal diffusion tensor MRI study. *Brain : a journal of neurology* 2007; **130**(Pt 8): 2211-9.

53. Kidd D, Thorpe JW, Thompson AJ, et al. Spinal cord MRI using multi-array coils and fast spin echo. II. Findings in multiple sclerosis. *Neurology* 1993; **43**(12): 2632-7.
54. Kidd D, Thorpe JW, Kendall BE, et al. MRI dynamics of brain and spinal cord in progressive multiple sclerosis. *Journal of neurology, neurosurgery, and psychiatry* 1996; **60**(1): 15-9.
55. Losseff NA, Webb SL, O'Riordan JI, et al. Spinal cord atrophy and disability in multiple sclerosis. A new reproducible and sensitive MRI method with potential to monitor disease progression. *Brain : a journal of neurology* 1996; **119 (Pt 3)**: 701-8.
56. Thorpe JW, Kidd D, Moseley IF, et al. Serial gadolinium-enhanced MRI of the brain and spinal cord in early relapsing-remitting multiple sclerosis. *Neurology* 1996; **46**(2): 373-8.
57. Thorpe JW, Kidd D, Moseley IF, et al. Spinal MRI in patients with suspected multiple sclerosis and negative brain MRI. *Brain : a journal of neurology* 1996; **119 (Pt 3)**: 709-14.
58. Barkhof F, Bruck W, De Groot CJ, et al. Remyelinated lesions in multiple sclerosis: magnetic resonance image appearance. *Archives of neurology* 2003; **60**(8): 1073-81.
59. Kolind SH, Deoni SC. Rapid three-dimensional multicomponent relaxation imaging of the cervical spinal cord. *Magnetic resonance in medicine* 2011; **65**(2): 551-6.
60. White ML, Zhang Y, Healey K. Cervical spinal cord multiple sclerosis: evaluation with 2D multi-echo recombined gradient echo MR imaging. *The journal of spinal cord medicine* 2011; **34**(1): 93-8.
61. Bergers E, Bot JC, van der Valk P, et al. Diffuse signal abnormalities in the spinal cord in multiple sclerosis: direct postmortem in situ magnetic resonance imaging correlated with in vitro high-resolution magnetic resonance imaging and histopathology. *Annals of neurology* 2002; **51**(5): 652-6.
62. Mews I, Bergmann M, Bunkowski S, Gullotta F, Bruck W. Oligodendrocyte and axon pathology in clinically silent multiple sclerosis lesions. *Multiple sclerosis (Houndmills, Basingstoke, England)* 1998; **4**(2): 55-62.
63. Bjartmar C, Kidd G, Mork S, Rudick R, Trapp BD. Neurological disability correlates with spinal cord axonal loss and reduced N-acetyl aspartate in chronic multiple sclerosis patients. *Annals of neurology* 2000; **48**(6): 893-901.
64. Cambron M, D'Haeseleer M, Laureys G, Clinckers R, Debruyne J, De Keyser J. White-matter astrocytes, axonal energy metabolism, and axonal degeneration in multiple sclerosis. *Journal of cerebral blood flow and metabolism : official journal of the International Society of Cerebral Blood Flow and Metabolism* 2012; **32**(3): 413-24.
65. Henderson AP, Barnett MH, Parratt JD, Prineas JW. Multiple sclerosis: distribution of inflammatory cells in newly forming lesions. *Annals of neurology* 2009; **66**(6): 739-53.
66. Nijeholt GJ, Bergers E, Kamphorst W, et al. Post-mortem high-resolution MRI of the spinal cord in multiple sclerosis: a correlative study with conventional MRI, histopathology and clinical phenotype. *Brain : a journal of neurology* 2001; **124**(Pt 1): 154-66.

67. Lovas G, Szilagyi N, Majtenyi K, Palkovits M, Komoly S. Axonal changes in chronic demyelinated cervical spinal cord plaques. *Brain : a journal of neurology* 2000; **123 (Pt 2)**: 308-17.
68. Bjartmar C, Kinkel RP, Kidd G, Rudick RA, Trapp BD. Axonal loss in normal-appearing white matter in a patient with acute MS. *Neurology* 2001; **57**(7): 1248-52.
69. Wujek JR, Bjartmar C, Richer E, et al. Axon loss in the spinal cord determines permanent neurological disability in an animal model of multiple sclerosis. *Journal of neuropathology and experimental neurology* 2002; **61**(1): 23-32.
70. Bieniek M, Altmann DR, Davies GR, et al. Cord atrophy separates early primary progressive and relapsing remitting multiple sclerosis. *Journal of neurology, neurosurgery, and psychiatry* 2006; **77**(9): 1036-9.
71. Rocca MA, Horsfield MA, Sala S, et al. A multicenter assessment of cervical cord atrophy among MS clinical phenotypes. *Neurology* 2011; **76**(24): 2096-102.
72. Lycklama a Nijeholt GJ, Barkhof F, Scheltens P, et al. MR of the spinal cord in multiple sclerosis: relation to clinical subtype and disability. *AJNR American journal of neuroradiology* 1997; **18**(6): 1041-8.
73. Shintaku M, Hirano A, Llena JF. Increased diameter of demyelinated axons in chronic multiple sclerosis of the spinal cord. *Neuropathology and applied neurobiology* 1988; **14**(6): 505-10.
74. Klein JP, Arora A, Neema M, et al. A 3T MR imaging investigation of the topography of whole spinal cord atrophy in multiple sclerosis. *AJNR American journal of neuroradiology* 2011; **32**(6): 1138-42.
75. Petzold A, Gveric D, Groves M, et al. Phosphorylation and compactness of neurofilaments in multiple sclerosis: indicators of axonal pathology. *Experimental neurology* 2008; **213**(2): 326-35.
76. Petzold A, Tozer DJ, Schmierer K. Axonal damage in the making: neurofilament phosphorylation, proton mobility and magnetisation transfer in multiple sclerosis normal appearing white matter. *Experimental neurology* 2011; **232**(2): 234-9.
77. Kidd D, Barkhof F, McConnell R, Algra PR, Allen IV, Revesz T. Cortical lesions in multiple sclerosis. *Brain : a journal of neurology* 1999; **122 (Pt 1)**: 17-26.
78. Geurts JJ, Bo L, Pouwels PJ, Castelijns JA, Polman CH, Barkhof F. Cortical lesions in multiple sclerosis: combined postmortem MR imaging and histopathology. *AJNR American journal of neuroradiology* 2005; **26**(3): 572-7.
79. Kangarlu A, Bourekas EC, Ray-Chaudhury A, Rammohan KW. Cerebral cortical lesions in multiple sclerosis detected by MR imaging at 8 Tesla. *AJNR American journal of neuroradiology* 2007; **28**(2): 262-6.
80. Schmierer K, Parkes HG, So PW, et al. High field (9.4 Tesla) magnetic resonance imaging of cortical grey matter lesions in multiple sclerosis. *Brain : a journal of neurology* 2010; **133**(Pt 3): 858-67.
81. Geurts JJ, Blezer EL, Vrenken H, et al. Does high-field MR imaging improve cortical lesion detection in multiple sclerosis? *Journal of neurology* 2008; **255**(2): 183-91.
82. Nelson F, Poonawalla AH, Hou P, Huang F, Wolinsky JS, Narayana PA. Improved identification of intracortical lesions in multiple sclerosis with phase-

sensitive inversion recovery in combination with fast double inversion recovery MR imaging. *AJNR American journal of neuroradiology* 2007; **28**(9): 1645-9.
83. Nelson F, Poonawalla A, Hou P, Wolinsky JS, Narayana PA. 3D MPRAGE improves classification of cortical lesions in multiple sclerosis. *Multiple sclerosis (Houndmills, Basingstoke, England)* 2008; **14**(9): 1214-9.
84. Nelson F, Datta S, Garcia N, et al. Intracortical lesions by 3T magnetic resonance imaging and correlation with cognitive impairment in multiple sclerosis. *Multiple sclerosis (Houndmills, Basingstoke, England)* 2011; **17**(9): 1122-9.
85. Sethi V, Yousry TA, Muhlert N, et al. Improved detection of cortical MS lesions with phase-sensitive inversion recovery MRI. *Journal of neurology, neurosurgery, and psychiatry* 2012; **83**(9): 877-82.
86. Sethi V, Muhlert N, Ron M, et al. MS cortical lesions on DIR: not quite what they seem? *PLoS One* 2013; **8**(11): e78879.
87. Kearney H, Yiannakas MC, Abdel-Aziz K, et al. Improved MRI quantification of spinal cord atrophy in multiple sclerosis. *Journal of magnetic resonance imaging : JMRI* 2013.
88. Nagara H, Inoue T, Koga T, Kitaguchi T, Tateishi J, Goto I. Formalin fixed brains are useful for magnetic resonance imaging (MRI) study. *Journal of the neurological sciences* 1987; **81**(1): 67-77.
89. Tovi M, Ericsson A. Measurements of T1 and T2 over time in formalin-fixed human whole-brain specimens. *Acta radiologica (Stockholm, Sweden : 1987)* 1992; **33**(5): 400-4.
90. Blamire AM, Rowe JG, Styles P, McDonald B. Optimising imaging parameters for post mortem MR imaging of the human brain. *Acta radiologica (Stockholm, Sweden : 1987)* 1999; **40**(6): 593-7.
91. Schmierer K, Thavarajah JR, An SF, Brandner S, Miller DH, Tozer DJ. Effects of formalin fixation on magnetic resonance indices in multiple sclerosis cortical gray matter. *Journal of magnetic resonance imaging : JMRI* 2010; **32**(5): 1054-60.
92. Schumann CM, Buonocore MH, Amaral DG. Magnetic resonance imaging of the post-mortem autistic brain. *Journal of autism and developmental disorders* 2001; **31**(6): 561-8.
93. Pfefferbaum A, Sullivan EV, Adalsteinsson E, Garrick T, Harper C. Postmortem MR imaging of formalin-fixed human brain. *NeuroImage* 2004; **21**(4): 1585-95.
94. Schmierer K, Wheeler-Kingshott CA, Tozer DJ, et al. Quantitative magnetic resonance of postmortem multiple sclerosis brain before and after fixation. *Magnetic resonance in medicine* 2008; **59**(2): 268-77.
95. Kim TH, Zollinger L, Shi XF, Rose J, Jeong EK. Diffusion tensor imaging of ex vivo cervical spinal cord specimens: the immediate and long-term effects of fixation on diffusivity. *Anatomical record (Hoboken, NJ : 2007)* 2009; **292**(2): 234-41.
96. De Groot CJ, Bergers E, Kamphorst W, et al. Post-mortem MRI-guided sampling of multiple sclerosis brain lesions: increased yield of active demyelinating and (p)reactive lesions. *Brain : a journal of neurology* 2001; **124**(Pt 8): 1635-45.
97. Schmierer K, Scaravilli F, Barker GJ, Gordon R, MacManus DG, Miller DH. Stereotactic co-registration of magnetic resonance imaging and histopathology in

post-mortem multiple sclerosis brain. *Neuropathology and applied neurobiology* 2003; **29**(6): 596-601.
98. Nijeholt GJ, Nicolay K, Barkhof F. Postmortem MR appearance of the spinal cord in MS at 4.7 T (P306). *Journal of neurology* 1997; **244(Suppl)**: S65-S6.
99. Bot J, Kamphorst W, Barkhof F, et al. Post-mortem MR appearnace of Spinal Multiple Sclerosis at 4.7T: correlation with histopathology. *Proc ISMRM 1999* 1999; (1): 998.
100. Mottershead JP, Schmierer K, Clemence M, et al. High field MRI correlates of myelin content and axonal density in multiple sclerosis--a post-mortem study of the spinal cord. *Journal of neurology* 2003; **250**(11): 1293-301.
101. Gilmore CP, Geurts JJ, Evangelou N, et al. Spinal cord grey matter lesions in multiple sclerosis detected by post-mortem high field MR imaging. *Multiple sclerosis (Houndmills, Basingstoke, England)* 2009; **15**(2): 180-8.
102. Klawiter EC, Schmidt RE, Trinkaus K, et al. Radial diffusivity predicts demyelination in ex vivo multiple sclerosis spinal cords. *NeuroImage* 2011; **55**(4): 1454-60.
103. Budde MD, Kim JH, Liang HF, et al. Toward accurate diagnosis of white matter pathology using diffusion tensor imaging. *Magnetic resonance in medicine* 2007; **57**(4): 688-95.
104. MacKay A, Whittall K, Adler J, Li D, Paty D, Graeb D. In vivo visualization of myelin water in brain by magnetic resonance. *Magnetic resonance in medicine* 1994; **31**(6): 673-7.
105. Gersonde K, Tolxdorff T, Felsberg L. Identification and characterization of tissues by T2-selective whole-body proton NMR imaging. *Magnetic resonance in medicine* 1985; **2**(4): 390-401.
106. Menon RS, Mackay AL, Flibotte S, Hailey JRT. Quantitative separation of NMR images of water in wood on the basis of T2. *Journal of Magnetic Resonance* 1989; **82**: 205-10.
107. Menon RS, Allen PS. Application of continuous relaxation time distributions to the fitting of data from model systems and excised tissue. *Magnetic resonance in medicine* 1991; **20**(2): 214-27.
108. Whittall KP, MacKay AL, Graeb DA, Nugent RA, Li DK, Paty DW. In vivo measurement of T2 distributions and water contents in normal human brain. *Magnetic resonance in medicine* 1997; **37**(1): 34-43.
109. Moore GR, Leung E, MacKay AL, et al. A pathology-MRI study of the short-T2 component in formalin-fixed multiple sclerosis brain. *Neurology* 2000; **55**(10): 1506-10.
110. Laule C, Leung E, Lis DK, et al. Myelin water imaging in multiple sclerosis: quantitative correlations with histopathology. *Multiple sclerosis (Houndmills, Basingstoke, England)* 2006; **12**(6): 747-53.
111. Laule C, Kozlowski P, Leung E, Li DK, Mackay AL, Moore GR. Myelin water imaging of multiple sclerosis at 7 T: correlations with histopathology. *NeuroImage* 2008; **40**(4): 1575-80.
112. Kolind SH, Madler B, Fischer S, Li DK, MacKay AL. Myelin water imaging: Implementation and development at 3.0T and comparison to 1.5T measurements. *Magnetic resonance in medicine* 2009; **62**(1): 106-15.

113. Laule C, Yung A, Pavolva V, et al. High-resolution myelin water imaging in post-mortem multiple sclerosis spinal cord: A case report. *Multiple sclerosis (Houndmills, Basingstoke, England)* 2016.
114. Minty EP, Bjarnason TA, Laule C, MacKay AL. Myelin water measurement in the spinal cord. *Magnetic resonance in medicine* 2009; **61**(4): 883-92.
115. Stanisz GJ, Kecojevic A, Bronskill MJ, Henkelman RM. Characterizing white matter with magnetization transfer and T(2). *Magnetic resonance in medicine* 1999; **42**(6): 1128-36.
116. Remahl S, Hildebrand C. Changing relation between onset of myelination and axon diameter range in developing feline white matter. *Journal of the neurological sciences* 1982; **54**(1): 33-45.
117. Koenig SH, Brown RD, 3rd, Spiller M, Lundbom N. Relaxometry of brain: why white matter appears bright in MRI. *Magnetic resonance in medicine* 1990; **14**(3): 482-95.
118. Bjarnason TA, Vavasour IM, Chia CL, MacKay AL. Characterization of the NMR behavior of white matter in bovine brain. *Magnetic resonance in medicine* 2005; **54**(5): 1072-81.
119. Nave K-A. Glial cells supply nerve fibres with energy-rich metabolic products. 2012. http://www.mpg.de/5786721/glial_cells_metabolites.
120. Harkins KD, Xu J, Dula AN, et al. The microstructural correlates of T1 in white matter. *Magnetic resonance in medicine* 2015.
121. Deoni SC, Dean DC, 3rd, O'Muircheartaigh J, Dirks H, Jerskey BA. Investigating white matter development in infancy and early childhood using myelin water faction and relaxation time mapping. *NeuroImage* 2012; **63**(3): 1038-53.
122. Miele A, Pan J, Walker L, et al. B-75Neural Correlates of Emerging Executive Functioning in 2-5 Year Olds. *Archives of clinical neuropsychology : the official journal of the National Academy of Neuropsychologists* 2014; **29**(6): 565.
123. Spader HS, Ellermeier A, O'Muircheartaigh J, et al. Advances in myelin imaging with potential clinical application to pediatric imaging. *Neurosurgical focus* 2013; **34**(4): E9.
124. Miele A, Pan J, Walker L, et al. B-74The Relationship of Myelin Content and Measures of Executive Functioning in Typically Developing Children. *Archives of clinical neuropsychology : the official journal of the National Academy of Neuropsychologists* 2014; **29**(6): 564.
125. Deoni SC, Dean DC, 3rd, Piryatinsky I, et al. Breastfeeding and early white matter development: A cross-sectional study. *NeuroImage* 2013; **82**: 77-86.
126. Kolind S, Sharma R, Knight S, Johansen-Berg H, Talbot K, Turner MR. Myelin imaging in amyotrophic and primary lateral sclerosis. *Amyotrophic lateral sclerosis & frontotemporal degeneration* 2013; **14**(7-8): 562-73.
127. Kitzler HH, Su J, Zeineh M, et al. Deficient MWF mapping in multiple sclerosis using 3D whole-brain multi-component relaxation MRI. *NeuroImage* 2012; **59**(3): 2670-7.
128. Lankford CL, Does MD. On the inherent precision of mcDESPOT. *Magnetic resonance in medicine* 2013; **69**(1): 127-36.
129. Deoni SC, Kolind SH. Investigating the stability of mcDESPOT myelin water fraction values derived using a stochastic region contraction approach. *Magnetic resonance in medicine* 2014.

130. Zhang J, Kolind SH, Laule C, MacKay AL. How does magnetization transfer influence mcDESPOT results? *Magnetic resonance in medicine* 2014.
131. Ou X, Gochberg DF. MT effects and T1 quantification in single-slice spoiled gradient echo imaging. *Magnetic resonance in medicine* 2008; **59**(4): 835-45.
132. Crooijmans HJ, Scheffler K, Bieri O. Finite RF pulse correction on DESPOT2. *Magnetic resonance in medicine* 2011; **65**(3): 858-62.
133. Bouhrara M, Reiter DA, Celik H, Fishbein KW, Kijowski R, Spencer RG. Analysis of mcDESPOT- and CPMG-derived parameter estimates for two-component nonexchanging systems. *Magnetic resonance in medicine* 2015.
134. Liu F, Block WF, Kijowski R, Samsonov A. Rapid multicomponent relaxometry in steady state with correction of magnetization transfer effects. *Magnetic resonance in medicine* 2015.
135. Agosta F, Rovaris M, Pagani E, Sormani MP, Comi G, Filippi M. Magnetization transfer MRI metrics predict the accumulation of disability 8 years later in patients with multiple sclerosis. *Brain : a journal of neurology* 2006; **129**(Pt 10): 2620-7.
136. Brochet B, Dousset V. Pathological correlates of magnetization transfer imaging abnormalities in animal models and humans with multiple sclerosis. *Neurology* 1999; **53**(5 Suppl 3): S12-7.
137. Schmierer K, Scaravilli F, Altmann DR, Barker GJ, Miller DH. Magnetization transfer ratio and myelin in postmortem multiple sclerosis brain. *Annals of neurology* 2004; **56**(3): 407-15.
138. Filippi M, Rocca MA, Martino G, Horsfield MA, Comi G. Magnetization transfer changes in the normal appearing white matter precede the appearance of enhancing lesions in patients with multiple sclerosis. *Annals of neurology* 1998; **43**(6): 809-14.
139. Moll NM, Rietsch AM, Thomas S, et al. Multiple sclerosis normal-appearing white matter: pathology-imaging correlations. *Annals of neurology* 2011; **70**(5): 764-73.
140. Vavasour IM, Laule C, Li DK, Traboulsee AL, MacKay AL. Is the magnetization transfer ratio a marker for myelin in multiple sclerosis? *Journal of magnetic resonance imaging : JMRI* 2011; **33**(3): 713-8.
141. Naismith RT, Xu J, Tutlam NT, et al. Increased diffusivity in acute multiple sclerosis lesions predicts risk of black hole. *Neurology* 2010; **74**(21): 1694-701.
142. Naismith RT, Xu J, Klawiter EC, et al. Spinal cord tract diffusion tensor imaging reveals disability substrate in demyelinating disease. *Neurology* 2013; **80**(24): 2201-9.
143. Oh J, Zackowski K, Chen M, et al. Multiparametric MRI correlates of sensorimotor function in the spinal cord in multiple sclerosis. *Multiple sclerosis (Houndmills, Basingstoke, England)* 2012.
144. Alexander AL, Hurley SA, Samsonov AA, et al. Characterization of cerebral white matter properties using quantitative magnetic resonance imaging stains. *Brain connectivity* 2011; **1**(6): 423-46.
145. Stikov N, Campbell JS, Stroh T, et al. In vivo histology of the myelin g-ratio with magnetic resonance imaging. *NeuroImage* 2015; **118**: 397-405.
146. Henderson E, McKinnon G, Lee TY, Rutt BK. A fast 3D look-locker method for volumetric T1 mapping. *Magnetic resonance imaging* 1999; **17**(8): 1163-71.

147. Steinhoff S, Zaitsev M, Zilles K, Shah NJ. Fast T(1) mapping with volume coverage. *Magnetic resonance in medicine* 2001; **46**(1): 131-40.
148. Shah NJ, Zaitsev M, Steinhoff S, Zilles K. A new method for fast multislice T(1) mapping. *NeuroImage* 2001; **14**(5): 1175-85.
149. Deichmann R, Hahn D, Haase A. Fast T1 mapping on a whole-body scanner. *Magnetic resonance in medicine* 1999; **42**(1): 206-9.
150. Clare S, Jezzard P. Rapid T(1) mapping using multislice echo planar imaging. *Magnetic resonance in medicine* 2001; **45**(4): 630-4.
151. Smith SA, Edden RA, Farrell JA, Barker PB, Van Zijl PC. Measurement of T1 and T2 in the cervical spinal cord at 3 tesla. *Magnetic resonance in medicine* 2008; **60**(1): 213-9.
152. Hurley SA, Yarnykh VL, Johnson KM, Field AS, Alexander AL, Samsonov AA. Simultaneous variable flip angle-actual flip angle imaging method for improved accuracy and precision of three-dimensional T1 and B1 measurements. *Magnetic resonance in medicine* 2012; **68**(1): 54-64.
153. Wood TC. Improved formulas for the two optimum VFA flip-angles. *Magnetic resonance in medicine* 2015.
154. Oh SH, Bilello M, Schindler M, Markowitz CE, Detre JA, Lee J. Direct visualization of short transverse relaxation time component (ViSTa). *NeuroImage* 2013; **83**: 485-92.
155. Vasilescu V, Katona E, Simplaceanu V, Demco D. Water compartments in the myelinated nerve. III. Pulsed NMR results. *Experientia* 1978; **34**(11): 1443-4.
156. Filippi M, Rocca MA. MRI evidence for multiple sclerosis as a diffuse disease of the central nervous system. *Journal of neurology* 2005; **252 Suppl 5**: v16-24.
157. Bouhrara M, Spencer RG. Improved determination of the myelin water fraction in human brain using magnetic resonance imaging through Bayesian analysis of mcDESPOT. *NeuroImage* 2015.
158. Grossman RI, Gomori JM, Ramer KN, Lexa FJ, Schnall MD. Magnetization transfer: theory and clinical applications in neuroradiology. *Radiographics : a review publication of the Radiological Society of North America, Inc* 1994; **14**(2): 279-90.
159. Crooijmans HJ, Gloor M, Bieri O, Scheffler K. Influence of MT effects on T(2) quantification with 3D balanced steady-state free precession imaging. *Magnetic resonance in medicine* 2011; **65**(1): 195-201.
160. Boulant N. T1 and T2 effects during radio-frequency pulses in spoiled gradient echo sequences. *Journal of magnetic resonance (San Diego, Calif : 1997)* 2009; **197**(2): 213-8.